

Nagra

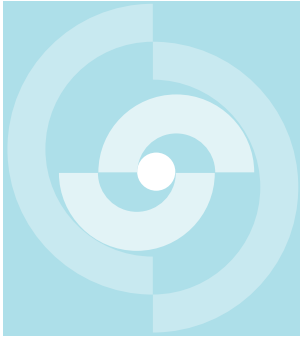
Nationale
Genossenschaft
für die Lagerung
radioaktiver Abfälle

Cédra

Société coopérative
nationale
pour l'entreposage
de déchets radioactifs

Cisra

Società cooperativa
nazionale
per l'immagazzinamento
di scorie radioattive



TECHNICAL REPORT 87-32

Crosshole Investigations – Results from Borehole Radar Investigations

O. Olsson
L. Falk
O. Forslund
L. Lundmark
E. Sandberg

May 1987

Swedish Geological, Sweden

Nagra

Nationale
Genossenschaft
für die Lagerung
radioaktiver Abfälle

Cédra

Société coopérative
nationale
pour l'entreposage
de déchets radioactifs

Cisra

Società cooperativa
nazionale
per l'immagazzinamento
di scorie radioattive

TECHNICAL REPORT 87-32

Crosshole Investigations – Results from
Borehole Radar Investigations

O. Olsson
L. Falk
O. Forslund
L. Lundmark
E. Sandberg

May 1987

Swedish Geological, Sweden

Der vorliegende Bericht betrifft eine Studie, die für das Stripa-Projekt ausgeführt wurde. Die Autoren haben ihre eigenen Ansichten und Schlussfolgerungen dargestellt. Diese müssen nicht unbedingt mit denjenigen des Auftraggebers übereinstimmen.

Le présent rapport a été préparé pour le projet de Stripa. Les opinions et conclusions présentées sont celles des auteurs et ne correspondent pas nécessairement à ceux du client.

This report concerns a study which was conducted for the Stripa Project. The conclusions and viewpoints presented in the report are those of the authors and do not necessarily coincide with those of the client.

Das Stripa-Projekt ist ein Projekt der Nuklearagentur der OECD. Unter internationaler Beteiligung werden von 1980-86 Forschungsarbeiten in einem unterirdischen Felslabor in Schweden durchgeführt. Diese sollen die Kenntnisse auf folgenden Gebieten erweitern:

- hydrogeologische und geochemische Messungen in Bohrlöchern
- Ausbreitung des Grundwassers und Transport von Radionukliden durch Klüfte im Gestein
- Verhalten von Materialien, welche zur Verfüllung und Versiegelung von Endlagern eingesetzt werden sollen
- Methoden zur zerstörungsfreien Ortung von Störzonen im Fels

Seitens der Schweiz beteiligt sich die Nagra an diesen Untersuchungen. Die technischen Berichte aus dem Stripa-Projekt erscheinen gleichzeitig in der NTB-Serie der Nagra.

The Stripa Project is organised as an autonomous project of the Nuclear Energy Agency of the OECD. In the period from 1980-86, an international cooperative programme of investigations is being carried out in an underground rock laboratory in Sweden. The aim of the work is to improve our knowledge in the following areas:

- hydrogeological and geochemical measurement methods in boreholes
- flow of groundwater and transport of radionuclides in fissured rock
- behaviour of backfilling and sealing materials in a real geological environment
- non-destructive methods for location of disturbed zones in the rock

Switzerland is represented in the Stripa Project by Nagra and the Stripa Project technical reports appear in the Nagra NTB series.

Le projet Stripa est un projet autonome de l'Agence de l'OCDE pour l'Energie Nucléaire. Il s'agit d'un programme de recherche avec participation internationale, qui sera réalisé entre 1980 et 1986 dans un laboratoire souterrain, en Suède. Le but de ces travaux est d'améliorer et d'étendre les connaissances dans les domaines suivants:

- mesures hydrogéologiques et géochimiques dans les puits de forage
- chimie des eaux souterraines à grande profondeur
- écoulement des eaux souterraines et transport des radionucléides dans les roches fracturées
- comportement des matériaux de colmatage et de scellement des dépôt finals
- méthodes de localisation non destructive des zones de perturbation de la roche

La Suisse est représentée dans le projet Stripa par la Cédra. Les rapports techniques du projet Stripa sont publiés dans la série des rapports techniques de la Cédra (NTB).

ABSTRACT

The borehole radar method has been developed and applied to the localization and characterization of fracture zones in crystalline rock. In a geological medium such as crystalline rock there is a significant attenuation of the radar waves, increasing with frequency. There is, however, a frequency window from a few MHz to a few hundred MHz where the wave aspect of the radar dominates and acceptable ranges can be achieved.

A new borehole radar system has been designed, built and tested. The system consists of borehole transmitter and receiver probes, a signal control unit for communication with the borehole probes, and a computer unit for storage and display of data. The system can be used both in singlehole and crosshole modes and probing ranges of 115 m and 300 m, respectively, have been obtained at Stripa. The borehole radar is a short pulse system which uses center frequencies in the range 20 to 60 MHz, corresponding to wavelengths of a few meters in the rock.

Single hole reflection measurements have been used to identify fracture zones and to determine their position and orientation. The zones often cause strong and well defined reflections originating from the resistivity change at the edges of the zones. The exact orientation of the zones can be determined by combining data from several boreholes.

Reflections are also observed in crosshole measurements. A new technique has been developed for the analysis of crosshole reflection data which in principle allows the orientation to be uniquely determined if the boreholes are not in the same plane.

The travel time and amplitude of the first arrival measured in a crosshole experiment can be used as input data in a tomographic analysis. Tomographic inversion has given detailed information about the extent of fracture zones in the plane spanned by the boreholes as well as a quantitative estimate of their electrical properties.

The radar method has been intensively tested at Stripa and has been shown to be an efficient instrument for locating and characterizing fracture zones. It is a unique instrument combining a resolution on the order of meters with probing ranges of about a hundred meters.

Keywords: Borehole radar, reflection, crosshole tomography, fracture zones, site investigations.

RESUME

La méthode du radar en puits de forage a été développée et appliquée pour la localisation et la caractérisation de zones fracturées dans une roche cristalline. Les ondes radar sont atténuées de façon significative dans une formation géologique telle des roches cristallines, atténuation qui croît avec la fréquence. On a toutefois un créneau de fréquences allant de quelques MHz à quelques centaines de MHz dans lequel l'aspect ondulatoire du radar prédomine et des portées acceptables peuvent être atteintes.

Un nouveau système de radar pour puits de forage a été conçu, réalisé et testé. Le système comprend une sonde émettrice et réceptrice, une unité de contrôle des signaux assurant la communication avec les sondes, ainsi qu'un ordinateur pour le stockage et la présentation des données. Le système peut être utilisé aussi bien dans un seul puits qu'entre-puits, des portées de 115 m et même 300 m ayant été atteintes à Stripa. Le radar en puits de forage est un système à impulsions courtes qui utilise des fréquences centrales dans le domaine de 20 à 60 MHz, ce qui correspond à des longueurs d'onde de quelques mètres dans la roche.

Des mesures de réflexion à partir d'un puits de forage unique ont été réalisées pour identifier des zones fracturées et pour déterminer leur position et orientation. Ces zones provoquent souvent de fortes réflexions bien définies en raison du saut de résistivité à leur limite. L'orientation exacte de ces zones peut être déterminée en combinant les données provenant de plusieurs puits de forage.

Des réflexions sont également observées dans les mesures entre-puits. Une nouvelle technique a été développée pour l'analyse des données de réflexions entre-puits qui en principe permet la détermination univoque de l'orientation, si les forages ne sont pas situés dans le même plan.

Le temps de parcours et l'amplitude des premières arrivées relevées dans un essai entre-puits peuvent être utilisés comme données d'entrée pour une analyse tomographique. L'inversion tomographique a fourni des informations détaillées sur l'étendue de zones fracturées dans le plan déterminé par les deux forages de même que des estimations quantitatives de leurs propriétés électriques.

La méthode radar a été amplement testée à Stripa et s'est révélée être un instrument efficace pour localiser et caractériser des zones fracturées. C'est un instrument remarquable combinant une résolution de l'ordre de mètres et des portées d'investigation d'environ une centaine de mètres.

ZUSAMMENFASSUNG

Die Methode des Bohrlochradars wurde entwickelt und angewendet um Kluftzonen in kristallinem Fels zu lokalisieren und zu charakterisieren. In einem geologischen Medium wie kristallinem Gestein erfahren die Radarwellen eine signifikante, mit der Frequenz zunehmende Dämpfung. Es gibt jedoch ein Frequenzfenster im Bereich von wenigen MHz bis zu ein paar hundert MHz, in dem der Wellenaspekt des Radars vorherrscht und akzeptable Reichweiten erreicht werden können.

Ein neues Bohrloch-Radarsystem wurde entworfen, gebaut und getestet. Das System besteht aus Bohrloch-Sendersonden und -Empfängersonden, einer Signalkontrolleinheit für die Kommunikation mit den Bohrlochsonden und einem Computer zur Speicherung und Ausgabe von Daten. Das System kann sowohl im Einzelbohrloch-Modus als auch im "Crosshole"-Modus angewendet werden. In Stripa wurden Untersuchungsbereiche von 115 und 300 m erreicht. Das Bohrlochradar ist ein Kurzpuls-System, das Mittelfrequenzen im Bereich von 20 bis 60 MHz benutzt, entsprechend Wellenlängen von ein paar Metern im Fels.

Einzelloch-Reflexionsmessungen wurden benutzt, um Kluftzonen zu identifizieren und ihre Position und räumliche Orientierung zu bestimmen. Diese Zonen verursachen oft starke und gut ausgeprägte Reflexionen, die vom Widerstandswechsel beim Zonenübergang herrühren. Die genaue Orientierung der Zonen kann durch Kombination von Daten mehrerer Bohrlöcher bestimmt werden.

Reflexionen wurden auch bei "Crosshole"-Messungen beobachtet. Eine neue Technik wurde für die Analyse von "Crosshole"-Reflexionsdaten entwickelt, welche im Prinzip erlaubt, die Orientierung zu bestimmen, falls die Bohrlöcher nicht in der gleichen Ebene liegen.

Die Laufzeit und Amplitude des Ersteinsatzes in einem "Crosshole"-Experiment können als Eingabedaten in einer tomographischen Analyse verwendet werden. Tomographische Inversion ergab detaillierte Information über die Ausdehnung der Kluftzonen in der Ebene zwischen den Bohrlöchern, sowie eine quantitative Schätzung ihrer elektrischen Eigenschaften.

Die Radarmethode wurde in Stripa ausgiebig getestet und erwies sich als wirksames Instrument zur Lokalisierung und Charakterisierung von Kluftzonen. Es ist ein einzigartiges Instrument, das eine Auflösung im Meterbereich mit Reichweiten von ca. hundert Metern kombiniert.

TABLE OF CONTENTS

	Page
ABSTRACT	
SUMMARY	
1 INTRODUCTION	1
1.1 General background	1
1.2 Experimental site	2
1.2.1 Borehole configuration	2
1.2.2 Geological characteristic	5
2 THE BOREHOLE RADAR SYSTEM	10
2.1 System design objectives	10
2.2 Description of the radar system	11
2.2.1 General description	11
2.2.2 Measurement procedure	12
2.2.3 Control unit	16
2.2.4 Transmitter	19
2.2.5 Receiver	20
2.2.6 Antennas	20
2.2.7 Fiber optic cable	21
2.2.8 Microcomputer and software	21
3 ELECTROMAGNETIC WAVE PROPAGATION IN ROCK	26
3.1 Electromagnetic waves	26
3.2 Antennas	28
3.3 Electromagnetic properties of rocks	30
3.3.1 Theoretical formulas	30
3.3.2 Experimental results	32
3.4 Propagation of radar waves	43
3.4.1 The radar equation	43
3.4.2 Radar resolution	49
3.5 Reflection by fracture zones	50
3.6 In situ determination of attenuation and velocity	62
4 SINGLE HOLE MEASUREMENTS	68
4.1 The principle of singlehole measurements	68
4.2 Calculation of nomograms for different reflectors	70
4.3 Signal processing	77
4.3.1 Matched filters	78
4.3.2 Bandpass filters	81
4.3.3 Deconvolution filtering	81
4.3.4 Attenuation compensation	83
4.3.5 Reflection coefficient plots	87
4.3.6 Two dimensional filtering	87
4.4 Results from singlehole measurements	90
4.5 Determination of zones	99
5 CROSSHOLE MEASUREMENTS	111
5.1 General	111
5.2 Tomographic analysis	112
5.2.1 Definition of the problem	112

5.2.2	Preparation of data for tomographic inversion	118
5.2.3	Data quality and corrections	121
5.2.4	Results of tomographic inversion	128
5.3	Crosshole reflection analysis	140
5.3.1	Method of analysis	140
5.3.2	Examples of crosshole reflection analysis	144
6	RADAR DESCRIPTION OF THE CROSSHOLE SITE	152
6.1	Definition of fracture zones	152
6.2	The basic model	153
6.3	Geometrical description of all zones	156
7	DISCUSSION AND CONCLUSIONS	179
7.1	The borehole radar system	179
7.2	Reflection measurements	180
7.3	Tomography	182
7.4	The properties of fracture zones	183
7.5	Prospects for future work	184
	ACKNOWLEDGEMENTS	185
	REFERENCES	186
	APPENDICIES	
Appendix A.	Results from singlehole reflection measurements at the Stripa mine.	189
Appendix B.	List of reflections identified at the Crosshole Site.	241
Appendix C.	Results of tomographic inversion of crosshole radar data.	246

SUMMARY

A pulse radar system has been developed and used to investigate fracture zones in crystalline rock. The pulses are a few meters long and by measuring the propagation time one can accurately determine the position of reflectors, such as fracture zones, tunnels etc. The main limitation is the attenuation of the radar waves in the rock: the measured range still exceeds 100 m in Stripa granite, however. It has also been shown experimentally that the fracture zones are effective reflectors of radar waves and that they can early be recognized and positioned by radar waves.

The radar system is a short pulse system operating in the frequency range 20 to 60 MHz. The system consists of borehole transmitter and receiver probes which are connected to a signal control unit by optical fibers. Resistively loaded dipole antennas are used to minimize the time duration of the transmitted pulse. The signal control unit is used for communication with the borehole probes and for control of the measurement. A field computer unit is used for display on a color screen, storage, processing, and printout of the recorded data. The borehole radar system is designed to be used both in singlehole and crosshole measurements.

Measurements of the electrical properties at radar frequencies show that the dielectric constant of granite has a value of about 5 and that it is essentially independent of frequency while the conductivity increases with frequency. The conductivity at radar frequencies is significantly higher than at zero frequency. Samples recovered from fracture zones show a slight increase in dielectric constant while the conductivity is about 30% higher than for unfractured rock. The difference in properties is correlated with the porosity of the samples. The data obtained on the electrical properties of core samples agree with the values obtained from in situ measurements. The velocity of radar pulses is 120 m/us in the Stripa granite corresponding to a dielectric constant of about 6. The attenuation is about 30 dB/100 m at 22 MHz and 50 dB/100m at 60 MHz.

In a singlehole reflection measurement the transmitter and receiver are moved along the same hole at a fixed separation distance and the propagation time of reflected pulses is measured. When the transmitter and receiver are moved along the hole a characteristic pattern is generated on the radar maps depending on the geometry of the

reflectors. Point reflectors give rise to hyperbolas while fracture planes are represented by lines. Reflections are generated by discontinuities in the electric properties of the rock. At Stripa the majority of the reflections have been caused by fracture zones.

The borehole geometry has made it necessary to use dipole antennas which make the radar images axially symmetric. Consequently the complete orientation of a fracture plane can not be determined from one borehole. However, by combining results from several holes a unique determination may be obtained. A technique has been developed which is based on representing the possible orientations in a Wulff projection. The technique has been applied at the Crosshole site where the predictions have been shown to agree with observed positions of fracture zones in the drift and in the boreholes.

In the singlehole reflection measurements fracture zones have been observed at distances of 115 m from the borehole at a frequency of 22 MHz. If the frequency is increased to 60 MHz the range is roughly halved but the resolution is considerably increased. At the higher frequency water filled boreholes with a diameter of 76 mm have been observed at distances up to 40 m.

Reflections are also observed in crosshole measurements. The reflection geometry is different compared to the singlehole measurements and the data have to be analysed in a different fashion. A new technique has been developed for analysis of crosshole reflection data which in principle allows the orientation of a fracture plane to be determined uniquely if the boreholes are not in the same plane. If the holes are in the same plane there appears an ambiguity between two possible orientations.

In crosshole measurements the travel time and the amplitude of the first arrival have been determined. Tomographic inversion has then been made using both travel times and amplitudes. The measurements were made in such a way as to provide an even distribution of rays in the plane between two boreholes and a high ray density. Six tomographic sections were measured, each containing almost 1300 rays.

The travel time and the amplitude of the first arrival have been extracted by an automatic procedure. The data have been converted to residual travel times and amplitudes after integration with borehole coordinate information. The outcome of a tomographic inversion has turned out to be sensitive to errors in the input data, e.g.

coordinate errors and offset errors. Procedures have been developed to identify such errors and correct for them.

The tomograms provide a map of the distribution of radar velocity and attenuation in plane sections between the boreholes. A number of features (fracture zones) characterized by low velocity and high attenuation have been identified. These features appear in the same locations both in travel time and amplitude tomograms. For intersecting crosshole sections the features appear in the same position at the intersection lines. The consistency of the results is a clear indication that the tomograms represent the physical properties of the rock and not some artifact produced by the equipment or the inversion procedure.

A three dimensional model describing the geometry of fracture zones has been constructed of the experimental site in the Stripa Mine. The model is based on results from singlehole reflection, crosshole reflection and crosshole tomography. Four major zones have been identified and also some zones of smaller magnitude. The zones are found to be roughly planar but there are undulations from the average plane. Variations in thickness and electrical properties of the zones have also been noticed. The zones identified at the site belong to two different sets with different orientations. The fracture zones within each set have roughly the same orientation.

The development of the radar technique has opened new possibilities for the investigation of crystalline rock. The investigations at Stripa have demonstrated that radar is an efficient instrument for the location and characterization of fracture zones. The radar is unique in that it combines a resolution on the order of meters with investigation ranges on the order of hundreds of meters. The flexibility of the Stripa radar system, which makes it possible to apply the system in three different investigation modes, has made it possible to construct detailed and reliable three dimensional models of the extent and properties of fracture zones. The velocity and attenuation variations directly measured by radar have been shown to be related to the fracturing and water content of the Stripa granite.

INTRODUCTION

1.1

GENERAL BACKGROUND

The Crosshole Program of the Stripa Project has the objective to develop methods for site characterization which can give information on the suitability of a site for final disposal of radioactive wastes through non-destructive testing. The research program has included development of radar, seismic and hydraulic investigation methods. The radar and seismic methods have been developed with the objective to localize and characterize fracture zones. The results of the geophysical methods (radar and seismics) were then to be compared with the results from the hydraulic investigations to assess how well the geophysical methods could be used to predict the groundwater flow paths through crystalline rock.

Radar has been used for geological characterization since the early 1970'ies. Radar systems operating from the ground surface have been used for the determination of permafrost thickness (Annan and Davis, 1976), groundwater prospecting, peat surveys (Ulriksen, 1982) and the location of buried pipes and cables. Commercially available systems normally operate in the frequency range 80-900 MHz.

Radar has also been used in boreholes and drifts in rock salt mines to detect fractures, rock salt boundaries, drifts, and boreholes (Thierbach, 1974, Unterberger, 1978, Nickel, Sender, Thierbach, Weichart, 1983). The attenuation of radar waves in rock salt is quite small and radar probing ranges of several kilometers have been reported. Crystalline rock is a medium with considerably higher attenuation than rock salt and this requires radar systems with high output power and receiver sensitivity to obtain acceptable investigation range. Prior to the start of the Crosshole Program radar systems for application in crystalline rock have for example been developed by Nilsson (1983) and Wright and Watts (1982).

Based on the experience available from the radar experiments referred to above the radar method was considered to have a potential for giving some of the information on the location, extent and physical properties of fracture zones required in the characterization of a site for future disposal of high level waste. At the onset of the radar development within the Crosshole Program the radar

method was intended for detailed investigations of rock volumes with characteristic dimensions on the order of 50 m. The research program should include testing of available equipment, design and construction of a new system, field tests, and development of interpretation techniques.

The purpose of this report is to describe the the radar method and to give an account of the results achieved during the development of the radar system. The theoretical background of the radar method and its application in a geologic environment are considered in detail. The equipment developed as a part of the project is described as well as the application of the radar system in different measurement configurations. A sample of results obtained from measurements at Stripa is presented in this report to illustrate various aspects of the radar method. The complete set of measurements results obtained during the project is presented in the Appendicies. Results relating to the radar method are also presented in the following Stripa Project reports:

- Olsson, O., Sandberg, E., Nilsson, B. The use of Borehole radar for the detection of fractures in crystalline rock. (IR 83-06).
- Olsson, O. and Sandberg, E. Crosshole investigations - Preliminary design of a new borehole radar system. (IR 84-08).
- Magnusson, K-Å., Carlsten, S., Olsson, O. Crosshole investigations - Physical properties of core samples from borehole F1 and F2. (IR 87-10).

A three dimensional model of the fracture zones discovered by the radar method is included in this report together with a description of the interpretation procedure. In this report the radar model is only to a limited extent compared with results obtained by other methods. A more extensive evaluation and correlation of the radar results with the geological investigations and the results obtained with the seismic and the hydraulic methods will be given in the final report of the Crosshole Program.

1.2 EXPERIMENTAL SITE

1.2.1 Borehole configuration

The bulk of the radar measurements have been performed at a specially prepared experimental site at the 360 m level in the Stripa mine. Six boreholes have been drilled from essentially the same position at the end of a drift. The boreholes

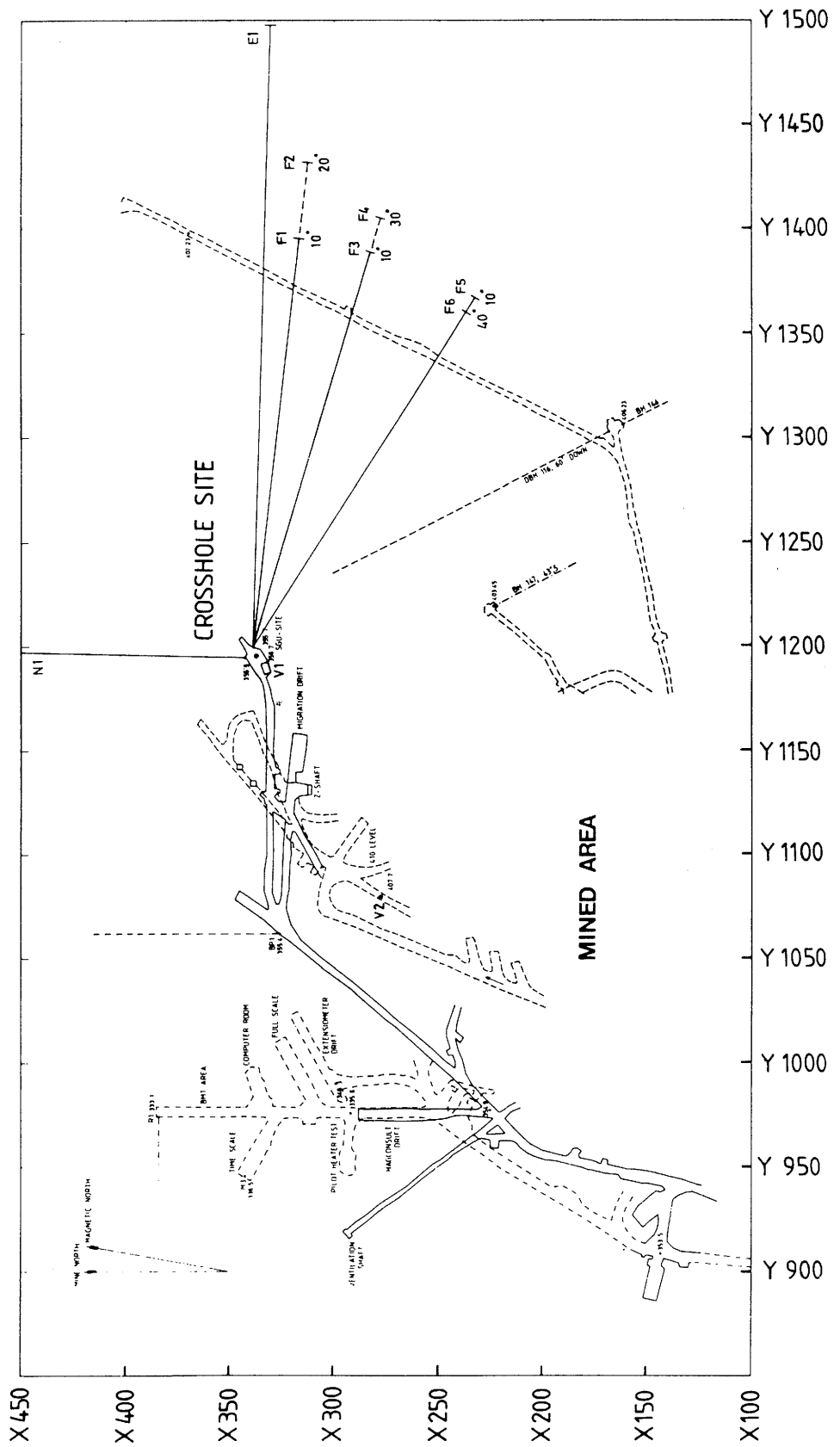


Figure 1.1 Plan view of the Stripa mine at the 360 m and 410 m levels showing the position of the Crosshole site with the boreholes F1 to F6.

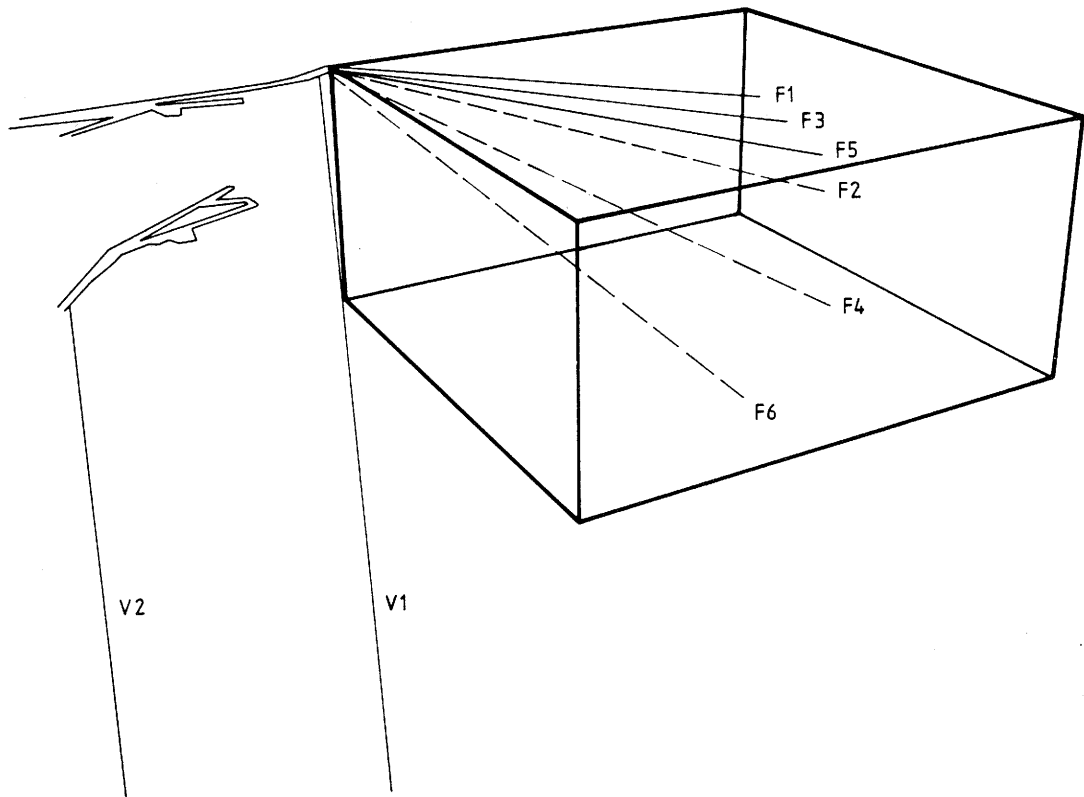


Figure 1.2 Perspective view of the boreholes at the Crosshole site.

Table 1.1. Position of boreholes F1-F6, in the local mine coordinates, declination from mine north (in degrees), inclination below horizontal plane (in degrees), and length (m).

Bore-hole	X	Y	Z	Decl.	Incl.	Length
F1	337.454	1199.291	355.437	96.25	10.20	200.10
F2	337.450	1199.242	355.895	95.86	20.57	249.88
F3	336.508	1199.063	355.434	106.19	10.14	199.80
F4	336.480	1199.125	355.994	106.25	30.96	250.04
F5	335.538	1199.106	355.445	122.14	10.14	200.04
F6	335.575	1199.046	355.741	121.92	40.16	250.05

are drilled in a fanlike fashion in such a way that they outline a tilted pyramid with a height of approximately 200 m and a base of roughly the same length.

The location of the boreholes in relation to the drifts in the mine and a perspective view of the borehole layout is shown in Figures 1.1 and 1.2. The boreholes named F1, F3, and F5 are 200 m in length and the boreholes F2, F4, and F6 250 m. The exact location, length and direction of the boreholes are listed in Table 1.1. An old investigation drift at the 410 m level passes just below and close to the ends of the semi-horizontal holes F1, F3, and F5. The three boreholes E1, N1 and V1 which were drilled as a part of the Hydrogeological and Hydrogeochemical Investigation program and which also originate in the same drift as the F-holes have also been used for radar measurements.

1.2.2 Geological characteristics

The site has been characterized through a comprehensive program of what might be called "conventional" singlehole geological and geophysical investigations. The measurements were performed to provide detailed understanding of the geology of the site and a substantial data base with which the results of the crosshole measurements can be compared (Carlsten, Magnusson and Olsson, 1985).

The borehole investigation program has comprised geological mapping of the core, TV-inspection and geophysical borehole measurements: resistivity, single-point resistance, sonic, gamma-gamma, neutron, self-potential, natural gamma, magnetic susceptibility, temperature and salinity of the

borehole water. Singlehole hydraulic tests have been performed in order to obtain information on the distribution of hydraulic permeability and heads at the site.

The experimental site is situated within a granitic pluton which outcrops in a supracrustal belt with structures striking mainly NE-SW. Due to the relatively mild tectonism since the intrusion, the Stripa granite is generally unfoliated. The Stripa granite is a grey or reddish, fine to medium grained, relatively uraniferous granitic rock. The granitic matrix is composed mainly of quartz, plagioclase, microcline and with smaller amounts of muscovite and chlorite. The granite shows abundant fracturing and deformation on a microscopic scale and frequently also on a megascopic scale as well. The age of the Stripa granite is approximately 1 700 million years. (Wollenberg, Flexser, Anderson, 1980; Carlsten, 1985).

In the detailed characterisation of the Crosshole site presented by Carlsten, Magnusson, and Olsson (1985) the rock has been classified in two categories; rock mass and deformed units. The rock mass consists essentially of the undeformed and unaltered parts of the Stripa granite with no well defined structural features. The rock mass also includes a few thin pegmatites generally less than 0.1 m thick, one aplite (0.15 m), a single 0.2 m thick amphibolite and a few cm-thick quartz veins. The granite of the rock mass between the deformed units is massive, fine to medium grained and grey to pale reddish in colour.

The deformed units correspond to what can loosely be defined as fracture zones. The deformed units generally constitute the most fractured sections in the boreholes. In these major units, tectonized sections, breccias and mylonites generally occur together and form a wide unit with a complex pattern of deformation. These major units are red colored whereas the undeformed granite is grey. The major units also exhibit other signs of alteration such as chloritization and alteration skin on fractures. In the major units cavities often occur filled or partly filled with idiomorphic crystals. Most of these major units can be correlated between the boreholes and the extension of these units can be followed in this way. In all, six major units could be correlated between the boreholes and were named; A, B, C, D, E and F. Also, a minor unit of deformed rock can be traced between the boreholes, named unit 1. However, in a few cases, alteration, tectonized sections, breccias and mylonites also occur in rather thin (up to dm-thick) discrete zones, isolated in wide sections of the undeformed granitic rock mass between the major units.

The following types of alteration have been observed in the core: chloritization, red colouring of the rock mass, red colouring along fractures, hematite stained fracture surfaces and alteration skin on fractures such as ferrogenous alteration.

The breccias constitute rock crushed into fragments which are cemented and healed together by a matrix of complex nature. The matrix consists of quartzitic material, ferrogenous material, calcite, fluorite healing and chlorite healing. There are two dominating types of healing, one dark dense mainly epidote-chlorite matrix and one calcite-fluorite matrix. The calcite matrix often contains idiomorphic crystals of calcite and to a lesser extent fluorite. Idiomorphic crystals are characteristic of open-cavity growth mechanism, where development of typical crystal forms can progress unhindered. Massive calcite healing occurs only in some of the breccias. The fragments in the brecciated rock varies from cm-large angular fragments to finely crushed almost mylonitic rock. The breccias with angular fragments are generally healed by a calcite-fluorite matrix. Also, in some cases the fragments have been elongated. In the breccias open cavities occur with no visible secondary mineralisation and cavities filled or partly filled with idiomorphic crystals, mainly calcite and fluorite. The cavities are often elongated parallel to the breccia and vary in size, from less than 1 mm to 5 mm in width. This is in agreement with measurements on core samples which have shown that the breccias are rather porous and have porosities of approximately 1 % up to 2 % (cf. Section 3.3 and Magnusson, Carlsten and Olsson, 1987). The mylonites are finely crushed rock healed by a very dense often banded matrix and they contain no idiomorphic crystals.

The extension of the major units as they were deduced from the "conventional" singlehole investigations are presented in Figure 1.3 and the borehole intersections of each unit is given in Table 1.2. The units generally have a width ranging from a few meters up to about 10 to 20 meters. The units have a similar strike to NE-NNE and a steep dip toward ESE or WNW. Two of the units namely 1 and C have a dip toward WNW and the rest of the units towards ESE. Unit E constitutes the front of a tectonized and brecciated red-stained granite of which the unit F also constitutes a part. The units E and F are followed by other probably subparallel units not reached by the boreholes, except for the 300 m long borehole E1. However, there also occur some discrete zones of deformation, such as breccia, isolated in the wide sections of grey undeformed granite. These discrete zones are much more difficult to recognize in the adjacent

boreholes and the extension of these zones could not be determined through correlation between the boreholes.

The relatively comprehensive knowledge obtained from the singlehole investigations is due to dense drilling, especially close to the drift, and an extensive investigation program. This set of data has provided a structural model of the site with which the results from the radar, seismic and hydraulic tests have been compared. The inclusion of these novel investigation techniques has of course provided data which has called for a revision of the model presented in Figure 1.3. The correlation of this model and the radar results will be discussed below.

Table 1.2. Position of deformed units in the boreholes F1-F6 as obtained from the single hole investigations (Carlsten, Magnusson, and Olsson, 1985).

Bore-hole	Unit 1	A	B	C
F1	12.3- 24.0	36.1- 39.4	95.5- 97.2	117.5-125.0
F2	12.0- 26.0	42.0- 47.0	111.0-113.0	113.0-126.0
F3	13.2- 15.0	37.0- 41.0	-	93.0-108.0
F4	12.0- 22.0	52.0- 55.0	-	100.0-110.0
F5	10.0- 17.0	36.0- 43.0	-	90.0- 96.0
F6	12.0- 18.0	65.0- 71.0	-	95.0-106.0

Bore-hole	Unit D	E	F
F1	135.9-147.0	172.0-200.1	-
F2	182.3-189.6	201.0-206.0	214.0-249.9
F3	118.0-124.0	151.5-165.0	171.0-200.0
F4	189.0-203.0	225.0-250.0	-
F5	100.0-106.0	138.0-146.0	161.0-200.0
F6	237.0-243.0	-	-

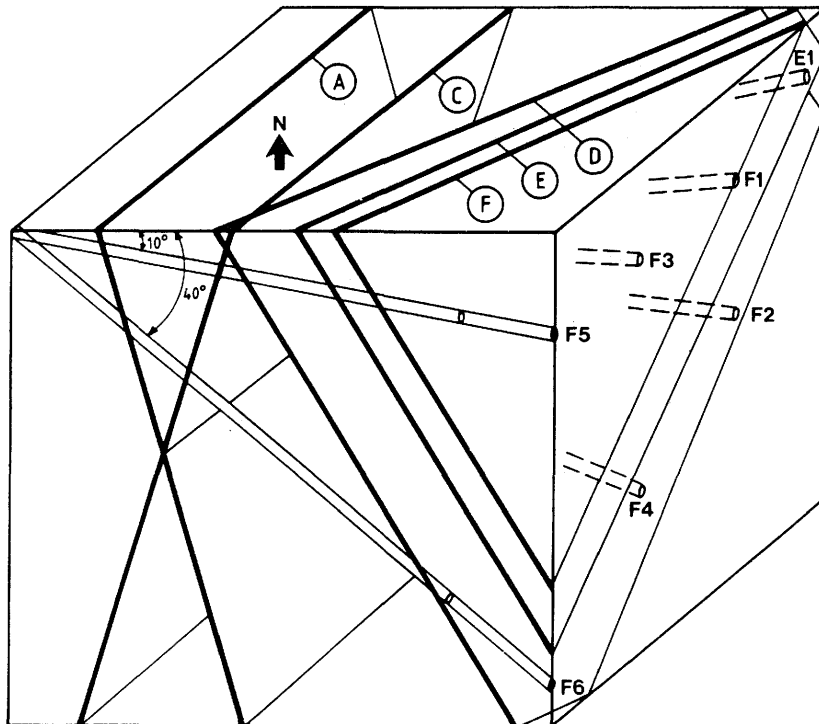


Figure 1.3 Block diagram showing the interpreted extension of the major units based on the singlehole data from the site characterization program (excluding unit B).

THE BOREHOLE RADAR SYSTEM

2.1 SYSTEM DESIGN OBJECTIVES

Before the design of a new radar system was started a thorough analysis was performed to define the basic features of a borehole radar system which would satisfy the objectives of the crosshole program, i.e. to detect fracture zones in granitic rock. This analysis resulted in a set of system design objectives and a preliminary design for a new borehole radar system (Olsson and Sandberg, 1984).

The following criteria were set up for the new radar system:

- The system should be capable of both single- and crosshole measurements.
- There should be no wave propagation on cables along the borehole since such waves would interfere with reflections from objects far from the borehole.
- The dynamic range of the system should be as large as possible to obtain maximum range.
- The system gain should be well calibrated to facilitate accurate measurements of attenuation and subsequent tomographic analysis of the data.
- The system should be capable of measuring travel time in an absolute sense in order to provide data for tomographic analysis.
- It should be possible to perform processing and presentation of data directly in the field.

Based on literature data on the electric properties of rocks and water at high frequencies (Cook, 1975; Nilsson, 1978) it was assumed that frequencies below 100 MHz would give acceptable range and resolution. A total dynamic range, i.e. ratio of transmitted power to detectable power, of 135 dB was considered to be achievable and was expected to result in a probing range of approximately 100 m.

The borehole probes were designed for a borehole diameter of 76 mm and a pressure of 100 Bar, corresponding to a borehole depth of 1000 m.

Prior to the start of this project a borehole radar system had been developed by Nilsson (1983) at Boliden Mineral AB for applications in mineral prospecting. A series of tests was performed with this system to study its capability of mapping fracture zones. Measurements were made in Stripa and Finnsjön and the results indicated that the radar would be a valuable tool for detection of fracture zones (Olsson, Sandberg, and Nilsson, 1983). The experience with the Boliden system was generally positive and it was decided to base the design of the Stripa system on the basic principles which had been applied in the Boliden system.

During the design and construction of the new system it has proved possible to meet all the design criteria. In some aspects it has even been possible to construct a better system than was originally envisaged, e.g. a total dynamic range of 150 dB has been achieved and measurements can be performed in boreholes with a diameter of 56 mm. (The reduction in size of the borehole probes to make them fit in 56 mm holes was funded separately by the Swedish Nuclear Fuel and Waste Management Co., SKB.)

2.2 DESCRIPTION OF THE RADAR SYSTEM

2.2.1 General description

The radar system consists of four different parts:

- a microcomputer with two 5 inch floppy disc units for control of measurements, data storage, data presentation and signal analysis,
- a control unit for timing control, storage and stacking of single radar measurements,
- a borehole transmitter for generating short radar pulses,
- a borehole receiver for detection and digitization of radar pulses.

The radar system works in principle in the following manner: A short current pulse is fed to the transmitter antenna, which generates a radar pulse that propagates through the rock. The pulse is made as short as possible to obtain high resolution. The pulse is received by the same type of antenna, amplified, and registered as a function of time. The receiver may be located in the same borehole as the transmitter or in any other borehole. From the full wave record of the signal the distance (travel time) to a reflector, the strength of the reflection, and the attenuation and

delay of the direct wave between transmitter and receiver may be deduced.

The system works in principle like a sampling oscilloscope, i.e. for each pulse from the transmitter only one sample of the received electric signal is taken at a specific time. When the next pulse is generated a new sample is taken which is displaced slightly in time. Thus, after a number of samples a replica of the entire signal is recorded as a function of time. The sampling frequency and the length and position of the sampled time interval can be set by the operator.

Optical fibers are used for transmission of trig signals from the computer to the borehole probes and for transmission of data from the receiver to the control unit. The optical fibers have no electrical conductivity and thus will not support waves propagating along the borehole. Another advantage of optical fibers is that they can not pick up electrical noise and as the signal is digitized down-hole there will be no deterioration of the signal along the cable. The quality of the results will thus be independent of cable length.

There is no direct connection between the transmitter and the receiver. Both probes are instead connected directly to the control unit and the transmitter and the receiver can be put into the same or separate boreholes. In other words, the radar may be used for both singlehole and crosshole measurements. The system also provides absolute timing of the transmitted pulses and a calibrated gain in the receiver which makes it possible to measure the travel time and the amplitude of the radar pulses in a crosshole measurement to provide the data needed for a tomographic analysis.

The computer unit and the control unit are shown in Figure 2.1 and the borehole probes in Figure 2.2. The block diagram of the control unit, transmitter and receiver is shown in Figure 2.3 and the technical specifications of the system are given in Table 2.1.

2.2.2 Measurement procedure

The radar system is designed to make field operations fast and simple. The performance of a borehole measurement is a relatively straightforward task.

First power (220 V, 50 Hz) is supplied to the computer and the control unit and the RS 232 interfaces of these units are connected with a cable. The three optical fibers connecting the

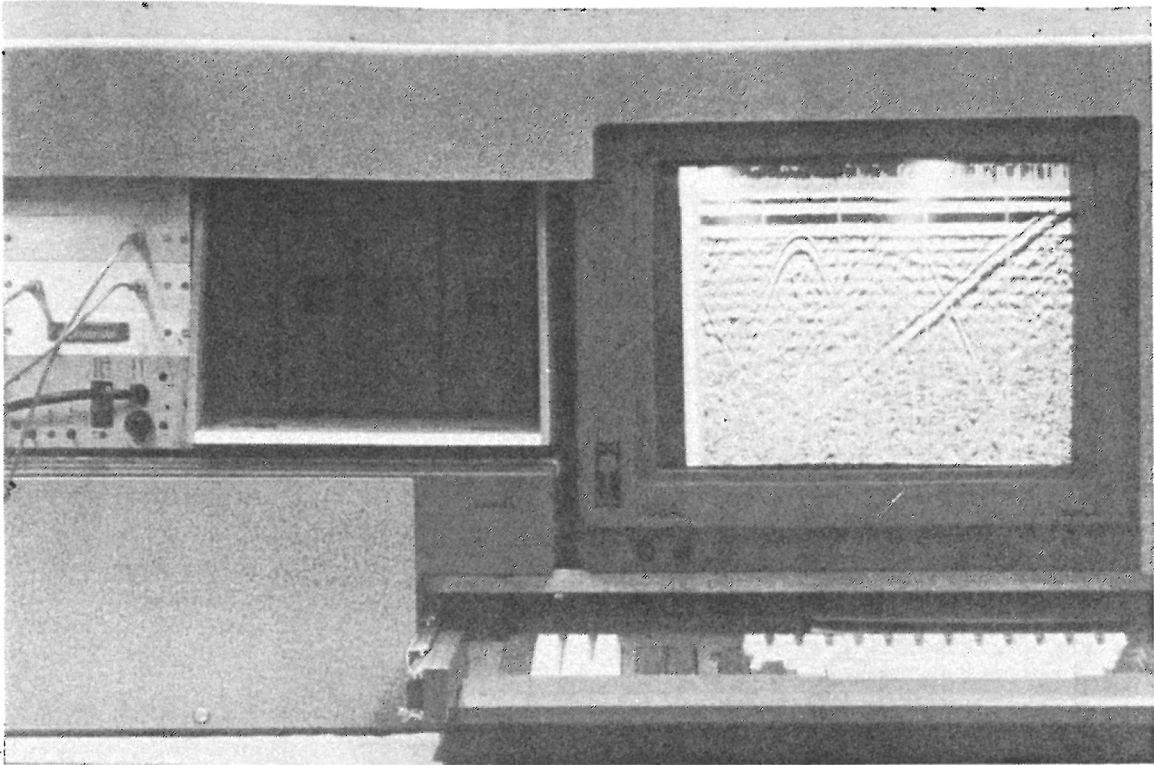


Figure 2.1 The borehole radar system units; computer unit and control unit.

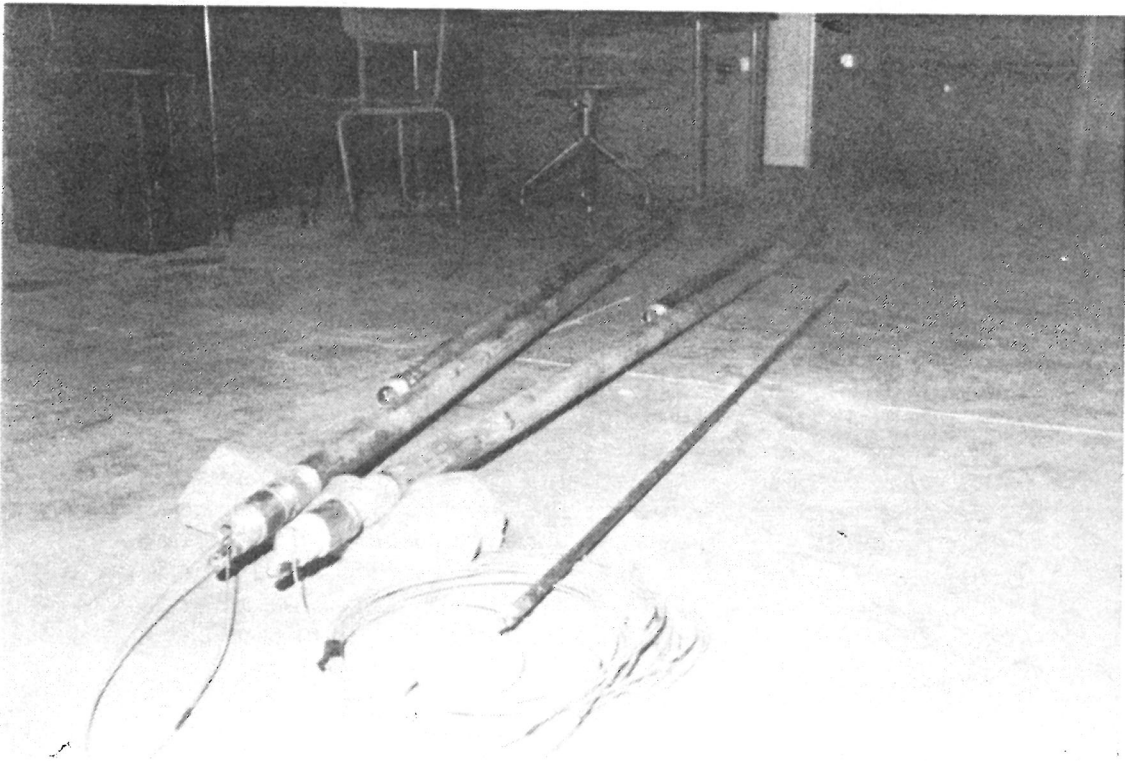


Figure 2.2 Borehole transmitter and receiver with batteries.

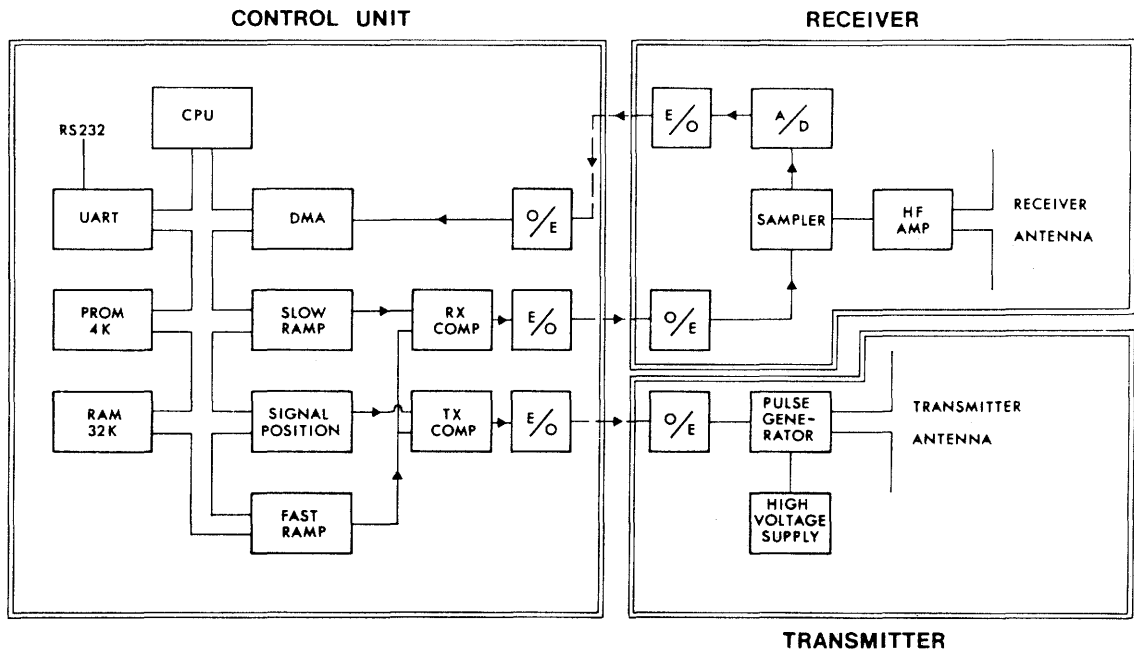


Figure 2.3 Block diagram of the borehole radar system.

control unit to the borehole probes are connected and the battery packs are mounted on the transmitter and receiver respectively. Power is switched on to all units and the measurement program is started on the computer unit (Section 2.2.8).

After initialization of a data disc and selection of the variable parameters the borehole probes are put into the hole. In horizontal holes the probes are pushed into the boreholes by glass fiber rods with a length of 2 meters. If the holes are slightly dipping it is possible for two persons to push the probes to a borehole depth of 250 to 300 m. In vertical holes the probes are lowered down the borehole using a kevlar cable mounted on a winch. In singlehole measurements transmitter and receiver are kept at a fixed distance from each other by means of glass fiber rods both in horizontal and in vertical holes.

Table 2.1. Technical specifications of the borehole radar system.

General

Frequency range	20-80 MHz
Total dynamic range	150 dB
Sampling time accuracy	1 ns
Maximum optical fiber length	1000 m
Maximum operating pressure	100 Bar
Outer diameter of transmitter/receiver	48 mm
Minimum borehole diameter	56 mm

Transmitter

Peak power	500 W
Operating time	10 h
Length	4.8 m
Weight	16 kg

Receiver

Bandwidth	10-200 MHz
A/D converter	16 bit
Least significant bit at antenna terminals	1 μ V
Data transmission rate	1.2 Mb/s
Operating time	10 h
Length	5.4 m
Weight	18 kg

Control unit

Microprocessor	RCA 1806
Clock frequency	5 MHz
Pulse repetition frequency	43.1 kHz
Sampling frequency	30-1000 MHz
No of samples	256-4096
No of stacks	1-32767
Time window	0-11 μ s

When the measurement of a single trace is completed the computer displays the recorded signal as a function of time. The signal is also displayed with amplitude coded in different colors. When several measurements are made their color coded traces are displayed next to each other on the screen and thus a radar map is generated. When a signal trace has been recorded on the floppy discs the computer unit gives an audio signal to indicate that it is time for the operator to move the probes to the next measurement position. Reflection measurements are normally carried out with a separation of measurement points of 1 m. Each measurement takes

about 20-40 s depending on the number of samples and stacks. This corresponds to about 100 m of measured borehole per hour in one meter steps.

2.2.3 Control unit

The control unit is designed to perform a limited number of well defined tasks, namely:

- determination of sampling frequency and position of transmitted pulse in relation to the registered time window (signal position);
- determination of time duration of recorded signal;
- generation of trig pulses to transmitter and receiver;
- storage of digital data from the receiver;
- stacking of a single trace;
- transmission of data to external microcomputer.

The control unit is built round the microprocessor RCA 1806, which is an 8-bit CMOS-processor with 16-bit registers.

The sampling of the received signal is in principle performed as in a sampling oscilloscope, i.e. for each pulse produced by the transmitter only one sample is taken and a replica of the entire signal is obtained as described above. The trig pulses to the borehole probes are generated by comparing two voltages which increase with time at different but constant rates. The principle of the sampling process and the position of the time window is schematically shown in Figures 2.4 and 2.5.

The block named 'fast ramp' in Figure 2.3 generates a sawtooth voltage with a period, $T = 23.2 \mu\text{s}$, corresponding to a frequency of 43.1 kHz. The 'fast ramp' voltage is compared with the 'slow ramp' and when the voltages are equal a trig pulse to the receiver is generated. In the same way the trig pulse to the transmitter is generated by comparing of the 'fast ramp' with a constant voltage termed 'signal position'. The timing diagram is shown in Figure 2.5.

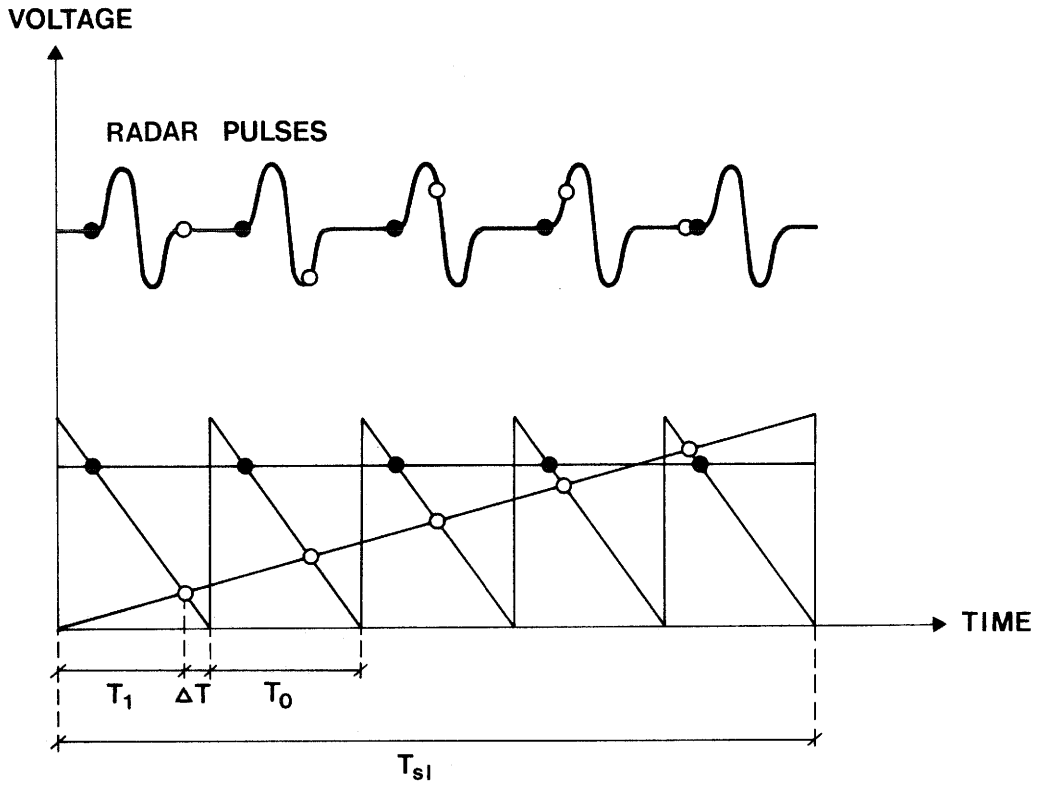


Figure 2.4 Principal diagram of timing signals for sampling process.

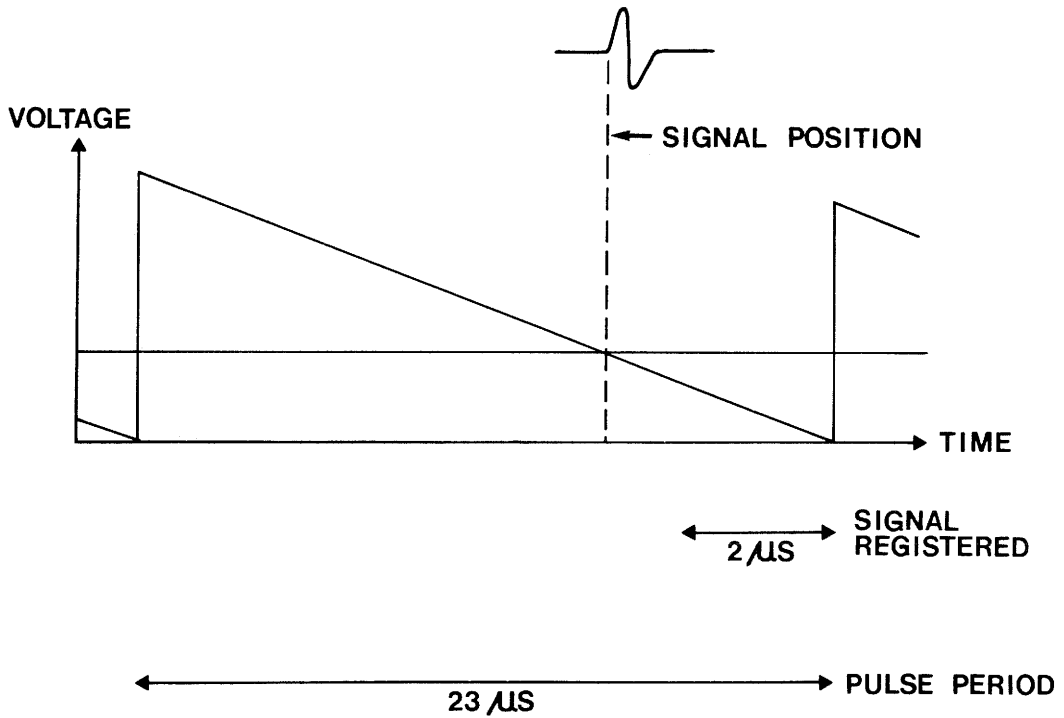


Figure 2.5 Generation of trig signal to transmitter, showing the relation of 'signal position' to the registered time window.

The sampling frequency is determined by the relative rise time of the 'slow ramp' compared with the rise time of the 'fast ramp'. Figure 2.6 shows how the sampling frequency is calculated. From the figure the following equation system is obtained

$$y_1 = \tan \alpha (T_o - \Delta t) \quad (2.1)$$

$$y_2 = \tan \beta \Delta t \quad (2.2)$$

When $y_1 = y_2$ we get

$$\Delta t = \frac{T_o}{(\tan \beta / \tan \alpha) + 1} \quad (2.3)$$

The sampling frequency is as $f_s = 1 / \Delta t$. The relationship between α and β is

$$\frac{\tan \alpha}{\tan \beta} = \frac{T_{s1}}{T_b} \quad (2.4)$$

This gives the following expression for the sampling frequency in terms of the periods of the slow and fast ramps, respectively.

$$f_s = \left[\frac{T_{s1}}{T_b} + 1 \right] \frac{1}{T_o} \quad (2.5)$$

The clock frequency $f_{cl} = 4.313$ MHz is divided by a factor N determined by the operator and fed to a 14-bit counter. The period of the slow ramp is then

$$T_{s1} = 2^{14} N T_{cl} = \frac{2^{14} N}{f_{cl}} \quad (2.6)$$

The period of the fast ramp, T_o , which may be considered the time base of the system, is determined by the clock frequency

$$T_o = 100 T_{cl} = 23.2 \mu s$$

Based on the equations given above the general expression for the sampling frequency can be written in terms of the system parameters

$$f_s = \left[2^{14} N \frac{T_{cl}}{T_b} + 1 \right] \frac{1}{T_o} \quad (2.7)$$

and $N=2N'$ where N' is the input data to the control unit.

The sampling frequency is thus set by giving the appropriate command to the microprocessor with the parameter N' , which may be any integer in the range 2 to 999. The signal position is set by another command followed by an integer parameter, M , in the range 0 to 255. The 'signal position' determines at what time the radar pulse is emitted by the transmitter. The parameter, M , allows the time base, T_b , to be divided into 256 parts and should be chosen in such a way that the radar pulse is received within the registered time window. The length of the registered time window depends on the sampling frequency and the number of samples per trace. The time T_b has been set to 11 μ s.

The 16-bit serial data from the borehole receiver are converted into 8-bit words and stored in the RAM-memory by a DMA-interface (Direct Memory Access) which allows a high data transfer rate (1.2 MBaud). Using the 32 Kbyte memory it is possible to store a maximum of 4096 samples per trace. The 16-bit data is stacked by adding it to a 32-bit word; this allows a maximum of 32767 stacks. When a measurement of a single trace, including stacking, has been completed the data is transferred to an external computer through an RS232 interface.

The program in the control unit memory allows the operator to set the variable parameters from the external computer. The program also controls the measurement and stacking of each trace, and the transfer of data to the external computer (for details see Olsson and Sandberg, 1984).

2.2.4 Transmitter

The transmitter consists of a high voltage generator (DC/DC converter) which charges a transmission line. When a trig pulse is received by the transmitter the transmission line will be discharged through a transistor working in the avalanche mode. The duration of the pulse is proportional to the length of the transmission

line, e.g. a 1 m long transmission line will give a pulse width of 10 ns.

There are restrictions on the pulse repetition period, T_p , due to the charging time of the DC/DC converter and the speed of data transmission from the receiver to the control unit. With the selected pulse repetition rate of 43.1 kHz the DC/DC converter is designed to charge the transmission line within 23.2 μ s. Within the same time the received data must be digitized and transmitted from the receiver to the control unit (Olsson and Sandberg, 1984).

The choice of a fiber optic link between the probes and the control unit makes it necessary to use a rechargeable battery pack as a power supply. The battery pack has a capacity allowing for at least 10 hours of continuous operation.

2.2.5 Receiver

The antenna signal is amplified by a high frequency amplifier before it is sampled by a track and hold circuit. The amplifier is designed to cover the frequency range 10 - 200 MHz. The sampled signal is digitized by an A/D converter with a resolution of 16 bits. The digital data is converted to serial form and transmitted through the optical fiber to the control unit. The transmission of a 16-bit word in 20 μ s requires a data transmission rate of 1.2 Mbits/s. The whole conversion and transmission process takes about 20 μ s which is compatible with the selected pulse repetition frequency, 43.1 kHz.

The power to the receiver is also supplied by means of a rechargeable battery pack.

2.2.6 Antennas

The current pulse generated by the transmitter is converted into radiated energy by the antenna. In an analogous fashion the receiver antenna converts the energy of the electromagnetic wave into a voltage pulse which is amplified and converted into a digital signal in the receiver.

In order to obtain high resolution in range it is necessary to transmit a sufficiently short pulse. Thus, in the construction of a short pulse radar system it is essential to reduce the ringing of the system to a minimum. This implies that all parts of the electronic system must have large bandwidth. In particular the antennas and the impedance matching of the antennas to the electronic circuits must be considered.

Theoretical calculations and experimental tests have been performed for different antenna types and a resistively loaded dipole was finally chosen. The bandwidth of a dipole antenna can be increased by introducing resistive loads increasing with the distance from the feeding point (Wu and King, 1965). The resistive loading of the antennas is accomplished by inserting resistors between sections of brass foil. The electronics package is located in the middle of the dipole antenna and will thus constitute a part of the antenna. The length of the electronics package is 53 cm for both transmitter and receiver.

Antennas have been designed for the following center frequencies: 25, 45, and 60 MHz. The center frequency of each antenna is essentially determined by the antenna length, which is about half a wavelength. The radar propagation velocity in the Stripa granite is 120 m/ μ s and the 25 MHz antenna is thus 2.4 m long.

2.2.7 Fiber optic borehole cable

The borehole probes communicate with the control unit by optical fibers. This will eliminate any disturbing reflections due to wave propagation along the borehole which usually occurs when electrically conductive cables are used. Two fiber links are used to transmit timing information for the sampling process to the transmitter and the receiver and one fiber link is used to transmit the digital data from the receiver to the control unit (Figure 2.3).

The optical fiber cable is of the graded index type. The optically active core has a diameter of 50 μ m and the outer diameter of the glass fiber is 125 μ m. The light source used is a LED transmitting light with a wavelength of 890 nm. Photodiodes are used as optical receivers.

Special optical connectors are mounted on the fiber cables to connect the fiber to the optical transducers or to attach the ends of two fibers to each other. The fiber connectors are screwed into conical adaptors for accurate centering and may be connected or disconnected at will. The connectors are epoxy glued to the fiber and polished to reduce energy losses in the joints.

2.2.8 Micro computer and software

The microcomputer is an ABC806 standard desktop computer system which has been mounted into a special field box to make it more rugged and easy

to transport. The microcomputer is based on the Z80 8-bit microprocessor and runs under the operating system ABC-DOS. The system includes two 5-inch floppy disk units where the measured data is stored. The radar system software includes the following facilities:

- selection of parameters controlling the measurement, e.g signal position, sampling frequency, number of samples and number of stacks;
- control of measurement;
- display of radar results on color screen or matrix printer;
- signal processing including Fourier transformation, correlation, deconvolution and/or bandpass filtering;
- display of the signal or spectrum of single traces.

The software package developed for the borehole radar is written in BASIC II, which is a dialect of Basic supplied with the microcomputer ABC806.

The borehole radar software package consists of a main program, called RADAR, and several subprograms which are used to perform different operations. The radar program package is initiated by the program COMSTART. This program loads the FFT routines, which are written in assembler, allocates memory, and sets a number of default parameters. The program also reads and loads parameters from the status and information files on the data disc before it chains to the main program, RADAR. All subprograms can be reached from the main program; when the execution of a subprogram is completed the control returns to the main program. The general structure of the program package is shown in Figure 2.7. The command menus of the main program and the subprograms are shown in Figure 2.8.

The software package consists of the following programs:

Program	Function
COMSTART	- startup program, setting of default parameters
RADAR	- main program, analysis and display of individual measurements
MEASURE	- control of measurement, selection of variable parameters, input of information about measurement, display of data
PLOTTIME	- plot of radar data in time domain
PLOTFFT	- plot of data in Fourier domain
INITPARA	- initialization of filter parameters
AUTO	- signal processing of complete borehole measurement
SPECIAL	- extraction of travel times and amplitudes of first arrival
BACKUP	- data backup program

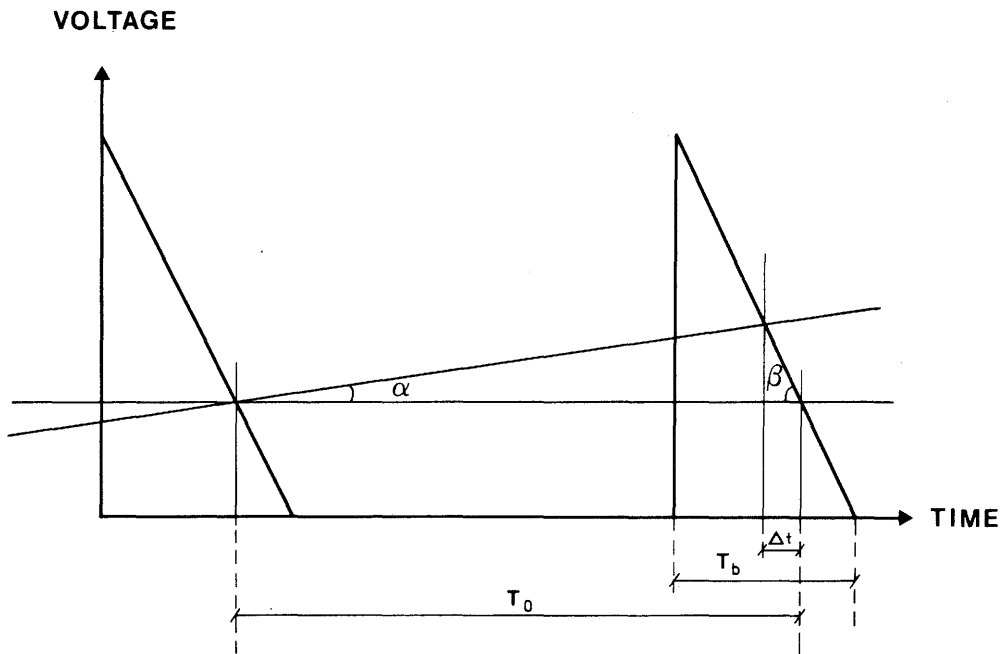


Figure 2.6 Timing diagram used for calculation of sampling frequency.

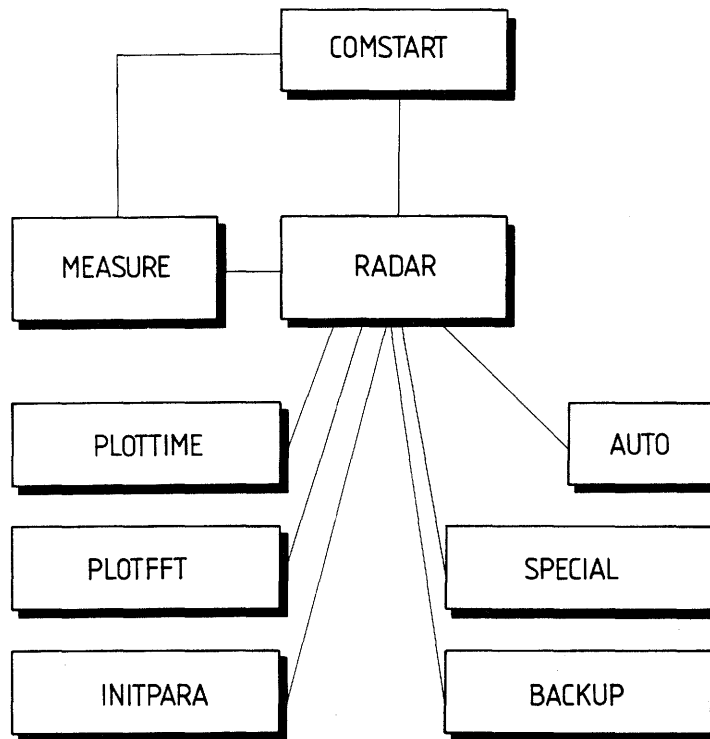


Figure 2.7 Block diagram of the borehole radar software package.

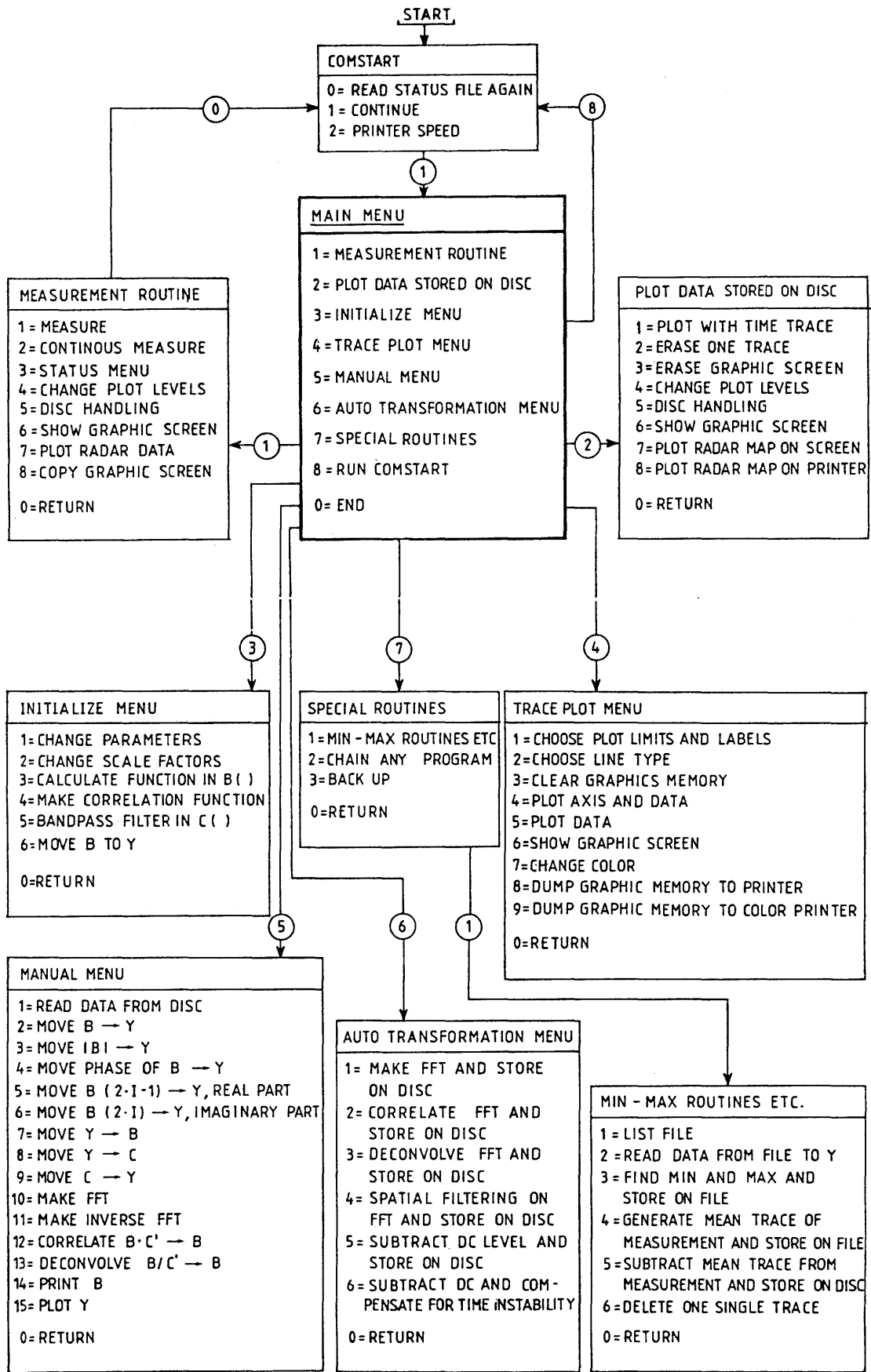


Figure 2.8 Flow chart and command menus of the borehole radar software package.

3.1 ELECTROMAGNETIC WAVES

In a radar system the propagation time of a pulse is used to determine the distance to a reflecting object. This simple principle requires that the pulse is sufficiently short to allow an accurate measurement of the time. It is also necessary that the medium allows more propagation of a constant velocity and without too much attenuation of the pulse.

Both conditions can be satisfied in rock for radio waves, though the practical limitations are quite severe. A radar pulse can never be shorter than the wavelengths used to propagate the pulse so it would be preferable in this respect to use short wavelengths. On the other low attenuation is only possible for sufficiently long wavelengths. It is interesting that the necessary compromise leads to a few meters wavelength both for radio waves and seismic waves in the investigation of the crosshole site although the actual speeds of propagation differ enormously.

The speed and attenuation of radio waves in rock can be derived in detail from the electromagnetic equations. This allows both an accurate formulation of the conditions for wavepropagation and a theoretical calculation of the achievable range and resolution which turns out to be in excellent agreement with the results.

In practically all current radar applications radar waves propagate through the atmosphere where the attenuation of the radar waves is small. The attenuation of electromagnetic waves in geological media is normally high and shows a strong frequency dependance. Geological media are generally opaque at optical and microwave frequencies while at low frequencies (below 1 MHz) the electromagnetic field loses its wave character and diffusion type processes dominate. Radar systems designed for geological work use a frequency window where the wave character of the field is still significant and the attenuation is low enough to yield useful probing ranges.

In the description of radar propagation in geological media it is useful to define a number of

concepts relating to wave propagation in media with significant attenuation.

The electromagnetic field is described by Maxwell's equations (a time dependence $\exp(-i\omega t)$ is suppressed in the following equations):

$$\nabla^2 \bar{E} + k^2 \bar{E} = 0 \quad (3.1)$$

where

$$k^2 = \omega^2 \epsilon \mu + i \omega \mu \sigma \quad (3.2)$$

ϵ = dielectric constant
 μ = magnetic permeability
 σ = electrical conductivity
 $\omega = 2 f\pi$ = angular frequency

One solution of equation (3.1) is a plane wave propagating for example in the z-direction and linearly polarised along the x-axis.

$$E_x(z,t) = E_x(0) \exp(i(kz - \omega t)) \quad (3.3)$$

The parameter k is termed the wave number and has the dimension of inverse length. The real part of k is associated with the wavelength (λ) and the imaginary part with the attenuation of the wave

$$\begin{aligned} k_{re} &= 2\pi / \lambda \\ k_{im} &= \alpha = 1 / \delta \end{aligned} \quad (3.4)$$

The parameter α is called the attenuation constant and its inverse, δ , is the skin depth which is a measure of the distance over which the amplitude of a plane wave decreases by a factor $1/e$.

It is also useful to define the parameter Q which determines whether a medium will support electromagnetic wave propagation or not. Q is the quotient of the real to the imaginary part of the square of the wave number k .

$$Q = \frac{\omega \epsilon}{\sigma} \quad (3.5)$$

The real and imaginary parts of the wave number, k , may be expressed in terms of Q in order to demonstrate its physical significance

$$k = k_{re} + ik_{im}$$

$$k_{re} = \omega \left[\frac{\epsilon \mu}{2} \right]^{1/2} \left\{ \left[1 + \left(\frac{1}{Q} \right)^2 \right]^{1/2} + 1 \right\}^{1/2} \quad (3.6)$$

$$k_{im} = \omega \left[\frac{\epsilon \mu}{2} \right]^{1/2} \left\{ \left[1 + \left(\frac{1}{Q} \right)^2 \right]^{1/2} - 1 \right\}^{1/2}$$

In the high frequency limit where $Q \gg 1$ we obtain the following expression for the skindepth

$$\delta = \frac{2}{\sigma} \sqrt{\frac{\epsilon}{\mu}} = \frac{2\rho}{Z} \quad (3.7)$$

where Z is the wave impedance and ρ the resistivity of the medium. The skin depth thus depends on the electrical permittivity and conductivity of the medium. In most geological media, except e.g. iron ore, the relative magnetic permeability may be considered constant and close to the vacuum value. Thus its effect may be disregarded in most cases.

Note that the skindepth in this frequency range is independent of the frequency, while for low frequencies it is inversely proportional to the square root of the frequency. This is however only the case if the electrical properties of the rock are independent of the frequency. As will be seen below this is usually not the case. In the high frequency approximation we may express Q in terms of the skindepth and the wavelength in the following manner

$$Q = \pi \frac{\delta}{\lambda} \quad (3.8)$$

Q is a measure of the number of wavelengths that the field will propagate in a given medium before it is significantly attenuated. It is clear that if $Q \gg 1$ electromagnetic energy will propagate as waves and can be described in such terms as propagation, reflection, refraction and so on. If $Q \ll 1$ there will be no wave propagation and diffusion type processes will dominate.

3.2

ANTENNAS

Due to the small radius of the borehole a linear wire antenna must normally be used. A wire antenna

may in some aspects be approximated by an electric dipole. The electric field generated by such an antenna is cylindrically symmetric with respect to the dipole axis and is described by the following equation:

$$\bar{E}(r,t) = \frac{\mu_0}{4\pi} \bar{c}(r) \int a(\theta,\phi) \frac{e^{-\alpha r}}{r} e^{i(2\pi r/\lambda - \omega t)} G(\omega) d\omega \tag{3.9}$$

where $a(\theta,\phi)$ is a function describing the radiation lobes and $G(\omega)$ is the Fourier spectrum of the radiated field close to the antenna. The vector 'c' indicates the direction of the electric field whose amplitude is proportional to the magnitude of the antenna current. The direction of c is given by

$$\bar{c}(r) = (\bar{p} \times \bar{r}) \times \bar{r} \tag{3.10}$$

where 'p' is the orientation of the dipole.

For antennas shorter than a wavelength there will be a single lobe and the maximum of the radiated energy will be in a direction perpendicular to the dipole axis (p). If the antenna is longer than one wavelength the lobe will split up as shown in Figure 3.1.

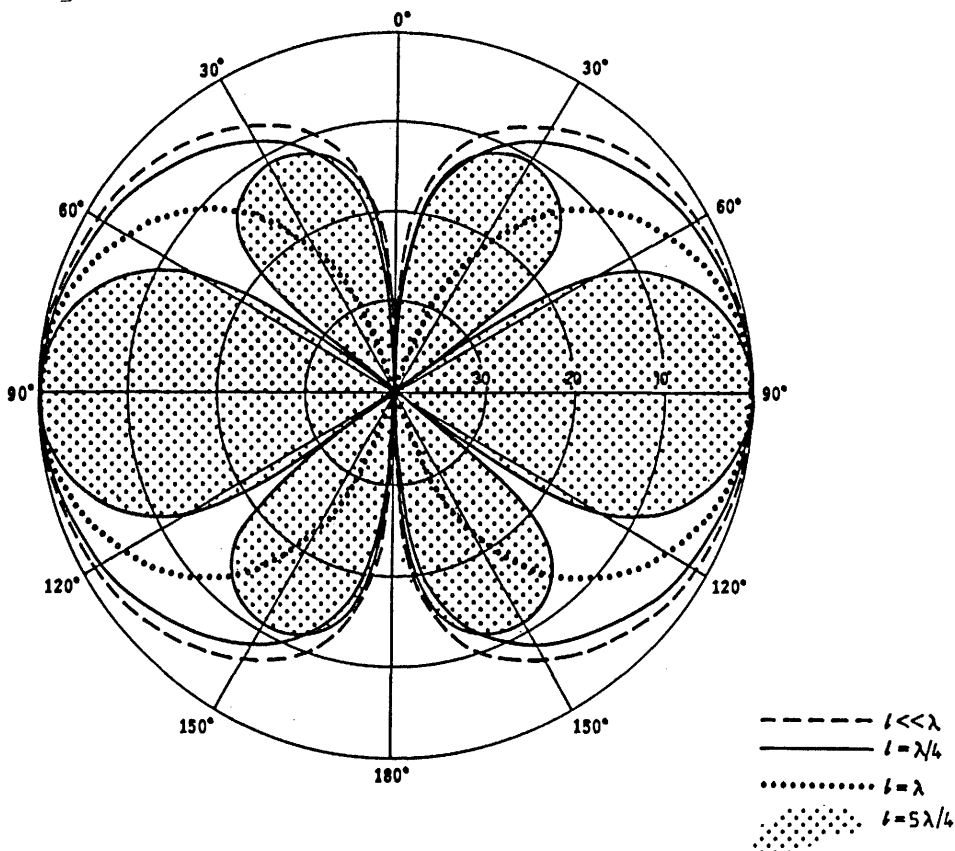


Figure 3.1 Radiation patterns from antennas of different lengths. Power levels are given in dB below maximum power.

In general the electromagnetic field can be described in terms of two orthogonal polarizations defined by the direction of the electric field vector. The field generated by a dipole source is linearly polarized with the electric field in the plane spanned by the dipole and the direction of propagation. Scattering by inhomogeneities in the rock will normally cause depolarization of the field. It should also be noted that the reflection coefficient is different for the two polarizations (see section 3.5).

It follows from equation (3.9) that the amplitude of the electric field decreases due to geometrical spreading (the factor $1/r$) and attenuation, $\exp(-\alpha r)$. The attenuation is generally frequency dependent and consequently a transmitted pulse will change shape due to differences in damping of the different frequency components of the signal.

3.3 ELECTROMAGNETIC PROPERTIES OF ROCK

It was shown in the previous section that the propagation of electromagnetic waves through rock is essentially described by the wave number, k (see equation 3.2). The value of k is a function of the frequency of the applied field and the dielectric constant, magnetic permeability, and electrical conductivity. It should be noted that the values of these parameters are generally frequency dependent. The data published on the electric properties of rocks have mostly been obtained at very low frequencies, which for practical purposes correspond to direct current (DC).

The frequency dependence implies that the character of radar propagation through rock can not be inferred by inserting the commonly measured DC-values of the electric properties into equations (3.2-3.8). Instead the data corresponding to the radar frequencies must be used. The practical possibilities of predicting radar performance in different rocks is limited by the fact that data published on the electrical properties at radar frequencies (above 10 MHz) is relatively scarce.

3.3.1 Theoretical formulas

The electric bulk properties of rocks are determined by the type and distribution of the mineral constituents and the pore fluid. For many rock types the presence of conducting minerals is insignificant and can be neglected. In these cases the bulk conductivity of a rock sample will be determined by the pore volume and the properties of

the pore fluid. An empirical relation was established by Archie (1942) for such rocks relating the bulk conductivity to the pore volume and the conductivity of the pore fluid:

$$\sigma = a \sigma_w \phi^m \quad (3.11)$$

where

σ = formation conductivity
 σ_w = pore fluid conductivity
 ϕ = porosity
 a = dimensionless parameter, for saline solutions
 'a' is approximately 1.
 m = cementation factor, normally in the range 1 to 2.2.

Archie's law was originally established from measurements on sedimentary rocks, but has now been shown to be applicable also to igneous rocks (Brace, Orange, and Madden, 1965; Brace and Orange, 1968; Magnusson, Carlsten, and Olsson, 1987). In igneous rocks, which normally have porosities less than 1 %, surface conduction along thin water films and pore grain interfaces may become significant compared to volume conduction by ions through the pore spaces (Brace, Orange, and Madden, 1965, Nelson, Magnusson, and Rachiele, 1982). The surface conduction effect can be included as a modification to Archie's law by adding a conductive element in parallel to the volume conduction through the pore water

$$\sigma = \sigma_s + \sigma_w \phi^m \quad (3.12)$$

where

σ_s = electrical surface conductivity.

In a theoretical study followed by experiments on artificial rock samples Sen, Scala, and Cohen (1981) studied several models relating the bulk properties of the rock to the properties of the pore fluid and the pore volume. They derived a self-similar model which according to their experiments gives the best fit to the experimental data. The model considers the rock to be composed of nonconducting grains coated by water and it takes into account the local effects around each grain. A basic feature of this model is that it accounts for electrically connected pores even at low porosities. The model results in an equation relating the properties of the rock matrix and the pore fluid to the bulk properties. The formula has the form of the Hanai (1968)-Bruggeman (1935) equation, but is quite different in content. The equation derived by Sen et. al. (1981) has the form:

$$\frac{\epsilon_m^* - \epsilon^*}{\epsilon_m^* - \epsilon_w^*} \left(\frac{\epsilon_w^*}{\epsilon^*} \right)^L = \phi \quad (3.13)$$

where

- ϵ^* = $\epsilon + i (\sigma/\omega)$
 ϵ^* = bulk dielectric constant of water saturated rock
 ϵ_m^* = complex dielectric constant of rock matrix
 ϵ_w^* = complex dielectric constant of pore fluid
 ϕ = porosity
 L = depolarization factor.

In (3.13) $\epsilon^* = k^2/\omega^2 \mu$ is used instead of the wave number, k . The use of either k or ϵ^* is arbitrary and is usually governed by convenience and traditions. It is sometimes customary to give the dielectric constant, ϵ , or the electric conductivity τ or both an imaginary component. This is actually not necessary as the electromagnetic properties of a medium is fully described by the real and imaginary parts of the square of the wavenumber k^2 .

The exponent, L , is called the depolarization factor and is considered to be independent of the frequency, while all other parameters may vary with frequency. Sen et. al. (1981) showed that the depolarization factor characterizes the geometry of the grains in the rock matrix. The value of L is related to the form of the grains in the following way:

- $L=1/3$ for spheres
 $L=0$ for needles with their axis parallel to the field
 $L=1/2$ for cylinders with their axis perpendicular to the field.

In the zero frequency limit equation (3.13) approximates to Archie's law in the form

$$\sigma = \sigma_w \phi^{1/(1-L)}$$

For spheres where $L=1/3$ this gives $\sigma = \sigma_w \phi^{3/2}$.

3.3.2 Experimental results

A total of 94 core samples were taken from the boreholes F1 and F2 in order to study the physical properties and the high frequency electrical properties in particular and to put those properties in relation to the geological characteristics of the core. Measurements have been

made of porosity, density, resistivity, magnetic properties and IP(Induced Polarization)-effect. The samples have been characterized geologically and thin sections were made of 26 samples which were studied in detail. The core samples were divided into two classes; samples taken from undeformed granite (rock mass) and samples taken from the major tectonized units as they had been defined in the "Description of the small scale site" (cf. Section 1.2 and Carlsten, Magnusson, and Olsson, 1985). Out of these samples 39 belonged to the class of undeformed rock and the remaining 55 to tectonized units. The results of these measurements have been presented in detail by Magnusson, Carlsten, and Olsson (1987) and only a brief review will be given here.

The density of the core samples exhibit very small variations around a mean value of $2\ 641\ \text{kg/m}^3$ except for a few very porous samples from unit B. The Stripa granite is essentially nonmagnetic with a mean susceptibility of $8\ 10^{-5}$ SI units. The average IP-effect was found to be 1.56 %. There is no significant difference in IP-values and magnetic properties depending on whether the samples are taken from undeformed or tectonized rock.

The low frequency electrical properties of the rock have been measured both on core samples and in situ. The single point resistance log has the highest resolution and is only sensitive to the conditions in the immediate vicinity of the borehole and can thus be expected to give results comparable with the core sample data. Figure 3.2 shows a densely sampled section of borehole F2. There is a very good correlation of the resistivity measured on core samples and the in situ measured single point resistance. The agreement in the location of the anomalies is excellent but the single point resistance log shows an averaging effect. Thus, we may conclude that the properties measured on the samples are representative of the in situ properties of the rock. The figure also shows good correlation between the fracture frequency and the electrical properties of the rock.

The study of the thin sections shows that the deformation of the rock that is observed on the macroscopic scale is also evident on a microscopic scale. The grain matrix in the tectonized units is more granular and has a much smaller grain size compared to the undeformed rock. In the tectonized units the grains are fractured and microbreccias and cavities occur frequently. This deformation on the microscopic scale as well as the fracturing on the macroscopic scale causes the difference in

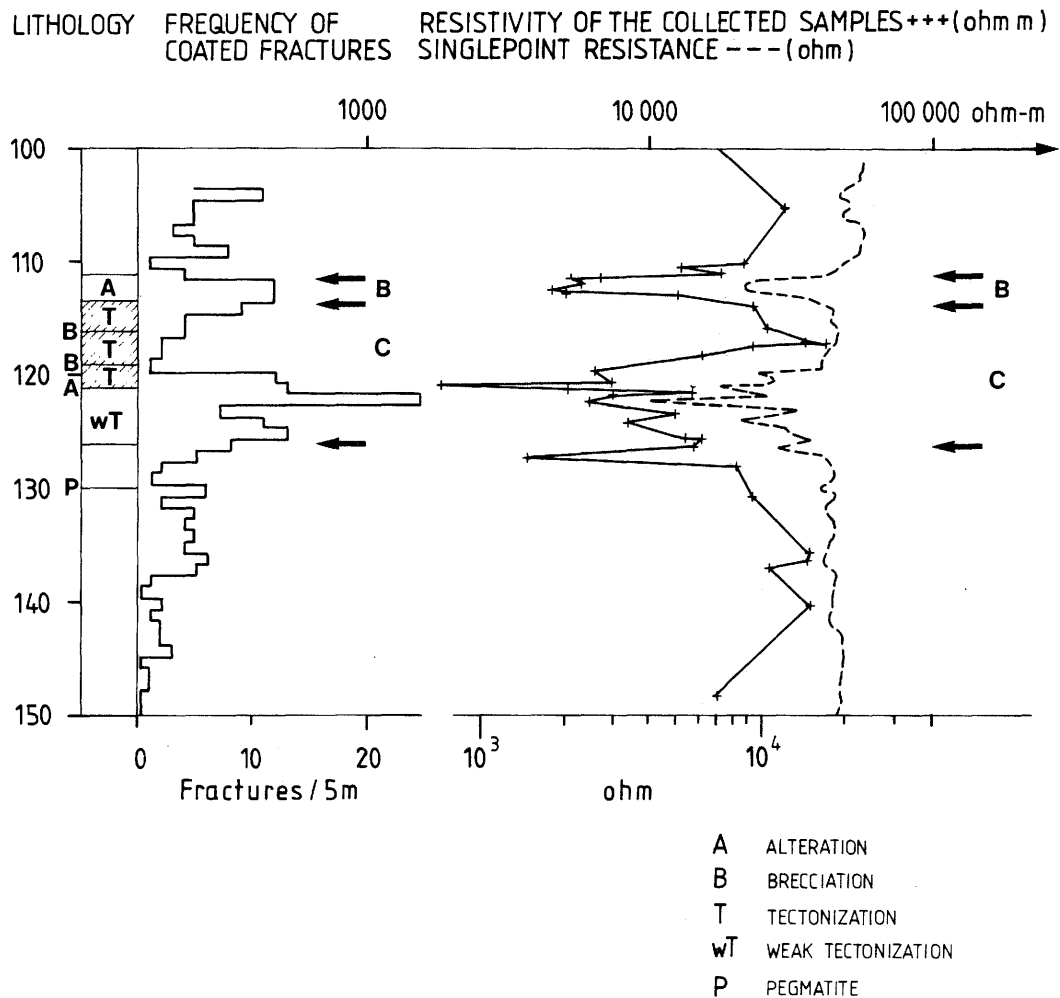


Figure 3.2 Schematic lithology, frequency of coated fractures, resistivity of the collected samples (DC-values) and the in situ measured contact resistance across units B and C in F2 showing that the position of the fracture zones is the same for all types of measurements.

physical properties between the tectonized rock and the undeformed rock.

The porosity which is measured on core samples will basically be representative of the matrix porosity. The reason is simply that porosity can only be measured on intact samples and consequently the samples are not likely to contain any open fractures that cut through the entire sample. The porosity measurements showed an average porosity of 0.25 % for the undeformed rock and a porosity of 0.63 % for the tectonized units, excluding unit B. Unit B is an anomalous unit of rock which has not been found elsewhere in the Crosshole site. It contains numerous cavities and circulation of water in these voids has resulted in a rather intense alteration. It is red colored and intensely fractured. The porosity measured on samples from unit B fall in the range 2 % to 10.5 %.

A cross-plot of the conductivity at zero frequency of the deformed units and the corresponding porosity is shown in Figure 3.3. If a surface conduction effect is included a fit to Archie's law is obtained with a correlation coefficient of -0.72. The cementation factor then becomes 1.5, in good agreement with the theory by Sen et.al. for rock with no preferred direction. (The data from unit B are not included in the fit to Archie's law.) The samples from undeformed rock fall into a cluster with low values both for porosity and resistivity and there is no correlation with Archie's law. The lack of correlation is probably due to measurement errors larger than the variation in properties for these samples.

The high frequency measurements of the electrical properties were carried out at the Department of Applied Geophysics at the University of Luleå, Sweden (Agmalm, 1985). Measurements were made both of dielectric constant and conductivity with a Q-meter where the sample is placed as a dielectric in a capacitor (Sherman, 1983). The properties were measured at 11 different frequencies in the range 25 kHz to 70 MHz. For each sample measurements were made on dry samples and on samples soaked in water with a resistivity of about 40 ohmm.

The dry samples have a dielectric constant with an average value of about 5 essentially independent of frequency (Figure 3.4). The conductivity increases with frequency to the power 0.68. The dry samples exhibit no difference in electric properties between major tectonized units and undeformed rock.

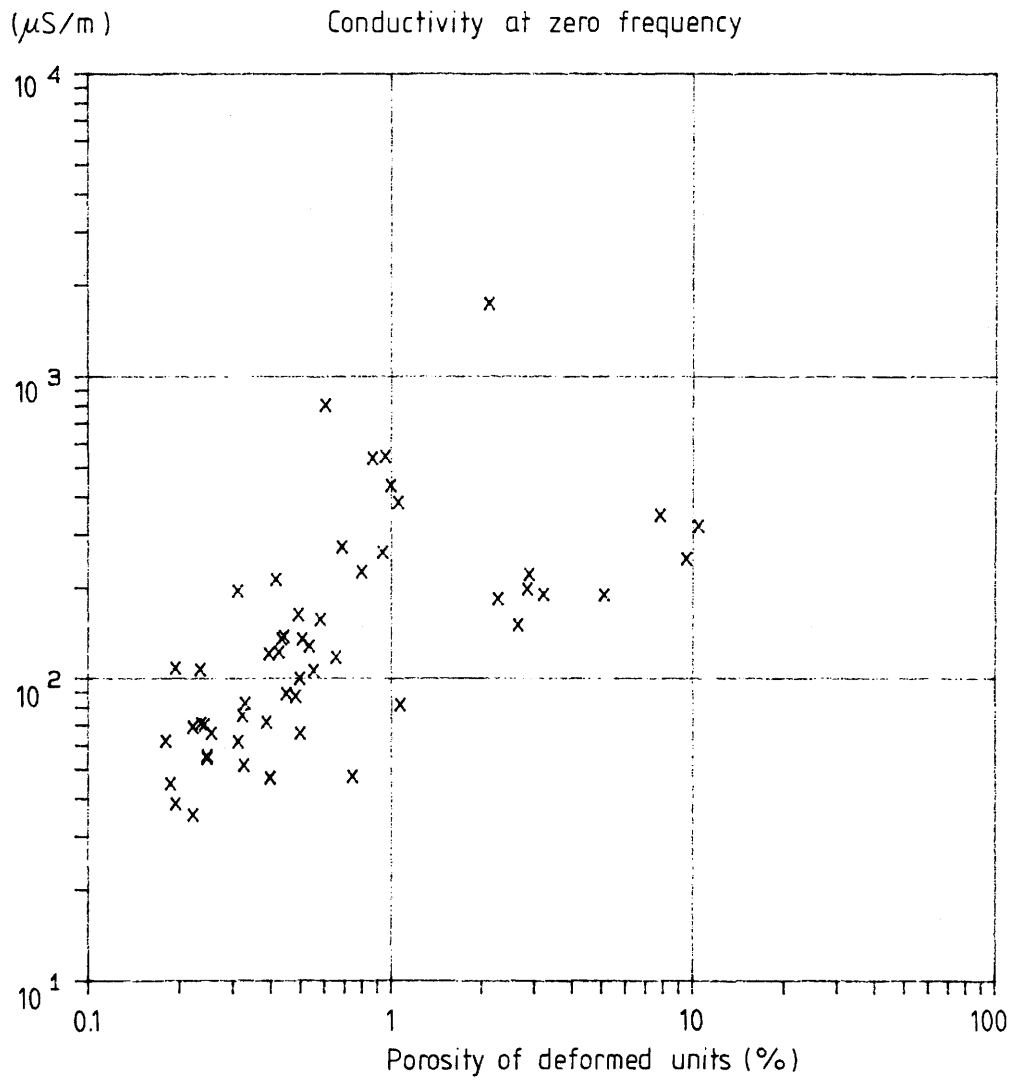


Figure 3.3 Cross-plot of DC-conductivity vs. porosity of samples from the tectonized units.

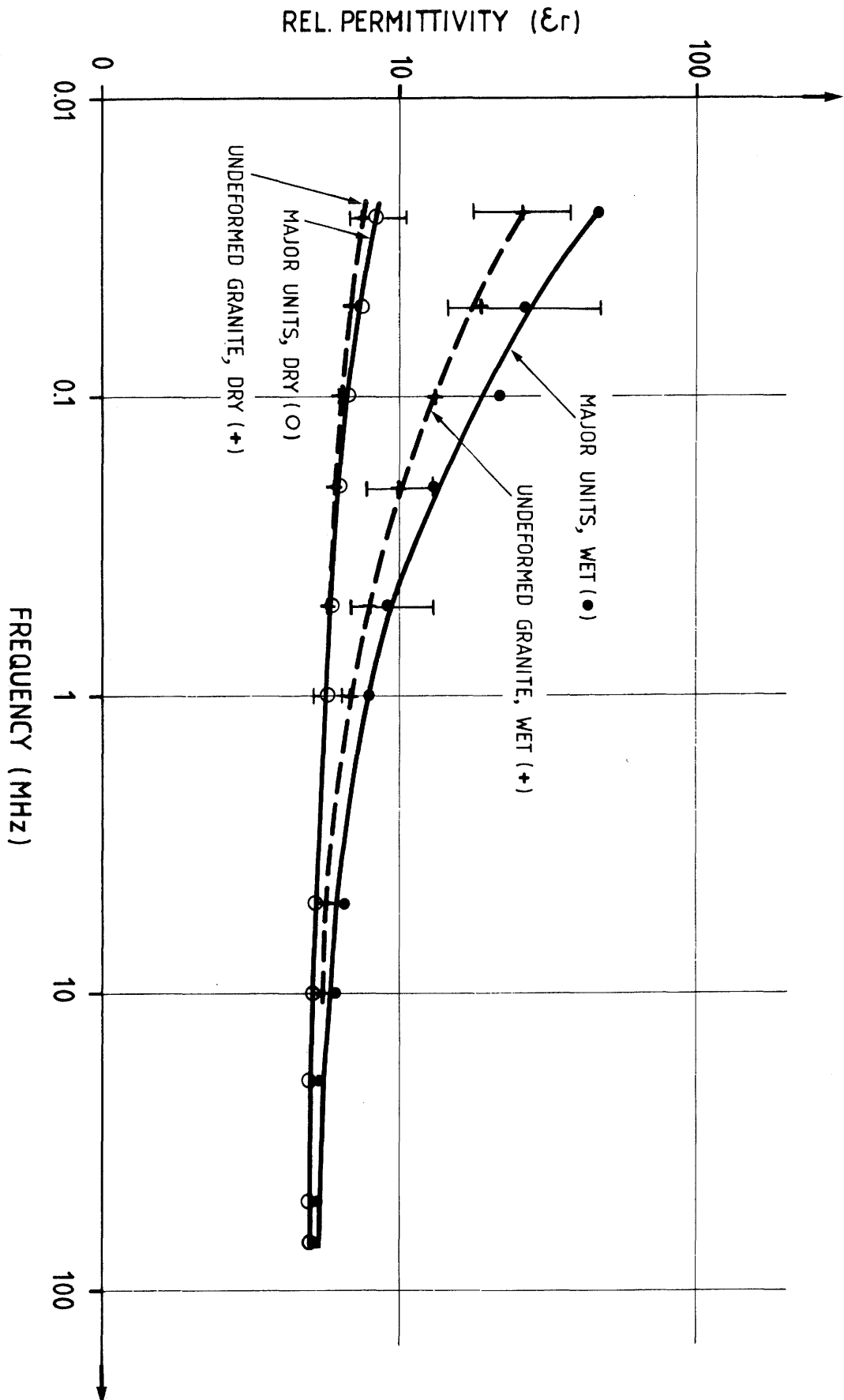


Figure 3.4

The dielectric constant as a function of frequency for different sets of core samples from the Crosshole site.

The wet samples have a high dielectric constant at low frequencies which gradually decays to become nearly constant for frequencies above a few MHz. There is then practically no difference in dielectric constant for samples from tectonized units and the undeformed rock. However, at the lower frequencies where the dielectric constant begins to increase it is higher for the tectonized units.

The conductivity of the wet samples is consistently higher for the tectonized samples compared with the undeformed samples (Figure 3.5). The conductivity of the tectonized rock is approximately twice that of the rock mass and the same factor holds for all frequencies. The conductivity increases with frequency raised to the power 0.38 both for the tectonized and the undeformed rock.

Figure 3.6 shows a cross-plot of zero frequency conductivity versus the conductivity at 20 MHz on samples from the deformed units. There is a good correlation between the measured values (the correlation coefficient $r=0.84$) but the range of variation in values is much less for the high frequency values compared to the DC-values. A consequence of this is that the slope of the least square fitted line is 1.63 rather than 1 which would have been expected. The reason for this discrepancy might be that there are two different physical principles behind the two measurements or that the measured samples were not made on exactly the same pieces of rock. The high frequency samples were smaller and thus less likely to contain fractures which would account for their smaller range of variation. If this assumption is correct we might expect the difference between undeformed and deformed rock to be larger in situ than indicated in Figure 3.5.

For the radar frequencies (20-40 MHz) the value of the dielectric constant is about 5.5 which according to theory corresponds to a propagation velocity of 128 m/ μ s. The resistivity of the undeformed rock in this frequency range varies from 1 500 ohmm to 3 000 ohmm, which gives skin depths in the range 19 m to 39 m (equation 3.7). These values of the skin depth correspond to attenuation values between 45 dB/100 m and 23 dB/100 m. The in situ measurements (Section 3.6) gave a velocity value of 120 m/ μ s and the attenuation 28 dB/100 m at 22 MHz. At 60 MHz the attenuation reaches 42 dB/100 m. The agreement between values obtained on core samples and in situ is thus quite good.

These data are also in rough agreement with those obtained in a comprehensive study by Cook (1975) of the electrical properties of core samples from a

large variety of rock types at radar frequencies. Cook concluded that low-loss radar propagation was possible in granites, limestones, coals, and dry concretes. Useful but shorter probing distances were predicted for gypsums, oil shales, dry sandstones, high-grade tar sands, and shists (Figure 3.7).

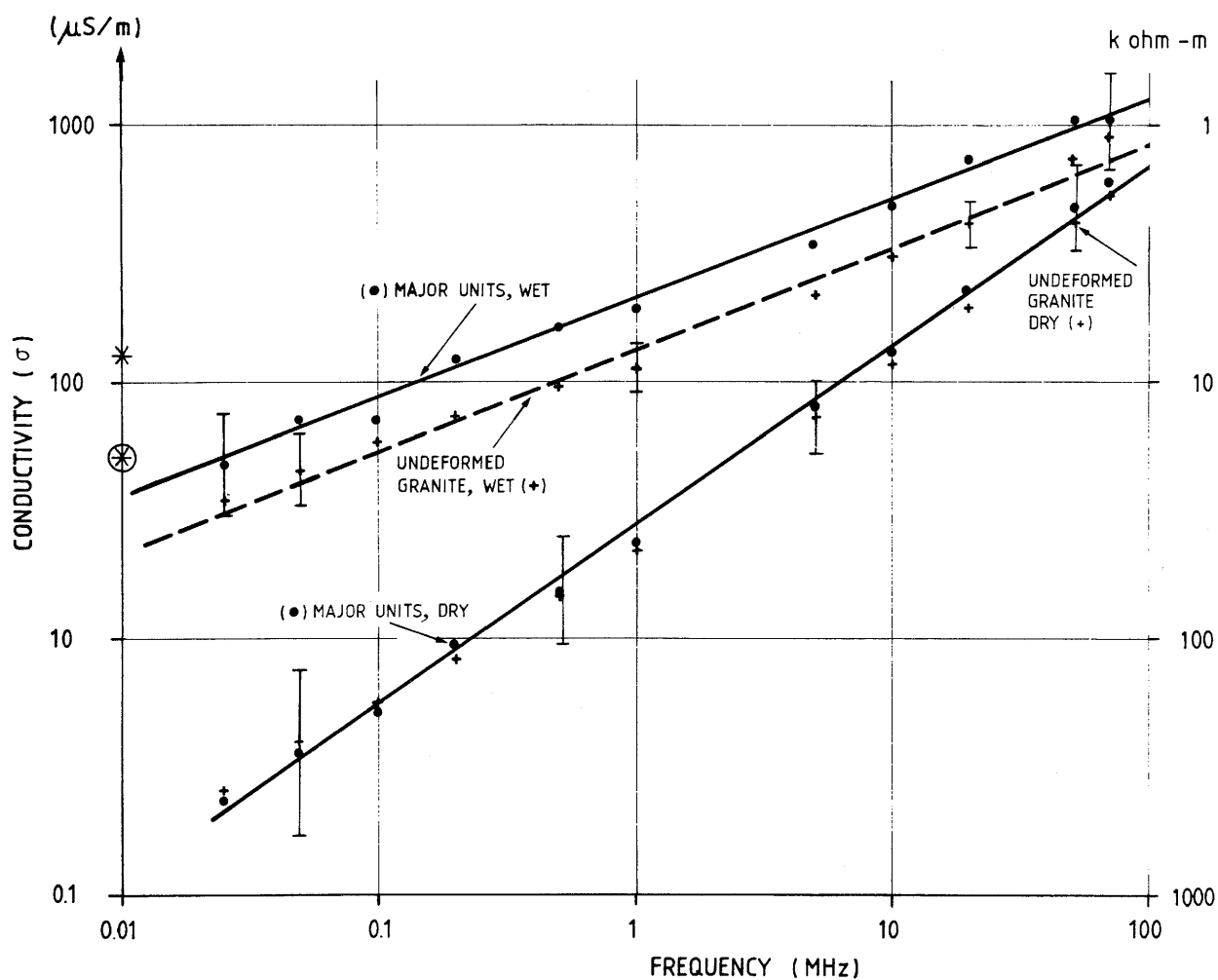


Figure 3.5

The conductivity as a function of frequency for different sets of core samples from the Crosshole site.

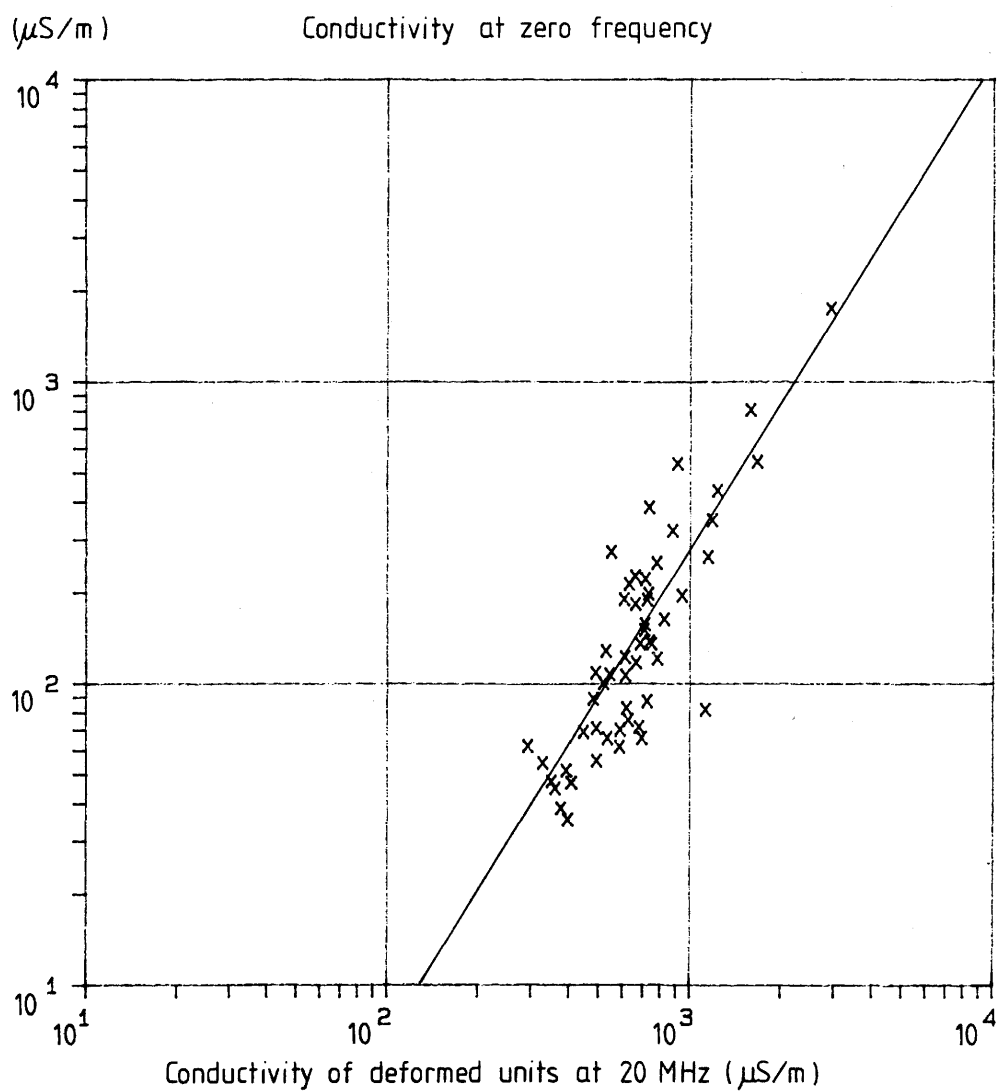


Figure 3.6 Cross-plot of DC-conductivity vs. the conductivity measured at 20 MHz for samples from the deformed units.

PROBING DISTANCE (m)

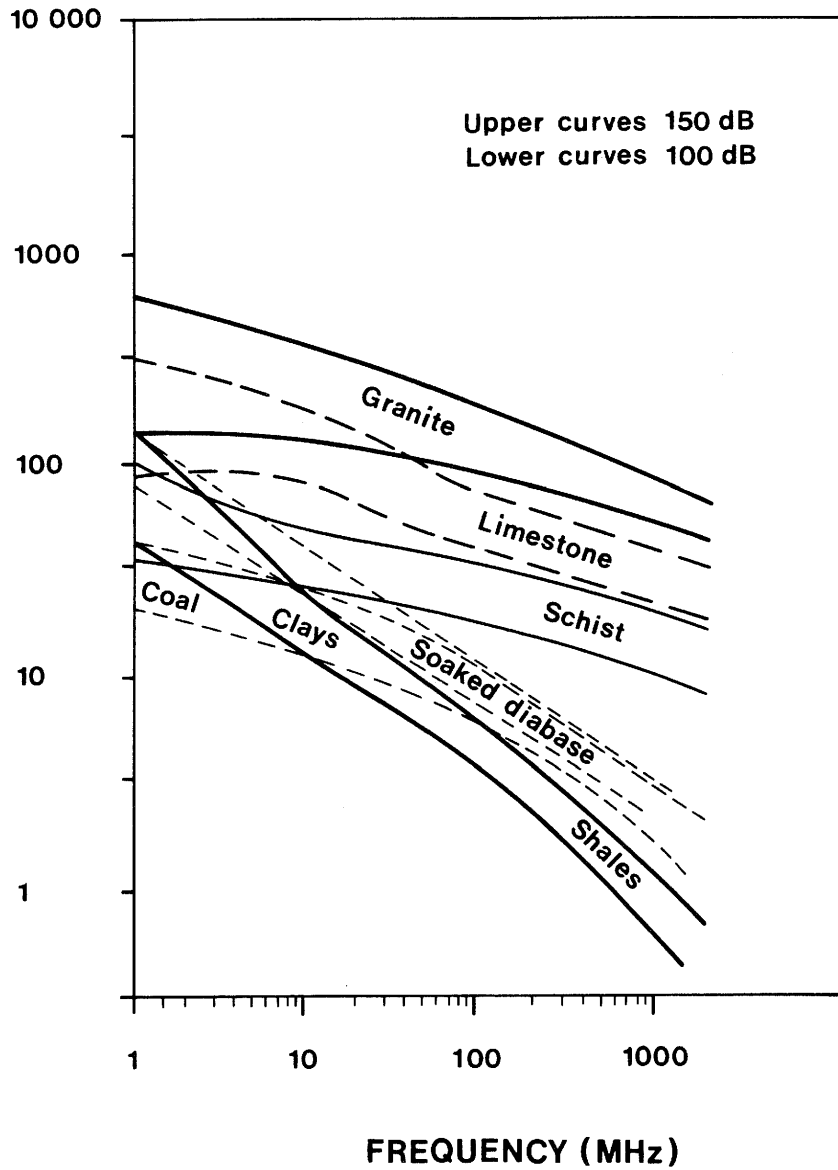


Figure 3.7 Estimated radar probing ranges for different rocks based on measurements on core samples (from Cook, 1975).

3.4 PROPAGATION OF RADAR WAVES

3.4.1 The radar equation

In the previous section it was shown that radar waves propagating through rock are significantly attenuated. The performance of a radar system is closely linked to the attenuation which to a large extent will determine the investigation range. The range is predicted by the radar equation which relates the received power to the transmitted power, the wavelength and also the size and shape of the reflecting target. In rock pointlike or plane reflectors are of greatest interest; in many cases a crosshole configuration is also adopted to measure the transmitted wave. In these three cases the radar equation has the following forms:

Pointlike reflector:

$$\frac{P_r}{P_t} = \frac{(G\eta\lambda)^2}{(4\pi)^3 R^4} \sigma e^{-4\alpha R} \quad (3.14)$$

where

G = antenna gain
 η = antenna radiation efficiency
 σ = target effective cross section in m^2
 λ = wavelength in m
R = range to target in m
 α = attenuation constant in Nepers/m.

Reflection from a plane:

$$\frac{P_r}{P_t} = \frac{(G\eta\lambda)^2 e^{-4\alpha R}}{(4\pi)^2 (2R)^2} |\gamma|^2 \quad (3.15)$$

where

γ = amplitude reflection coefficient for the plane
R = distance to plane.

Crosshole measurement:

$$\frac{P_r}{P_t} = \frac{(G\eta\lambda)^2 e^{-2\alpha R}}{(4\pi)^2 R^2} |1-\gamma|^2 \quad (3.16)$$

where

- $1-\gamma$ = amplitude transmission coefficient for a plane interface between transmitter and receiver
 R = distance between transmitter and receiver.

These equations indicate that longer wavelengths give larger range. This effect is further emphasized by the fact that attenuation decreases with increasing wavelength. But there are limits to the possibilities of obtaining additional range by increasing the wavelength since the resolution will deteriorate and finally the field would also lose its wave character.

The ratio of received to transmitted power is shown in Figures 3.8-3.11 as a function of distance. A plane reflector will of course give results equivalent to direct crosshole propagation of the pulse since one can consider the receiver to be mirrored in the plane. As an example the power ratio is calculated for a point reflector and direct propagation using the following parameters:

Antenna gain = 1.6 (representative value for a half-wavelength dipole)

Antenna radiation efficiency = 1 (a lossless antenna is assumed)

Target cross section = 1 m^2

Wavelength = 5.8 m in Figures 3.8-3.9 and 2.1 m in Figures 3.10-3.11. The corresponding frequencies are 22 and 60 MHz and the attenuation constant has been chosen accordingly.

These parameters have been selected for a lossless radar system. Losses in radar systems are often difficult to identify and quantify. Thus it is preferable to consider the lossless equivalent of a radar system when discussing its performance rather than to run into all the problems involved in estimating and evaluating losses. The essential parameter of a radar system relating to its range is the total dynamic range or the performance factor, i.e. the ratio of transmitted power to the smallest detectable power. If the total dynamic range is measured for a lossless system it is a well defined quantity, but if losses are included it becomes very difficult in practice to compare the merits of two systems. Section 3.6 will demonstrate how the total dynamic range can be measured for an equivalent lossless system.

The range curves in Figures 3.8-3.11 have the same general form. For small distances the received

power decreases with distance raised either to the power of two or four depending on the type of reflector. For larger distances attenuation will dominate and the power decreases exponentially. This means that if the sensitivity of the system is increased by a certain factor there will only be a linear increase in radar range. For example if the output power is doubled there will only be a 5 m increase in range for single hole measurements and 10 m for crosshole configurations in Stripa granite where the attenuation is 28 dB/100 m at 22 MHz. Thus to increase the radar range in a medium with significant attenuation would require a considerable increase in total dynamic range.

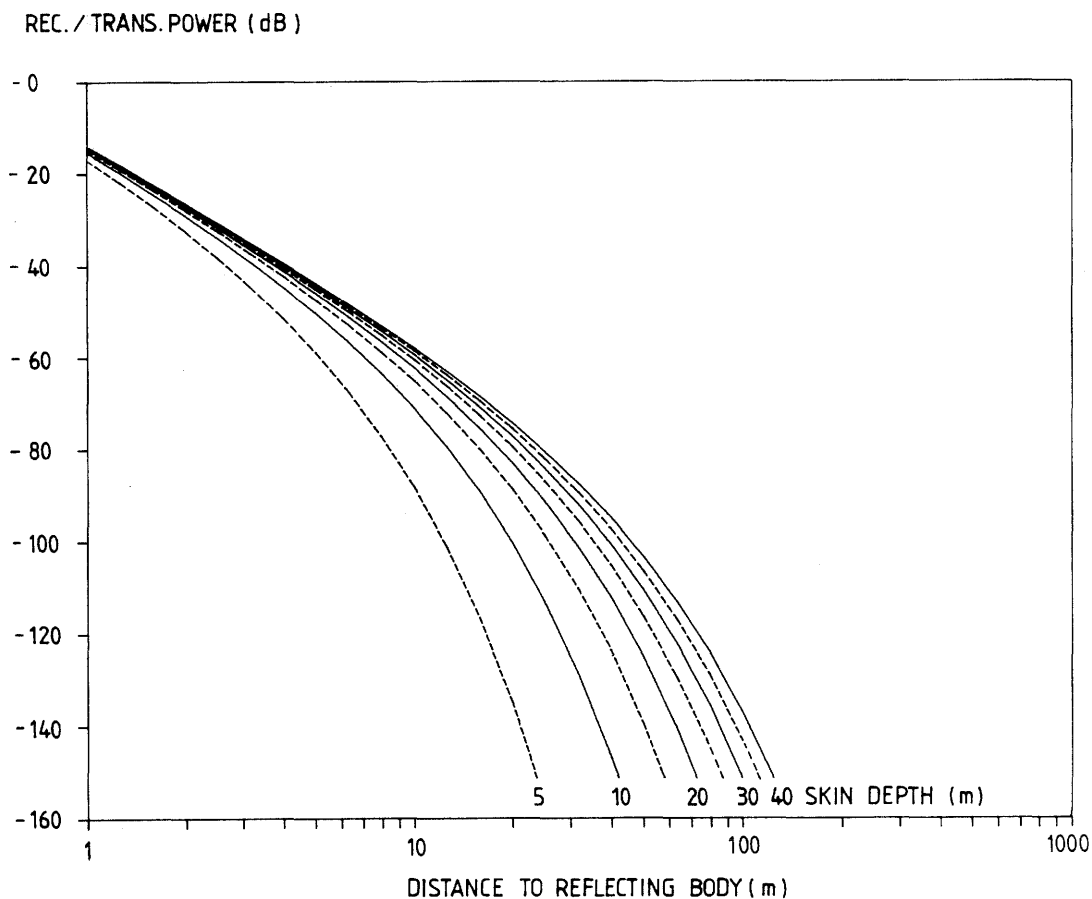


Figure 3.8 The ratio of received to transmitted power as a function of distance for a point reflector. The wavelength 5.8 m corresponds to a frequency of 22 MHz.

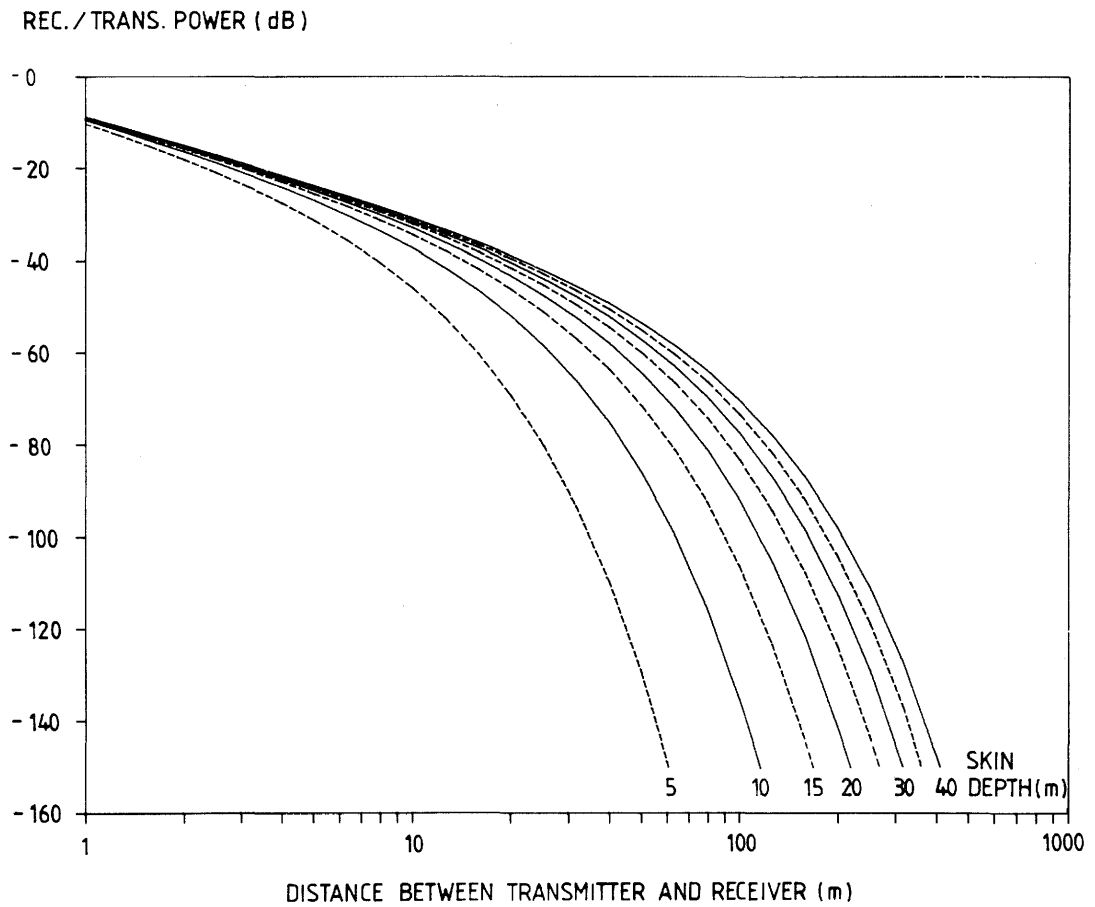


Figure 3.9 The ratio of received to transmitted power as a function of distance when the transmitter and receiver are in a crosshole configuration. The wavelength 5.8 m corresponds to a frequency of 22 MHz.

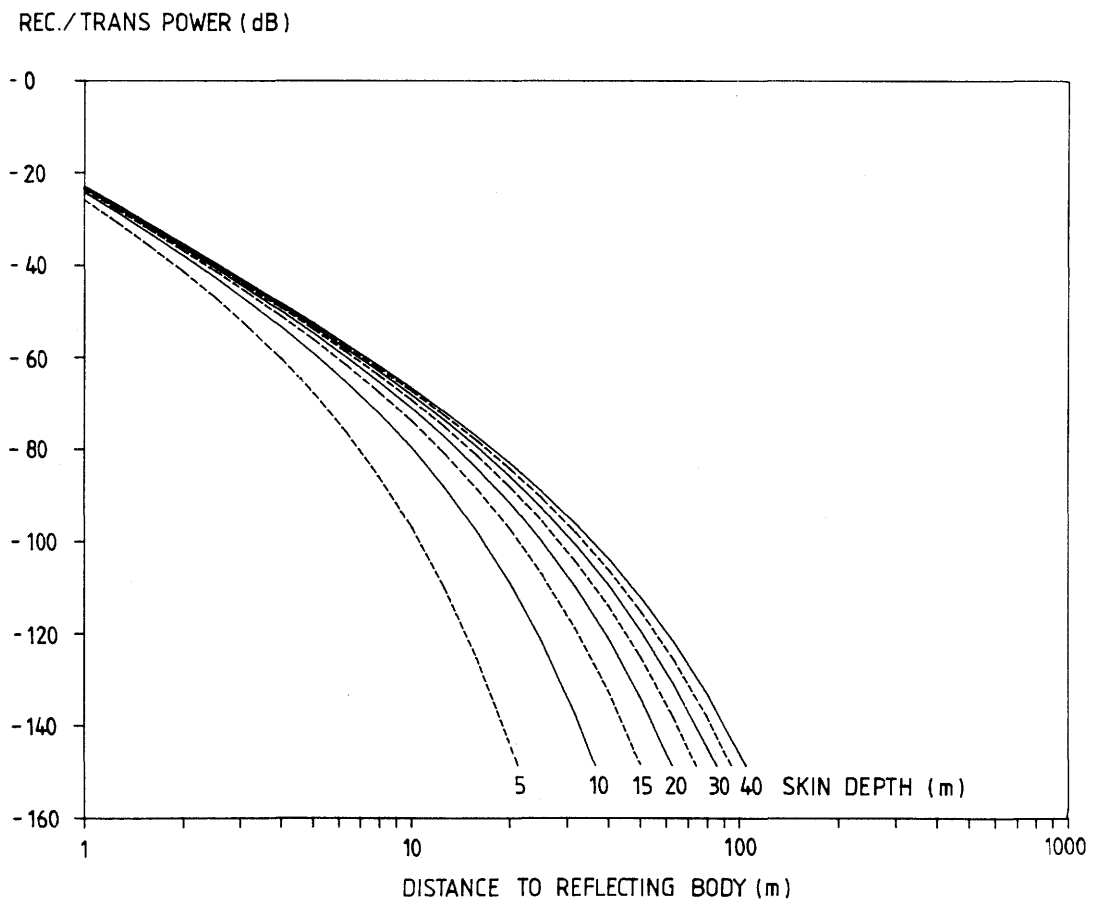


Figure 3.10 The ratio of received to transmitted power as a function of distance for a point reflector. The wavelength 2.1 m corresponds to a frequency of 60 MHz.

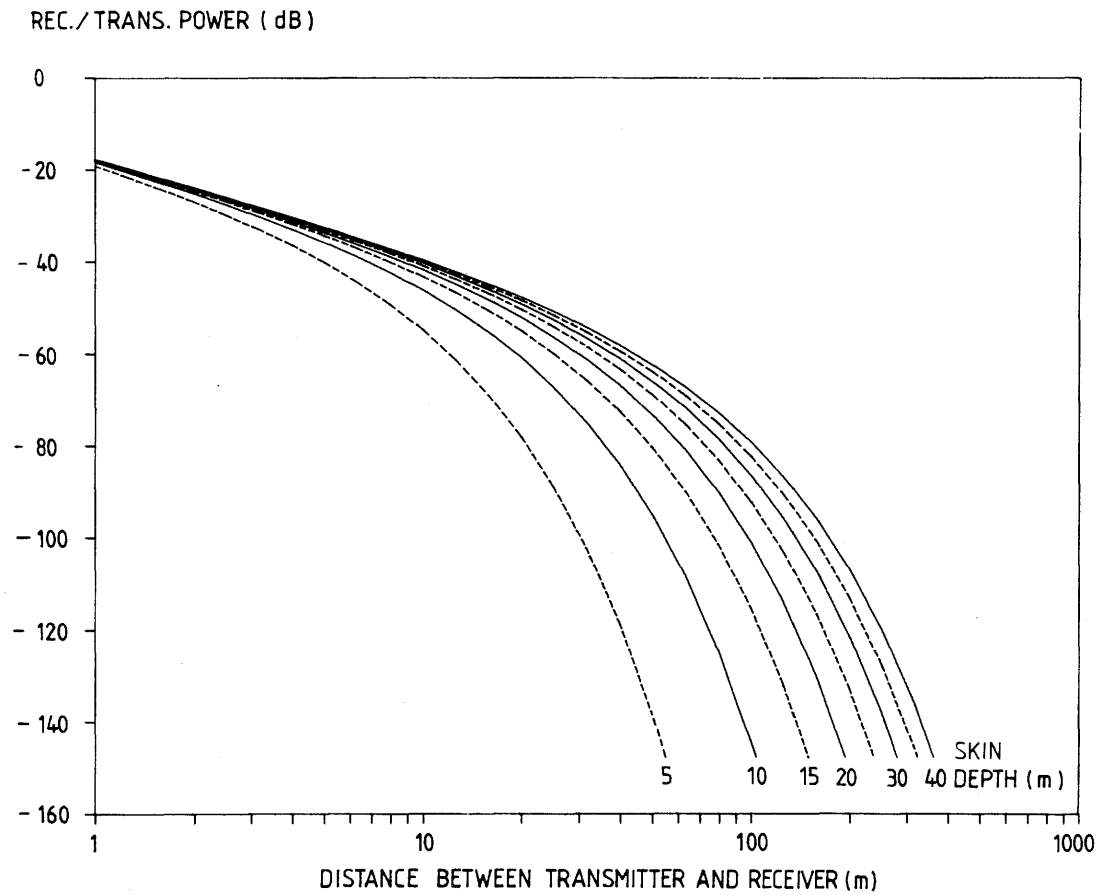


Figure 3.11 The ratio of received to transmitted power as a function of distance when the transmitter and receiver are in a crosshole configuration. The wavelength 2.1 m corresponds to a frequency of 60 MHz.

3.4.2 Radar resolution

The wave aspect of radar technique makes the borehole radar a unique instrument for investigating the properties of rock. The literature discussing the various aspects of wave propagation is vast and can not be reviewed in this report. However, there are some points of practical significance which deserve to be mentioned.

The resolution of objects or inhomogeneities that can be achieved with wave methods is normally on the order of a wavelength. In this context the term resolution normally refers to the limit where two objects located close to each other can be identified as separate objects. In a pulse radar system the resolution will approximately be equal to the pulse length and the shortest pulse that can be transmitted is roughly one wavelength long.

In most conventional radar systems, where wave propagation takes place in air, a radar pulse is many wavelengths long. But in these cases high frequencies are used and the resolution will still be good (centimeters to tens of meters). However, for subsurface applications the frequencies must be low and the wavelengths consequently long in order to produce any wave propagation. A subsurface radar must therefore be a short pulse system where the length of the pulse is roughly one wavelength in order to achieve the required resolution which is on the order of wavelengths. It should be noted that the equivalent of a short pulse system can also be obtained by various frequency synthesis methods.

It is important to keep in mind that even if the resolution as defined above will be roughly one wavelength smaller objects can sometimes be detected. Significant scattering of energy takes place if the scattering object has at least one length that is larger than a wavelength and if the contrast in electrical properties relative to the surrounding medium is sufficiently high. A typical example is provided by a thin electrical wire which will always be a good reflector if it is oriented parallel to the electrical field. Such a wire will act as an antenna and cause significant scattering of the pulse. If the wire is oriented perpendicularly to the direction of the electric field the coupling between the wire and the field will be small and there is little scattered energy. A borehole containing a metal pipe or conductive water will give rise to a similar response. A thin metal foil will in fact act almost like a perfect reflector. A planar structure such as a fracture zone with less contrast in the electrical properties may also cause substantial reflection if

its thickness is larger than about one tenth of a wavelength. The details of this important case is summarized in the next section.

3.5 REFLECTION BY FRACTURE ZONES

The reflection of radar waves from a fracture plane is caused by the change in electric properties that occurs between undeformed rock and fractures. The wavelength is several meters so it is sufficient for the change to take place over this distance. A direct comparison with the resistivity logs will confirm the essential correctness of this assumption: reflections usually occur where there are slopes in the resistivity curve.

The electric properties of rock can be described by two independent parameters, the dielectric constant and the resistivity, which both must be measured at the radar frequency. The resistivity is especially sensitive to frequency which explains the frequency dependence of the wave attenuation.

The reflection coefficient for an electromagnetic wave can be calculated in a straightforward manner. The calculations are complicated, however, since they depend on many parameters and one must integrate the result over all frequencies to obtain the reflection coefficient of a pulse. Our knowledge about the electric properties of the fracture zones is anyway quite limited. There are just a few measurements available made on core samples collected where the boreholes happen to penetrate the fracture zones (Magnusson et al. 1987). The reflection coefficient is therefore best estimated for an idealized model of the zone, e.g. a slab with prescribed values for the dielectric constant and the resistivity. This is the more justified since the area determining the reflection coefficient is approximately the size of the first Fresnel zone, i.e. a circle with radius $\sqrt{\lambda R}$, where R is the distance between the antenna and the reflection point and λ is the wavelength. This means that the radius is at least 10-20 m and all electric properties are averaged over this surface during reflection.

The dielectric constant ϵ' and the resistivity ρ can be combined into the complex dielectric constant (cf. Section 3.3)

$$\epsilon^* = \epsilon' + i\epsilon'' = \epsilon' + i(1/\rho\omega) \quad (3.17)$$

This expression shows that the relative importance of the real and imaginary parts depends on frequency. It can generally be assumed in radar applications that the real part is greater than the

imaginary part in undeformed rock since otherwise there would be no wave propagation at all. The resistivity of rock and fracture zones at radio frequencies has been measured by radar methods and also in the laboratory (see Section 3.3 and 3.6 for details). Some typical values used when calculating the amplitude reflection coefficient between two media, undeformed granite (medium 1) and fractured granite (medium 2), are summarized in Table 3.1.

Table 3.1. Typical values for the parameters used in calculating the reflection coefficient from the boundary between two media.

f (MHz)	ϵ'_1	ρ_1	ϵ'_2	ρ_2	ϵ''_1	ϵ''_2	$ r ^2(\%)$
22	5.5	2500	6.5	1000	.33	.82	.21
60	5.5	1500	6.5	500	.20	.60	.21

The reflection coefficient also depends on the polarization of the incident wave. In borehole radar experiments the wave will usually be linearly polarized due to the restrictions on the antenna imposed by the borehole. After reflection from a plane the electric field will remain linearly polarised in the same direction as long as single hole experiments are considered.

For the polarisation with the electric field in the incident plane the reflection coefficient r' is determined by a general formula, which for a thick zone corresponds to reflection from a halfspace:

$$r' = \frac{\epsilon_2 \cos \theta - (\epsilon_1 \epsilon_2 - \epsilon_1^2 \sin^2 \theta)^{1/2}}{\epsilon_2 \cos \theta + (\epsilon_1 \epsilon_2 - \epsilon_1^2 \sin^2 \theta)^{1/2}} \quad (3.18)$$

where θ is the angle of incidence.

This complicated expression simplifies in most cases of interest. For single hole measurements the pulses are reflected almost normally to the plane so the angle of incidence is small. Often the dielectric constants are of similar magnitude and then a simplification leads to

$$r' = (\epsilon_2 - \epsilon_1) / 4\epsilon_1 \quad (3.19)$$

This expression shows that for the parameters listed in table 3.1 sufficient energy may be reflected to give a measurable response.

A fracture zone can usually be approximated as a plane surrounded on both sides by a lossless medium. This description is valid for a fracture zone in granite, since the attenuation over a wavelength is rather small in unfractured rock. The reflection coefficient for a plane of thickness d is

$$r = r'(\exp(iu) - 1)/(\exp(iu) - r'^2) \quad (3.20)$$

where the phase factor

$$u = 2\omega \sqrt{\epsilon_1}/c (\epsilon_2 - \sin^2\theta)^{1/2} \quad (3.21)$$

This expression is only valid for a definite frequency f . In practice the reflection coefficient is almost always much less than unity, which leads to the simplified formula

$$r = r'(1 - \exp(iu)) \quad (3.22)$$

The reflected wave is then simply the superposition of two waves reflected from the front side and back side respectively. For a thin zone there is strong interference between these two components so we obtain

$$r = -iur' \quad (3.23)$$

Using the simplifications introduced previously for normal incidence the reflection coefficient becomes

$$r = -i (\Delta\epsilon/\epsilon_1) (d/\lambda) \quad (3.24)$$

where λ is the wavelength in the rock.

The previous formulas are valid for a linearly polarized plane wave with the electric field in the plane of incidence (TM-polarization). For electric dipole antennas the electric field is always in the plane defined by the antenna and the direction of propagation. TE-reflections mostly occur in crosshole reflections. However, as long as the angle of incidence is small there is little difference between the reflection coefficients for these two cases. The formulas corresponding to TE-polarization can be obtained by modifying (3.18) slightly and both formulas are given below in a different form which was used in the practical computations.

The fracture zone can be described in greater detail as a number of reflecting layers. The reflection coefficient can then be obtained from a recursion formula (Wait, 1970) which has already been used in previous calculations (Olsson and Sandberg, 1984). In the case when there are only two different media involved this formula gives

$$\gamma_{\tau} = \frac{-(Z_{\tau} - 1/Z_{\tau}) \sinh(iu_1 h_1)}{2 \cosh(iu_1 h_1) - (Z_{\tau} + 1/Z_{\tau}) \sinh(iu_1 h_1)} \quad (3.25)$$

where τ is 1 or 2 for TM and TE polarization respectively and two media, denoted by indices 0 and 1, are considered.

$$Z_1 = \frac{\mu_0}{\mu_1} \left[\frac{k_1}{k_0} \right]^2 \frac{u_0}{u_1} = \left[\frac{k_1}{k_0} \right]^2 \frac{u_0}{u_1} \quad (3.26)$$

$$Z_2 = \frac{\mu_0}{\mu_1} \frac{u_0}{u_1} = \frac{u_0}{u_1} \quad (3.27)$$

where $u_i^2 = k_i^2 - t^2$ and t is a real parameter which can be approximated by

$$t = k_0 \sin \theta$$

u_i = wavevector in m^{-1}
 k_i = the wavenumber in m^{-1}
 h_1 = thickness of the layer

In Figures 3.12 -3.17 the general behaviour of the reflection coefficient has been investigated for a number of parameters using Eq. (3.25). The most important question is which fracture thickness and electric contrast will cause a substantial reflection from a fracture zone. Figure 3.12 shows the reflection coefficient as a function of fracture width for the frequencies 22 and 60 MHz used in the radar measurements. The fracture parameters have been chosen in accordance with typical measured values. The curves demonstrate the simple behaviour predicted for reflections from thin fractures by Eq. 3.24.

Alternatively the frequency dependence can be plotted as in Figures 3.13 which shows the influence of the thickness of the zone on the reflection coefficient. The interference pattern calculated for higher frequencies can hardly be observed in practice since pulses are broadband and furthermore the properties of the fracture zones are expected to vary over the reflecting area. From this point of view the approximate formulas given previously are often just as useful as exact but idealized calculations.

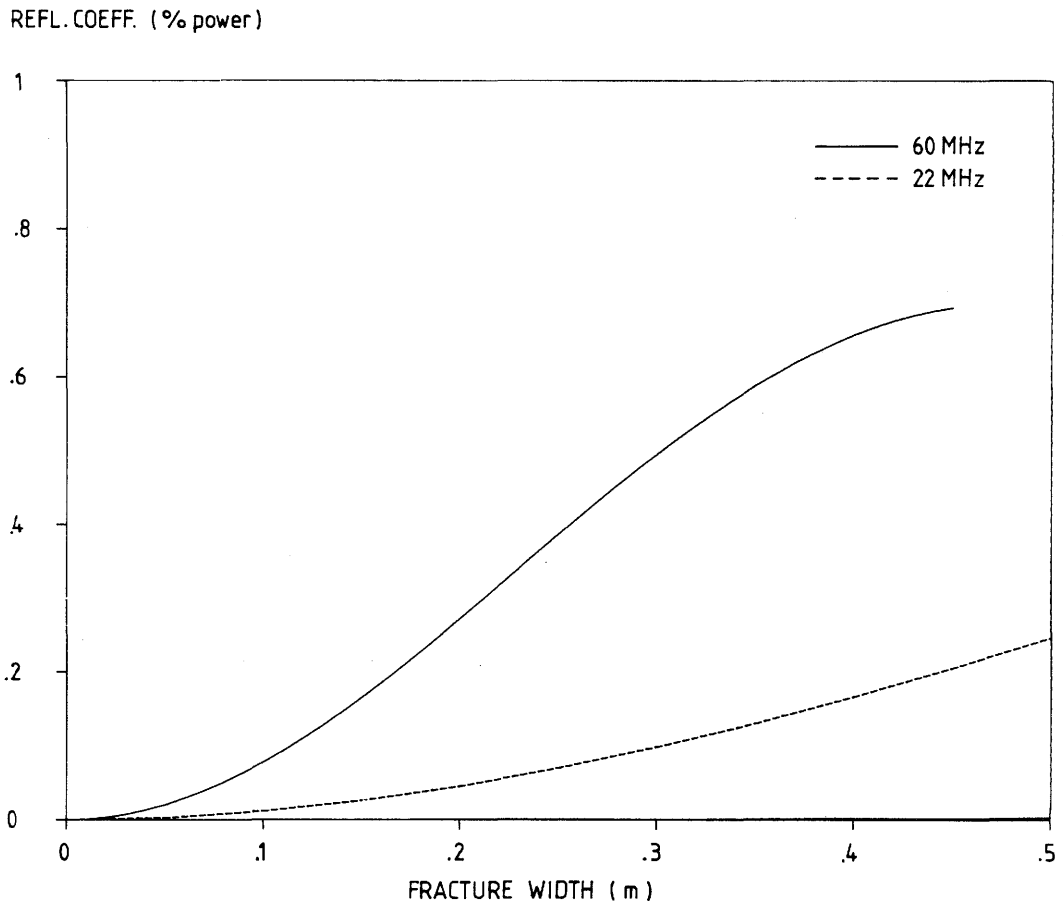


Figure 3.12 The reflection coefficient as a function of the width of a layer with dielectric constant 6.5 in a surrounding medium with dielectric constant 5.5. The resistivity of the medium is 2500 ohmm (dashed) and 1500 ohmm (solid) respectively while the resistivity of the layer is 1000 ohmm and 500 ohmm respectively. These parameters are typical of granite at 22 and 60 MHz.

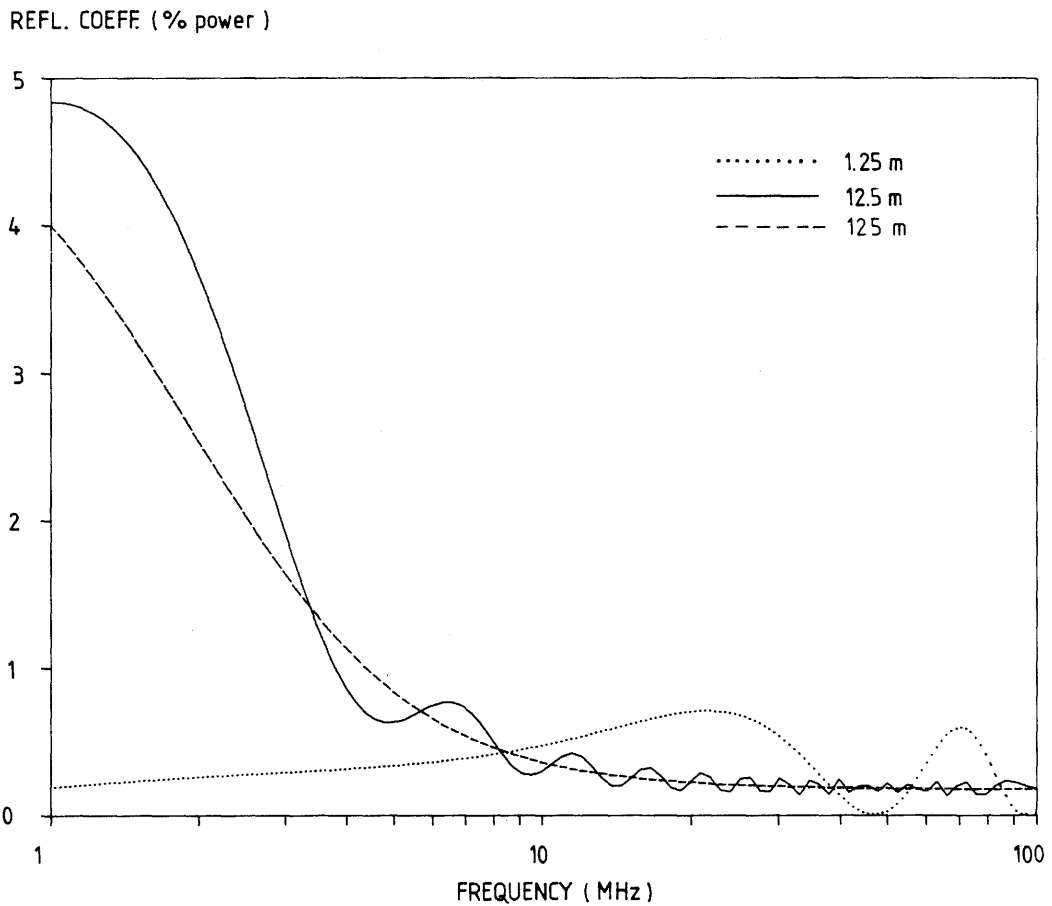


Figure 3.13 The reflection coefficient as a function of frequency for three layers 1.25 m (dotted), 12.5 m (solid) and 125 m (dashed) thick with dielectric constant 6.5 and resistivity 1000 ohmm in a surrounding medium with dielectric constant 5.5 and resistivity 2500 ohmm.

The effect of the electric properties of the zones is particularly interesting. The formulas show that both resistivity changes and changes in the dielectric constant can contribute to the reflection process. Thus in Figure 3.14 it is seen that a sharp decrease in resistivity may substantially increase the reflectivity. A detailed comparison using measured values seems to indicate that the dielectric constant is most important as seen in Figure 3.15, where the angular dependence has been calculated for the same parameters as before. If only the resistivity change is included the reflection coefficient becomes much smaller while the change in dielectric constant preserves the level of the curve. Since the changes in resistivity and dielectric constant in a fracture zone are both caused by increased water content there will anyway be a close correlation between reflectivity and the DC resistivity as measured by logging equipment.

The angular dependence is quite strong for large angles of incidence as seen in Figure 3.16. The difference between the two polarizations is evident: the TE reflection coefficient is monotonically increasing while the TM component has a minimum at the Brewster angle as seen in Figure 3.16. At glancing incidence the reflection coefficient will be close to unity for both polarizations.

It is often asked how much water is needed to produce the measured reflection coefficients. It is not certain that such a question is meaningful since the area of the layer must be quite large to reflect the pulse but for comparison the reflection coefficients of thin water layers have been calculated in Figure 3.17. Already 1 cm water will cause quite a strong reflection according to this calculation. The effect is entirely due to the large dielectric constant of water while the conductivity does not contribute at all.

It is rather complicated to determine the reflection coefficient from experiments since one must take into account the attenuation of the pulse during propagation. This is best done by comparing directly with rays that have propagated the same distance in the same rock mass. Some reflection coefficients have been calculated in this manner and they appear to be of the correct order of magnitude when compared with the theoretical formula. As an example the reflection coefficient of the prominent C zone at 22 MHz was found to be 1-5 % near normal incidence. Inserting numbers from laboratory measurements on the core samples (Agmalm, 1985) the reflection coefficient can be calculated for the idealized model discussed above.

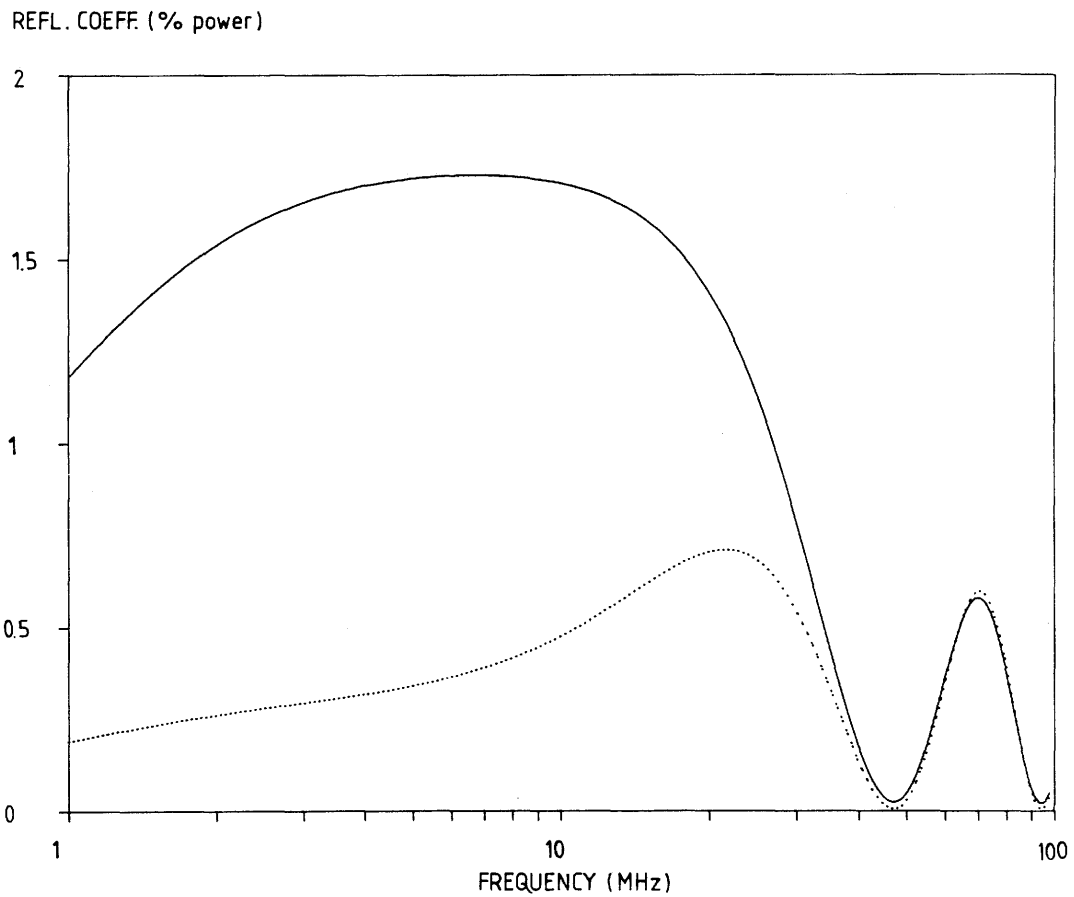


Figure 3.14 The reflection coefficient as a function of frequency for two layers; 1.25 m thick with dielectric constant 6.5 and resistivity 1000 ohmm (dotted) and 500 ohmm (solid) in a surrounding medium with dielectric constant 5.5 and resistivity 2500 ohmm.

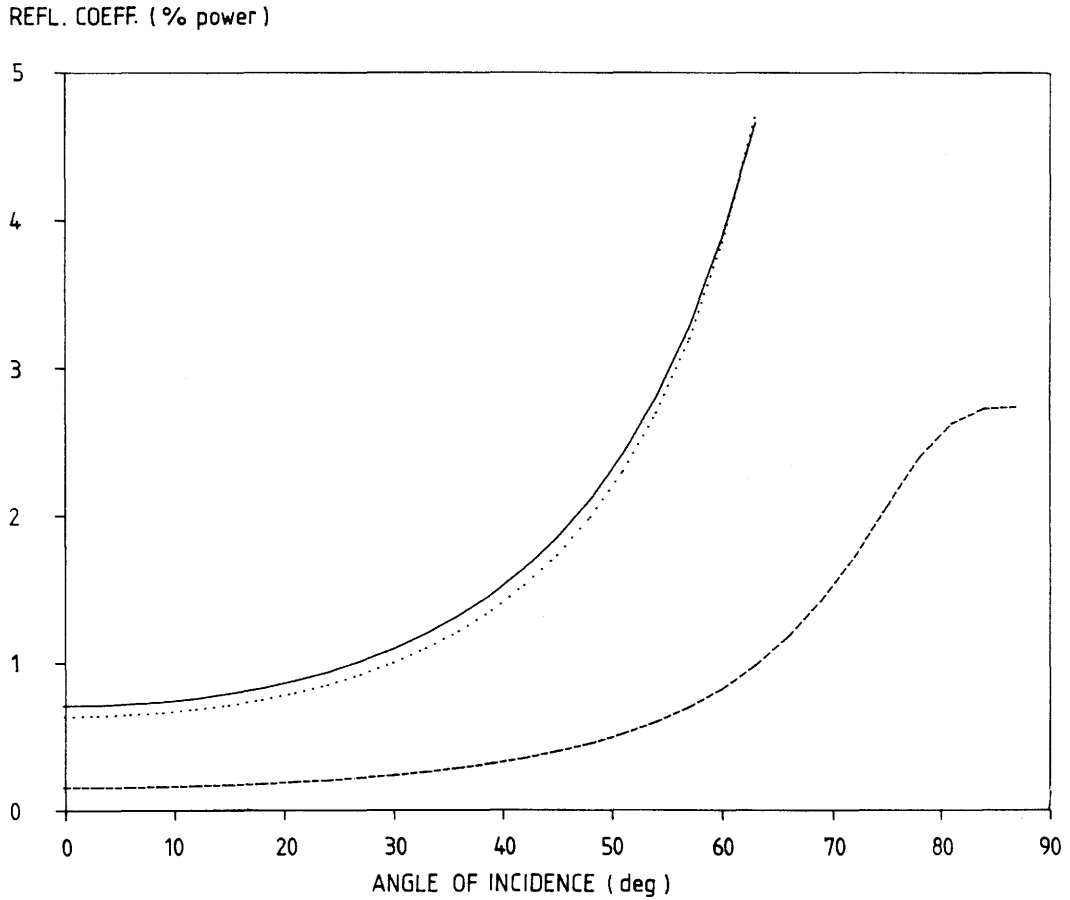


Figure 3.15 The reflection coefficient as a function of the angle of incidence for three layers 1.25 m thick at 22 MHz. The dielectric constant of the surrounding medium is 5.5 and the resistivity 2500 ohmm while the layer has dielectric constant 6.5 and resistivity 2500 (dotted), dielectric constant 5.5 and resistivity 1000 (dashed) and dielectric constant 6.5 and resistivity 1000 (solid).

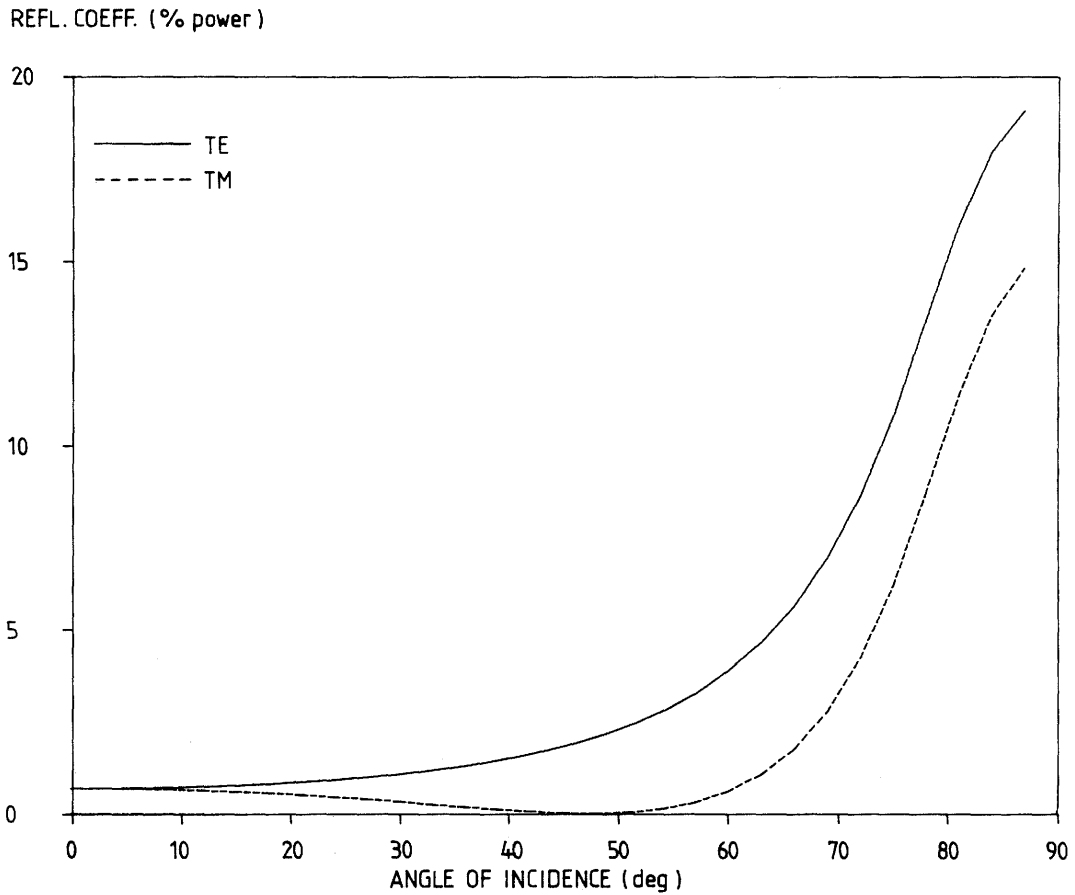


Figure 3.16 The reflection coefficient as a function of the angle of incidence and polarization at 22 MHz. The dielectric constant of the surrounding medium is 5.5 and the resistivity 2500 ohmm while the layer is 1.25 m thick with dielectric constant 6.5 and resistivity 1000. Electric field parallel to the reflecting surface (TE) is solid while electric field in the incident plane (TM) is dashed.

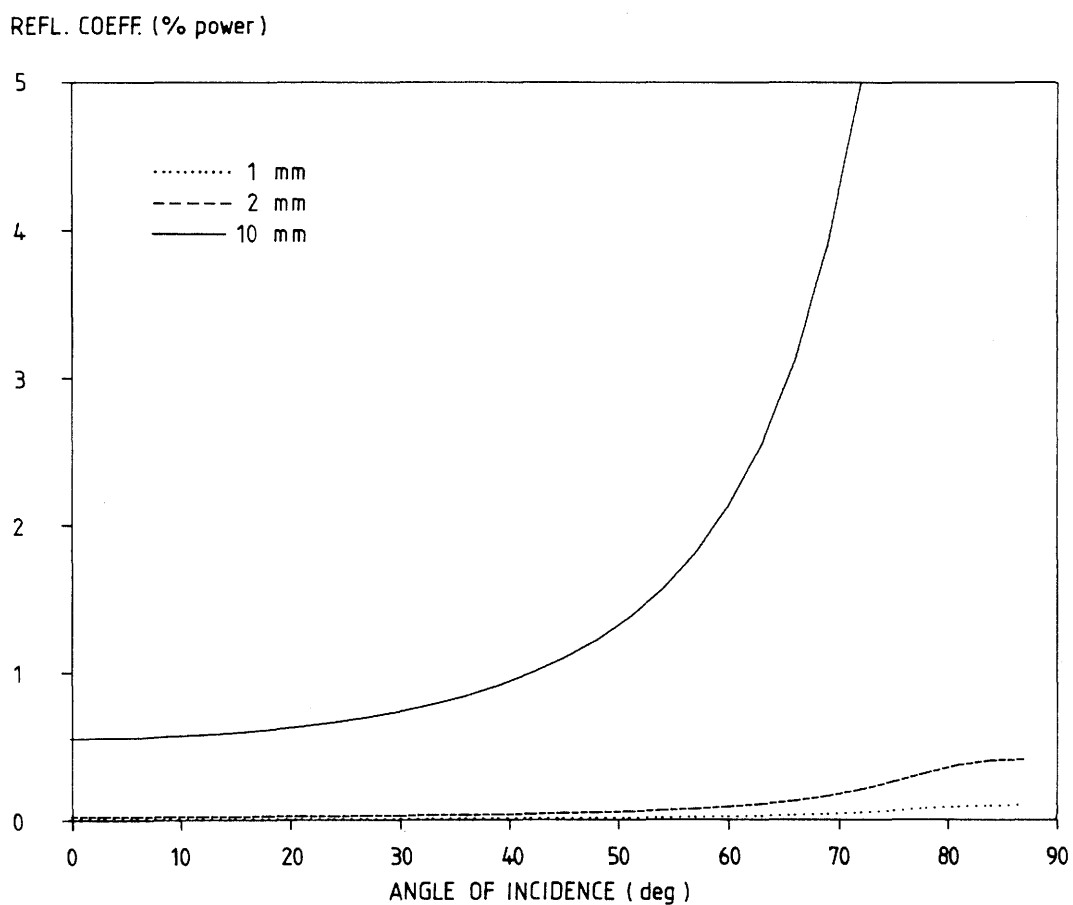


Figure 3.17 The reflection coefficient as a function of the angle of incidence for three thin water layers 1 mm (dotted), 2 mm (dashed) and 10 mm (solid) thick with dielectric constant 81 and resistivity 50 ohmm in a surrounding medium with dielectric constant 5.5 and resistivity 2500 ohmm.

Using a layer 8 m thick with a dielectric constant 7 and resistivity 200 ohmm surrounded by a rock with 5.5 and 2500 ohmm the reflection coefficient is 2-3 %, in excellent agreement with the measured values. However, this number depends critically on the unusually low resistivity of the zone; if the resistivity is 500 ohmm the reflection coefficients drops to under 1 %. This example shows clearly that reflections can in practice be caused both by contrasts in resistivity and dielectric constant.

3.6 IN SITU DETERMINATION OF ATTENUATION AND VELOCITY

The velocity and attenuation of the radar pulse can be obtained from crosshole measurements. Such measurements are also used to obtain the total dynamic range of an equivalent lossless system. Several crosshole measurements have been performed between the holes N1 and E1 at the Crosshole site (Figure 1.1) to obtain these parameters. During the measurements the transmitter and the receiver were always positioned at the same borehole depth in each borehole and moved simultaneously during the measurement. The boreholes are perpendicular and approximately straight which means that the relative position of the antennas was constant during the measurement. In this way no correction has to be made for the antenna radiation pattern, i.e. the fact that the antenna radiation depends on direction.

The resulting time-distance plot from one of these measurements is shown in Figure 3.18. The amplitude of the received signal is shown in grey scale, where black corresponds to large positive values, grey to zero and white to negative values. The travel time of the radar pulse is seen to increase linearly with distance as the probes are moved along the boreholes. The analysis of the data gives accurate information both about the velocity and the attenuation in the rock mass between the boreholes.

The simple borehole geometry makes it easy to determine the velocity of radar waves in the rock. The velocity is simply determined by the slope of the straight line in Figure 3.18, which is seen to be quite constant. The velocity of the radar waves in the Stripa granite was found to be $120 \text{ m}/\mu\text{s}$ at the center frequency 22 MHz used in this experiment. This corresponds to a relative dielectric constant of 6.3, which is in fair agreement with the value obtained from core samples, which was 5.4 for the frequency 20 MHz. Similar conclusions about the pulse velocity have been drawn from very detailed crosshole measurements performed during tomographic analysis, when every point in the plane between the boreholes is covered by rays. The velocity variation is found to be just a few percent, with a maximum reduction of 8-10 % in the strongly fractured areas. A theoretical calculation using the dielectric constant measured in the laboratory gives similar results.

The measured pulse velocity will later be used to interpret radar data. The calibration thus actually provides a comparison between geometrically measured distances in the Stripa mine and an error in

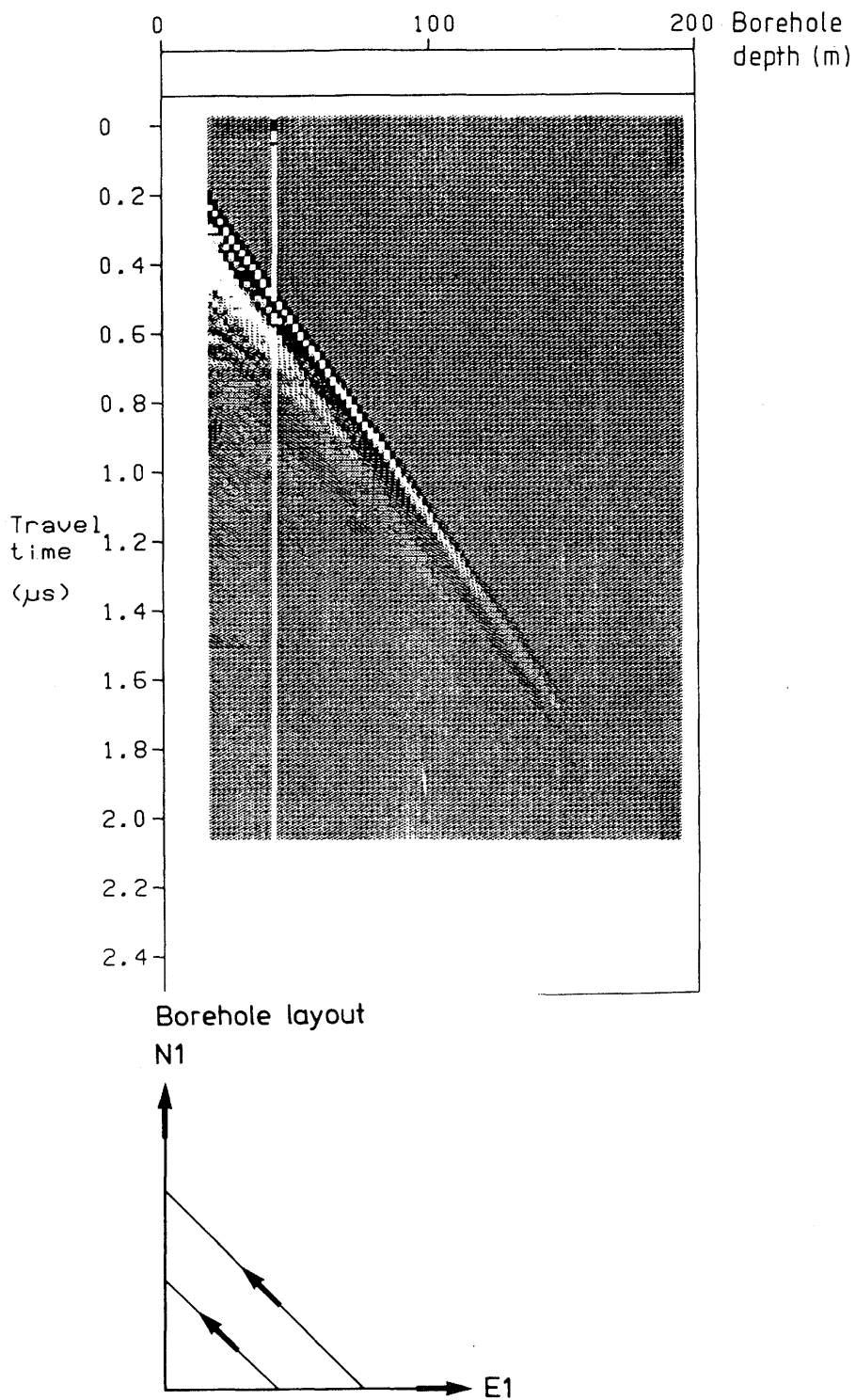


Figure 3.18 Crosshole measurement between E1 and N1 for velocity and attenuation calibration. The receiver and transmitter are always at the same depth in each borehole.

absolute time calibration will not affect the radar results. Calibration of the internal time base of the radar system has been performed by inserting short pieces of optical fibre in the line used for triggering the transmitter. The delay introduced in this way can be measured and compared with the known pulse velocity in the fibre. Consistent results were obtained for different fibre lengths proving that this method works well in practice.

The variation of the peak to peak amplitude of the directly propagated pulse as a function of distance is shown in Figure 3.19. The results of measurements performed between E1 and N1 with different equipments at 22 MHz are seen to be very similar although the absolute level varies due to amplification differences between the systems. At 60 MHz the attenuation has doubled so the radar range will be halved in this case (see Figure 3.20). Quite apart from energy losses during propagation the pulse height will be reduced by the frequency dispersion which tends to broaden the pulse. An exact determination of the attenuation constant for different frequencies can be performed by considering the amplitude of the Fourier components for different propagation distances. A number of such curves have been compared and the average amplitude attenuation coefficient was calculated (Sundqvist 1985). As seen in Figure 3.21 the results are in excellent agreement with values obtained from laboratory measurements of the resistivity in Stripa granite (Agmalm 1985).

Using the measured data one can also obtain a rough estimate of the system losses. Calibration measurements have shown that one bit of measured signal amplitude corresponds to 1 μV at the receiver antenna terminals. The minimum signal power detected by the system is thus about 0.01 pW since the input resistance is 50 ohms. The peak power radiated by the antenna can be estimated from the stored energy in the coaxial cable, which is about 30 μJ , and the pulse length, approximately 30 nsec. The peak power is thus about 1 kW and the ratio $P_t/P_r = 170$ dB.

When the theoretical formula (3.16) is used to calculate the received power using parameters typical for lossless dipoles one obtains a curve similar to but about 30 dB above the measured curve. System losses are thus approximately 30 dB, which is a reasonable value, since the radiation efficiency of a half wavelength resistive Wu-King antenna (see Section 2.2.7) is about 8 %, so the two antennas account for 22 dB of the losses. The remaining 8 dB may be ascribed to transmitter losses and poor matching.

RECEIVED POWER (dB) E1-N1 CALIBRATION

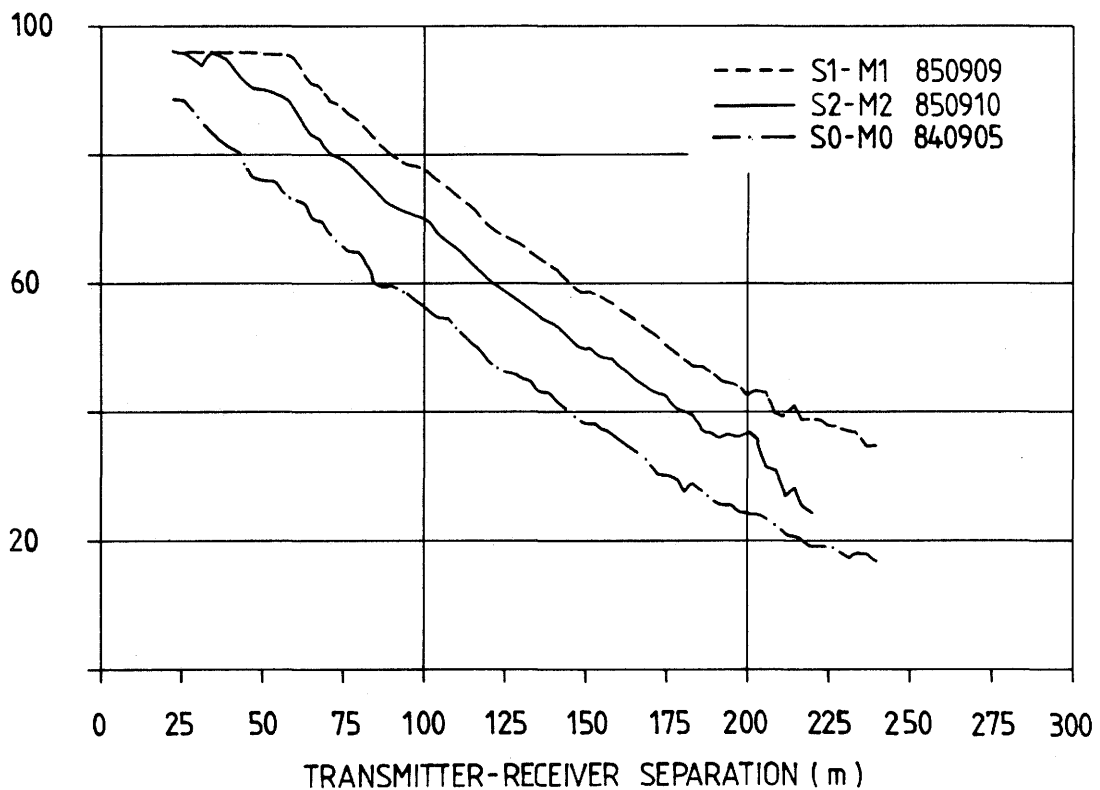


Figure 3.19 Calibration curves for three different radar systems based on measurements performed between E1 and N1 in September 1985. The center frequency was 22 MHz.

Received power (dB) E1-N1 calibration

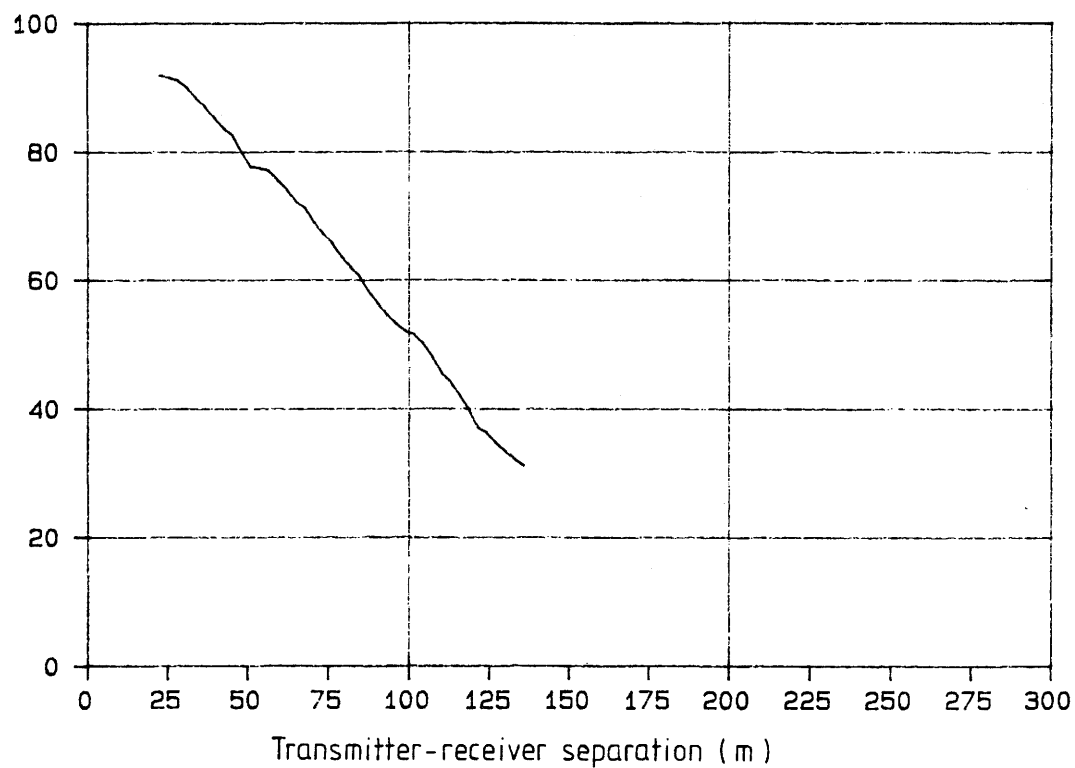


Figure 3.20 Calibration curve based on measurements performed between E1 and N1 in September 1985. The center frequency was 60 MHz.

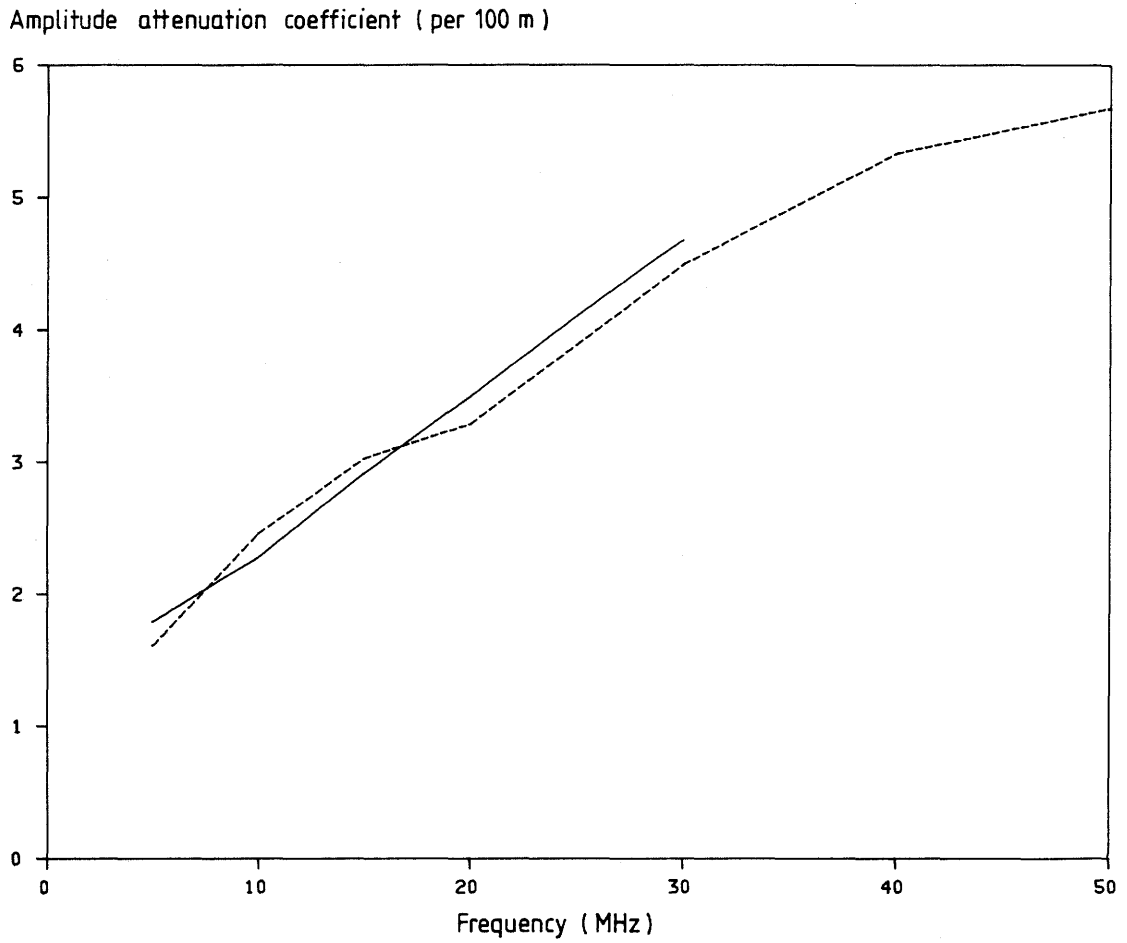


Figure 3.21 The amplitude attenuation coefficient in Nepers/100 m determined at different frequencies by radar (solid) and laboratory measurements of the resistivity (dashed).

SINGLE HOLE MEASUREMENTS

4.1 THE PRINCIPLE OF SINGLE HOLE MEASUREMENTS

The principle of a reflection measurement is depicted in Figure 4.1. The transmitter and receiver are lowered or pushed into the same hole while the distance between them is kept constant. The result is displayed in the form of a diagram where the position of the probes is shown along one axis and the propagation distance along the other axis. The amplitude of the received signal is shown in a grey scale where black corresponds to large positive signals, white to large negative signals and grey to small signals.

The distance to a reflecting object is determined by measuring the difference in arrival time between the direct and the reflected pulse. The basic assumption that the speed of propagation is the same everywhere in the rock mass has been verified during several crosshole measurements. As the radar is pushed step by step into the borehole the propagation time of the reflected pulse will vary in a manner typical of the reflector.

The two basic patterns are point reflectors and plane reflectors as shown in Figure 4.1. The point reflector pattern agrees rather well with the strong hyperbola shaped reflection at a borehole depth of 175 m in Figure 4.2. This reflection is caused by a drift which extends in a direction perpendicular to the borehole so the reflection point is the part of the tunnel closest to the borehole. This measurement was made at a center frequency of 22 MHz corresponding to a wavelength of approximately 5.5 m in rock while the diameter of the drift is approximately 3 m.

The fracture zones are characterized by the planar pattern. A plane reflector works like a mirror and is therefore the most efficient type of reflector and the only one likely to be observed at large range. As can be seen in Figure 4.2 some of the zones can be followed to a distance of 80 m from the hole. The range obtained is actually larger and in the measurement of the adjacent hole V1 a fracture zone was followed to a distance of 115 m (Figure 4.15). It is evident that the radar gives very detailed information about the extension of fracture zones at considerable distances from the boreholes. It is even possible to observe zones

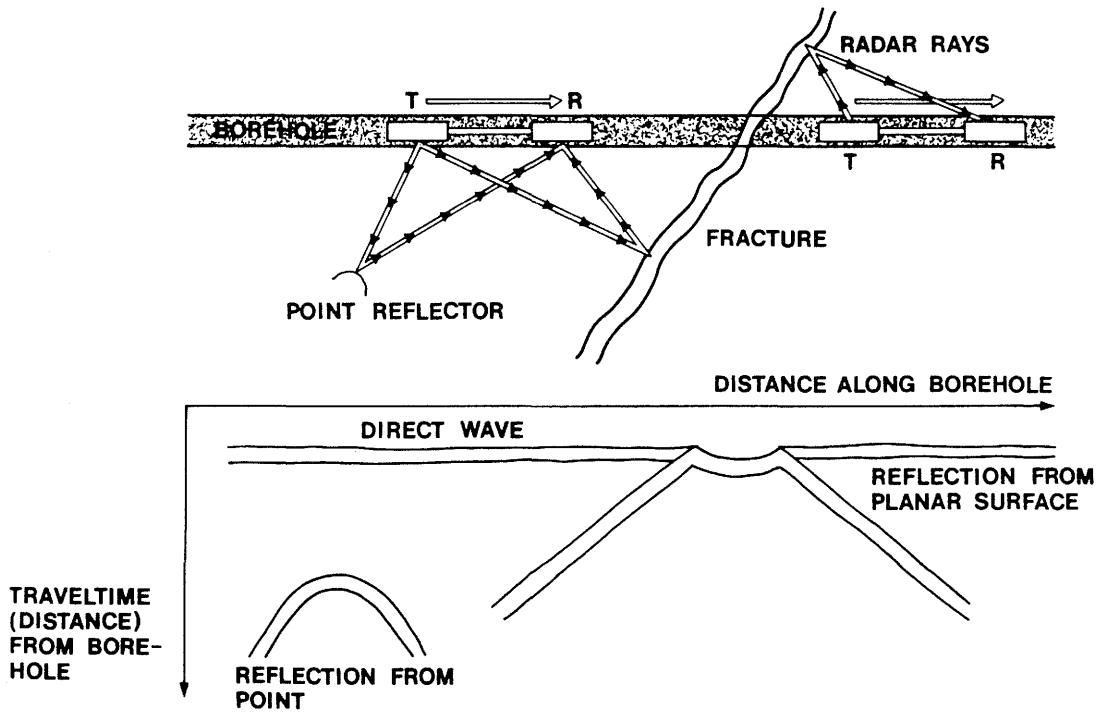


Figure 4.1 The principle of the borehole reflection radar and the characteristic patterns generated by plane and point reflectors.

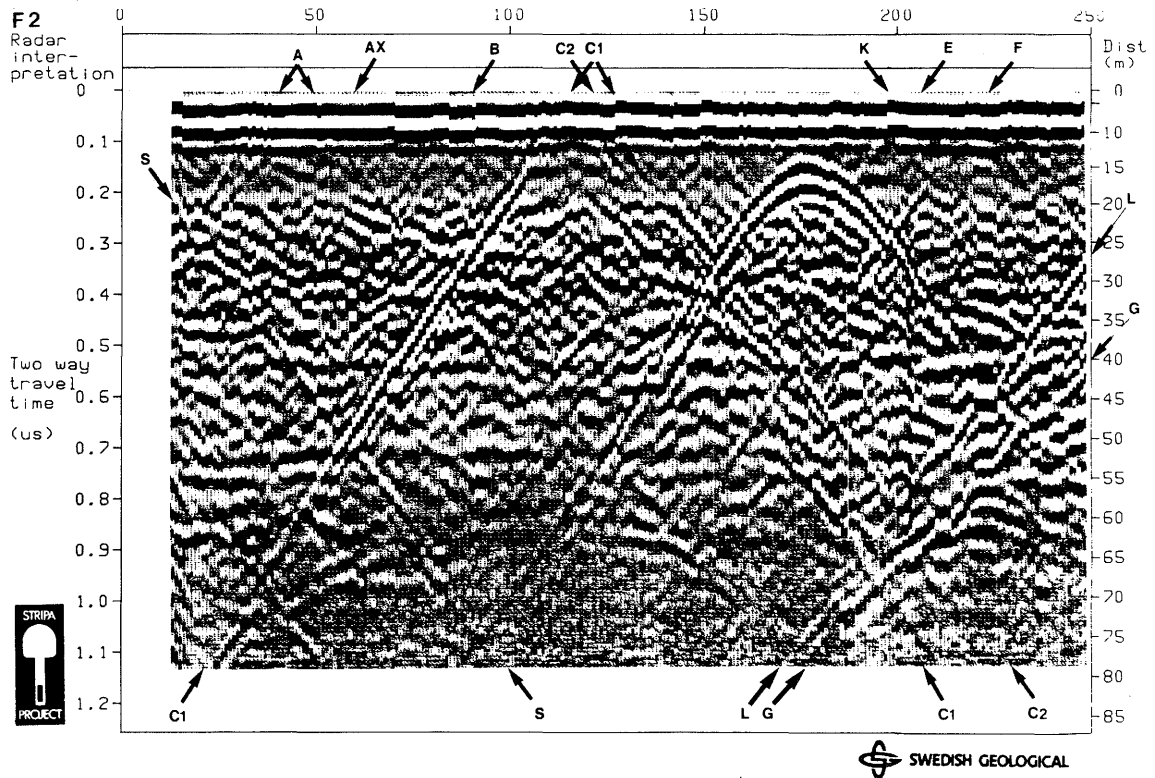


Figure 4.2 Radar reflection map from the borehole F2 at the Crosshole site in Stripa measured with a center frequency of 22 MHz.

which do not intersect the borehole like zone L in Figure 4.2. That zone would intersect the borehole at about 270 m if the drilling had continued that far (the hole actually ends at 250 m).

The radar can be modified to peak at different frequencies by varying the antenna length and making the appropriate changes in matching. The resolution of pointlike objects and lines, such as the boreholes themselves, improves when the wavelength is reduced. However, when the frequency increases from 22 to 60 MHz (the frequencies used in most measurements in Stripa) the attenuation is doubled which means that the range is halved. A low frequency like 22 MHz, corresponding to an attenuation of about 28 dB/100 m, is therefore preferable when one is searching for fracture zones with large extension.

From the radar reflection measurements it is possible to determine the angle of intersection between the hole and a fracture plane and also the point of intersection. This is done with the aid of a theoretically computed nomogram which is described in Section 4.2.

Since the borehole geometry made it necessary to use dipole antennas, the radar images in Figure 4.1 and 4.2 are cylindrically symmetric. Consequently one can not obtain the complete orientation of a fracture plane from measurements in a single borehole. The orientation can however be determined by combining results from two or more boreholes. The interpretation techniques for single hole measurements are described in detail in Section 4.5. A future possibility is the development of directional antennas that would be sufficiently efficient to overcome the limitations introduced by small borehole diameters.

The radar maps from all reflection measurements made in Stripa, within the phase II program, are included in Appendix A.

4.2 CALCULATION OF NOMOGRAMS FOR DIFFERENT REFLECTORS

When the radar system is used in the reflection mode the transmitter and receiver are moved along a borehole at a fixed distance, $2c$, from each other, see Figure 4.3. The radiation pattern of the antennas is axially symmetric around the borehole, so the origin of a reflection may be any point at a rotational ellipsoid with the focuses at the transmitter and receiver antennas respectively. When the antenna array is moved along the borehole the distance to the reflection point varies in a

definite way and a characteristic reflection pattern will appear in the plotted radar map.

The two most common types of patterns are caused by plane and point reflectors. For a pointlike reflector the two way traveltime, $2a$ (measured as a distance), will vary when the array is moved along the borehole according to the equation

$$2a = \sqrt{d^2 + (x+c)^2} + \sqrt{d^2 + (x-c)^2} \quad (4.1)$$

where

$2c$ = the distance between the antennas
 x = distance along borehole
 d = closest distance from the borehole to the point reflector

In the case of a planar reflector, such as a fracture zone intersecting the borehole, the two way traveltime, $2a$, will vary according to the formula

$$2a = 2 \sqrt{x^2 \sin^2 \theta + c^2 \cos^2 \theta} \quad (4.2)$$

where θ is the angle between the borehole and the fracture plane (see Figure 4.3). Equation 4.2 is valid when both transmitter and receiver are at the same side of the fracture zone; otherwise there will be no reflection. Note that the pattern is symmetric with respect to the intersection point between the plane and the borehole.

Using the equations (4.1) and (4.2) it is possible to calculate nomograms corresponding to different distances to a point object and for the different intersection angles of a plane. A nomogram is produced by plotting the value of $2a$ for different positions, x , of the radar in the borehole for angles between 0 and 90 degrees. Nomograms provide a simple technique for evaluating radar data and some typical nomograms for point and plane reflectors are depicted in Figures 4.4 and 4.5.

Typical line reflectors appear in some cases, for example drifts that do not intersect the borehole (line reflectors that intersect the boreholes will give the same reflection patterns as planes). This special case can for instance be seen in measurements from borehole N1 since the 3D migration drift is almost parallel with this borehole (see Figure 4.6).

For a line reflector the pulse propagation distance from the transmitter to the line reflector and back to the receiver is generally

$$L(t) = S_+(t) + S_-(t) \quad (4.3)$$

where

$$S_+(t) = \sqrt{d_0^2 + (t \cos \alpha - (x+c))^2 + (t \sin \alpha)^2}$$

$$S_-(t) = \sqrt{d_0^2 + (t \cos \alpha - (x-c))^2 + (t \sin \alpha)^2}$$

and

d_0 = the closest distance from the borehole to
the line

α = angle between line and borehole

t = a point on the reflecting line

By taking the derivative of the function L we get the minimum of L corresponding to the actual path of the reflected pulse. There will be two roots t_1 and t_2 ,

$$t'_1 = A + B$$

$$t'_2 = A - B$$

where

$$A = - \frac{\cos \alpha (d_0^2 + (c^2 - x^2) \sin^2 \alpha)}{2 x \sin^2 \alpha}$$

and

$$B = \sqrt{A^2 + \frac{d_0^2 \cos^2 \alpha}{\sin^2 \alpha}}$$

Thus the smallest distance to a reflection point will be $L(t') = S_+(t') + S_-(t')$ where t' is one of t'_1 or t'_2 .

Nomograms for line reflectors can be produced by plotting $L(t')$ for different borehole positions and angles, α , between the line and the borehole. However, a new nomogram must then be calculated for each minimum distance d_0 .

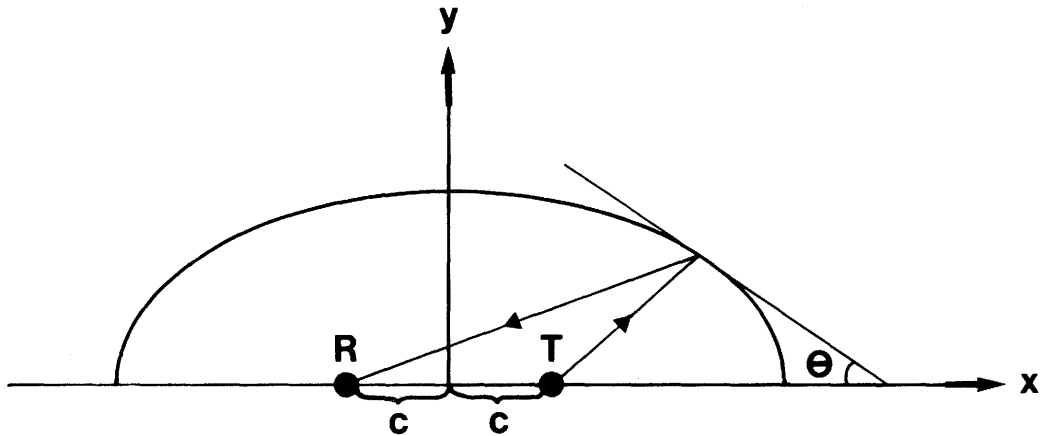


Figure 4.3 The possible reflection points corresponding to a particular reflection are on an ellipse with the major axis $2c$ (the distance between transmitter and receiver).

POINTLIKE REFLECTOR

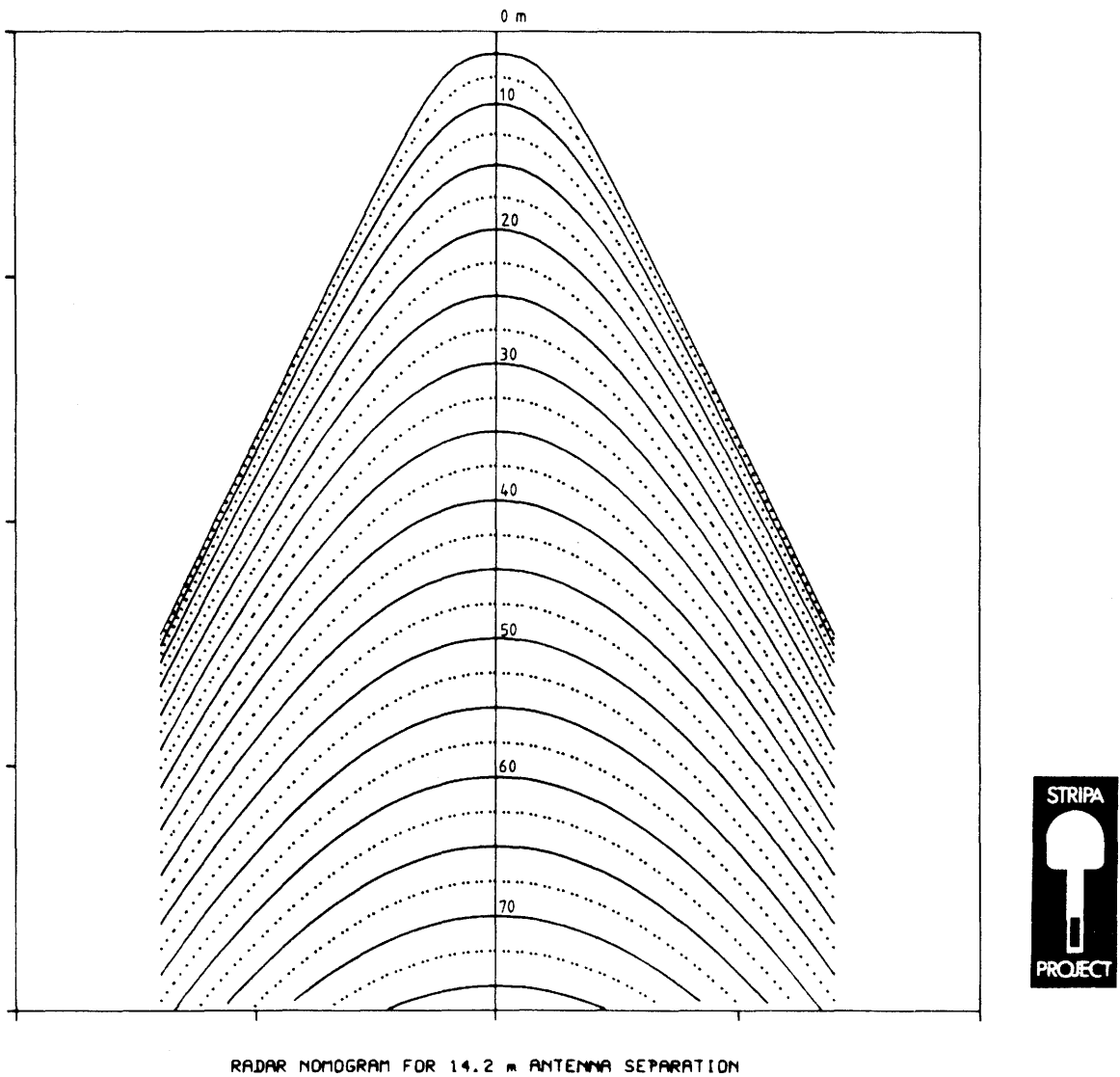


Figure 4.4 Radar nomogram for a point reflector.

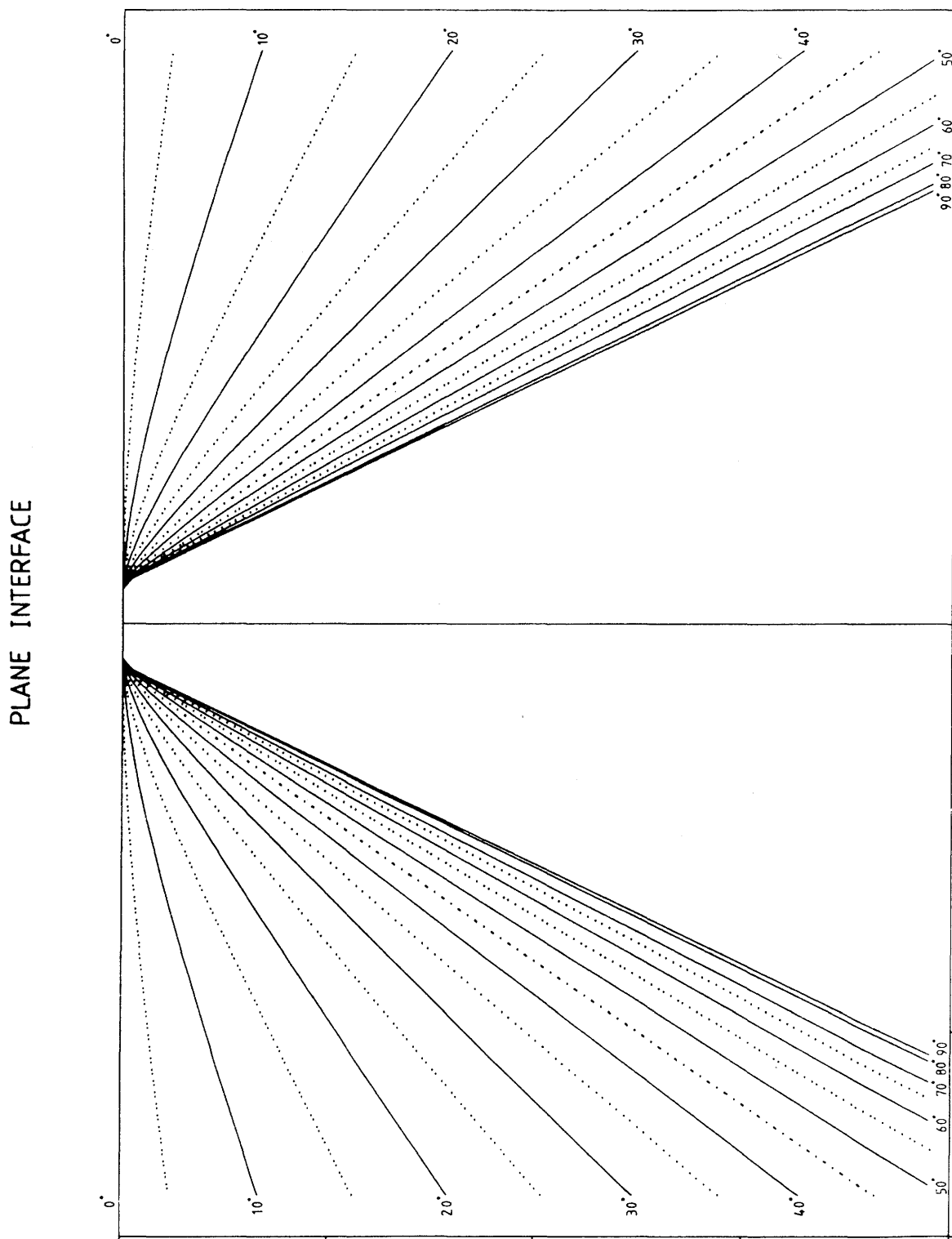


Figure 4.5 Radar nomogram for a plane reflector.

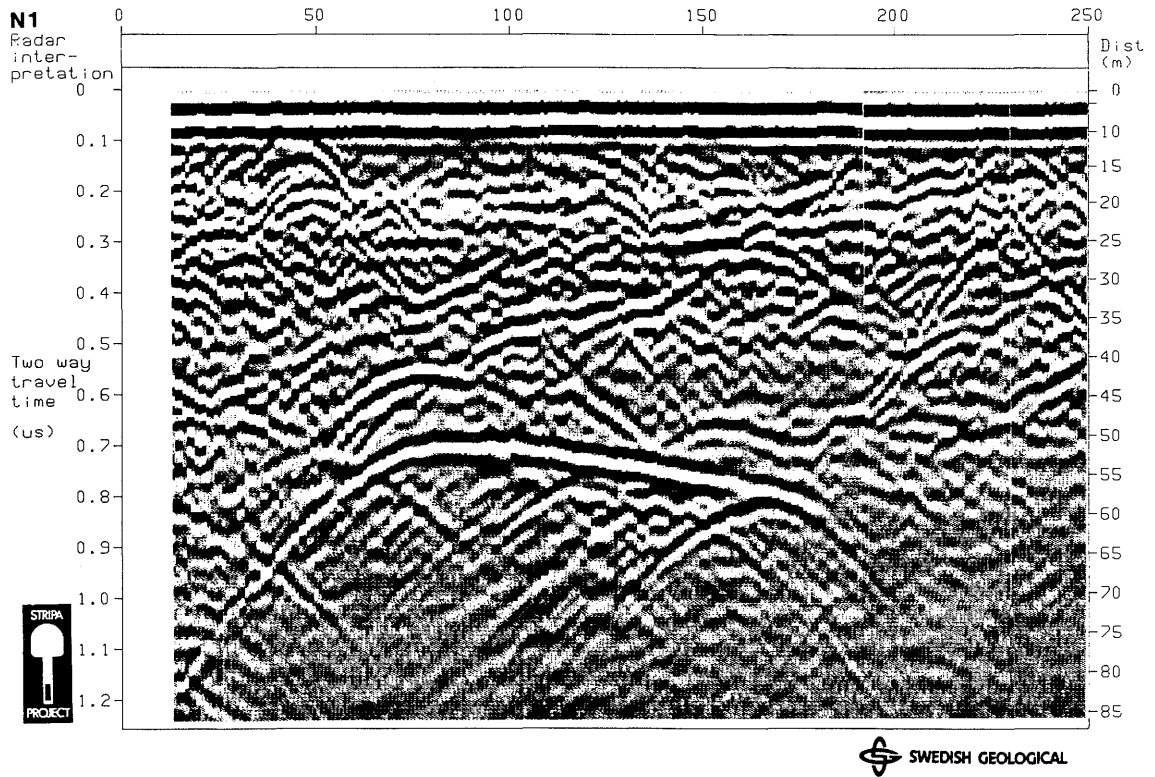


Figure 4.6 Radar reflection map from the borehole N1 at the Cross-hole site in Stripa measured with a center frequency of 22 MHz. The 3D migration drift is clearly visible.

4.3 SIGNAL PROCESSING

In a radar reflection measurement the transmitted pulses are reflected from inhomogeneities in the rock. The problem is to identify the reflected pulses from individual objects and to obtain an accurate travel time estimate for each reflex. This task is often complicated by deterioration of the radar signal caused by various effects. For example the transmitted pulse is not the ideal spike which would be desirable. It has a certain time duration, which if excessive is called ringing, and which will limit the attainable resolution. The varying attenuation for different frequency components will cause broadening of the pulse with time. The radar signal is also to some extent contaminated by random noise (mainly from the receiver amplifier). Digital signal processing is applied to the radar data in order to enhance the reflections which give information about the structure of the rock.

The rock in which the radar waves propagate will modify the transmitted signal. In this context the rock may be considered as a filter which acts on the transmitted signal and produces the received signal as its output. In addition to the filtered signal there is noise which is added to the signal. The received signal, $R(t)$, may be expressed as a convolution of the earth filter, $X(t)$, with the transmitted signal, $T(t)$, with the addition of noise, $N(t)$. Thus

$$R(t) = \int X(t-\tau)T(\tau)d\tau + N(t) \quad (4.4)$$

The earth filter, $X(t)$, is the impulse response of the earth, i.e. the response that would be obtained if the transmitted signal were a unit impulse. If the rock is considered to consist of a number of reflecting interfaces the earth filter would in principle consist of a series of unit impulses at different delay times and with amplitudes corresponding to the reflection coefficients. This means that in such a case the received signal would consist of replicas of the transmitted signal with different time delays and amplitudes. The purpose of filtering the received signal is to obtain an estimate of the earth filter function.

The discussion of filtering is often simplified by studying the processes in the frequency domain. If equation (4.4) is transferred to the frequency domain it becomes:

$$R(\omega) = X(\omega)T(\omega) + N(\omega) \quad (4.5)$$

A filter is then to be applied on the received signal in order to improve the signal in relation to a selected criterion. The filter is designated, $H(\omega)$, and the filtered output is called $Y(\omega)$. Thus,

$$Y(\omega) = H(\omega)R(\omega) \quad (4.6)$$

4.3.1 Matched filters

A matched filter is a filter which will process signals in an optimum manner as far as the signal to noise ratio is concerned. It can be shown that the optimum matched filter in the presence of white noise is a filter which is the complex conjugate of the input signal multiplied with an arbitrary time delay. Such a filter is often called a correlation filter.

Now we need an estimate of the earth filter, $X(t)$ or $X(\omega)$. It was stated above that the earth filter in principle consists of a series of spikes with different time delays and amplitudes. This implies that the received signal will be a sum of transmitted pulses. Thus, it is natural to use the complex conjugate of the transmitted signal as a filter, i.e. $H(\omega)=T^*(\omega)$. The filtered signal then becomes

$$Y(\omega) = X(\omega) T(\omega)T^*(\omega) + N(\omega)T^*(\omega) \quad (4.7)$$

Here we see that if the transmitted signal is a unit impulse then $T(\omega)T^*(\omega)=1$ and the best estimate of the earth function would be obtained. In reality the bandwidth of the transmitted pulse is limited and the earth response function will be distorted. It should be noted that the earth filter spectrum is multiplied by the square of the transmitted signal and that if the transmitted signal has a limited bandwidth then a matched filter will result in a signal with even smaller bandwidth. In other words: limited bandwidth corresponds to ringing, and if there is significant ringing in the transmitted pulse this type of filter will cause even more ringing.

Another problem is that the form of the transmitted signal is not really known. Estimates can be obtained from the received signal, but in practice it is difficult to find a representative signal which is not affected by inhomogeneities in the rock. Efficient matched filters can be obtained through the use of elementary functions which simulate the transmitted pulse. A good matched

filter for the radar signals can be generated from a sine wave oscillation modulated by a Gauss curve,

$$H(t) = A \sin(\omega t) \exp(-((t-t_0)/w)^2/2) \quad (4.8)$$

The parameters are adjusted so that the frequency of oscillation, phase and pulse width best fit the received signal. Selecting the parameters of the filter is to a large extent a matter of judgement and testing.

Figure 4.7 shows a plot of rawdata from borehole F3. The correlation or matched filtered radar plot is shown in Figure 4.8. Correlation filters generally lead to a strong reduction in random noise and give good results if the transmitted pulse is well defined and has little ringing. The correlation filters have been found to be efficient and easy to use and most results presented in this report have therefore been correlation filtered.

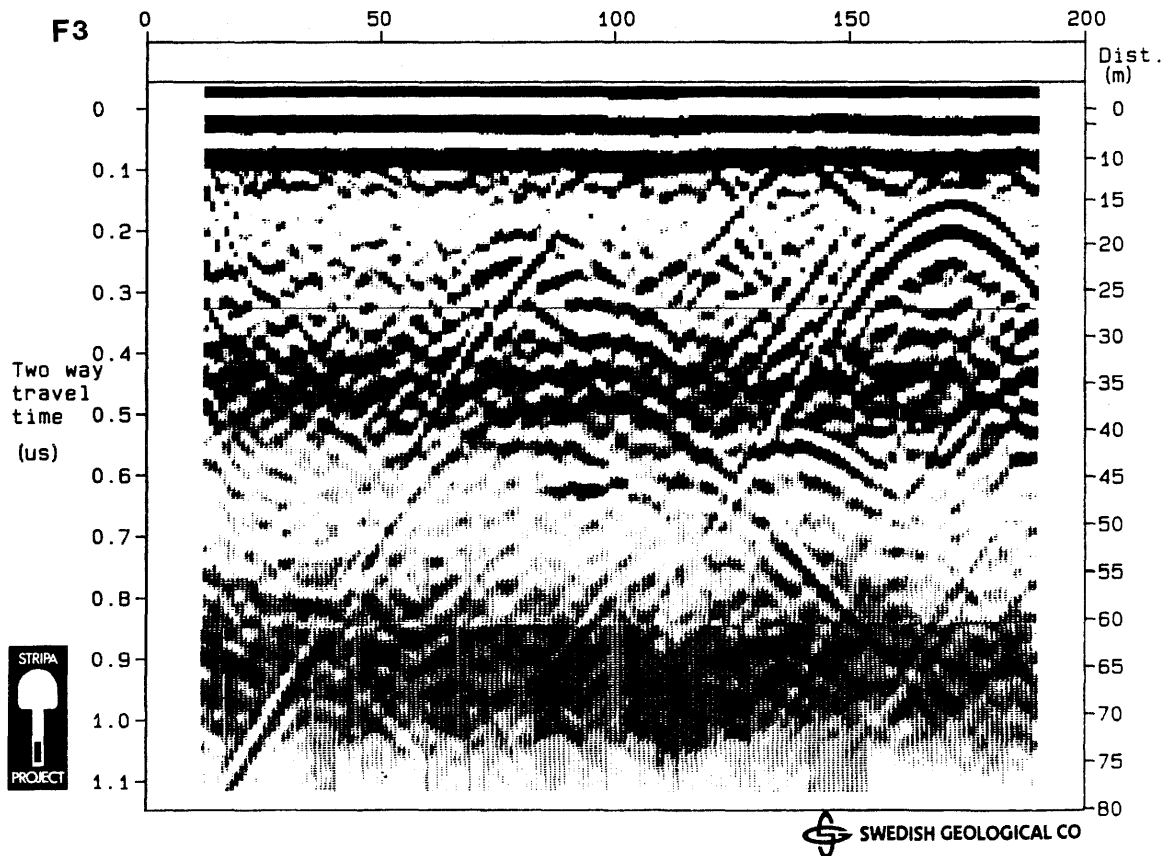


Figure 4.7 Radar map from borehole F3. Rawdata obtained at a center frequency of 22 MHz.

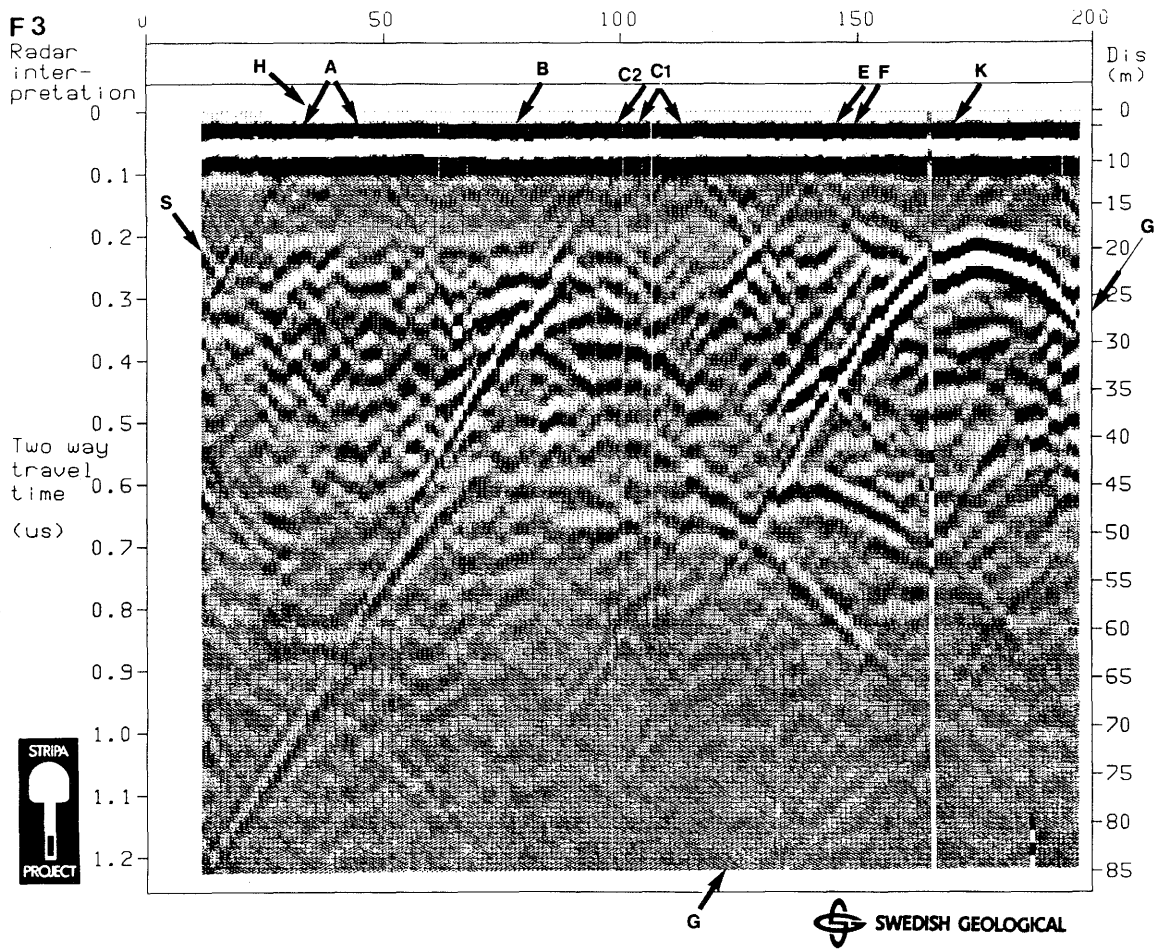


Figure 4.8 Correlation filtered radar map from borehole F3. Center frequency 22 MHz.

4.3.2 Band pass filters

Band pass filters are in many cases efficient for improving radar plots. In some radar measurements the received signal contains a low frequency oscillation which is caused by the receiver electronics. Bandpass filters are then useful for removing this oscillation and facilitate the amplification of the small signals received for large travel times.

The radar signals usually also contain some noise at the high frequencies where there is no energy in the transmitted signal. This noise can be removed by band pass filtering. It should be noted that a correlation filter in general also limits the frequency band of the filtered signal.

4.3.3 Deconvolution filtering

Some tests have also been performed with deconvolution filters. The idea behind deconvolution filtering is to try to reconstruct the earth filter function as closely as possible for an arbitrary input signal. A filter of the following type has been used:

$$H(\omega) = \frac{T'^{*}(\omega)}{T'(\omega)T'^{*}(\omega) + N'(\omega)N'^{*}(\omega)} \quad (4.9)$$

When this filter is applied to the received signal we obtain

$$Y(\omega) = \frac{T(\omega)T'^{*}(\omega)}{T'(\omega)T'^{*}(\omega) + N'(\omega)N'^{*}(\omega)} X(\omega) + \frac{T'^{*}(\omega)N(\omega)}{T'(\omega)T'^{*}(\omega) + N'(\omega)N'^{*}(\omega)} \quad (4.10)$$

where $T'(\omega)$ is an estimate of the transmitted signal and $N'(\omega)$ an estimate of the noise spectrum. The first term will give the earth filter function if the spectral power of the transmitted signal is much larger than the noise power and for frequencies where the noise power is larger than the signal power a small value will be obtained. The second term essentially consists of the correlation between the transmitted signal and the noise and since these signals are normally uncorrelated the term should be small.

In the design of this filter the estimated transmitted signal, $T'(\omega)$, is selected as a damped oscillation according to equation (4.8). Other

forms of the transmitted signal may also be used. The noise is assumed to be white noise which makes the noise factor in the denominator a constant. Experience shows that this filter is sensitive to noise and to spectral energy in the received signal outside the frequency band of the assumed transmitted signal. The filter output may be smoothed by increasing the noise factor in the denominator. If the noise factor is made very large the term $T'(\omega)T'^*(\omega)$ in the denominator may be neglected and the deconvolution filter becomes a matched filter, cf. equation (4.7). Tests with various filters of this type have been attempted but significant improvements were obtained only in a few cases. One example of deconvolution filtering is shown in Figure 4.9.

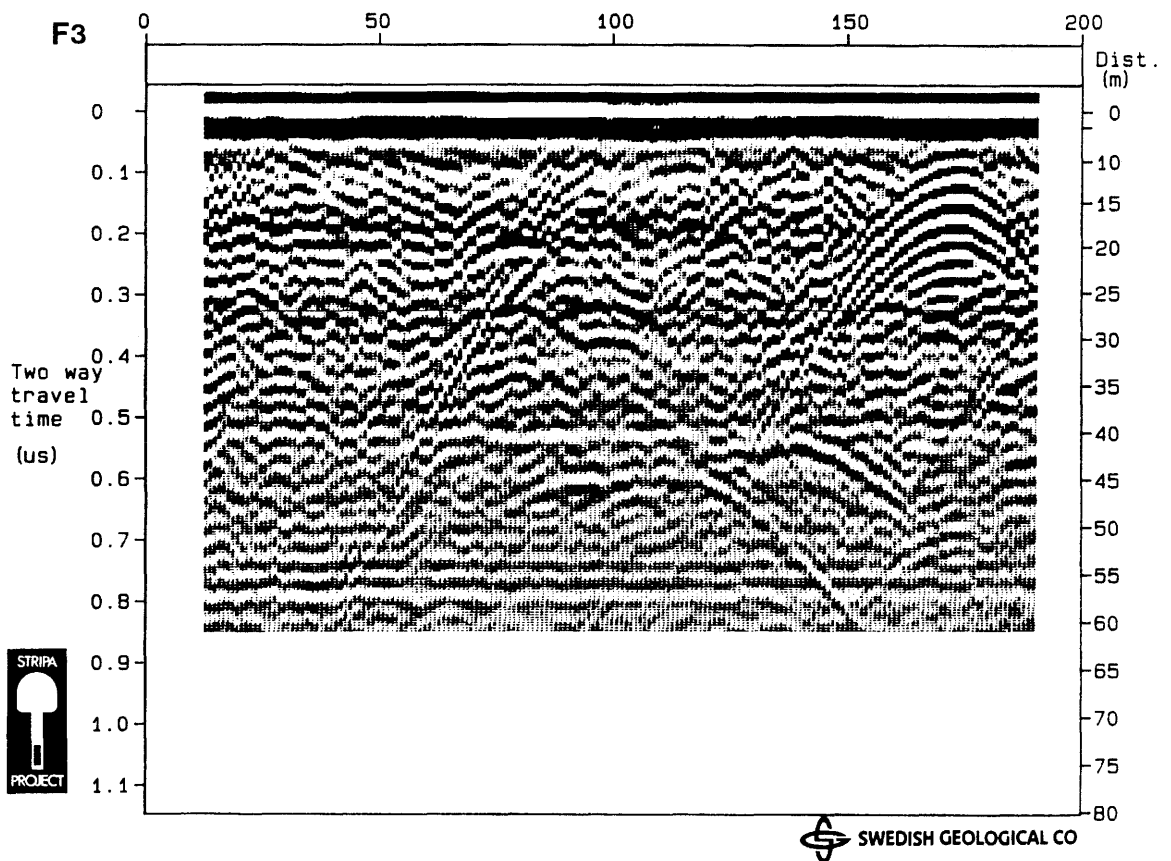


Figure 4.9 Deconvolution filtered radar plot from borehole F3. Center frequency 22 MHz.

4.3.4 Attenuation compensation

The radar signals are significantly attenuated as they propagate through the rock. The amplitude of each frequency component decreases according to $\exp(-\alpha(\omega)r)/r$ (cf. 3.9). Measurements on core samples (Agmalm, 1985, Section 3.3) and in situ data (Sundqvist, 1985) show that the attenuation constant increases approximately linearly with frequency. Consequently there will be a loss of high frequency energy in the signal as the propagated distance increases. In the time domain this leads to a broadening of the pulses.

The attenuation of the higher frequencies may be compensated by multiplying each spectral component with the inverse of the attenuation factor, i.e. $r \exp(\alpha(\omega)r)$. This function will cause a large amplification of the high frequencies where the signal consists of noise only. It is thus necessary to construct an attenuation function, $\alpha(\omega)$, that increases linearly with frequency for the low frequencies where the signal carries information and decreases rapidly for higher frequencies (Sundqvist, 1985). An example of the original and the compensated power spectrum for a radar pulse is shown in Figure 4.10. As can be seen the compensation modifies the spectrum significantly.

One problem with attenuation compensation filters is that the compensation must be made for a certain distance. For distances shorter than the selected one the signal will be overcompensated which results in ringing and for larger distances there will be undercompensation. The filter also enhances noise which is a serious problem. The noise can be reduced by combining the attenuation compensation with a matched filter. The improvements provided by such a combined filter can be quite significant as demonstrated in Figures 4.11 and 4.12 which display a borehole measurement before and after filtering.

In the analysis of the radar signals the phase dispersion has also been studied. It was found that the phase dispersion is insignificant in the frequency range covered by the radar (Sundqvist, 1985).

FOURIERSPECTRUM (Trace 40:120 m) COMPENSATED - - ORIGINAL —

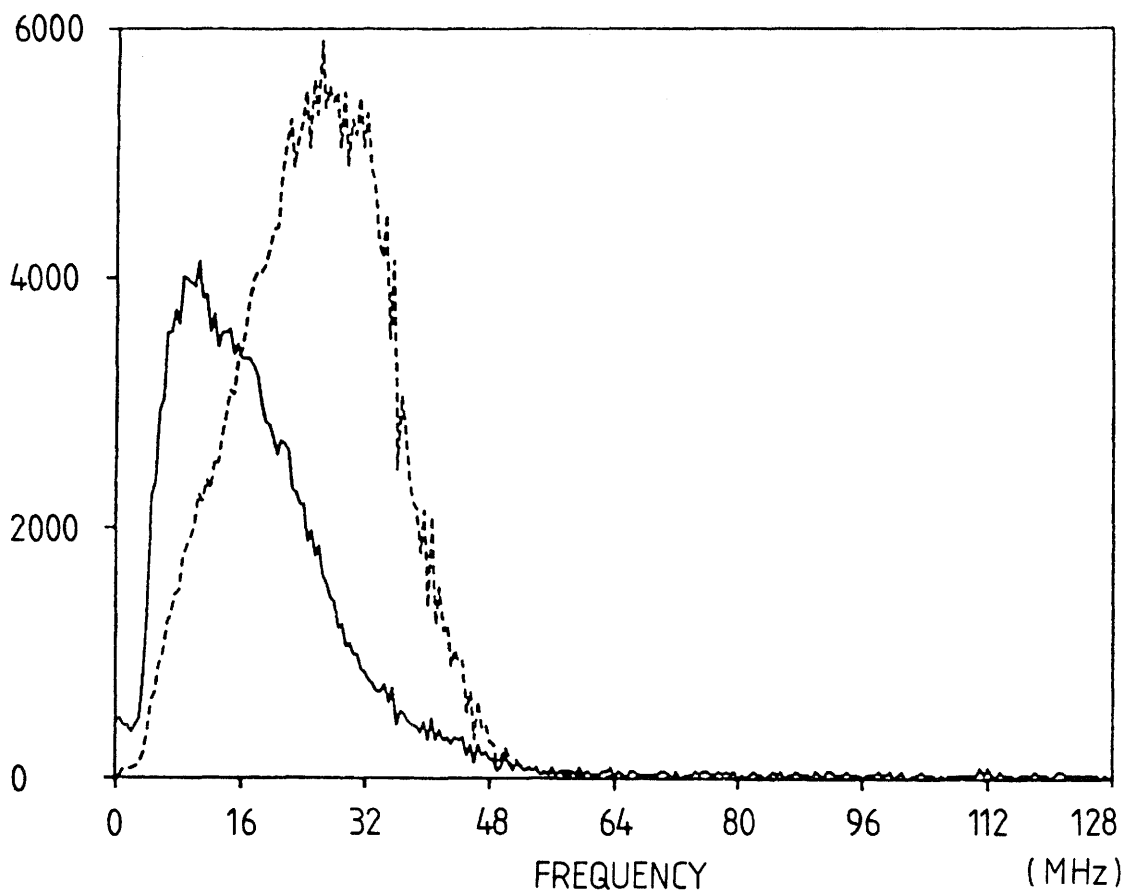


Figure 4.10 The Fourier spectrum of a radar pulse that has propagated 120 m through rock before and after attenuation compensation.

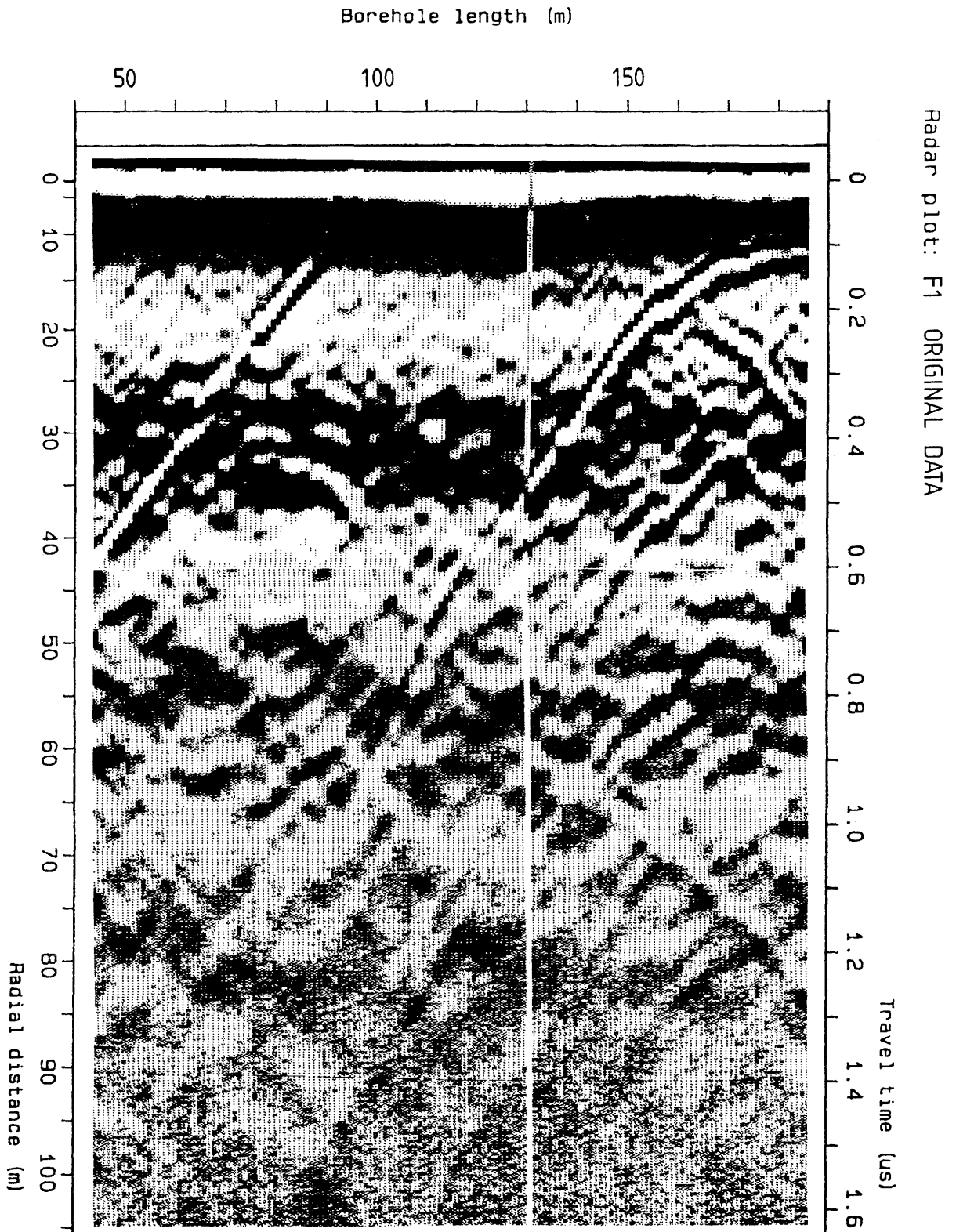


Figure 4.11 Original radar map from a reflection measurement in F1. Center frequency 22 MHz.

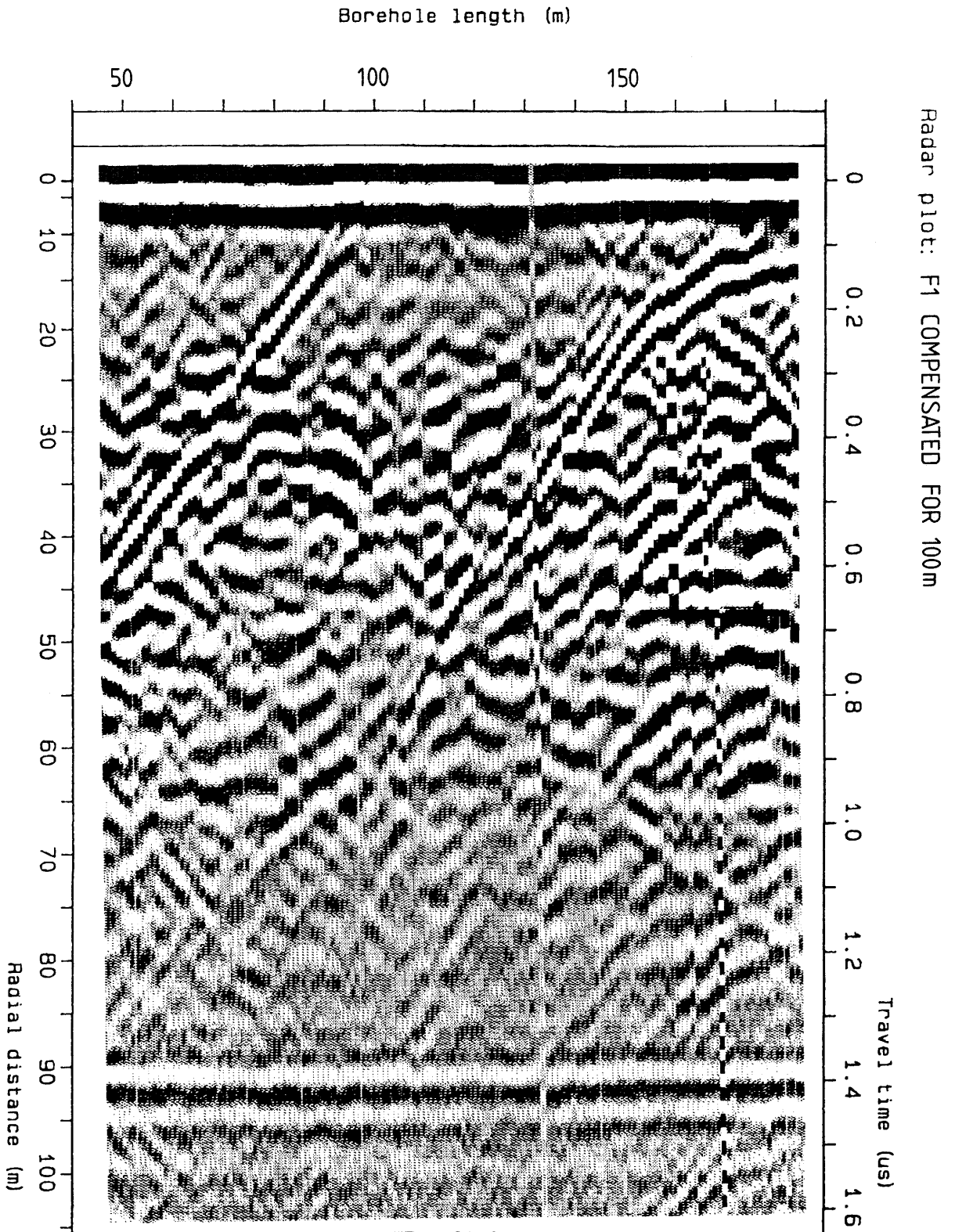


Figure 4.12 Radar map from borehole F1 (same as Figure 4.11) which has been filtered with an attenuation compensation filter combined with a matched filter. The compensation was made for a propagation distance of 100 m. Note that radial distance roughly corresponds to half the propagation distance.

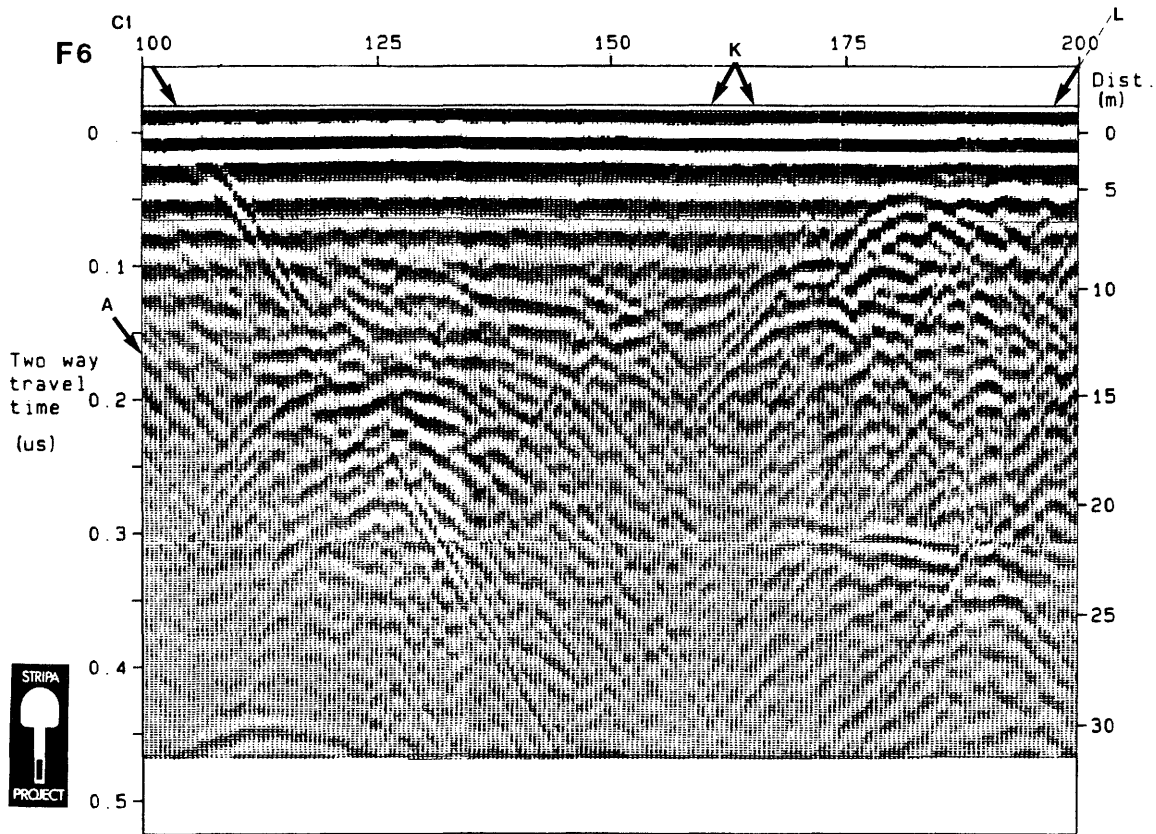
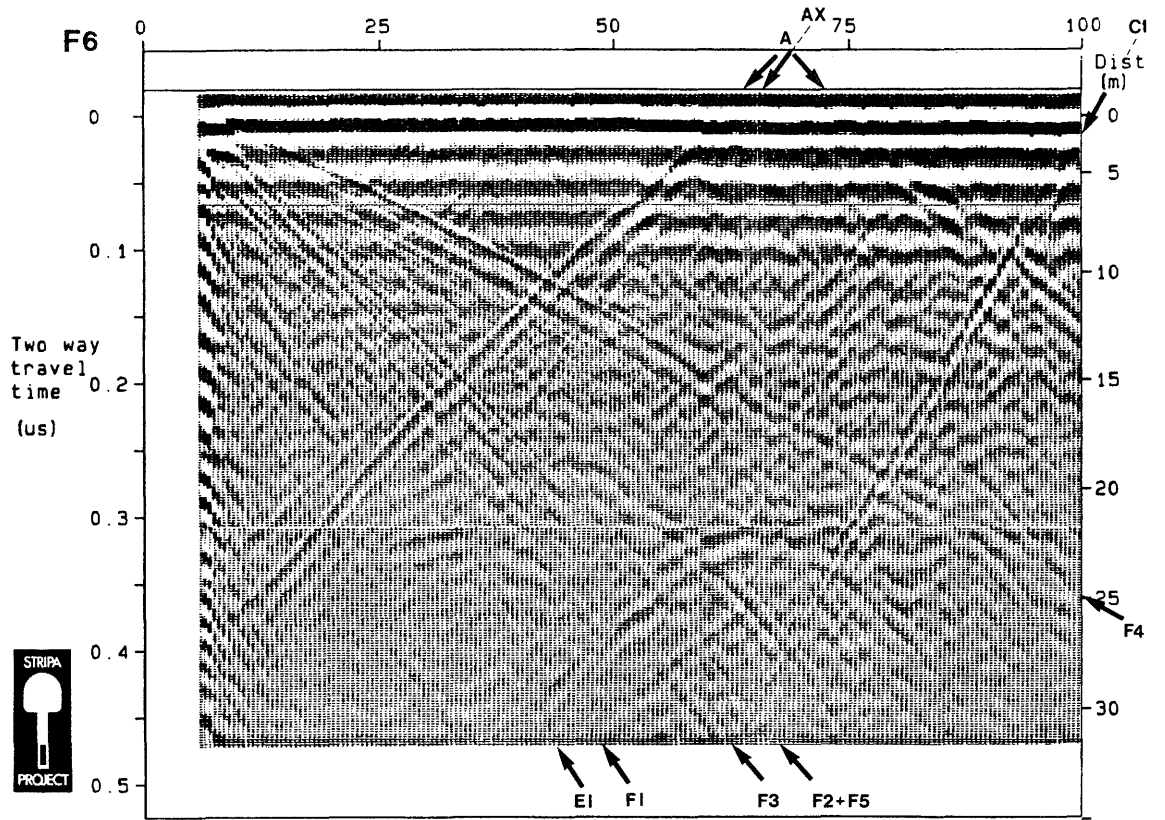
4.3.5 Reflection coefficient plots

As stated above the radar signals are rapidly attenuated. A consequence of this is that the dynamic range of the received signal is very large. The dynamic range of the Stripa radar system is 96 dB and this range must be displayed in a grey scale plot with an effective dynamic range of about 20 dB. To display the signals within this limited range a time variable gain is applied to the signal before plotting. This gain can be adjusted so that it compensates for the attenuation and the geometrical spreading of the signal. Thus, the function $vt \exp(\alpha vt)$ is multiplied to the signal trace using an attenuation constant typical for the center frequency. The resulting radar plot will then become a sort of pseudo reflection coefficient plot in that the amplitude of the reflected pulses is independent of the travel distance. However, the radiated energy also depends on the radiation lobes (cf. 3.9) and thus the energy received will depend on the angle of the reflector relative to the borehole. Hence, this type of plot will give the relative magnitude of the reflection coefficients for the planar reflectors (fracture zones) with the same orientation relative to the borehole. An example of such a plot is given in Figure 4.13.

4.3.6 Two dimensional filtering

In some cases ringing can be significant in the radar plots resulting in a series of parallel bands in the radar maps. Ringing can be removed by filtering the radar image with a moving average filter. The filter is constructed so that the average is formed of a number of traces adjacent to the trace to be filtered and the average is subtracted from the center trace. This is then done for all traces along the borehole. With this type of filter features in the radar signals which are similar for several adjacent traces will be removed. This includes ringing as well as structures nearly parallel to the borehole.

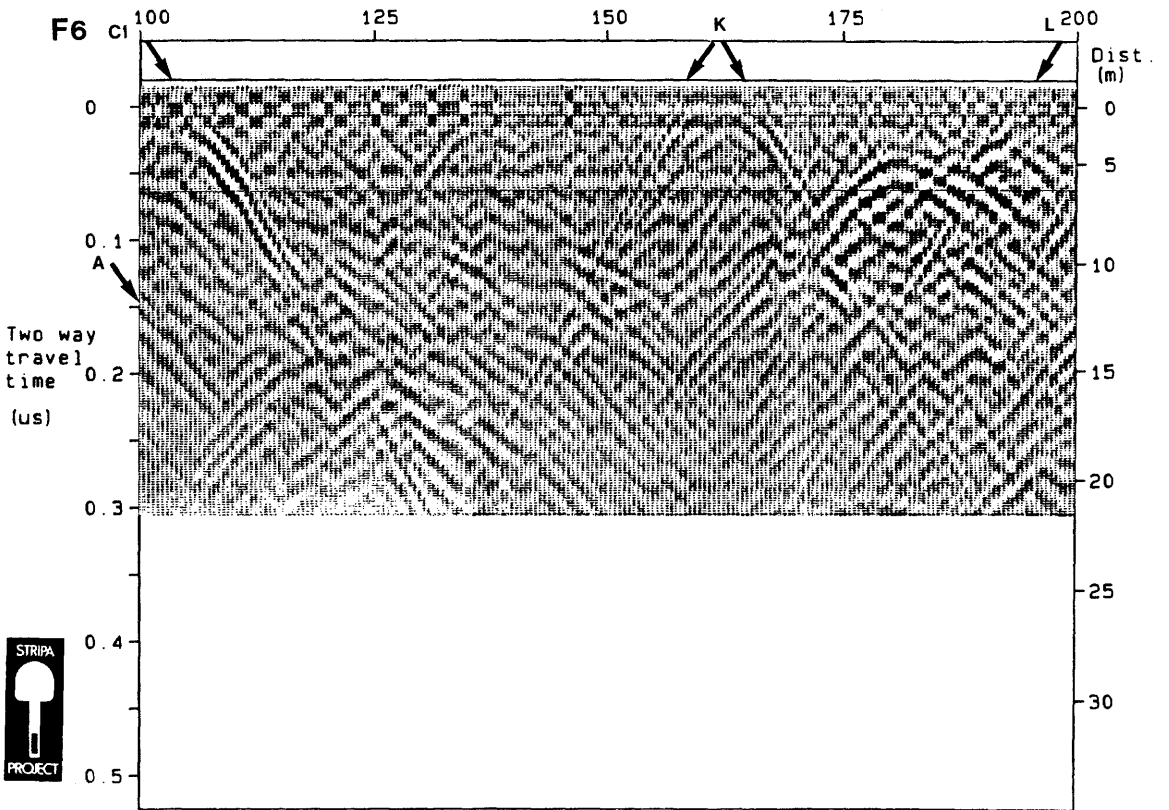
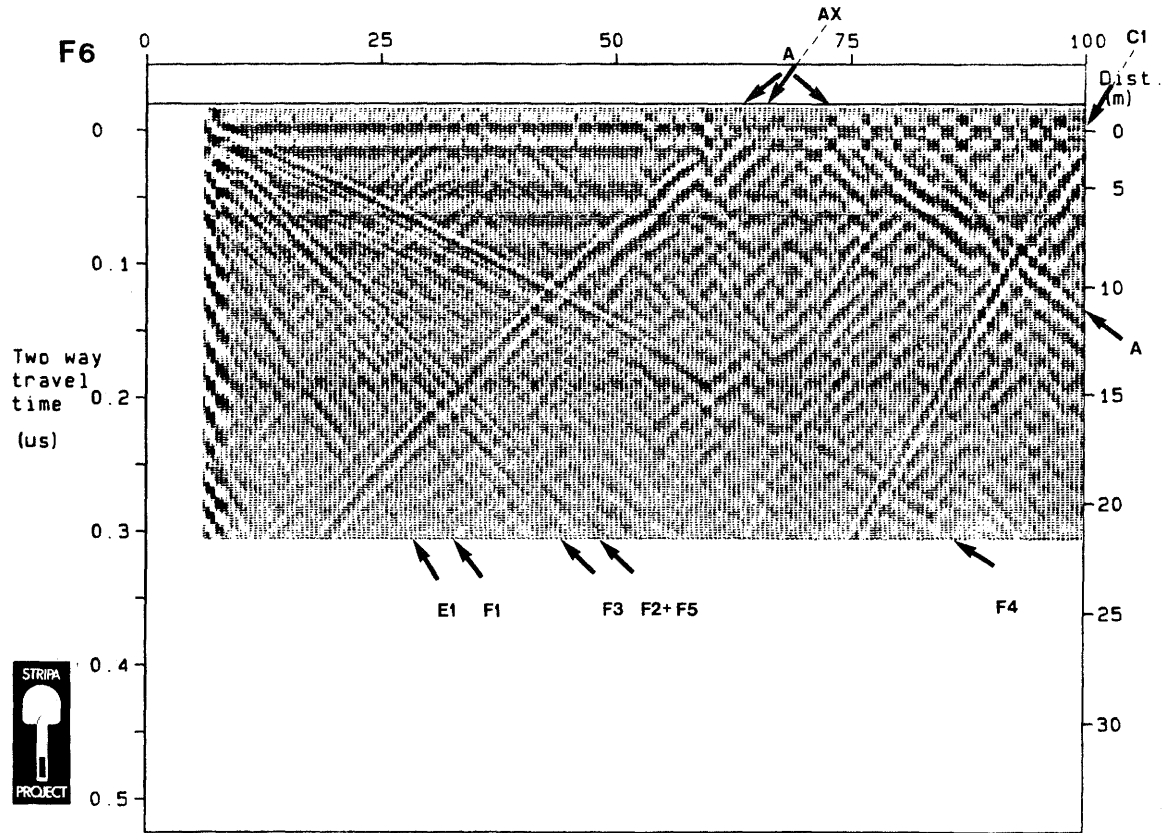
An example of a radar measurement filtered with a moving average is shown in Figure 4.14. In this example the ringing is almost completely removed and this improves the resolution significantly, especially close to the borehole as this is where the signal contains significant ringing. The amplitude of some of the reflections caused by structures nearly parallel to the hole have also been reduced significantly, cf. Figure 4.13 which displays data from the same measurement.



SWEDISH GEOLOGICAL CO

0.5 m step T-R distance 7.14 m $F_s=532.6$ MHz $v=120$ m/us

Figure 4.13 Pseudo reflection coefficient plot of band pass filtered data for borehole F6. Center frequency 60 MHz.



0.5 m step T-A distance 7.14 m $F_s=532.6$ MHz $v=120$ m/us

Figure 4.14 Radar data from F6 filtered with a moving average filter. Data is plotted with a time gain to obtain a pseudo reflection coefficient plot. Center frequency 60 MHz.

4.4

RESULTS FROM SINGLE HOLE MEASUREMENTS

Most of the measurements performed at the Crosshole site in Stripa are single hole radar measurements. In this section an overview of the results are given, while the following section is devoted to a detailed analysis of the results.

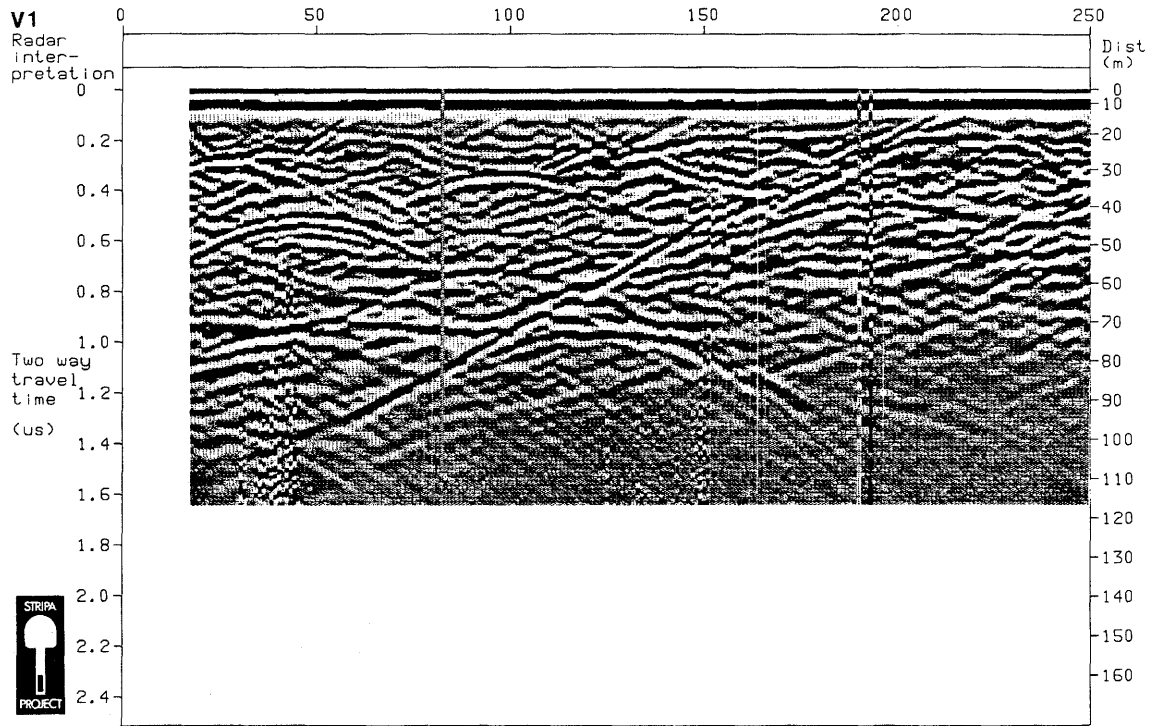
The typical radar map in Figure 4.2 shows that the radar system successfully solves the main object of the project, i.e. to detect fracture zones. Several zones are visible in this figure and the patterns agree with the theoretical description given in Section 4.1. The fracture zones must be quite plane since the patterns do not deflect noticeably from the predicted shape even when the zones can be followed over more than a hundred meters.

Centered at a borehole depth of about 170 m appears the prominent reflection from the drift shaped like the pattern of a point reflector (Equation 4.2). This drift passes quite near the borehole, about 20 m away, and it is almost perpendicular to the borehole which explains the pointlike nature of the pattern as described in Section 4.2.

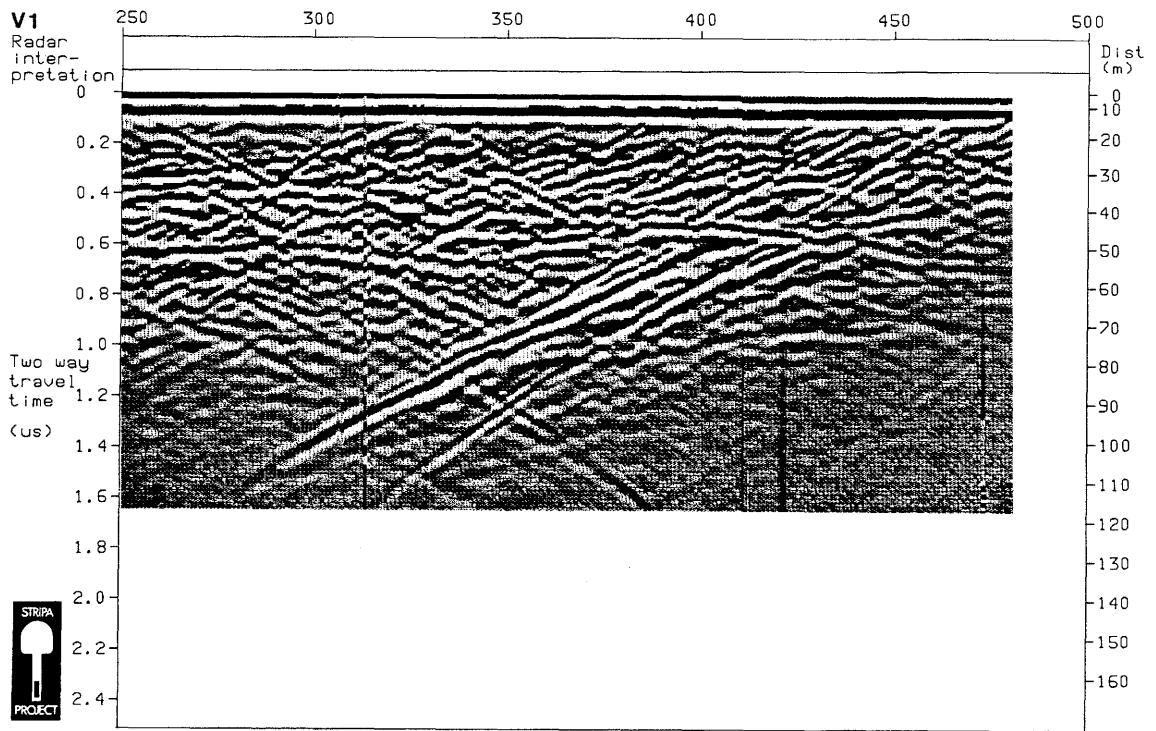
One of the most important characteristics of the radar system is the available range. The identification of fracture zones is greatly simplified if the reflection pattern can be followed over large distances. One can then also observe that the reflectivity appears to vary over a fracture zone. At 22 MHz the major zones can be traced to a range exceeding a hundred meter in Stripa granite as seen in Figure 4.15. This is of course the distance to the reflection point; it will depend on the intersection angle between the borehole and the fracture plane how far the reflection point really is from the borehole.

When the frequency of the system is increased the range decreases as seen in Figure 4.16 where the same measurement as in Figure 4.2 has been performed at 60 MHz center frequency. By comparing the extension of the fracture zones in Figures 4.2 and 4.16 it is easy to see that the range has been reduced to half the previous value. At the same time the resolution has been very much improved: fracture zones can be followed closer to the borehole and many more are visible than at lower frequencies.

The most dramatic change occurs for the boreholes themselves: at 22 MHz they can sometimes be faintly discerned in some radar maps while at 60 MHz they are clearly visible and very sharply defined. In Figure 4.16 several of them can be seen extending from the site at the origin of the diagram. The



SWEDISH GEOLOGICAL



SWEDISH GEOLOGICAL

Figure 4.15 Radar reflection map from the borehole V1 measured with a center frequency of 22 MHz.

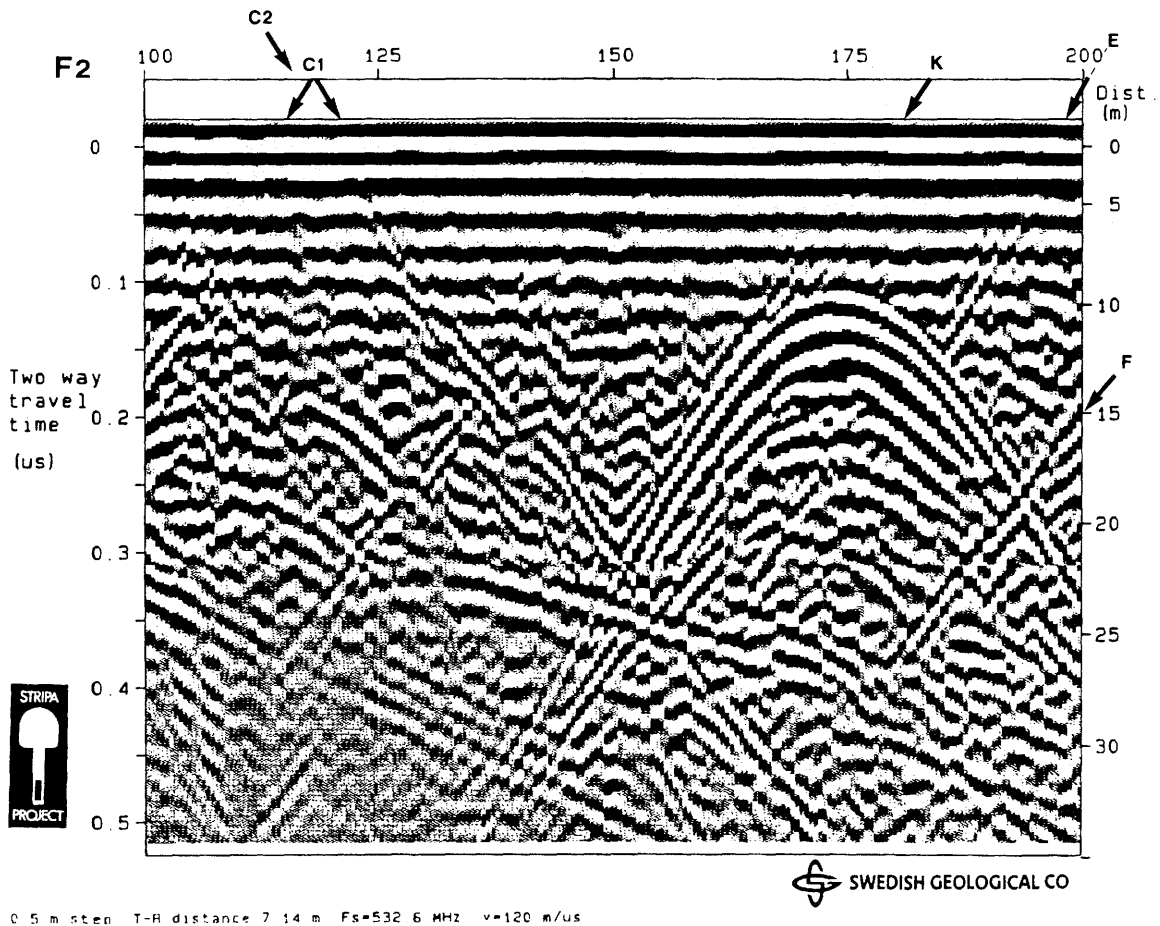
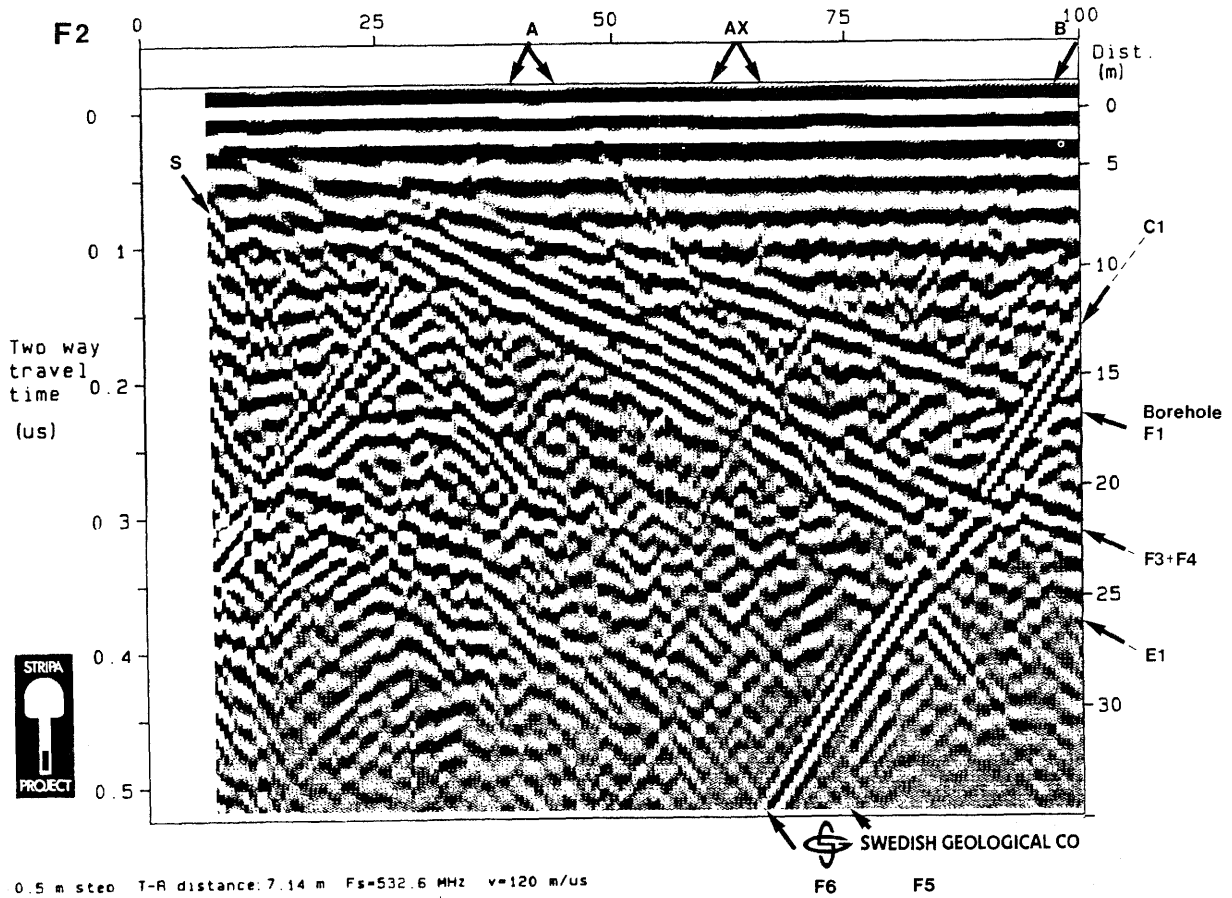


Figure 4.16 Radar reflection map from the borehole F2 measured with a center frequency of 60 MHz.

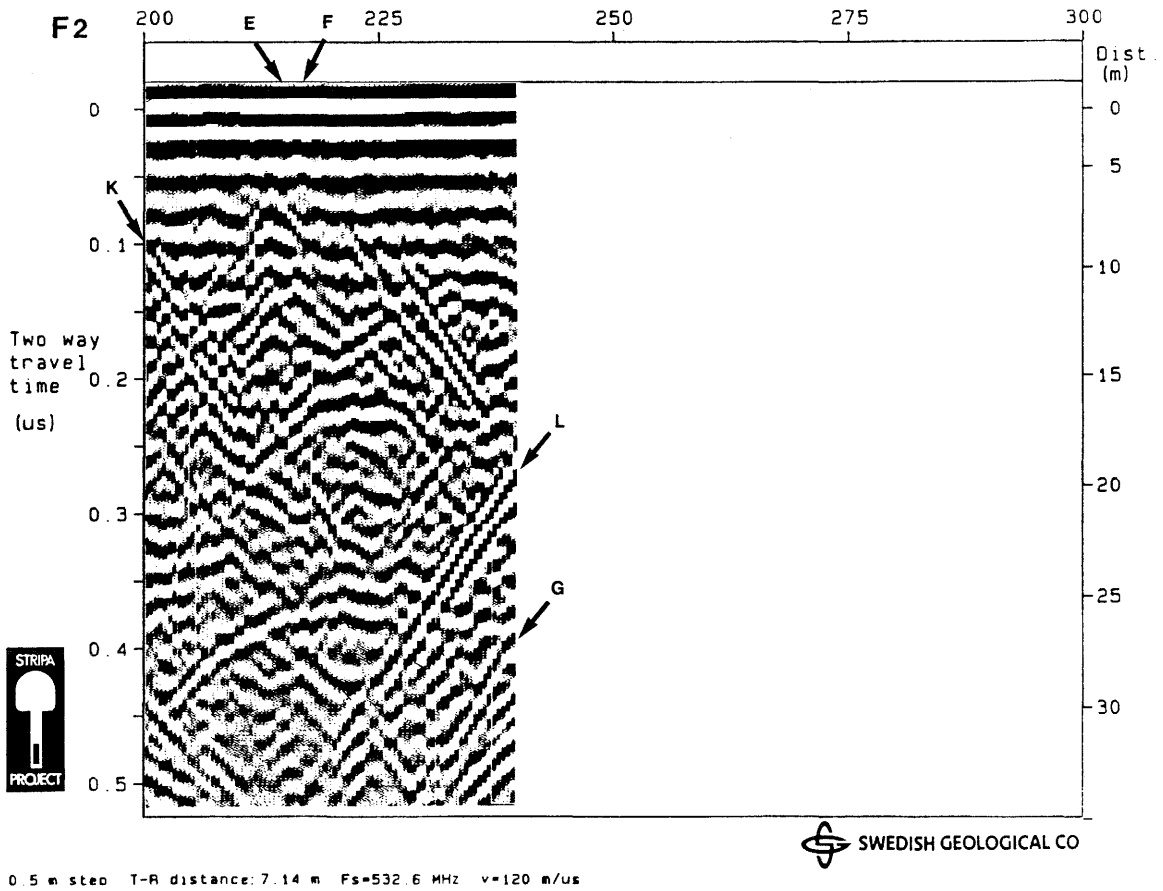


Figure 4.16 Radar reflection map from the borehole F2 measured with a center frequency of 60 MHz.

strong scattering is caused by water in the boreholes (diameter 76 mm): when the borehole is airfilled as at the beginning of borehole F6 the strength of the reflection is reduced. The position of the boreholes is well defined so the reflections provide an accurately known object suitable for calibration of the radar system. Such a calibration has been performed using all the 60 MHz measurements. It showed that the radar system works consistently and that the intersection angles can be determined quite accurately, down to one degree.

In single hole measurements the separation distance between the transmitter and receiver can be varied and Figures 4.17-4.19 show some examples of how this will affect the radar maps. When the separation distance is increased a shorter part of the borehole can be covered in a measurement and in practice this results in loss of information. In order to reach a particular reflection point a greater propagation distance will also be involved so the pulse will suffer more from attenuation.

Even more important is the information loss at close ranges. The reflected pulse can only be separated from the direct pulse between the transmitter and receiver if there is a sufficient time interval to resolve them. It is obvious that as the separation between the antennas increases so does the minimum distance to the borehole necessary to ensure resolution and this is confirmed in Figure 4.17. It would of course be desirable to place the antennas very close to each other in order to achieve resolution close to the borehole but the direct signal will then saturate the receiver. The only advantage of increasing the separation distance seems to be that the reflections from structures parallel and 10-20 m away from the borehole appear to be reduced, possibly because the incident pulse covers a larger area so that each weak reflector becomes less prominent.

During the measurements we have mainly identified fracture zones, tunnels and boreholes. One can however also observe other features of interest, such as mineral boundaries. A characteristic example is seen in a measurement from the surface at Stripa in borehole SBH1. Boundaries between leptite and granite occur at 50 m and 200 m as seen in the logging results (Nelson, Magnusson and Rachiele, 1982). In the radar plot, Figure 4.20, the leptite can be seen in two ways: between 50 and 200 m the range is decreased by the attenuation caused by leptite and one can also see reflections at these points in the borehole (the strong reflection extending from the origin is the ground surface).

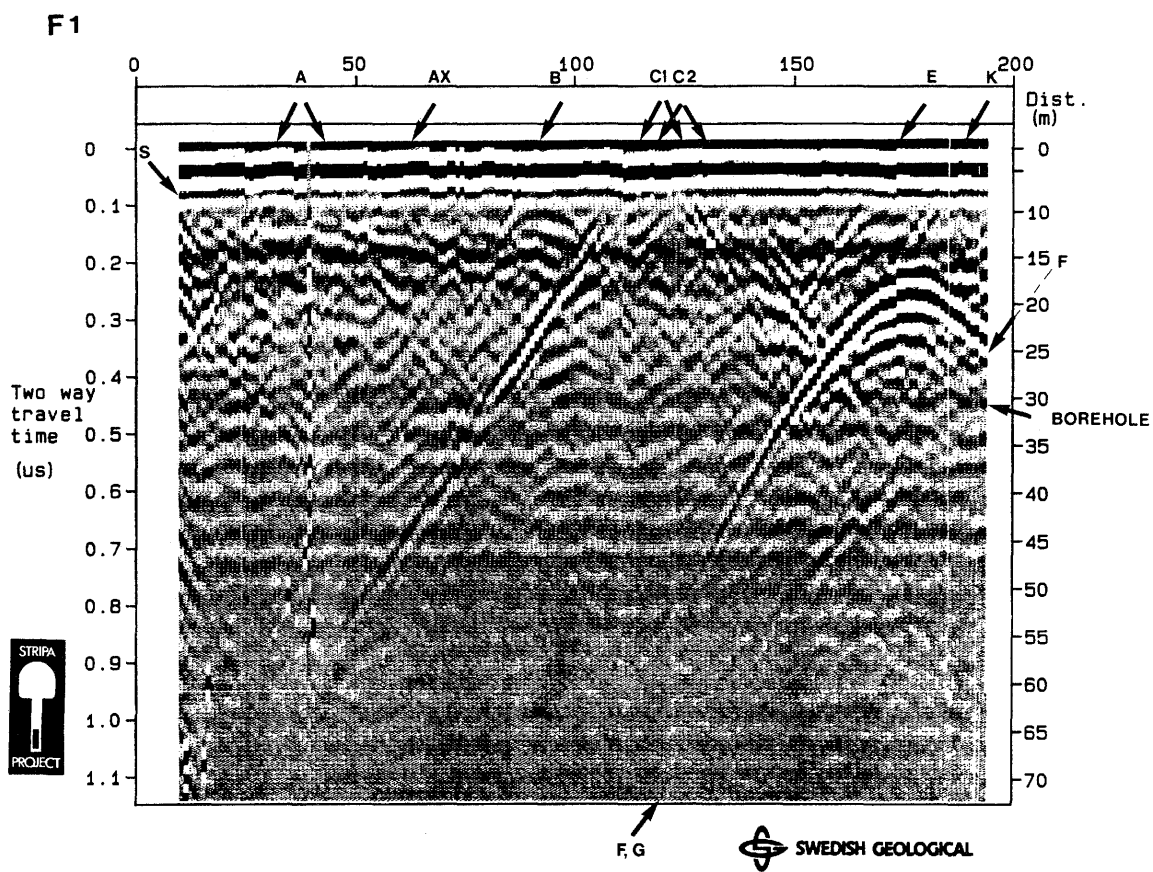


Figure 4.17 Radar reflection map from borehole F1 measured with a center frequency of 22 MHz. Transmitter receiver spacing 4 m.

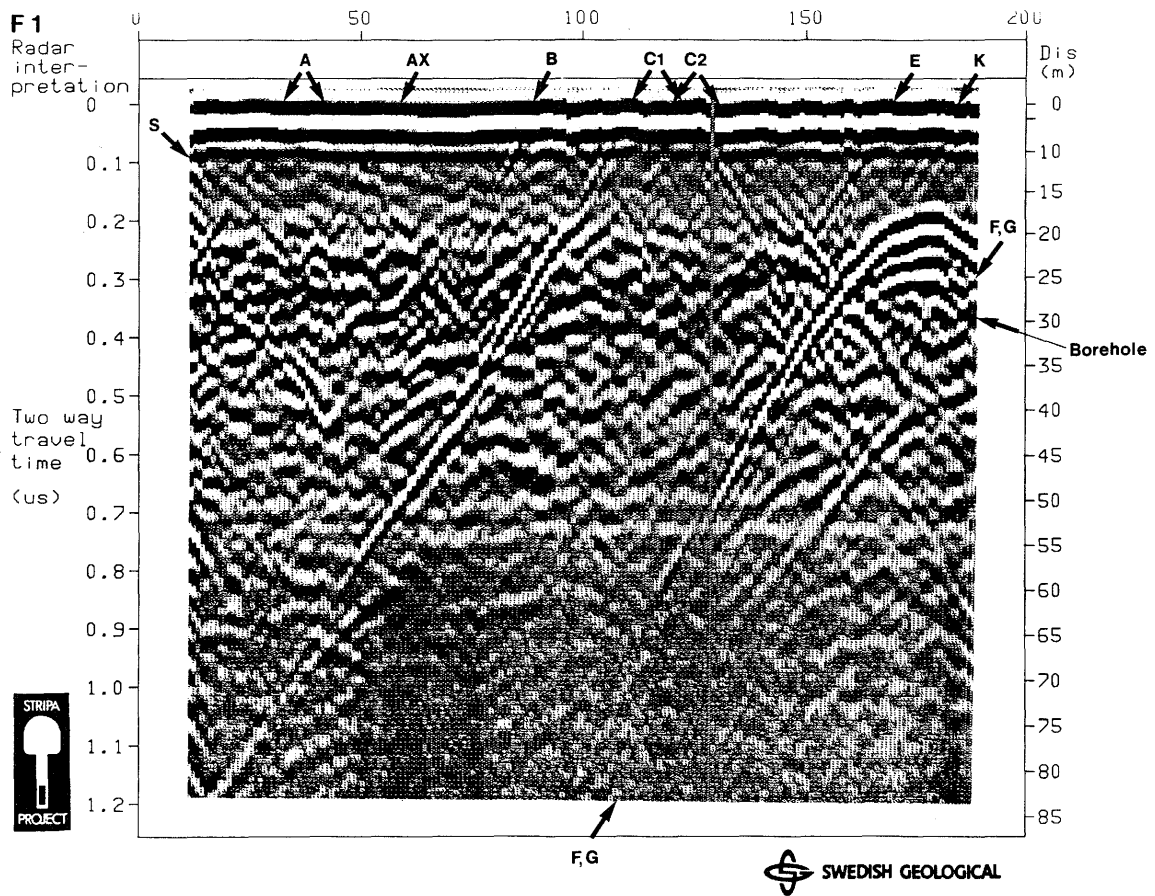


Figure 4.18 Radar reflection map from borehole F1 measured with a center frequency of 22 MHz. Transmitter receiver spacing 10 m.

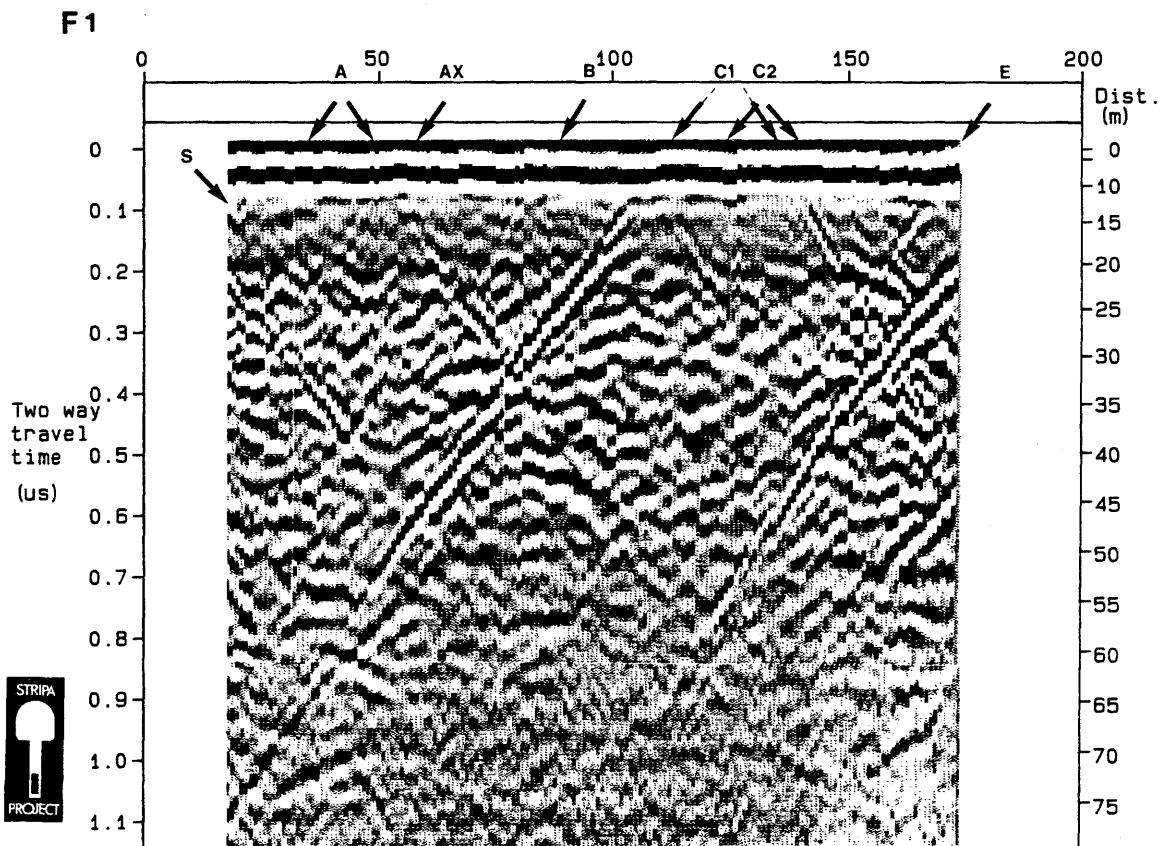


Figure 4.19 Radar reflection map from borehole F1 measured with a center frequency of 22 MHz. Transmitter receiver spacing 20 m.

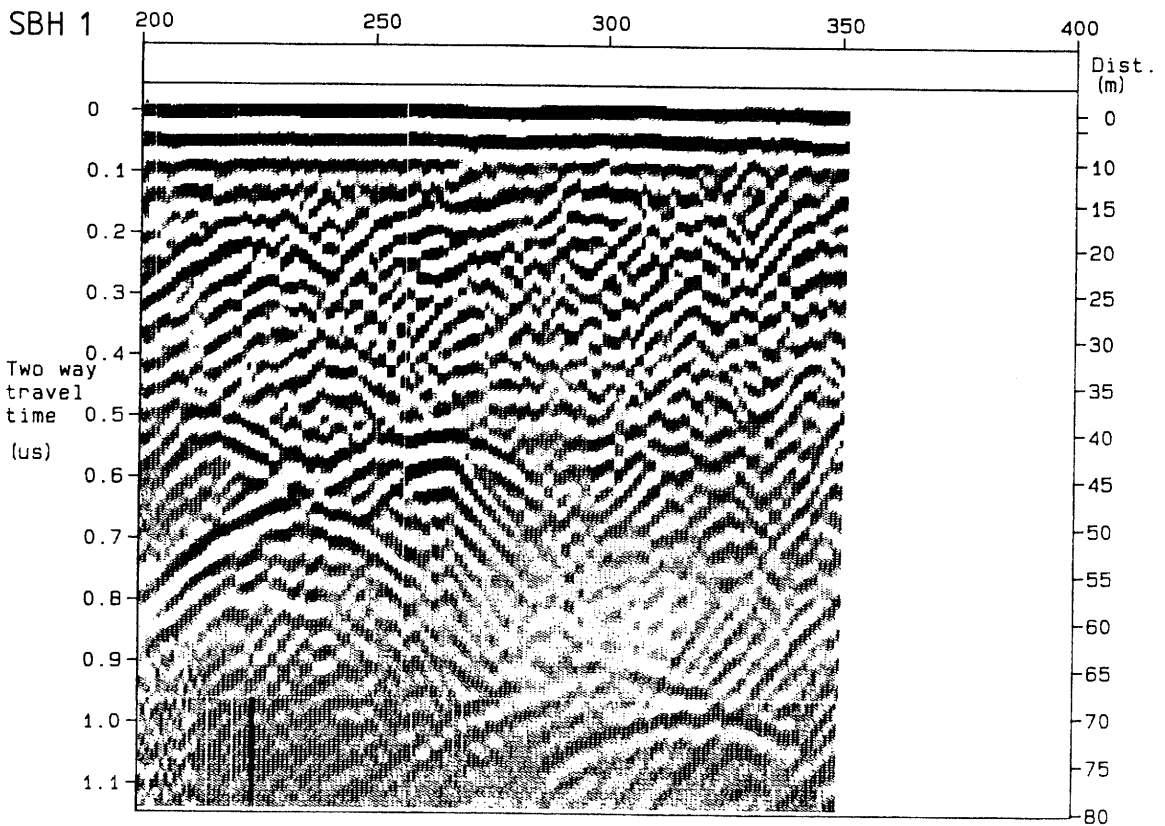
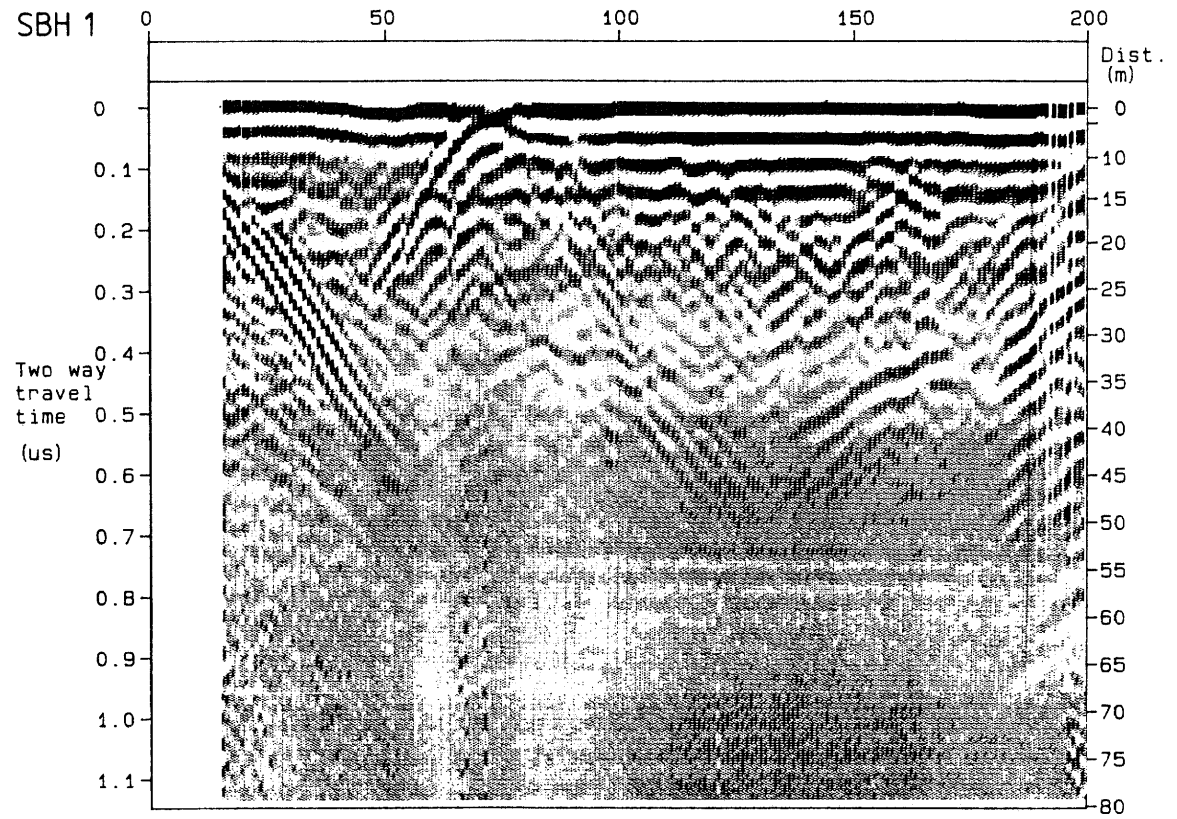


Figure 4.20 Radar reflection map from borehole SBH1 drilled from the ground surface at the Stripa mine. Center frequency 22 MHz.

4.5 DETERMINATION OF ZONES

It is possible to analyse the orientation of a fracture zone in a consecutive manner, checking at all times that the measured data is in reasonable agreement with previous data. The analysis is performed with the help of a computer program called CROSHOLE. This program calculates the possible orientations of a fracture plane when its angle of intersection with a borehole has been determined from a radar measurement (Figure 4.21). The program can also calculate the possible orientations of a fracture plane when two points of intersection have been determined from the radar maps.

The orientation of a plane as determined by the direction of the normal is plotted in a plane using the Wulff projection, which is a type of stereographic projection (see Figure 4.22). Points where the curves intersect will be candidates for the correct orientation of the plane.

Considering the large number of angles and intersection points obtained for each zone from measurements in the six boreholes at the Crosshole site it may appear simple to obtain the correct position of a plane. This is however not generally the case: one reason is the uncertainty in the measured values and the fact that the boreholes subtend a limited angle, but it also appears as if the assumption that the fracture zones are flat does not hold over large distances. This is confirmed by the variations in measured radar angles and also by the undulating shape of the zones observed in tomographic analysis and radar measurements when a zone passes nearly parallel to the borehole (as for example in Figure 4.20 of the lower part of borehole SBH1).

The intersection angles must be very accurately known when they are used to determine the orientation of a fracture plane. A calibration of the 60 MHz measurements was consequently performed by comparing the angles between the boreholes as measured by radar with the known position of the boreholes at the Crosshole site. The results are shown in Figures 4.23-4.24, where the geometrically determined angle has been plotted against the correction which must be added to a measured value to obtain the correct result. The scatter of the data indicates that the nomogram method at its very best is accurate to within ± 0.5 degrees for small angles. For large angles the uncertainty is several degrees.

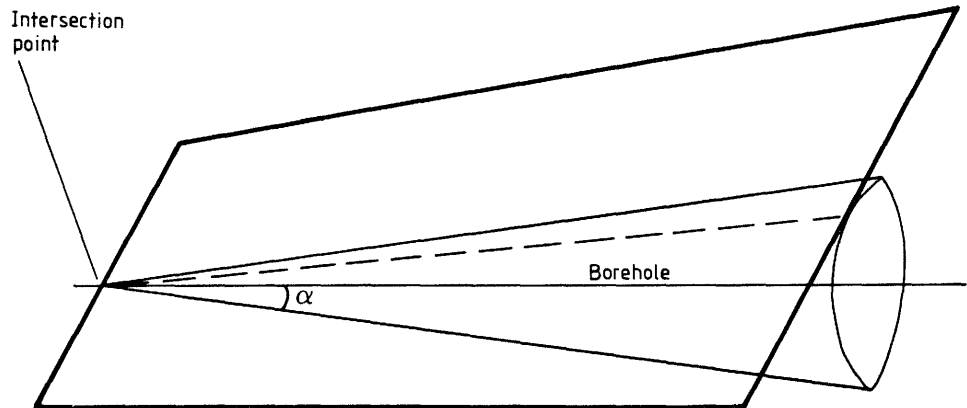


Figure 4.21 The possible orientations of a fracture plane when the intersection angle with the borehole has been determined.

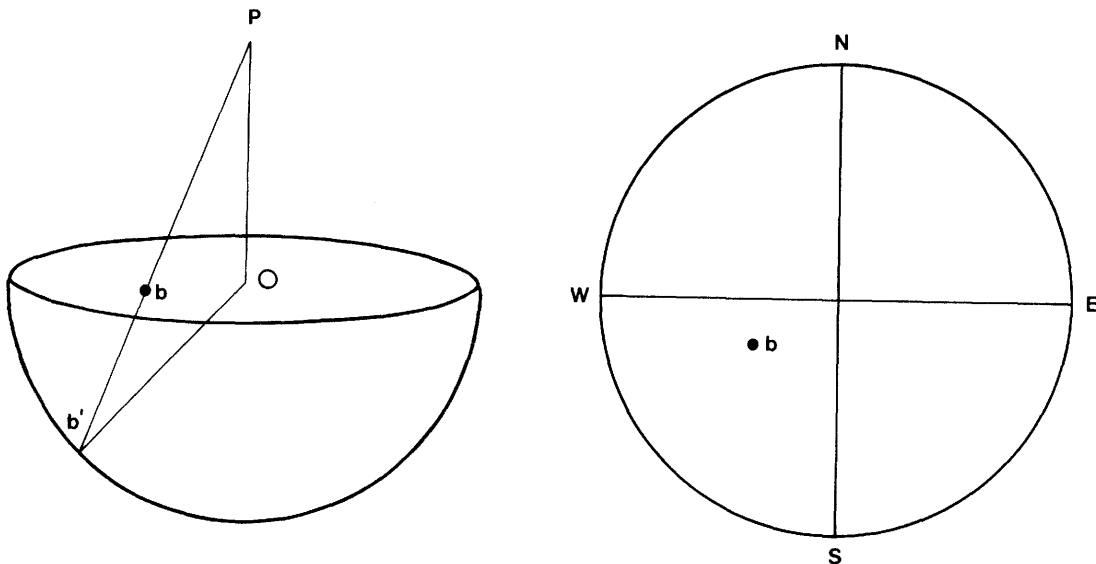


Figure 4.22 The principle of the Wulff projection.

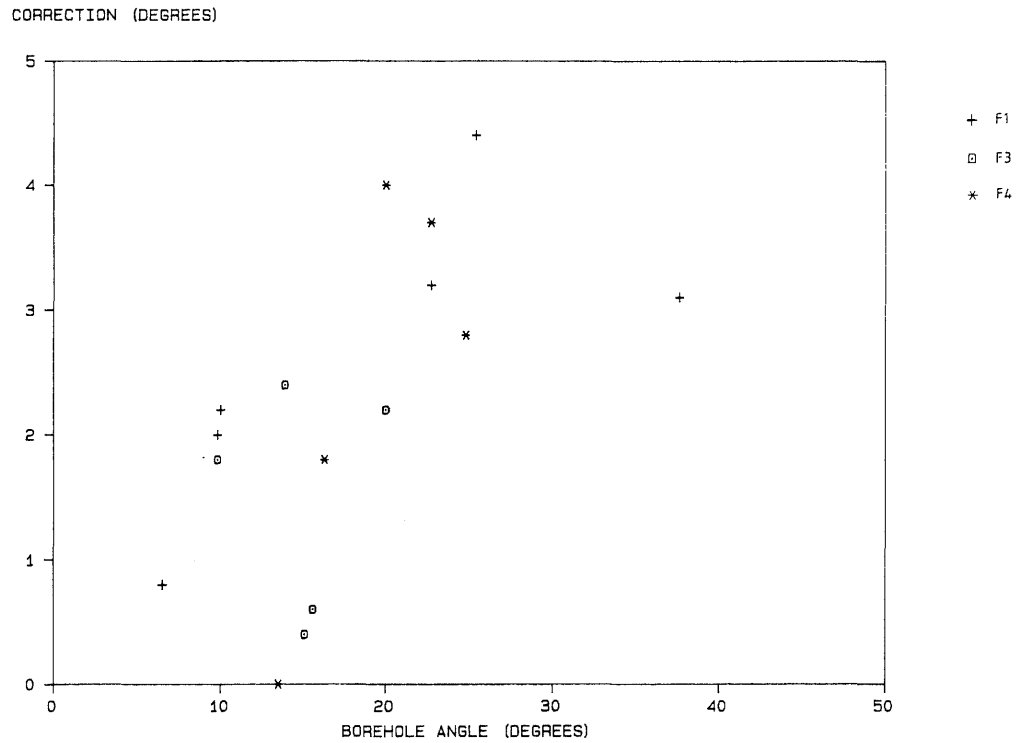


Figure 4.23 Measured values at 60 MHz of the angular correction plotted against the correct radar angle for boreholes F1, F3 and F4.

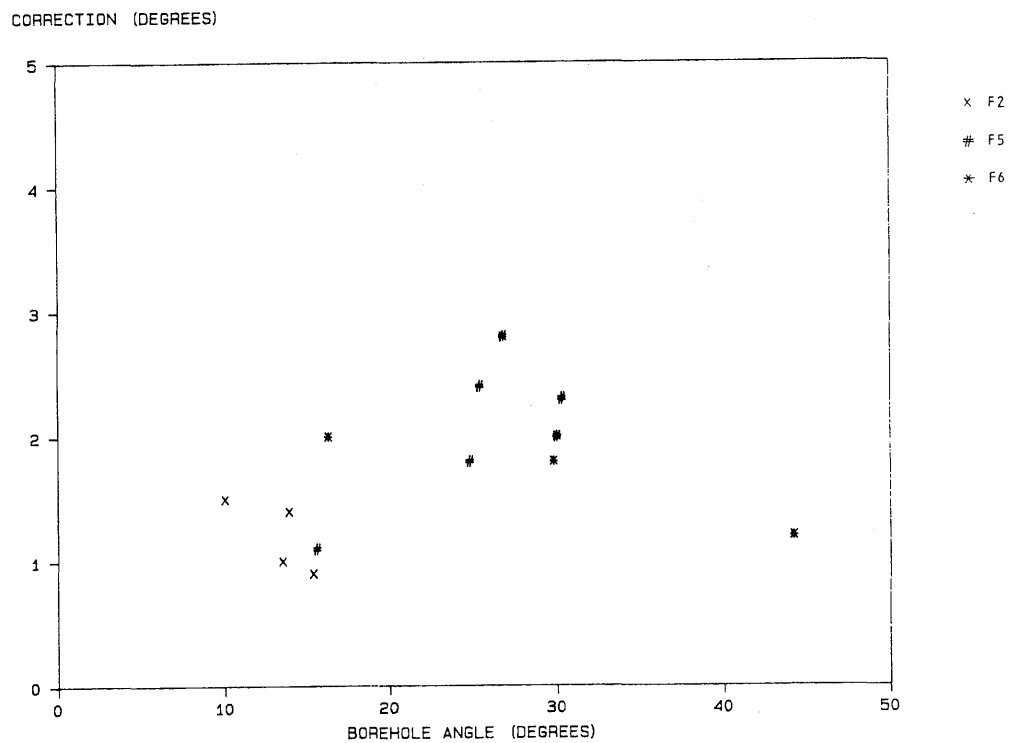


Figure 4.24 Measured values at 60 MHz of the angular correction plotted against the correct radar angle for boreholes F2, F5 and F6.

The diagrams 4.23-4.24 refer to measurements performed at two experimental sessions some months apart. Though the corrections are small it appears that the time base has changed somewhat between the two measurements since the slope is larger in the first figure. An error in the time base or the velocity used to calculate the nomogram will affect the large angles much more than the small ones so it is necessary to investigate the effect for a plane reflector. In the radar plots the asymptotes of a plane reflector have slopes proportional to $\sin \theta$ where θ is the intersection angle. If the time base is in error by a factor p the resulting error will then be given by the formula

$$\Delta\theta = \arcsin(p \sin\theta) - \theta \quad (4.11)$$

This curve was plotted for the values of p determined from Figures 4.23-4.24 and used to correct the measured values.

A few examples will demonstrate how the orientation of a zone can be calculated from the reflection measurements. A summary of results from the single hole measurements is presented in Chapter 6, which contains a description of the radar model of the Crosshole site.

A particularly clear example is offered by the so called site zone which passes directly through the Crosshole site. The reflection from this zone is easy to see in most radar plots and an inspection of the fracture zone at the site shows that it is 10-20 cm wide. When the normals corresponding to the measured radar angles are plotted in a Wulff diagram (Figure 4.25) a rather well defined intersection point is obtained in spite of the fact that the angles between the boreholes are small. Since we know in this case that only one zone is involved the scatter in the data points defines the accuracy that can at the very best be expected when one is interpreting unknown zones. It is obvious that boreholes at large angles to each other are particularly helpful if an accurate result is required: see for example the curve defined by borehole F5 in Figure 4.25. The curves actually seem to define two intersection points close to each other and it is at least possible that this is due to a real deviation of the zone from a plane since these points are defined by neighbouring boreholes: E1, F1, F3 and F2, F4, F6.

The second example will use zone A which is a prominent fracture zone, well known from the geological and geophysical investigations, since it is close to the site and consequently simple to

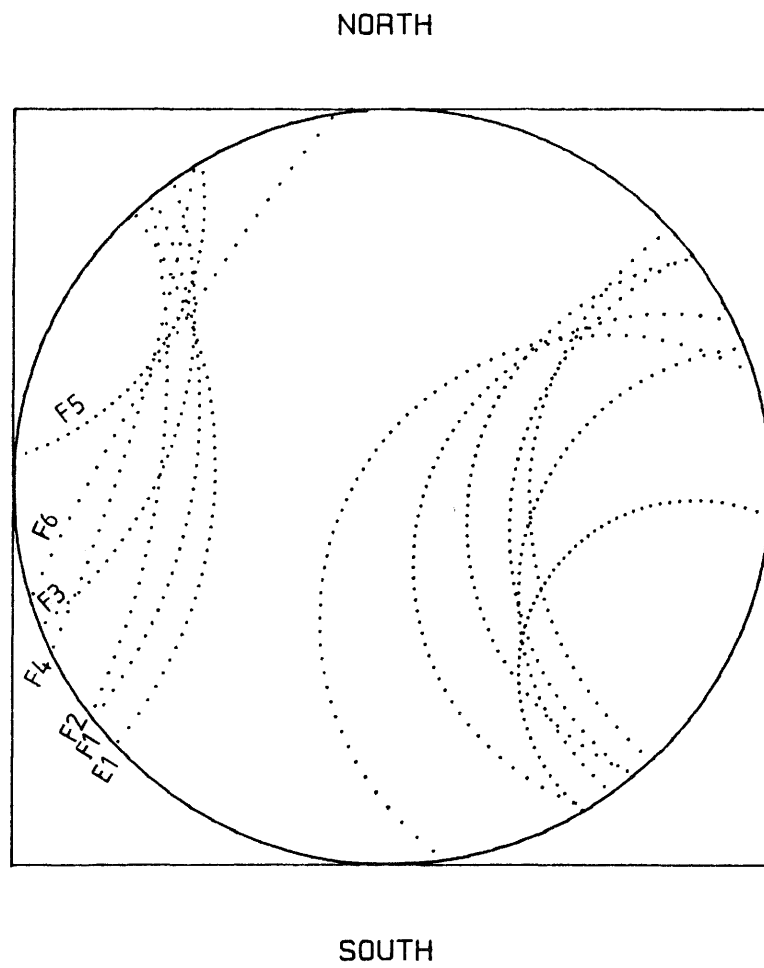


Figure 4.25 Wulff plot for the determination of the orientation of the fracture zone passing through the crosshole site.

correlate between the boreholes. In such cases it is easy to select the correct reflection in each borehole since the reflections are strong and can be followed over large distances: the criterion that the zone should have large range is often as useful as the strength of the reflection when one wants to decide which reflections are important in the analysis.

For zone A there is little doubt that the correct reflection has been selected but this does not mean that the interpretation is straightforward. The angle of intersection can be read off both from the right and left side of the reflection and the discrepancy between these two values is rather large for zone A: the reason is probably that too little is seen of the left side of the pattern (see for example Figure 4.16) but the angles are also large, which makes them sensitive to errors as explained in the description of the nomograms.

In Figure 4.26 the curves corresponding to the radar angles in three boreholes showing a well defined zone A have been plotted. The angles are given both for 22 and 60 MHz to show the differences obtained in these measurements.

Table 4.1 Radar intersection angles for zone A.

Borehole	Intersection angle			
	22 MHz		60 MHz	
	left	right	left	right
F1	64	48	59	58
F3	-	55	55	59
F5	62	62	63	57

It might appear that the data is scattered but apart from uncertainties in the readings the fracture zones are probably undulating which affects the results. The angles are determined by fitting the nomogram to the whole curve seen in the radar plot and this means that range is important in the determination, since for low frequencies more of the pattern is seen one probably obtains better readings in that case.

The curves in Figure 4.26 suggest several possibilities for the correct intersection point and this explains the difficulties met in the interpretation work if there are several intersecting zones. Zone A is however so well known that it is relatively easy to select angles from other

boreholes. When the best angles are chosen as in Figure 4.27 we obtain an almost perfect intersection of the curves.

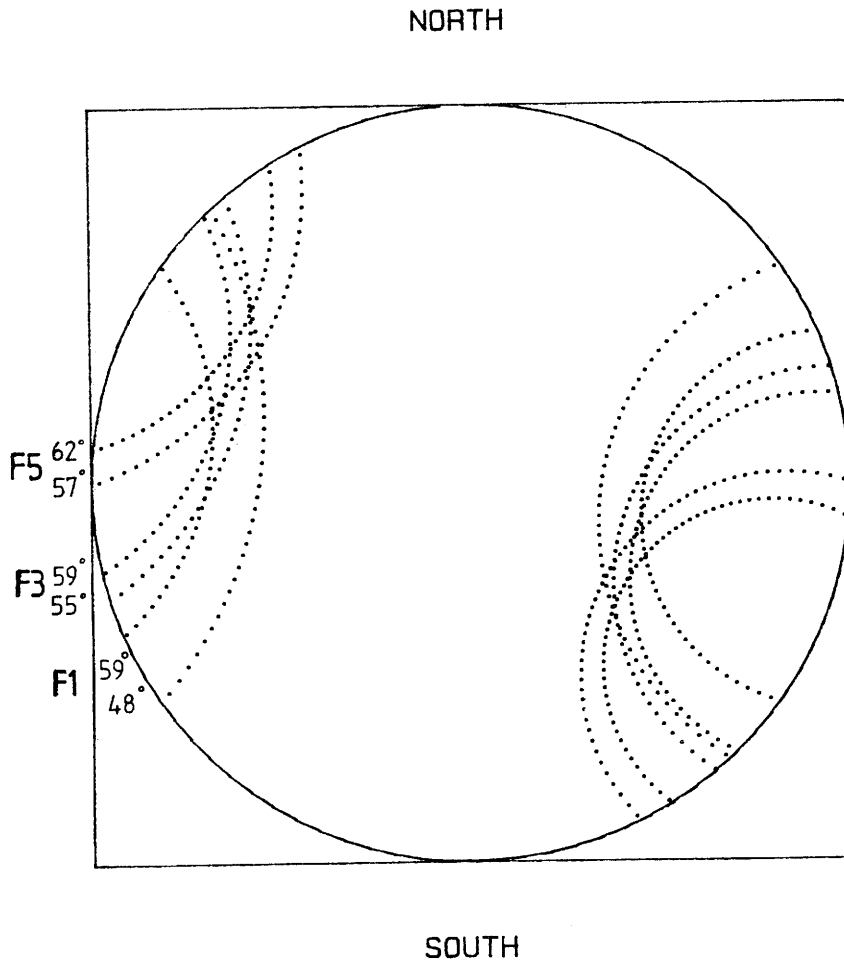


Figure 4.26 Wulff plot of the possible orientation of zone A derived from radar measurements showing results obtained at different frequencies (see Table 4.1).

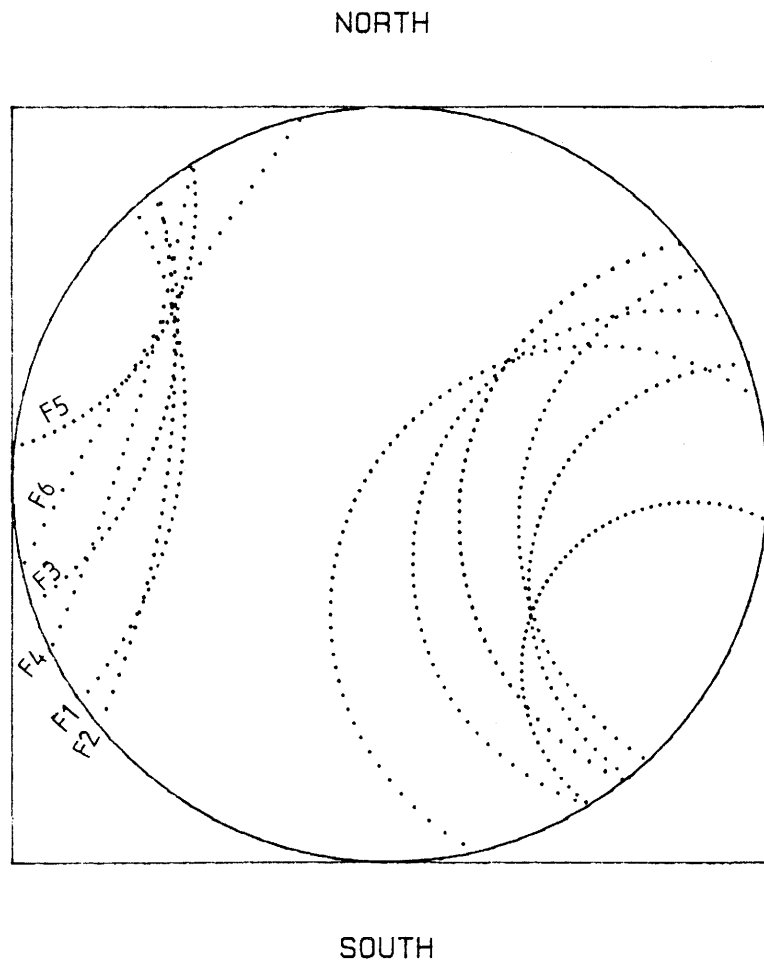


Figure 4.27 Wulff plot of the orientation of zone A derived from intersection angles measured in all boreholes.

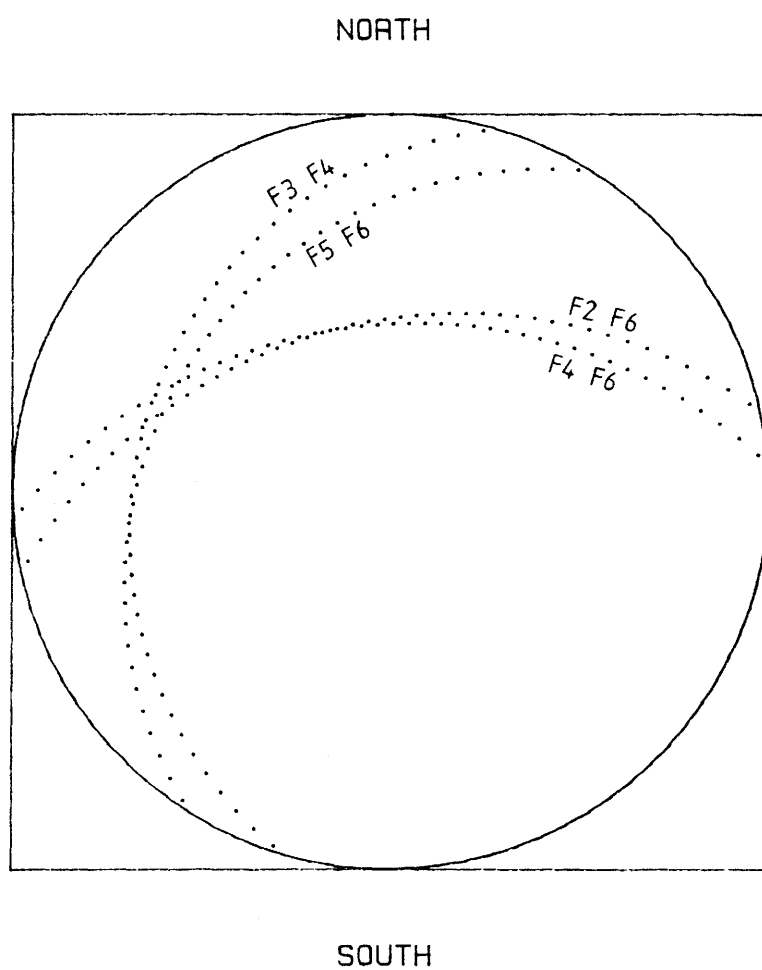


Figure 4.28 Wulff plot of the orientation of zone A derived from its intersection points with the boreholes.

This is encouraging but one must notice that when the intersection points of the zone with the boreholes are used in the analysis they give a slightly different orientation (Figure 4.28). One reason is probably that the intersection points give results that are very sensitive to errors, since the points are close to each other but it should also be noticed that the angles finally used in the analysis are mostly derived from the low frequency measurements. This means that the orientation of the zone is determined by an average over large distances while results obtained from intersection points or angles derived from high frequency measurements are corresponding to an average over a smaller area. If the zones really undulate as argued above this explains the differences between orientations obtained from large scale and small scale averages.

The measurement in borehole E1 can not be resolved in this way since there are two candidates in the correct area with reflection angles sufficiently similar for them both to pass near the intersection point. The final orientation of the zone is of course not affected much in this case but such coincidences can be confusing in doubtful cases.

As a final example consider zone E which must be correlated using the available data in a step by step procedure. Suitable reflections appear for example in F1 and F3. When the radar angles and intersection points are combined the three curves intersect as in Figure 4.29 and one can then check how well other reflections fit with this intersection. Figure 4.30 shows that quite good agreement is obtained between all the curves. Furthermore the orientation found in this way corresponds rather closely with the results for zone A and the site zone, i.e. the zones are more or less parallel in accordance with the general view on how fractures are formed in rock.

There are a number of reflections seen from each borehole and some might cause confusion. As an example consider the choice of two possible reflections for zone E in F5 (see Appendix A). Originally the intersection at 127 m borehole depth was selected but it appeared too weak when compared with the reflections in other boreholes. A slightly better fit was obtained both for radar angle and intersection point when the reflection at 150 m depth was considered. It might be noted that even the wrong choice would not have affected the orientation of the fracture zone too much. Thus even when the exact orientation is doubtful the position of a zone is often quite well known.

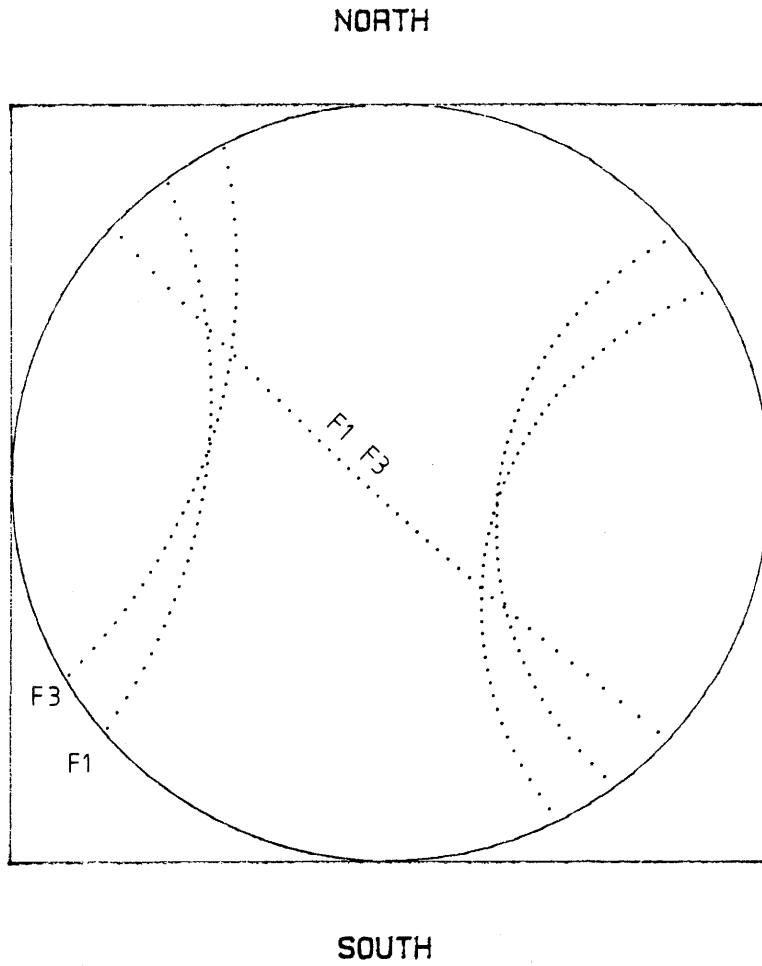


Figure 4.29 Wulff plot showing the possible orientation of zone E derived from radar measurements in boreholes F1 and F3.

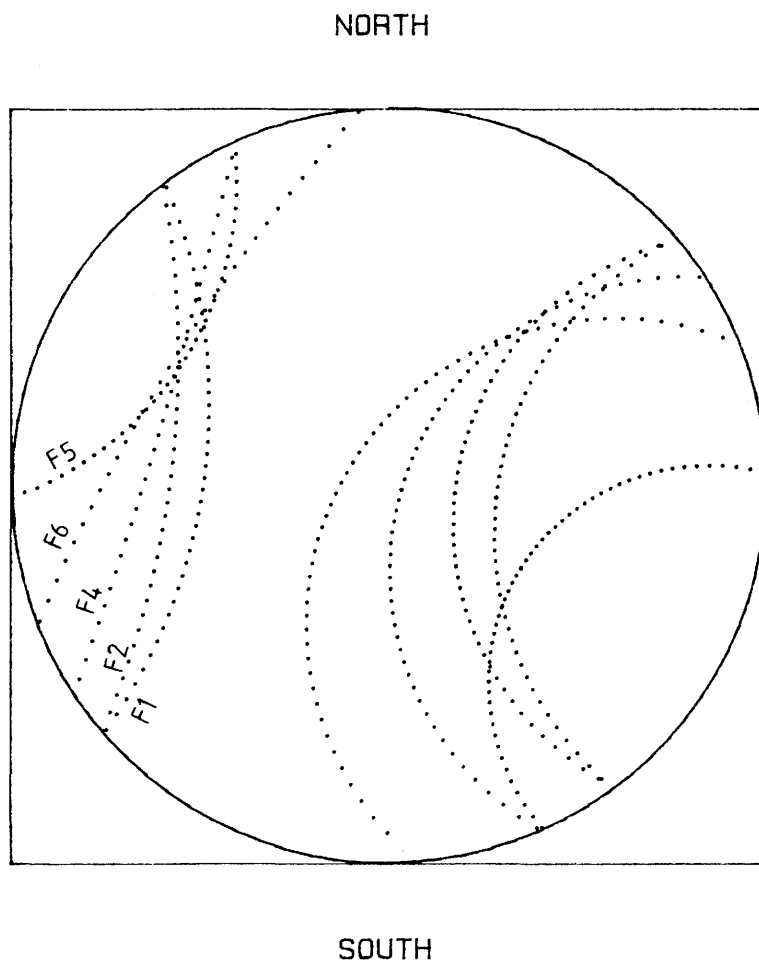


Figure 4.30 Wulff plot showing the orientation of zone E derived from radar measurements in all boreholes.

CROSSHOLE MEASUREMENTS

5.1 GENERAL

In a crosshole measurement the transmitter and receiver are placed in separate boreholes. For each position of the probes a full wave record of the signal is recorded. The signal may be analysed both with respect to the travel time and amplitude of the first arrival and with respect to the occurrence of later arrivals such as reflections. The objective of the crosshole radar measurements performed as a part of the Crosshole Program was to map the extension of fracture zones between boreholes through tomographic analysis. Hence, the measurement points were distributed to give optimal data for the tomographic analysis and the reflection data which was also obtained from the records can be considered more or less as a byproduct of the tomographic survey. If the objective had been to study reflections then the measurement points should have been distributed differently. It should also be noted that crosshole measurements provide a simple and efficient means for calibrating the radar system with respect to system losses as well as giving a radar velocity calibration for the single hole measurements (cf. Section 3.6).

Crosshole measurements have been made of the borehole sections listed in Table 5.1.

Table 5.1. Crosshole sections measured with borehole radar in the Stripa Mine.

Bore-hole 1	Measured section	Point sep.	Bore-hole 2	Measured section	Point sep.	Center freq.
F4	60-200 m	4 m	F1	50-190 m	4 m	22 MHz
F2	60-200 m	4 m	F5	60-200 m	4 m	22 MHz
F6	60-200 m	4 m	F1	60-200 m	4 m	22 MHz
F4	60-200 m	4 m	F5	50-190 m	4 m	22 MHz
F4	60-200 m	4 m	F5	50-190 m	4 m	60 MHz
F2	60-200 m	10 m	E1	60-200 m	2 m	22 MHz

The measurements were carried out in the following way: one of the probes was kept at a fixed position in the first borehole while the other probe was moved in the other hole where measurements were

made with fixed increments, normally 4 m. Such a set of measurements has been termed a borehole scan. After each scan the probe in the first hole was moved to the next position and the measurement in the second hole was repeated. This was continued until each borehole section had been fully measured.

According to the reciprocity theorem the transmitter and receiver are interchangeable and it is irrelevant in which of the holes each probe is placed. Consequently it is also irrelevant which probe is fixed or which is moving during each borehole scan. In most of these measurements the receiver has been used as the fixed probe while the transmitter has been moved in the other borehole. The reasons for this choice are mainly practical. The transmitter is slightly easier to move in and out of the boreholes as there is only one optical fiber connected to the transmitter.

Most of the crosshole sections measured at Stripa contain approximately 1300 rays. The time required for performing such a survey is roughly three working days.

5.2 TOMOGRAPHIC ANALYSIS

5.2.1 Definition of the problem

The general idea behind tomographic reconstruction is that information about the properties of the interior of a region can be obtained through measurements at the boundary. In general the transmitter and receiver probes are located at the boundary of the area and each ray connecting transmitter and receiver can in principle be considered to give the average of a measured property of the rock along the ray. In order to obtain an estimate of this property at a given point it is necessary that several rays pass close to the same point and that the rays have different directions and hence different information content. The requirement that several rays should intersect the same point puts severe constraints on the borehole geometry. The main restriction is that the source and receiver positions and hence the boreholes must be confined to the same plane.

In mathematical terms the tomographic problem can be formulated in the following way

$$d_i = \int_{T_i(m)} m(x) ds \quad (5.1)$$

where d_i is the measured data for ray number i . The objective of the tomographic inversion is to estimate the spatial distribution of some property, $m(x)$, characteristic of the medium (x denotes the spatial coordinates). The data is thought of as being a sum (line integral) of this property along the ray path, $T_i(m)$, from the transmitter to the receiver. The actual ray path depends on the properties of the medium, $m(x)$, and is normally the curve which gives the least possible travel time. The complex dependence of the ray paths, T_i , on the properties of the medium, $m(x)$, makes the problem nonlinear. The problem can be linearized by replacing the curves T_i with straight line segments, L_i , connecting sources and receivers.

In a crosshole measurement data can be extracted on the traveltimes and the amplitude of the direct wave between transmitter and receiver, i.e. the first arrival. It is assumed that the traveltimes can be constructed as a line integral of the slowness, $s(x)$, along the each ray, i.e.

$$d_i = \int_{L_i} (1/v(x)) ds = \int_{L_i} s(x) ds \quad (5.2)$$

The ray paths have here been assumed to be straight lines in order to make the equations linear and in this way simplify the inversion problem.

The amplitudes can not be obtained from a line integral directly but if the logarithm is taken of the data the problem is linearized and can be solved by tomographic inversion. The amplitude of the electric field radiated by the transmitter decays with distance according to (cf. 3.9)

$$E = c_t a(\theta) \exp(-\alpha r)/r \quad (5.3)$$

where $a(\theta)$ is the antenna radiation pattern and c_t some constant which determines the radiated power. The measured signal amplitude also depends on the receiver antenna gain. The received amplitude is thus obtained by multiplying equation (5.3) with the radiation pattern of the receiver antenna. This directional gain is identical to that of the transmitter if the same type of antennas are used. Hence the received amplitude is

$$E_r = c \frac{\exp(-\alpha r)}{r} a(\theta_1)a(\theta_2) \quad (5.4)$$

Taking the logarithm and rearranging terms we obtain

$$\alpha r = \int_{L_i} \alpha(x) ds = \ln \frac{c a(\theta_1) a(\theta_2)}{r E_r} \quad (5.5)$$

Here it has been assumed that the product αr can be constructed as a line integral of the attenuation along each ray. Thus, an inversion of the logarithm of the received amplitudes should give an estimate of the distribution of attenuation in the investigated plane. In equation (5.5) c represents a normalization constant describing the combined effects of transmitted power and receiver gain and E_r is the amplitude of the received electric field.

Equation (5.5) actually contains a number of approximations the validity of which is uncertain. First, (5.3) is really valid only for a single frequency and for propagation through a homogeneous medium. If each frequency is studied separately as in a continuous wave system there is no first arrival and the energy measured at the receiver will consist of contributions both from the direct wave and from reflections. This is in contradiction with the assumption in (5.5) where the response is assumed to depend only on the contributions along the ray path. The contribution from reflected waves is often called multipathing and is a common problem in all continuous wave systems.

On the other hand if a broadband pulse is transmitted, as is the case for the Stripa radar system, the first arrival is easily identified and the amplitude of the wave that has propagated directly from transmitter to receiver is readily obtained. However, the attenuation is different for different frequencies and (5.3) can only be considered as an approximation for some limited frequency band.

Another aspect of (5.2) and (5.5) is the comparatively large wavelength of the transmitted waves in relation to the distance between transmitter and receiver. This means that the ray approximation on which these equations are based is not exactly valid. A consequence is that the received data will not correspond to the average property along a ray but is rather the average of this property for a volume around the ray corresponding approximately to the first Fresnel zone.

While some of the errors involved in a tomographic analysis of borehole radar data have been described

it is difficult to assess theoretically the significance of the approximations and this will not be attempted here. Instead the results will in themselves demonstrate if the approximations were justified or not.

The next problem is to devise a procedure for inverting the data to obtain the distribution of slowness or attenuation in the plane between the boreholes. First the problem is discretized. The plane between the boreholes is divided into a number of cells and the line integral is calculated as a sum where the contribution from each cell is considered in proportion to the length of the ray within each cell, cf. Figure 5.1. The slowness or attenuation of each cell may be described either as a single value for each cell or more generally as a sum of basis functions, f_j , such that

$$m(x) = \sum_{j=1}^M b_j \cdot f_j(x) \quad (5.6)$$

The purpose of using basis functions instead of just a single value for each cell is that the basis functions can be made to represent some smoothing of the slowness values between adjacent cells. In some sense this also corresponds to an interpolation of slowness values between the midpoints of the cells. If the expansion into basis functions is inserted into (5.1) we obtain

$$d_i = \int_{T_i} m(x) ds = \sum_{j=1}^M b_j \int_{T_i} f_j(x) ds = \sum_{j=1}^M G_{ij} b_j \quad (5.7)$$

where the matrix G is defined by

$$G_{ij} = \int_{T_i} f_j(x) ds \quad (5.8)$$

The problem has now been transformed into a system of linear equations, where the number of equations corresponds to the number of rays, N , and the number of unknowns, b_j , to the number of cells, M . Hence, we may write

$$d = G b \quad (5.9)$$

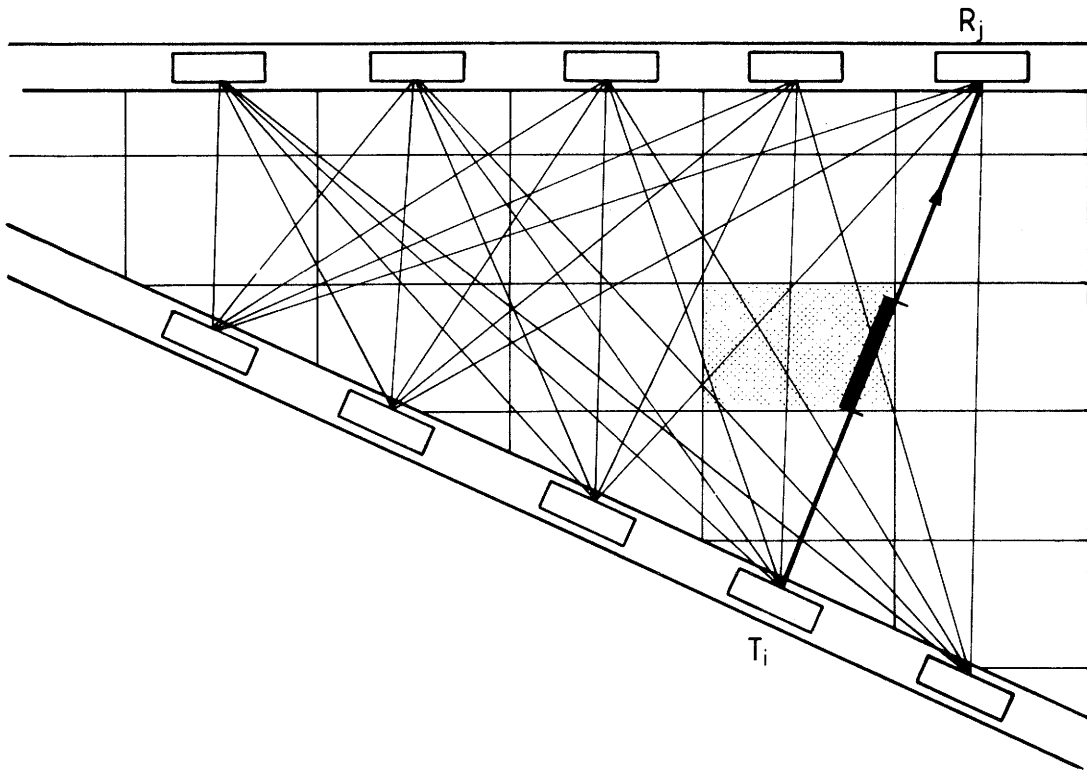


Figure 5.1 Generalized crosshole tomography geometry with a decomposition into cells and an example of a ray pattern. (T = transmitter, R = receiver).

This equation system can be both overdetermined and underdetermined at the same time and errors in the data may cause some equations to be in conflict. The most common method of solution for this type of equations is through minimization of some functional describing the difference between the solution and the data. The most natural functional is $|d - G b|^2$.

Experience shows that the equation system is often unstable and it is necessary to introduce some form of damping. An effective and natural way of introducing damping is to assume that the slownesses (or velocities) of adjacent cells are nearly equal. Introducing equations constraining the solution in this way leads to the minimization of the functional

$$|d - G b|^2 + \lambda^2 |C b|^2 \quad (5.10)$$

where the parameter λ is a measure of the damping and C is a matrix containing the equations for equal velocity in adjacent cells. λ determines the weight of the constraining equations and the practical consequence is that the differences in slowness between adjacent cells become limited to a certain extent. This type of damping gives a smoothed tomographic image without creating artifacts.

The solution to (5.10) has the following form

$$b = (G^T G + \lambda^2 C^T C)^{-1} G^T d \quad (5.11)$$

Here G and C are known and depend on the ray pattern and the division of the investigated area into cells. In other words they contain the geometrical information about the measurement. The term in the parenthesis is a square matrix which may be inverted through standard procedures and when this has been done a least squares estimate of b is obtained through matrix multiplication. However, the direct inversion of the matrix has practical limits since the matrix is large. The number of elements of $G^T G$ is M^2 , i.e. the number of cells squared, and this is for most problems a very large number (100 000 to 1 000 000) which prohibits the direct inversion of the matrix because of the enormous computing times involved. Note that the computing time required for inversion of a matrix is proportional to M^3 .

Instead iterative procedures must be used to obtain the solution. Several different iterative

algorithms have been tested within the framework of the Crosshole program. The conjugate gradient (CG) method is considered to be the most efficient one. The convergence is fast and hence few iterations are needed to arrive at the final solution. The CG-method has also been shown to give smaller computing times and better reconstructions of model examples than the other iterative methods. Hence, the CG-method has been used for all tomographic inversions presented in this report.

This description of tomographic inversion theory closely follows that of Ivansson (1984) who has studied the theoretical and computational aspects of tomographic inversion as a part of the Crosshole program. The Stripa Project Report 84-08 describes the inversion procedure in detail. That report also contains descriptions of different inversion algorithms and test examples where the algorithms are compared with respect to convergence, computing time requirements and errors. The appearance and character of artifacts in tomographic inversions are also discussed in detail. For a detailed discussion of these matters the reader is referred to that report.

5.2.2 Preparation of data for tomographic inversion

A typical example of a radar signal recorded from a crosshole measurement is shown in Figure 5.2. From this signal trace we want to determine the time of first arrival and the magnitude of the signal. This can be done in several ways and it is not evident which algorithm to choose. The magnitude presents a special problem as it is not exactly clear how the magnitude of a pulse should be defined. The most natural definition is integration of the instantaneous power of the pulse over the duration of the pulse. However, this immediately leads to the practical problem of how to define the end of the pulse, i.e. the point where the integration should stop. In this case noise may also contribute significantly to the result.

A tomographic survey normally includes a large number of rays (a few thousand). It is therefore of the utmost importance to arrive at some automatic procedure which can pick the data from the recorded traces, especially as a manual treatment of each ray would be extremely time consuming and hence costly. For the radar data we have adopted a simple approach which has proved reasonably efficient. An algorithm has been devised which picks out the maximum and the minimum of each trace and the time at which these events occurred. The travel time is then defined as the time to the maximum or minimum of the pulse and the amplitude is defined as the

difference between the maximum and the minimum, i.e. peak-to-peak amplitude.

This scheme is useful for radar signals as the first pulse in most cases also is the largest one. The procedure is normally not useful for seismic crosshole investigations as the maximum signal in that case is normally not obtained within the first pulse cycle. Figure 5.2 represents a typical radar pulse which has one minimum with the largest magnitude and two maxima of smaller but almost equal magnitude. If the maximum and minimum points are picked for a large number of traces the minimum will be picked consistently while either of the two maxima may be picked by the algorithm. The picking of the maximum travel times is thus sensitive to small changes in the pulse form which is not the case for the minimum times. The maximum travel times are normally picked inconsistently between different rays and are not suitable input data to the tomographic inversion. The peak-to-peak amplitudes have been shown to provide a satisfactory data set even if they also are affected by the dispersion of the pulse. More elaborate and accurate schemes for amplitude and time picking can certainly be devised but it has not been possible to include such efforts in the current Crosshole program.

The radar velocity (or slowness) shows small variations around an average value. It is then useful to put the crosshole data in such a form that these variations are studied rather than the absolute values. For this purpose we define the terms 'residual travelttime' and 'residual amplitude'. The range of variation of the attenuation is normally comparable to the average value but it is still useful to treat the amplitude data formally the same way as the travel time data. The residual data correspond to the measured data after subtraction of the expected data value which would have been obtained in a homogeneous medium with properties close to those of the investigated rock.

The residual travelttime, t_r , is defined as the measured travel time, t_m , after subtraction of the estimated travelttime \bar{m} for a homogeneous medium with a constant velocity, c_0 . The residual travelttime is then

$$t_r = t_m - r/c_0 \quad (5.12)$$

where r is the distance between transmitter and receiver.

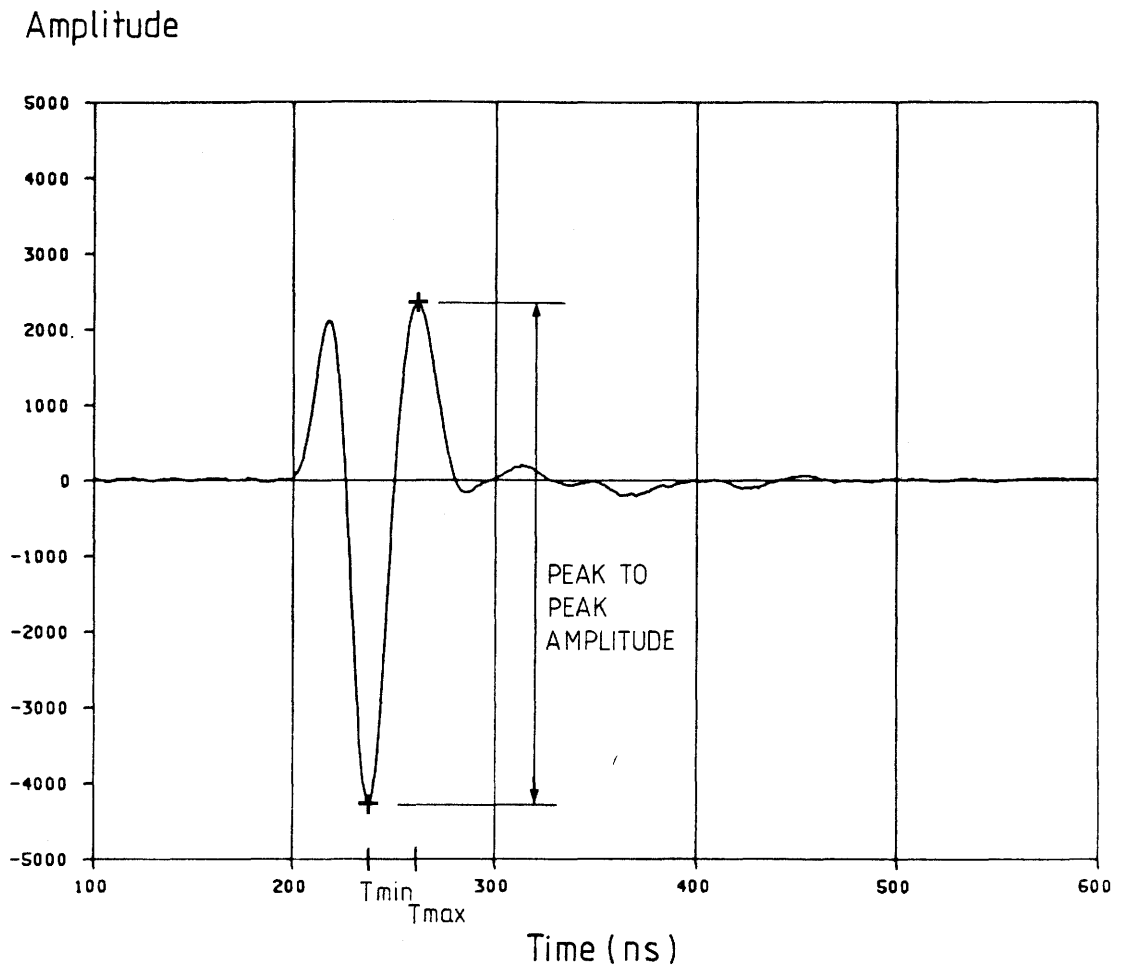


Figure 5.2 Radar signal obtained from a crosshole measurement after propagation through 50 m of granite.

The residual amplitude is defined as the ratio (expressed in dB) of the measured amplitude, E_m , to the estimated amplitude in a homogeneous medium with constant attenuation α_0 . The residual amplitude thus becomes

$$d_r = -20 \log_{10} \left[\frac{E_0}{E_m} \frac{\exp(-\alpha_0 r) a(\theta_1) a(\theta_2)}{r} \right] \quad (5.13)$$

where E_0 represents a reference level corresponding to the ratio of transmitted power to receiver sensitivity.

With this conversion into residual data it is possible to look at small variations from large average values. The residual data are also suitable for detecting systematic errors in the data and can be used for calibration of some system parameters.

The basic step in preparing data for tomographic inversion is to attach coordinates to the travel times and amplitudes. Data on borehole coordinates have to be obtained through borehole deviation measurements. These data are required to have an accuracy in the position of individual measurement points better than 1 m, but an accuracy better than 0.5 m is desirable.

After the travel time and amplitude data has been combined with the coordinates of the source and receiver points the residual data are calculated. As can be seen from (5.12) and (5.13) coordinate information is required for calculation of the residual data since these contain information on the distance between source and receiver and the relative angle of the antennas to the rays.

The tomographic inversion software requires the source and receiver points to be in the x-z plane and in order to accomplish this the coordinate system is rotated. In general all source and receiver points will not lie in the same plane due to the curvature of the boreholes or if the holes were drilled in such a way that no common plane exists. In such a case a plane will have to be chosen which fits best to the real borehole positions.

5.2.3

Data quality and corrections

The tomographic data is subject to a number of errors such as errors in time and amplitude picking, constant offset errors in time and gain, and coordinate errors. It is essential to

understand both the stochastic and systematic errors which may exist in the data set. The errors must be understood, quantified and corrected before a tomographic inversion is attempted. A good way of revealing errors is to plot the residual data as a function of the length of the rays. In order to understand these plots it is necessary to discuss the effect of different errors on the residual data.

The main errors in the residual travel time are due to imprecise knowledge of the zero time, i.e. the start time of the pulse, and the assumed velocity of the medium. Let us denote the travel time by t_m where we assumed the pulse to have been emitted at a time t_0 . Now, assume there is an error in the start time, Δt_0 , and in the velocity used for calculation of the residual travel time. The assumed velocity, c_0 , is related to the real velocity, c , in the following way

$$c = c_0 (1 + \delta c) \quad (5.14)$$

If these assumptions are inserted in (5.12) we obtain

$$\begin{aligned} t'_r &= t_m - t_0 - \Delta t_0 - r / (c_0 (1 + \delta c)) \\ &\approx t_m - t_0 - r / c_0 - \Delta t_0 + r \delta c / c_0 \\ &= t_r - \Delta t_0 + r \delta c / c_0 \end{aligned} \quad (5.15)$$

In this equation we can regard t_r as the real residual travel time while t'_r is the residual time including the errors caused by the last two terms. If we divide this equation by the length of the ray we get the residual slowness for the ray, s'_r :

$$s'_r = s_r - \Delta t_0 / r + \delta c / c_0 \quad (5.16)$$

Again we let the unprimed quantity define the error free value. Here it is important to note that an error in the assumed velocity will pose no problems as this will only lead to a constant offset in the residual slowness values and the error in the slowness estimate will be the same for all rays. Errors in the pulse transmission time will cause errors in the slowness estimate which depend on the length of the rays and hence are different for different rays. Offset errors of this type normally

generate artifacts in the resulting tomograms. A typical artifact caused by offset errors is a diagonal cross in the tomogram. This is consistent with the different size of error for the longest (i.e. diagonal) rays compared to the shorter ones.

An example of a plot of the residual travel times from the borehole section F4-F5 is shown in Figure 5.3. The measurement was made at a center frequency of 60 MHz, which corresponds to a wavelength of approximately 2 m. The bulk of the data points form a cluster centered along a straight line, which is indicated in the figure. This line is the best fit to the data points and represents the average residual travel time. The deviations from the line should then represent the inhomogeneities in the rock. If we compare with equation (5.15) we see that the slope of the line corresponds to the error in the assumed velocity and the intersection with the y-axis (at zero distance) to the error in the start time of the pulse.

There are also a number of points which fall outside the cluster. These points represent errors in the data. The points above the big cluster represent points with significant time delay. In these cases the maximum value has not occurred within the first cycle of the pulse and the travel time has been picked on one of the following cycles. The values below the line at a distance of about 120 m are caused by low signal amplitudes which makes the algorithm trigger on noise.

The amplitude data can be analysed in a similar fashion. Here we assume an average attenuation, α_0 , with an error, $\Delta\alpha_0$, such that

$$\alpha = \alpha_0 + \Delta\alpha_0 \quad (5.17)$$

We also assume that we have a percentage error, δE_0 , in the reference level, E'_0 , such that

$$E_0 = E'_0 \delta E_0 \quad (5.18)$$

In a fashion analogous to the error analysis of the residual travel times we obtain

$$\bar{d}_r \approx d_r - 20 \log_{10} \delta E_0 + 20 \Delta\alpha_0 r / \ln(10) \quad (5.19)$$

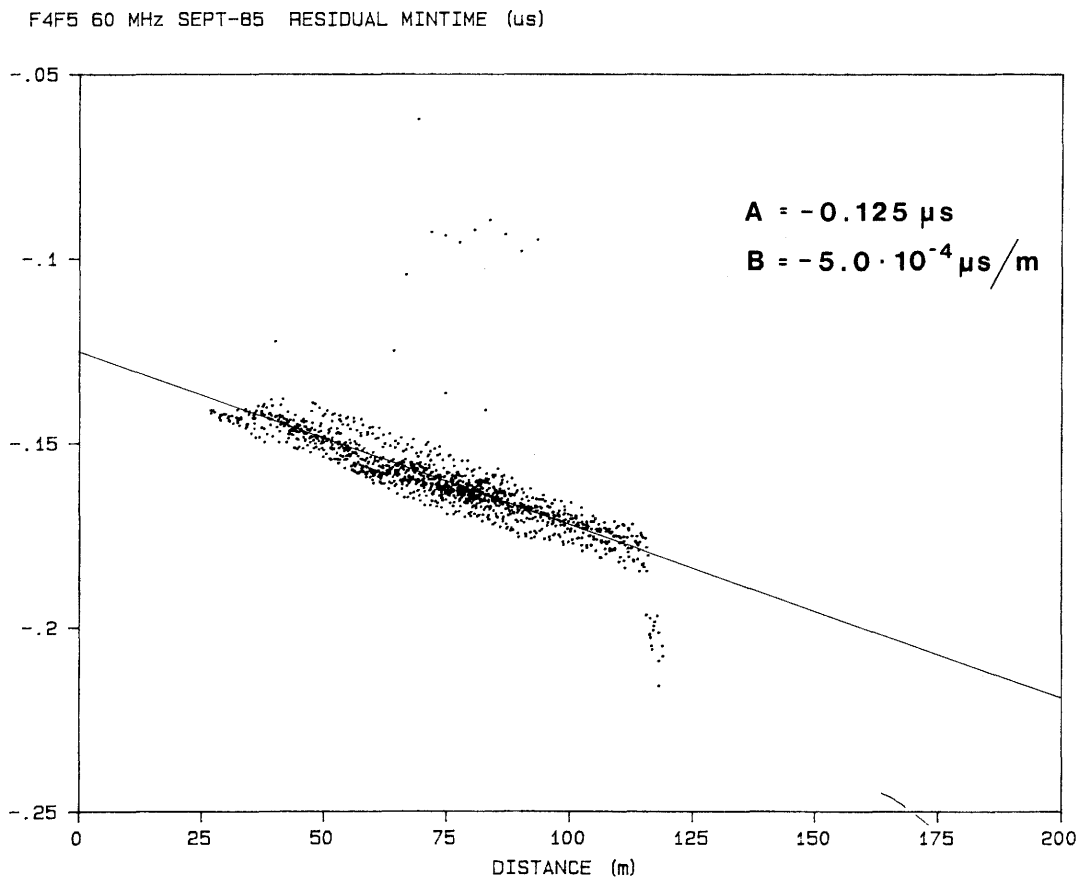


Figure 5.3 Residual traveltimes as a function of the distance between transmitter and receiver. Borehole section F4-F5, center frequency 60 MHz.

for the residual amplitudes. Again the offset error in the amplitude levels is the error which will affect the tomographic inversion most severely since it causes a systematic error which is different for rays of differing lengths.

Figure 5.4 shows the residual amplitude data from the same section as the previous figure. The residual amplitude data show a much larger spread in values than the corresponding travel time data. This is a general condition which has been observed in all measured sections. The data spread so much that it is difficult to define the line of best fit. In practice it has been found best to do the fitting by eye rather than by least squares methods since this gives the possibility to make a subjective weighting of different parts of the data set. In this case the slope of the line gives the error in the estimated attenuation and the intersection with the y-axis the error in the reference level.

The tail of points at distances greater than 120 m forming a straight line almost perpendicular to the best fit line are caused by noise. The apparently increasing amplitude for these data is due to the fact that the noise level is constant and does not change with distance.

Figure 5.3 and 5.4 contained a number of data points outside the general clusters of points which evidently were due to errors in the data. In that type of residual data plot it is very difficult to identify the individual ray which is in error. To simplify the identification of erroneous data a ray check plot like the one in Figure 5.5 is produced. In this plot the residual attenuation of every ray is displayed in a grey scale pixel. The location of the pixel is a function of the borehole depth in the respective holes. A plot like this is a mapping of the physical properties of the medium. Linear features should show up as points and vice versa. If we assume the properties of the medium to vary smoothly the ray check plot should also be smooth. Now data errors often show an erratic pattern and can be identified in plots like this one. An example is the black horizontal line appearing at a borehole depth of 120 m in F4 which evidently corresponds to a data error.

When the rays containing errors have been identified it is possible to go back to the recorded traces and try to select again the corresponding amplitudes or travel times which may have been erroneously defined by the automatic routine. In practice this has proven too laborious and time consuming so it has been simpler just to skip the rays containing errors before the

tomographic inversion is performed. The ray density in the radar crosshole measurements at Stripa has been high and the result of the tomographic inversion will in such cases not depend critically on whether a few rays are omitted. However, it is essential to exclude the rays containing significant errors as only a few such rays are sufficient to introduce artifacts in the tomograms. Rays with errors normally cause narrow linear features in the tomograms which can be seen in some of the tomograms presented in the next section.

F4F5 60 MHz SEPT-85 RESIDUAL AMPLITUDE (dB)

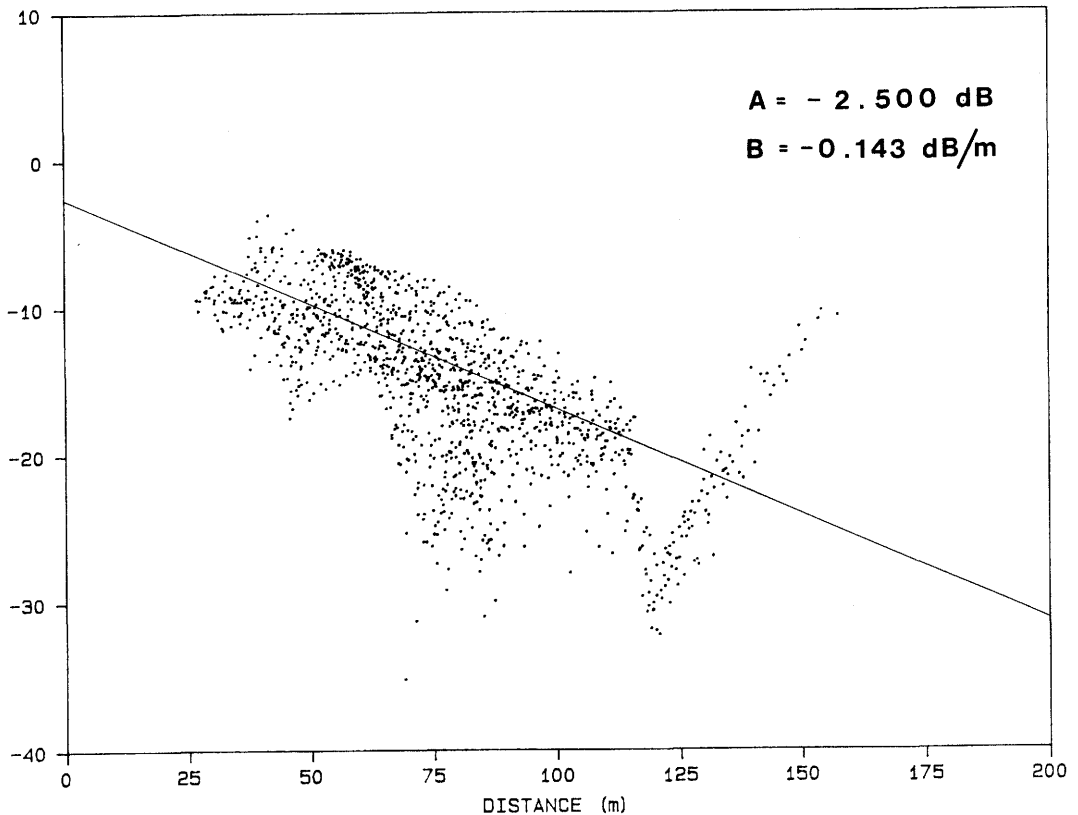


Figure 5.4 Residual amplitudes as a function of the distance between transmitter and receiver. Borehole section F4-F5, center frequency 60 MHz.

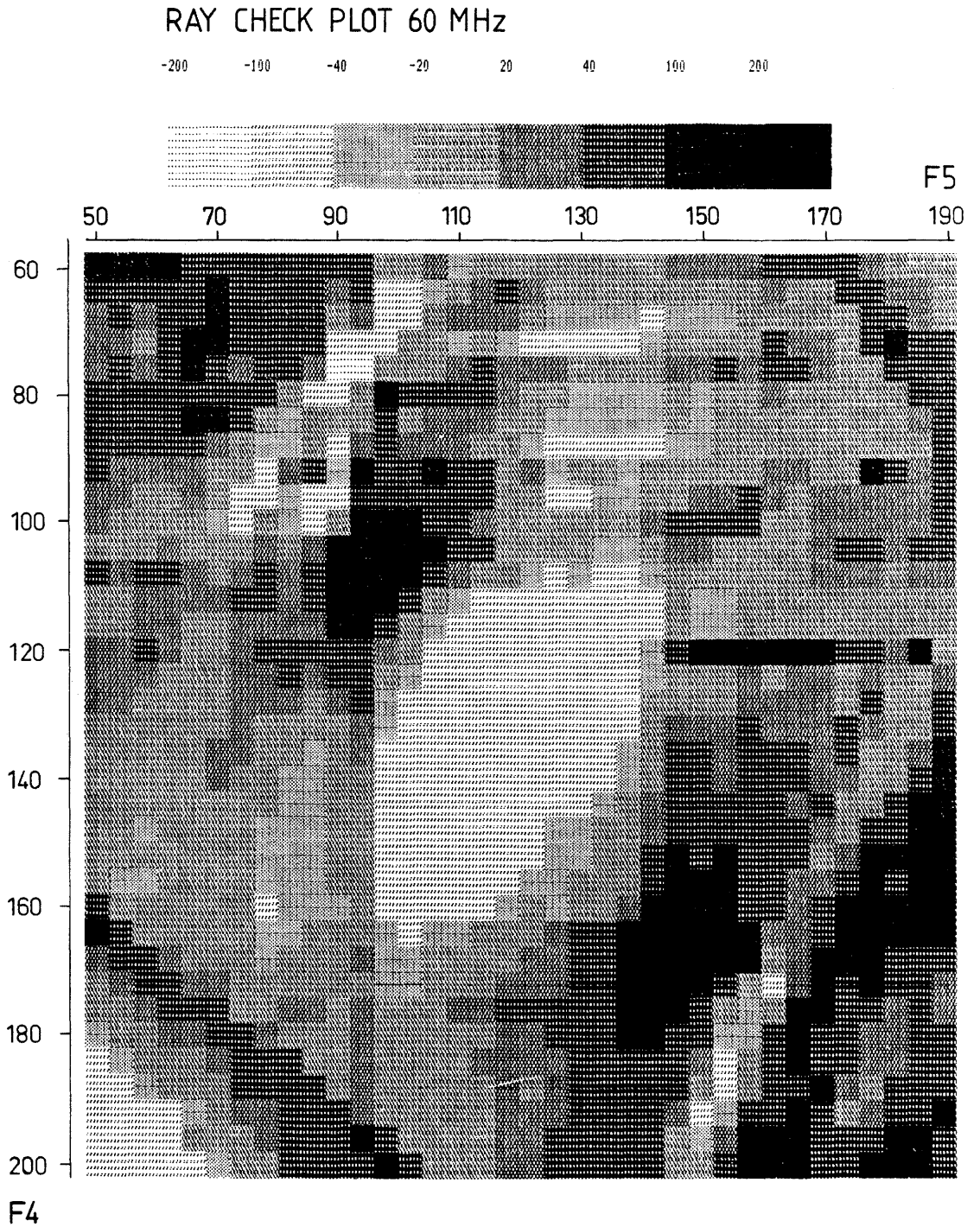


Figure 5.5 Ray check plot for residual attenuation. Borehole section F4-F5, center frequency 60 MHz.

5.2.4 Results of tomographic inversion

After a comparatively time consuming and tedious data checking and correction procedure the crosshole data are ready for tomographic inversion. The data from the crosshole sections measured at Stripa have been inverted both by direct inversion of the matrix and by the iterative CG-method. The algorithms and software used for the inversion have been developed as a part of the seismic research performed within the Crosshole program and this work is adequately described by Ivansson (1984).

All crosshole sections listed in Table 5.1, except one, have been measured with a high and uniform ray density. The distance between measurement points in the boreholes have for these sections been 4 m and the measured length in each borehole was 140 m. This has resulted in a total of 1296 rays for each section. After the data quality check between 1100 and 1200 rays remained which have been used in the tomographic inversion. Inversions have been performed with cell sizes of 5 m and 2.5 m, where the smaller cell size resulted in a total of 6 000 cells for the F1-F6 section, which was the largest one. Tests have been made with different values of the damping constant, λ . Large damping results in a smoothed tomographic image which is less sensitive to errors in the input data. While a smaller damping gives better resolution it is also more sensitive to errors. The normal strategy is to make the damping as small as possible in order to get high resolution without making the tomographic image too 'noisy'. For the Stripa data λ -values in the range 10 to 20 have given the best results. The damping constant λ has the dimension of length and is thus a measure of the distance over which the solution is averaged.

Figure 5.6 shows the result of the tomographic inversion of the residual travel times from the section F6-F1 with a cell size of 2.5 m. The distance between the ends of the boreholes is approximately 140 m and the length of the longest ray is about 170 m. The dark areas correspond to reduced velocities or increased slownesses. In section 3.2 it was shown that increased fracturing and the associated increase in water content (porosity) reduces the radar velocity and increases the attenuation. Hence, the dark areas correspond to fracture zones. Figure 5.6 displays the deviations in slowness from an average value of 8 300 ps/m which corresponds to a velocity of 120 m/ μ s. The range of variation of the slowness values in the tomographic solution is within the range +200 ps/m which gives a total variation of about 5 %. The radar velocity variations in the

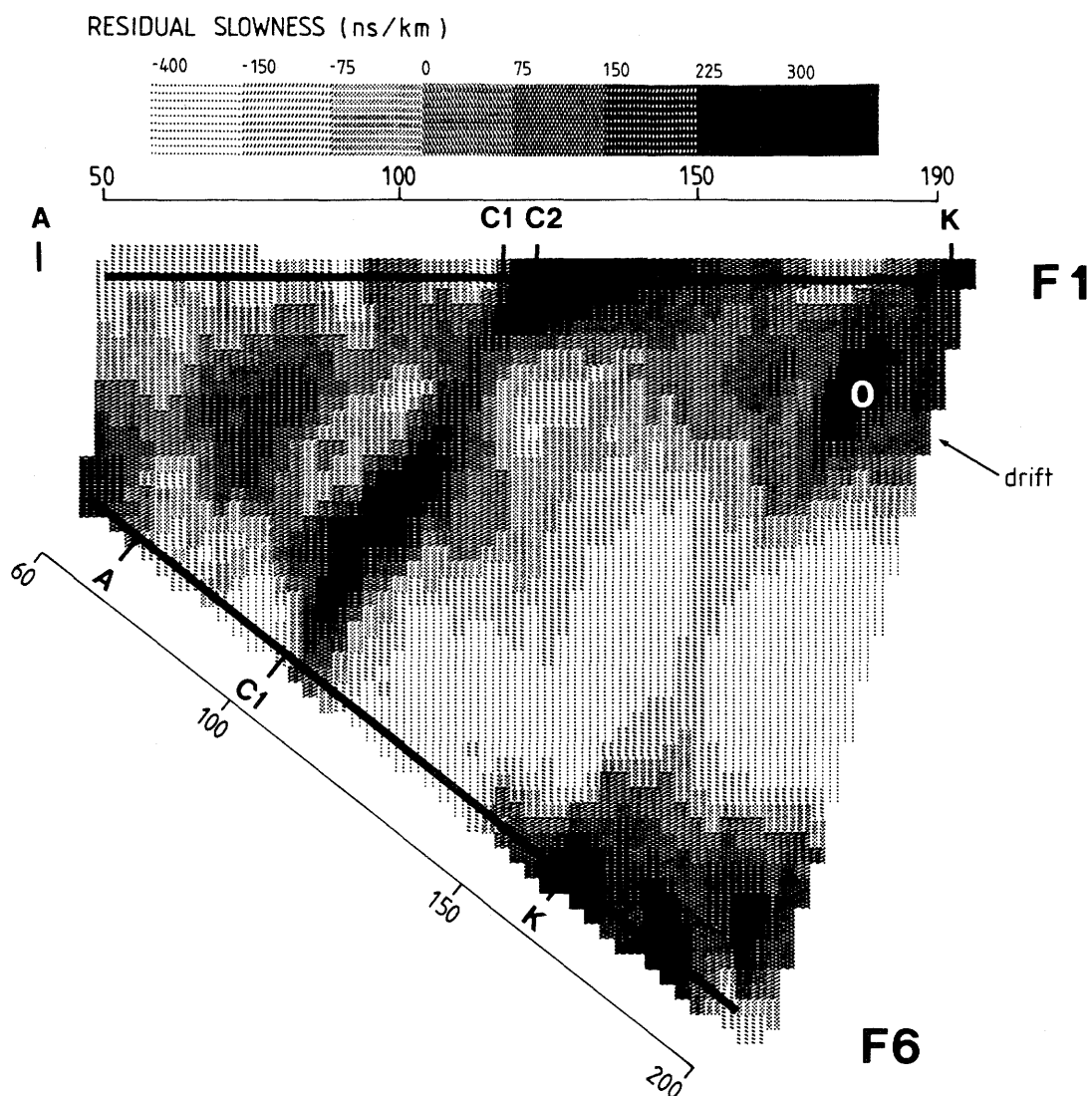


Figure 5.6 Tomographic reconstruction of slowness distribution for the borehole section F6-F1 based on residual travel time data. Cell size 2.5 m. Center frequency 22 MHz.

Stripa granite can thus be considered to be relatively small and ray bending should not be a serious problem.

The two fracture zones C and K are the most marked features appearing in the tomogram. The extent of these zones in the plane between the boreholes agrees well with their known intersection with the boreholes which have been marked in the figure. There is also evidence of a low velocity zone connecting C in F1 with A in F6. A remarkable feature is the low velocity patch along this zone. The tomogram also indicates lateral variations in the width and velocity of the zones C and K and there are reasons to believe that these variations are real and reasonably well described by the tomogram. Zone K passes close to the drift and it is not possible to resolve the zone and the drift in this image.

A useful check of the tomogram is possible because the sections F1-F6 and F1-F4 partly coincide. A comparison shows that the tomograms are very similar confirming that the observed structures are real. Similar comparisons have been made with the other tomographic sections by collecting the tomograms in a three dimensional plastic model. One can then check that the observed fracture zones intersect the borehole planes in a consistent way and that the intersections also agree with the observations on the cores and radar reflection measurements. (The complete set of tomograms obtained at the Crosshole site is shown in Appendix C).

A tomographic inversion of the same data but with a cell size of 5 m is shown in Figure 5.7. The smaller cell size results in a smoother image due to the better interpolation of the slowness values between adjacent cells. The inversion was made with the same damping constant ($\lambda=10$ m) for the two cell sizes which has the effect that the resolution is not noticeably improved by a reduction in cell size. The tomographic images obtained with the different cell sizes are actually very similar and the result does not critically depend on the cell size. However, the images obtained with the smaller cell size is much more attractive to the eye and have consequently been used in the examples below.

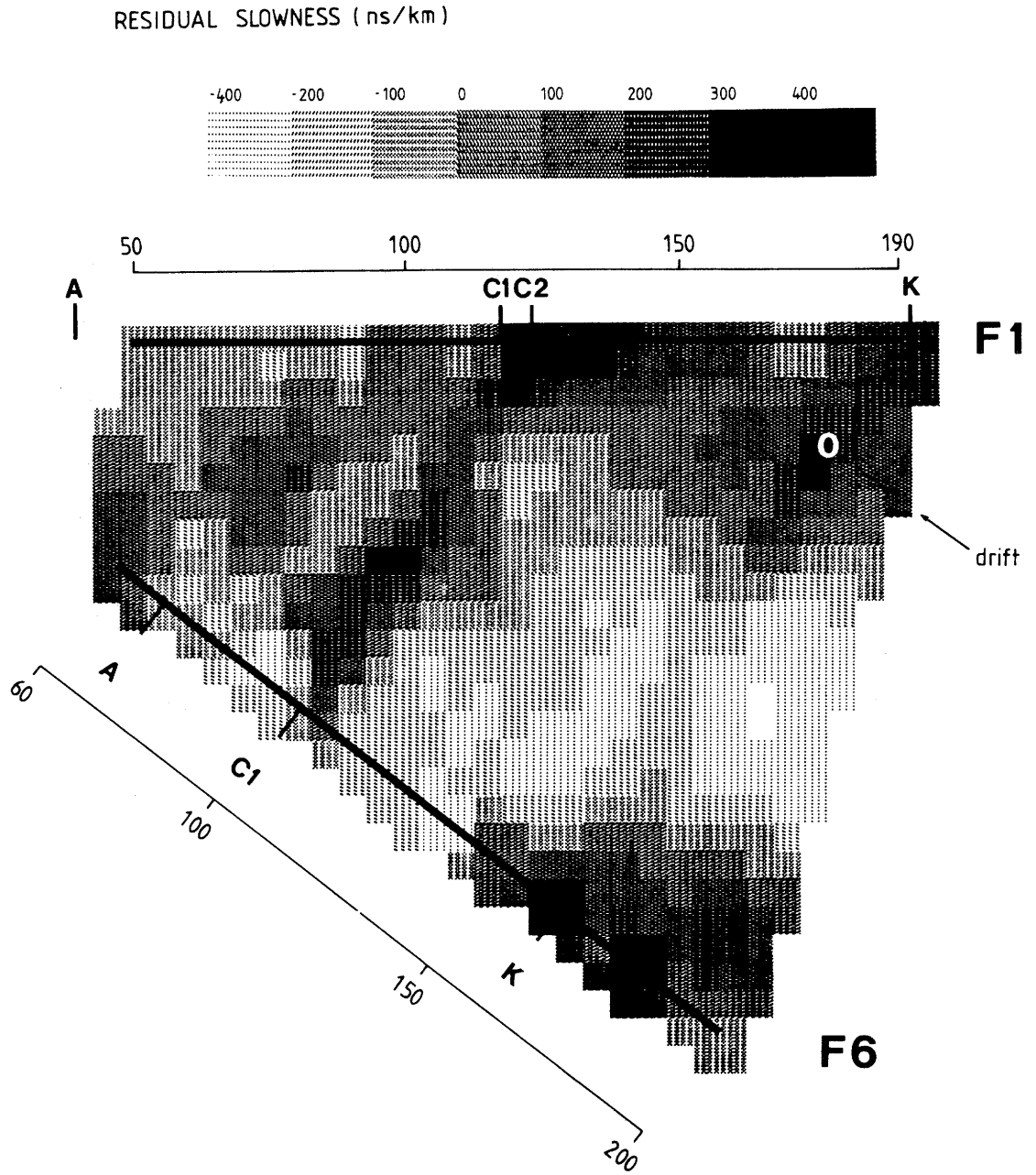


Figure 5.7 Tomographic reconstruction of slowness distribution for the borehole section F6-F1 based on residual travel time data. Cell size 5 m. Center frequency 22 MHz. Same input data as for Figure 5.6.

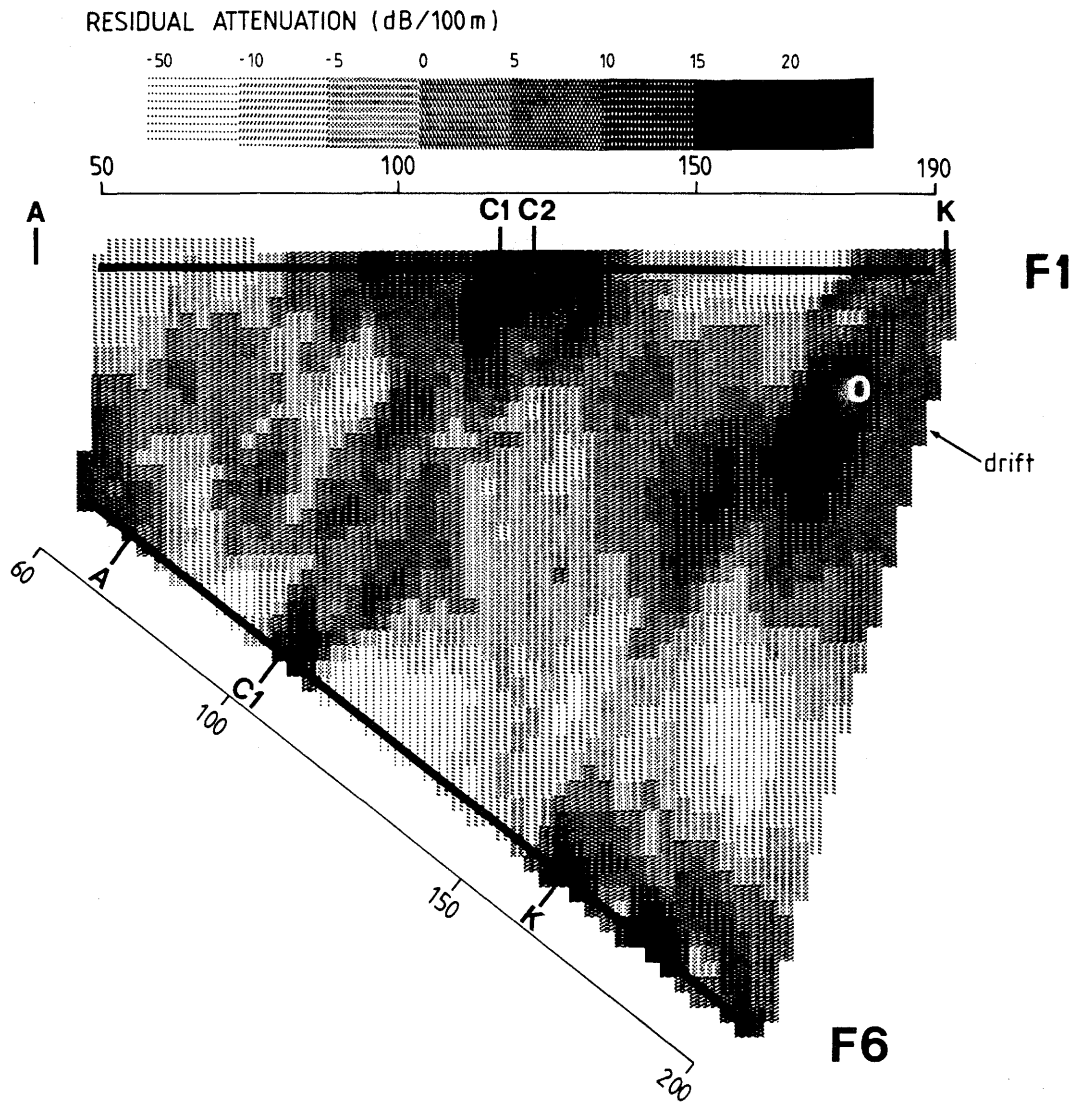


Figure 5.8 Tomographic reconstruction of attenuation distribution for the borehole section F6-F1 based on residual amplitude data. Cell size 2.5 m. Center frequency 22 MHz.

Figure 5.8 shows the variation in attenuation in the plane between F1 and F6 obtained from an inversion of the residual amplitudes. Dark areas correspond to high attenuation which in principle should be areas of 'poor rock' or fracture zones. The variations are displayed relative to an average attenuation of 28 dB/100 m. The range of variation in the attenuation data is from 20 dB/100 m to more than 50 dB/100 m. Variations in attenuation are thus much larger than the variations in velocity for radar waves. It must be stressed that the attenuation of the propagating wave is due to absorption, i.e. heating of the rock. The losses caused by reflections at the fracture zones are entirely negligible. This is important because otherwise the apparent attenuation would depend on the direction of propagation.

The main features in the figure are the zones C and K and the drift. In the attenuation tomogram the resolution seems to be better than in the corresponding velocity tomogram. For example, zone C appears to consist of two parts and the passage of zone K close to the drift is resolved. In spite of some differences between the tomograms in Figures 5.6 and 5.8 the similarities between the two are striking. This is evidence that the tomograms represent real geological features and that the result is not some artifact generated by the method itself. It should be remembered that the data behind the two tomograms is based on measurements of two different properties of the electromagnetic field which represent different properties of the rock. The magnitude of variation of these properties is also drastically different, i.e. a few percent compared to several hundred percent.

The appearance of the drift in the tomograms deserves a special discussion. The drift passing between the boreholes at the Crosshole site is filled with air. This makes the drift a high velocity and low attenuation anomaly. However, in the attenuation tomogram it appears as a high attenuation feature. The drift will scatter energy by reflection and hence causes a shadow zone permitting little radar energy to pass through. The drift thus appear as an attenuating object in the tomograms.

The drift is not normally seen in the velocity tomograms due to the algorithm used for picking the travel times. The radar velocity in the drift is about 3 times higher than in the surrounding rock and the radar wave passing through the drift will thus arrive before the wave that passes around it through the rock. The pulse is of course really deformed in a complicated way but this simplified

picture serves to illustrate the basic principle. An example is seen in Figure 5.9 which presents a crosshole scan from the section F4-F5. The early arrival is clearly seen before the main wave which gives rise to the hyperbola shaped feature in the figure. The magnitude of the wave passing through the drift is much smaller than the later arriving wave which has passed through the rock. The algorithm used for picking travel times and amplitudes will miss such an event since it picks the event with the maximum amplitude.

The tomographic inversion of the travel times for section F2-F5 provides an example of this (see Figure 5.10). The fracture zones C and K are clearly identified also in this tomogram, but here it is clear that the drift does not cause any velocity anomaly.

Figures 5.11 and 5.12 display attenuation tomograms from section F4-F5 obtained at two different frequencies. The average attenuation at these two frequencies is significantly different. The average attenuation increases from 28 dB/100 m at 22 MHz to 42 dB/100 m at 60 MHz. In spite of these large differences in absolute values both tomograms show variations from the average value which are roughly of the same magnitude. The same features can also be identified in both images but some differences in the detailed structure of the features between the two measurements can be observed. A general feature is that the fracture zones appear to be somewhat wider in the 22 MHz measurement. This also applies to the drift which in the 22 MHz measurement appears to be connected to zone K. As can be expected there is less resolution at the lower than at the higher frequency.

A total of six crosshole sections have been measured at the Crosshole site and tomographic reconstruction have been made of both traveltime and amplitude data. The complete set of results is presented in Appendix C and only representative examples have been given here. The complete set of tomographic results represents two different properties of the rock and borehole sections which intersect in space. The most striking characteristic of this set of results is their consistency. The travel time and amplitude data generally show the same features at the same positions except for the drift which does not show up in the travel time tomograms. For the crosshole sections which intersect we note that the fracture zones identified in each individual tomogram also intersect at the correct position. The consistency of these results show that in spite of all the approximations made and the errors contained in the data the tomographic inversion gives results which

are representative of the geological conditions in the rock.

The tomograms show fewer features than the reflection measurements. This is natural as the data on which the tomographic inversion is performed is generated by an averaging process (integration) and this tends to remove the effects of small anomalies.

Crosshole reflection measurements

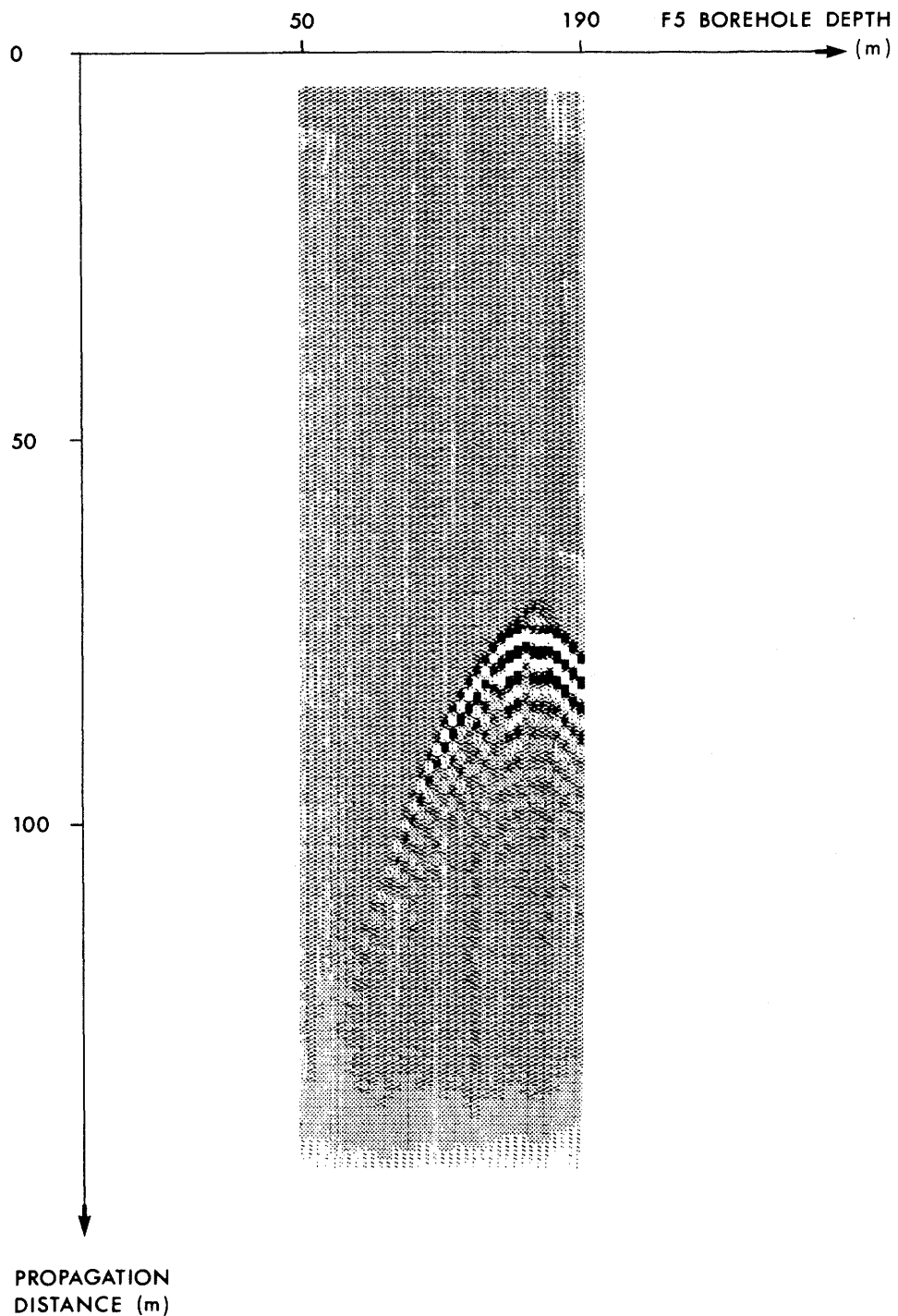


Figure 5.9 Crosshole scan from measurement of the section F4-F5 with a center frequency of 60 MHz, source in F4, at 184 m. The wave passing through the drift is seen as the early arrival at the top of the hyperbola.

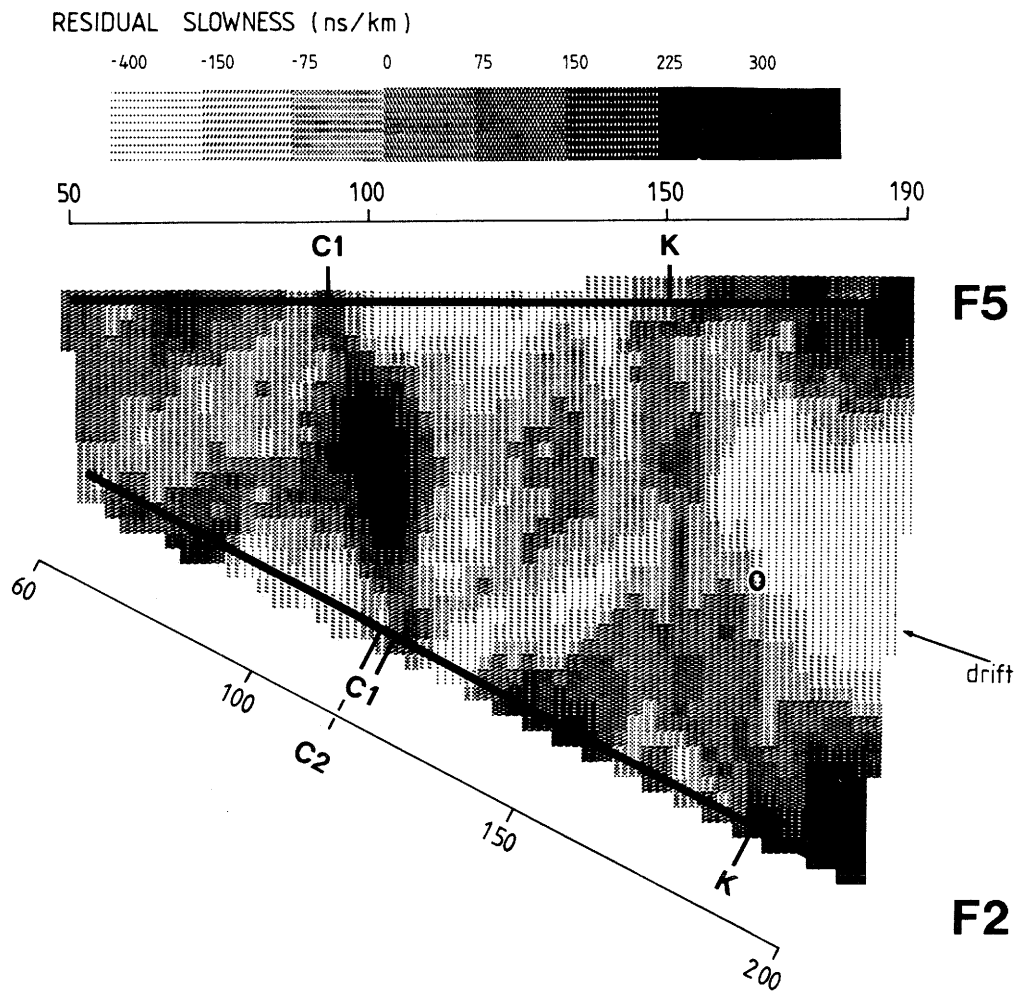


Figure 5.10 Tomographic reconstruction of slowness distribution for the borehole section F2-F5 based on residual travel time data. Cell size 2.5 m. Center frequency 22 MHz.

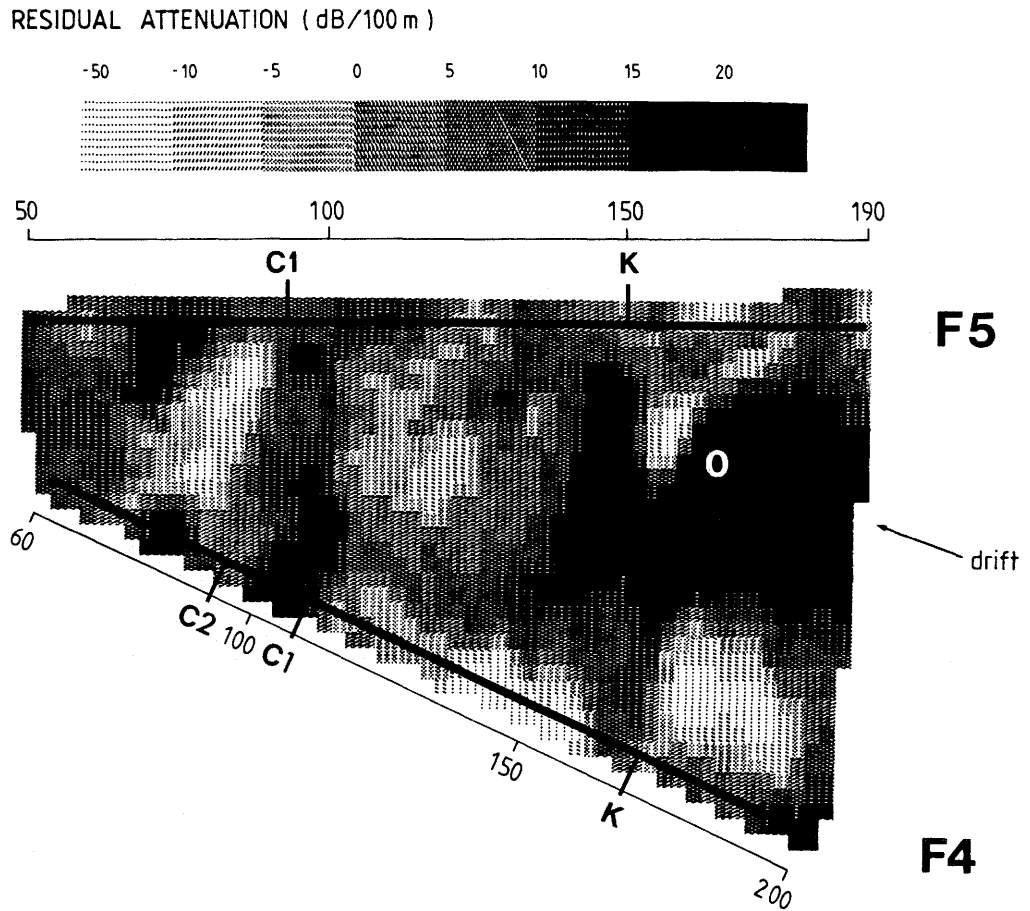


Figure 5.11 Tomographic reconstruction of amplitude distribution for the borehole section F4-F5 based on residual amplitude data. Cell size 2.5 m. Center frequency 22 MHz.

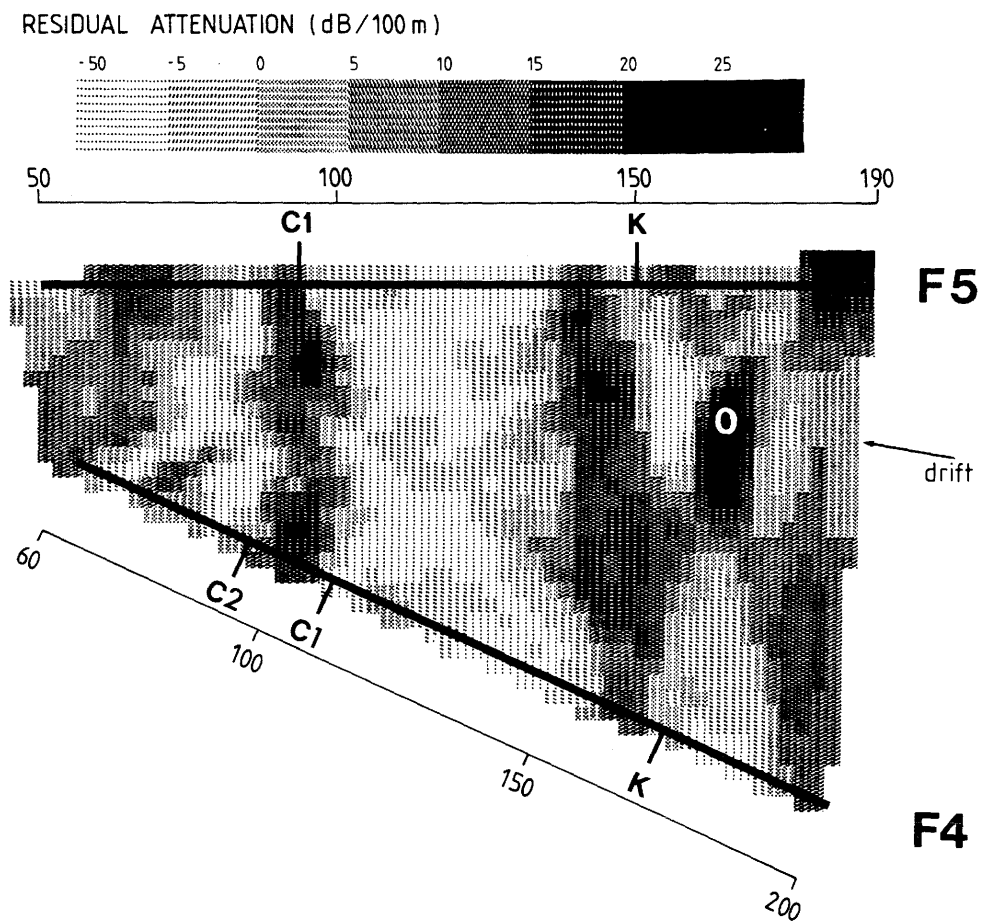


Figure 5.12 Tomographic reconstruction of amplitude distribution for the borehole section F4-F5 based on residual amplitude data. Cell size 2.5 m. Center frequency 60 MHz.

5.3 CROSSHOLE REFLECTION ANALYSIS

When the transmitter and receiver are in different boreholes reflected pulses are observed after the directly propagated pulse has arrived. The direct pulse is the only part of the signals used in the tomographic analysis so the crosshole reflections provide additional independent information about the fracture zones.

Compared with single hole measurements previously invisible zones can be observed since the reflection geometry has changed considerably. Additional information about the orientation of the zones can also be expected. This was confirmed by the interpretation of data obtained at Stripa and in other measurements. It is particularly interesting that crosshole reflections in principle provide a complete determination of the orientation of a fracture zone. This is due to the additional freedom provided by a bistatic radar configuration. The disadvantage of the method is mainly that the analysis becomes more complicated and that the reflected signals may be weak since the reflected pulse will have a longer path to propagate than in single hole measurements. In the following section the method of analysis is presented and an example calculated in detail.

5.3.1 Method of analysis

Figure 5.13 shows a typical result from a borehole scan performed between boreholes F1 and F6 at the Crosshole site. During this measurement the transmitter was moved along F1 while the receiver was kept at a fixed position in F6. As the transmitter is moved the direct pulse registered by the receiver in F6 traces a hyperbola. After the direct pulse there arrive several pulses reflected from fracture zones. If the reflections are caused by fracture planes these curves are also hyperbolas. It is however difficult to use this geometrical information to extract information directly from the radar maps. A different method of analysis has therefore been used.

The bistatic radar configuration is defined in Figure 5.14. The receiver and transmitter are in known positions described by the vectors \bar{x}_0 and \bar{x}_1 . The distance l propagated by the direct pulse is given by the expression

$$l^2 = (\bar{x}_0 - \bar{x}_1)^2 \quad (5.20)$$

Crosshole reflection measurements

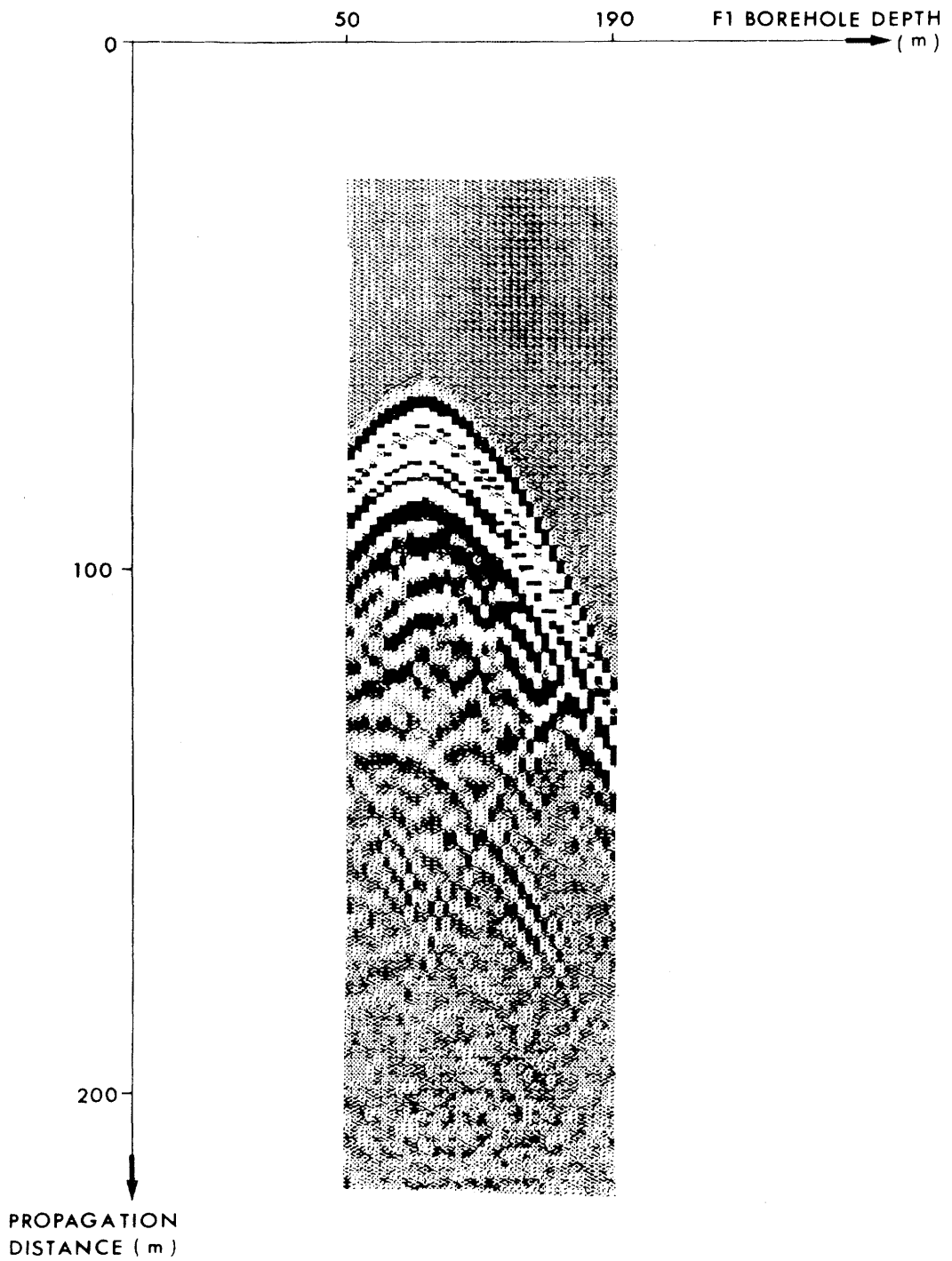


Figure 5.13 Radar map obtained with receiver fixed in F6 at 112 m while the transmitter was moved in F1. Center frequency 22 MHz.

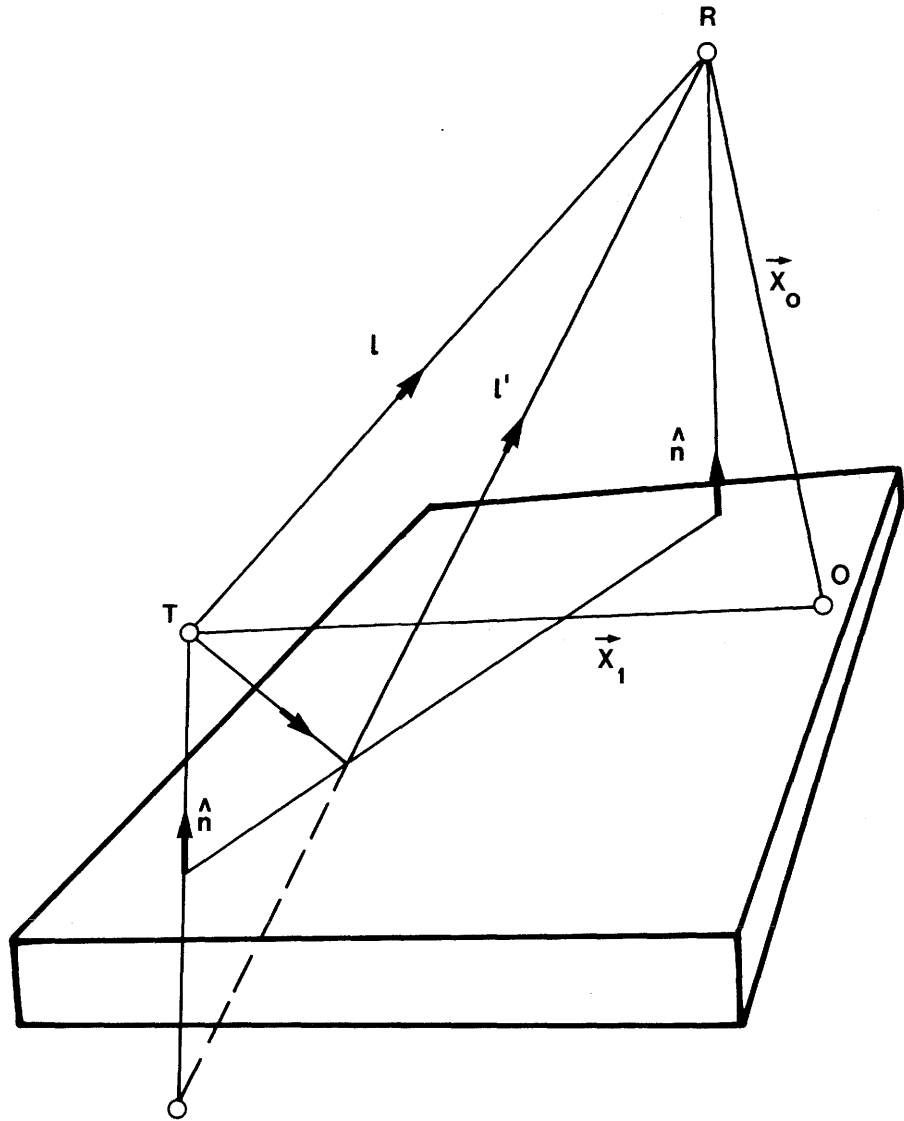


Figure 5.14 Principal ray paths in a bistatic radar configuration where the ray is reflected in a plane. T = transmitter, R = receiver, l = direct wave, l' = reflected ray, \vec{x}_0 = location vector of receiver, \vec{x}_1 = location vector of transmitter, \hat{n} = normal vector to plane.

The distance propagated by the reflected pulse is given by a similar expression containing the unknown position \bar{x}_s of the receiver mirrored in the fracture plane^s:

$$l'^2 = (\bar{x}_s - \bar{x}_1)^2 \quad (5.21)$$

When the receiver position is reflected in the fracture plane it appears at a position

$$\bar{x}_s = \bar{x}_0 - 2n(\bar{x}_0 \cdot \bar{n}) \quad (5.22)$$

where \bar{n} is the unit normal vector of the plane, i.e. the quantity to be determined. This formula is only valid if the origin is in the reflecting plane. This appears to make it useless, since the position of the plane is unknown, but there is fortunately one exception. When the transmitter is near the fracture plane the reflected and direct pulses intersect in the diagram (Figure 5.13) since they have then propagated the same distance. One can thus determine where the borehole intersects the fracture plane and define a suitable origin at that point.

A simplification of the vector formulas leads to the expression

$$l'^2 = l^2 + 4(\bar{x}_0 \cdot \bar{n})(\bar{x}_1 \cdot \bar{n}) \quad (5.23)$$

In principle all quantities in this formula except the vector \bar{n} can be obtained from the measured data so from two or more measurements the two independent components of the unit vector \bar{n} can be determined. This analysis can be compared with the special case of a single hole measurement where the receiver and the transmitter are moved along the same borehole at a fixed distance $2c$ so that

$$\bar{x}_0 = (x_1 + 2c) \bar{a} \quad (5.24)$$

Here \bar{a} is a unit vector along the borehole and x_1 is the borehole coordinate. The previous formula then simplifies to the well known expression for single hole measurements (cf. 4.1)

$$l'^2 = (2c)^2 + 4(\bar{a} \cdot \bar{n})^2 x_1 (x_1 + 2c) \quad (5.25)$$

which is a hyperbola in the radar diagram. From this equation the scalar product ($\bar{a} \cdot \bar{n}$) can be determined immediately, which gives the angle between the fracture plane and the borehole. However, no more information about the orientation of the plane can be derived from the equation due to the axial symmetry of the single hole configuration. The bistatic configuration provides full information about \bar{n} , but the results can not be directly interpreted as orientation angles. The amount of analysis necessary for an interpretation can be judged from the following examples.

5.3.2 Examples of crosshole reflection analysis

When a reflection has been identified in a radar picture the propagation times (or lengths) l and l' can be determined for each position of the transmitter. Since l is already known from the position of the antennas in the borehole one can use this information to calibrate the length scale and determine the zero of l and l' in the radar map. In the Stripa measurements this was done very accurately during the tomographic work.

The equation (5.23) indicates that one should plot the difference $l'^2 - l^2$, which is a linear function of borehole depth x_1 for a plane reflector. Reflections are sometimes difficult to determine exactly in the radar pictures, since they are often weak and interference with stronger signals (especially the direct wave) can cause apparent deflections of the curve. It is consequently a useful test to plot the difference for each observed reflection and check that the lines are straight. After this control the slope and point of intersection with the abscissa are determined. The difficulty of identifying the reflections is often due to spatial aliasing which could be remedied by a smaller separation of measurement points in the borehole where the probe is moved.

As an example consider the radar crosshole measurement between F1 and F6 in Figure 5.15 for a receiver fixed 156 m in F6. Since there are several reflections in this diagram it may appear difficult to separate them. In particular there are probably two strong reflections intersecting the direct wave for a transmitter position about 170-200 m into F1. A test of different ways of separating the reflections indicated that only one choice gave two straight lines in Figure 5.16, i.e. two zones were identified and separated by this method. The position of the fracture zones previously established from single hole reflection have been indicated in the figure for comparison. One can not

Crosshole reflection measurements

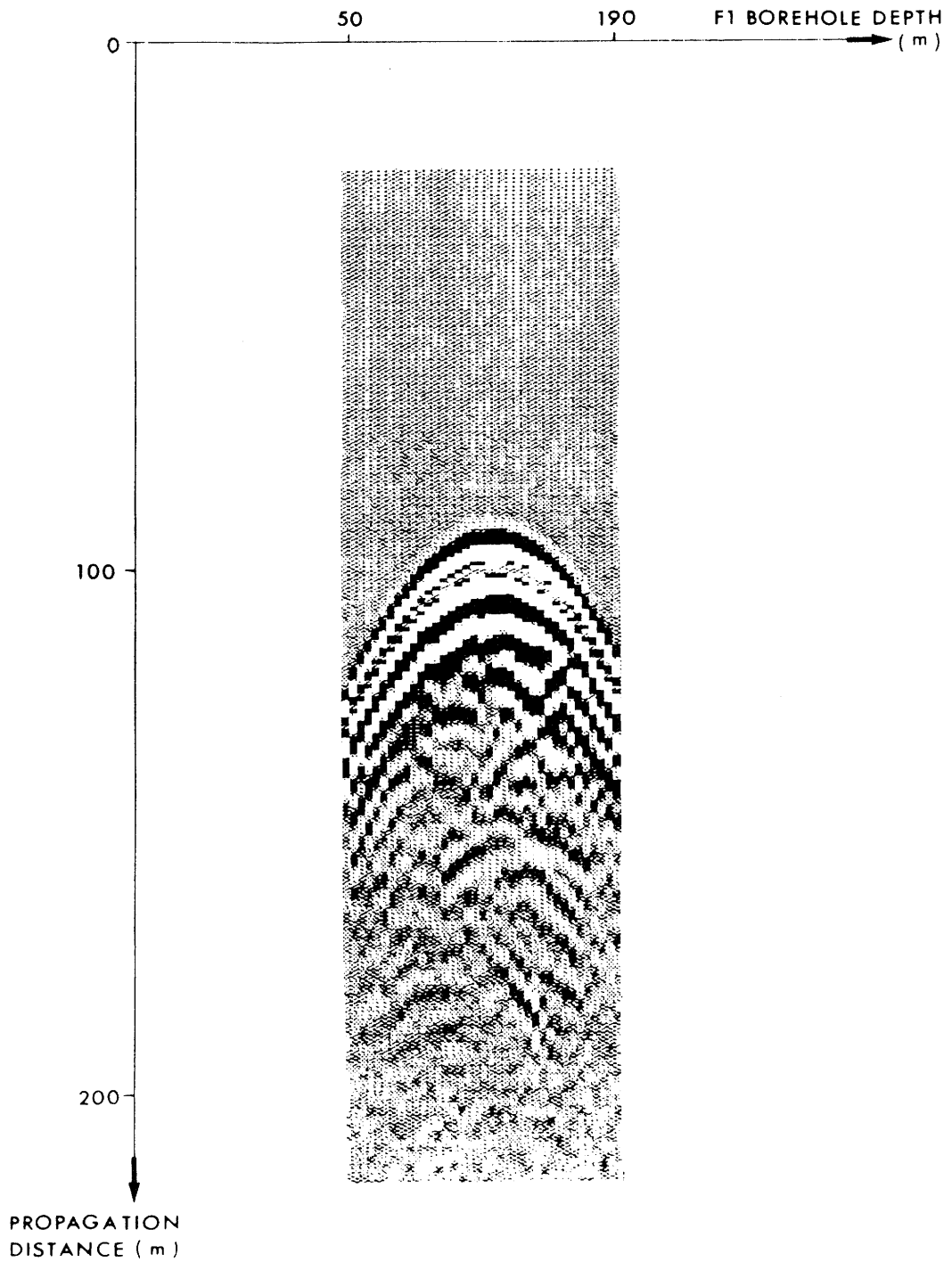


Figure 5.15 Radar map obtained with receiver fixed in F6 at 156 m while the transmitter was moved in F1. Center frequency 22 MHz.

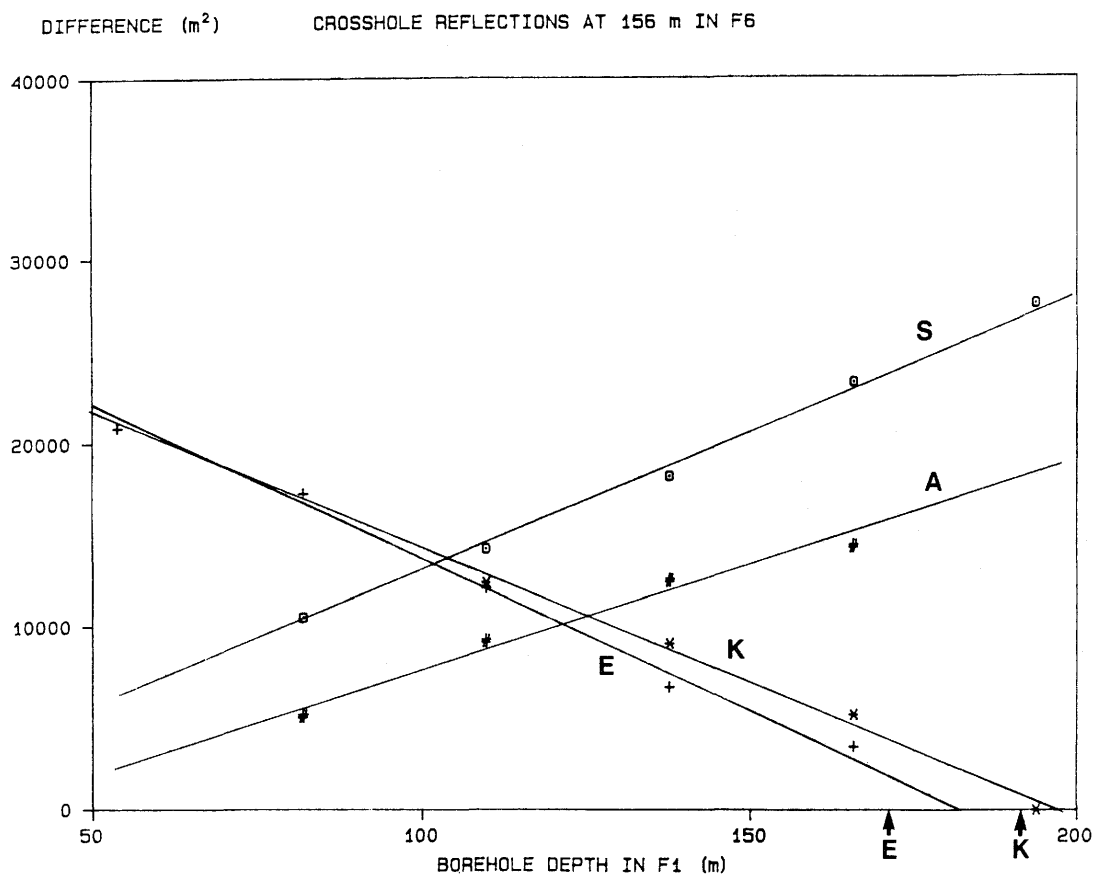


Figure 5.16 Plot of $l_1^2 - l_2^2$ for two zones intersecting F1. Data from measurement shown in Figure 5.15. The position of the zones established by single hole measurements have been indicated.

expect perfect agreement because entirely different reflection points are involved in single and crosshole measurements. The calculated orientations are then affected because the fracture zones are not entirely flat as we have to assume during calculations.

One of these lines intersects the abscissa (borehole F1) at 180 m. The same analysis applied to measurements performed with the receiver at other positions in borehole F6 indicates that in each case there are straight lines intersecting the abscissa at this point (Figure 5.17). Consequently there is a reliable identification of this zone, called E in the single hole measurements where its intersection was determined to be about 171 m in F1. In most other cases the scatter of the intersections has been greater; it is therefore valuable if one can follow the reflections of a particular zone from picture to picture to identify it in that way. This method sometimes fails, however, since there is a large variation in the quality of the crosshole reflection maps, presumably because the antenna efficiency is affected when the probes pass through fractured rock.

In order to determine the orientation of the zone we put the origin of the coordinate system at the intersection point, 180 m in F1. Each line will then give one equation for the components of the normal vector \bar{n} of the plane, since the slope is determined by the equation

$$l'^2 - l^2 = 4(\bar{x}_0 \bar{n})(\bar{t} \bar{n}) x_1 \quad (5.26)$$

where \bar{t} is the unit vector along the borehole. In order to treat all slopes in a symmetric way it is however better to plot the slopes against x_0 since this is a linear function according to (5.26).

Figure 5.18 shows that the linear relationship is well satisfied. The intersection with the abscissa corresponds to the intersection of the fracture zone with the borehole: thus zone E intersects F6 at about 250 m. This value should be compared with the value 270 m found in the single hole measurements. The difference can be neglected since the zone intersects F6 obliquely (the angle is 27°) which makes the intersection point rather uncertain. (Another candidate is found at 240 m.) It should also be remembered that in crosshole measurements the pulse is reflected from other parts of the plane than in single hole measurements

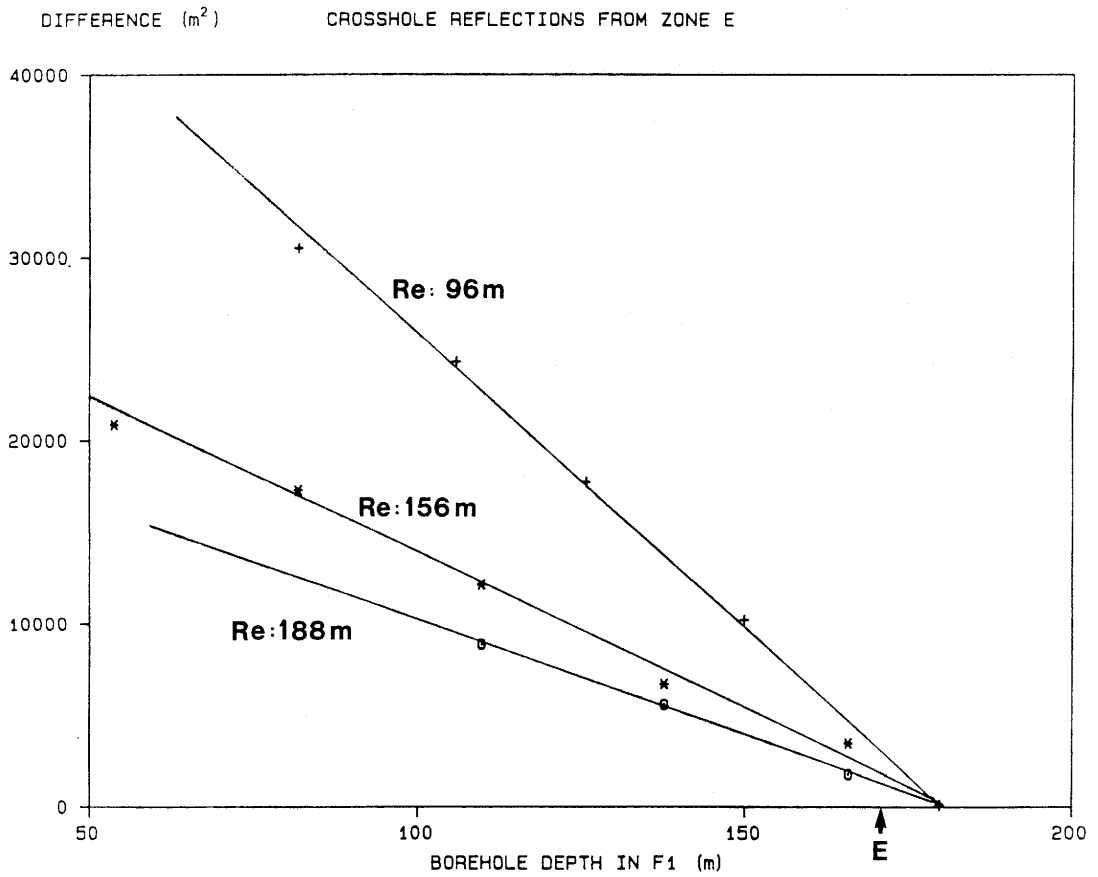


Figure 5.17 Plot of $l_1^2 - l_2^2$ for zone E in the crosshole reflection measurements between F1 and F6. Receiver fixed at 96, 156 and 188 m in F6. Center frequency 22 MHz.

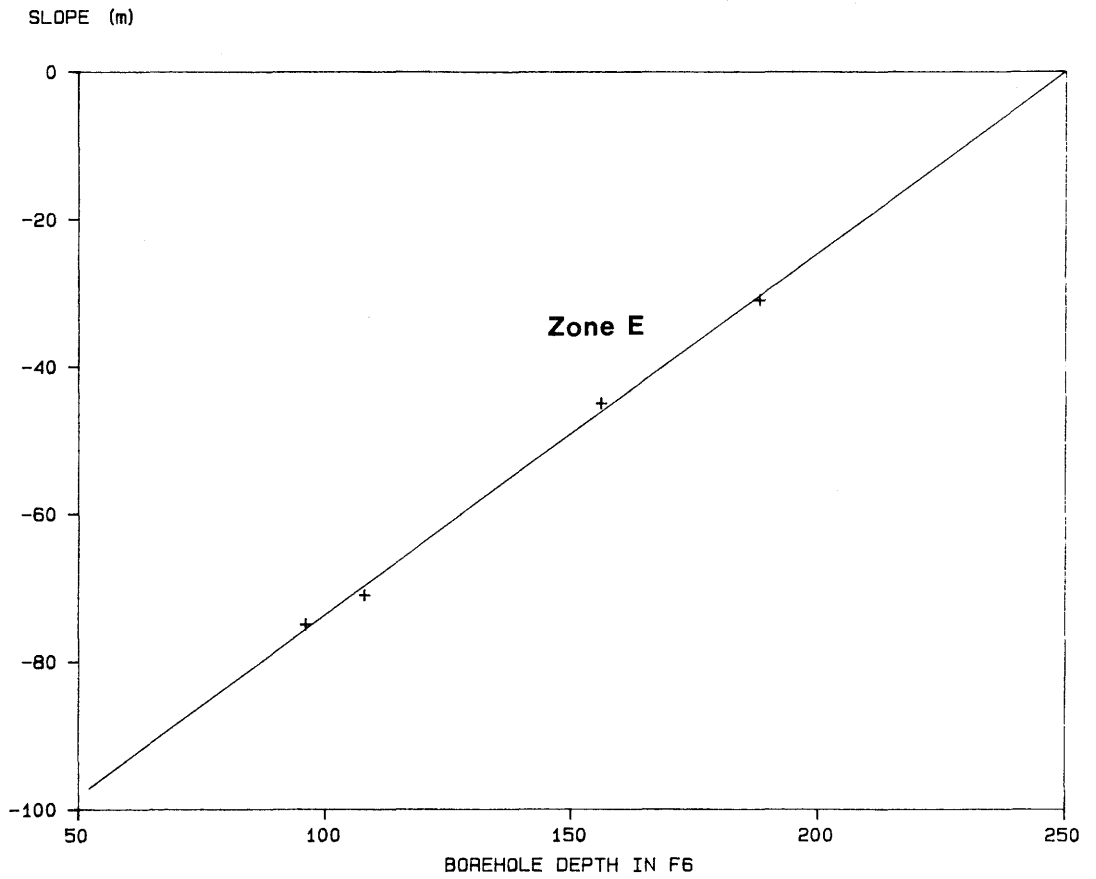


Figure 5.18 Plot of the slopes vs receiver position in F6 using the data for zone E in Figure 5.17. Crosshole reflection measurements between F1 and F6. Center frequency 22 MHz.

so the fracture zone must be very plane to give consistent results.

When the intersections of zone E with both boreholes have been obtained only one parameter is needed to describe the orientation of the fracture zone. It is obtained from the slope of the line in Figure 5.18 which defines the quantity $(\bar{n} \cdot \bar{t})(\bar{n} \cdot \bar{u})$ where \bar{t} and \bar{u} are the unit vectors along the boreholes. Solving this equation, taking into account that the plane is already fixed at two points, one obtains two possible solutions. This remaining ambiguity is resolved by comparing with single hole data. The orientation of zone E obtained in this way is in reasonable agreement with the single hole results but not perfect (about 10° off).

In view of the complications of the method it is difficult to assess directly the quality of the data. It is consequently important to see how good the results are for another well known zone, namely A. This zone is reasonably well seen in the F4-F5 crosshole measurement and three lines were obtained intersecting F5 at 30 m. The corresponding intersection determined from single hole experiments is at 36 m. The slopes of the lines are plotted in Figure 5.19. The intersection with the abscissa (borehole F4) is then approximately at 55 m while the corresponding intersection determined in single hole experiments is at 54 m. The slope of the line in Figure 5.19 is 0.66 while single borehole measurements give about 0.60. The value is rather sensitive to errors in the radar angles so the agreement must be regarded as fair.

The results given above have shown that crosshole reflection measurements can be a powerful method of determining the position of fracture zones. It is sensitive to the quality of the data and the investigation has been of a preliminary nature since it is difficult to find sufficiently many strong and well defined reflections from each zone. A considerable improvement should be possible when the experiments are directly planned to investigate crosshole reflections using image processing to simplify the identification of reflections.

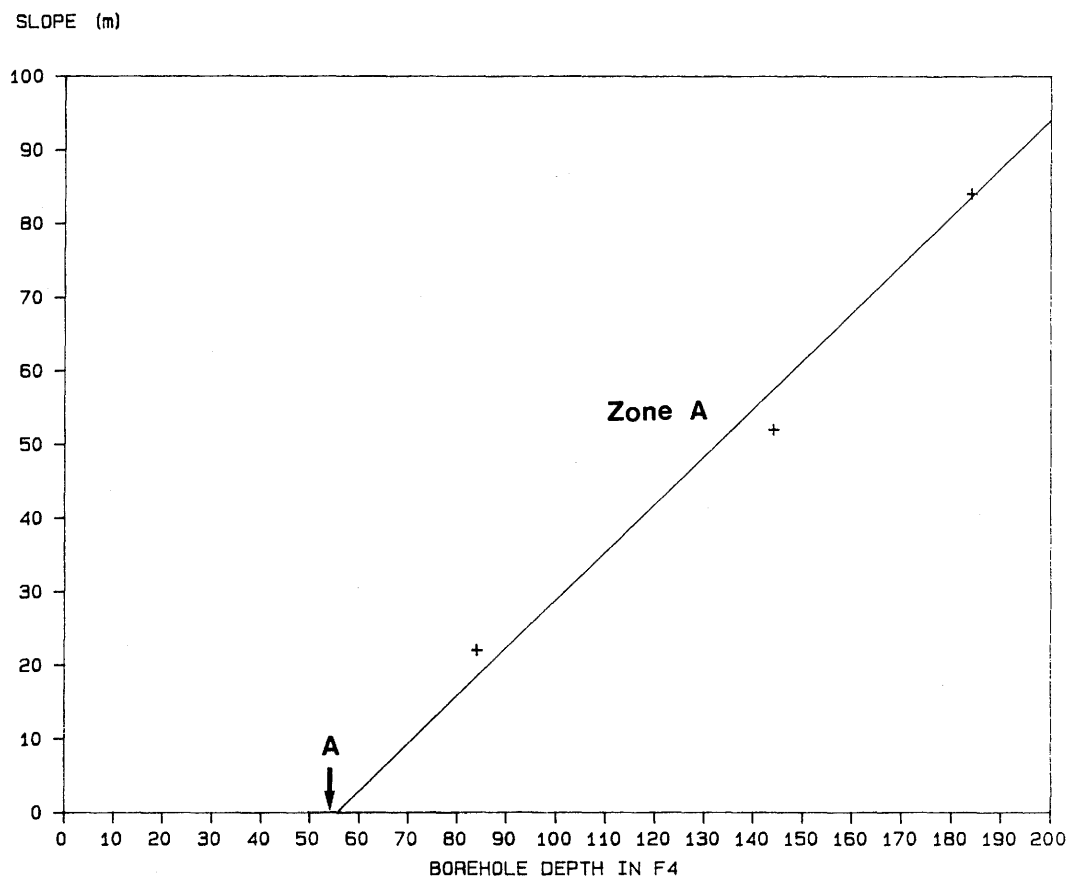


Figure 5.19 Plot of the slopes obtained for zone A using the crosshole reflection measurements between F4 and F5. The abscissa is the receiver position in F4. Center frequency 22 MHz.

6.1 DEFINITION OF FRACTURE ZONES

By combining data from single hole and crosshole reflection measurements with the results of tomographic analysis at the Crosshole site a consistent model has been formulated of the distribution of fracture zones. It is particularly notable that no inconsistencies were encountered when the different methods were used to determine the position of fracture zones.

Geologically fracture zones are zones of weakness in the rock characterized by increased fracturing. A single fracture can by itself reflect very little energy and it is rather the average properties of the rock that can be detected by the radar. From the radar point of view a fracture zone is a flat structure in which the electric conductivity and the dielectric constant have higher values than in the surrounding rock. The electric properties are basically determined by the increased water content of fractured rock and are thus closely related to the water flow in the rock. The change in the electric parameters will cause the radar waves to be partly reflected at the surface of a zone while the transmitted wave is attenuated during propagation through the fractured rock. The measurements in Stripa have shown that fracture zones are effective reflectors of radar waves. They are easy to identify in the radar maps due to the characteristic pattern produced when the radar probes are moved along the borehole. Fracture zones discovered by radar can often directly be identified with the geologically determined units and there are few cases where the correspondence can not be established in detail.

The position of a fracture zone can be described by its intersections with the boreholes. Since the measurements have shown that the reflecting zones are quite flat when considered on a sufficiently large scale it is however more convenient to define the position of a zone by its intersection with a definite borehole (F3) and its orientation, determined by the dip and strike of the fracture plane. The strike is measured from north, in a 360 degree system. The strike direction is defined in such a way that a strike of 0° implies a dip towards E and a strike of 180° a dip towards W.

6.2 THE BASIC MODEL

A rather small set of fracture zones dominate the radar measurements in the Crosshole site. They appear to be strongly fractured, judging from the radar response, and are furthermore persistent, since they appear in all boreholes and produce reflections at great distances from the boreholes. They are therefore considered to be of particular interest for the investigation and they have been included in a basic model of the site which is described in this section. All zones discovered during the radar investigations are described in the next section, which also summarizes the geometrical data derived from radar measurements and used to calculate the orientation of the fracture zones.

The prominent structures are named A, C, K and L and are included in the basic model of the site shown in Figure 6.1. These fracture zones are all strong radar reflectors and are observed in most single hole reflection measurements: the exception is zone L which is sometimes too far from the site to be seen. Zones A, C and K have also been observed in crosshole reflection measurements.

It is noticeable that three of the units (C, K, and L) are almost parallel in agreement with the established view on how fracture zones are formed. In fact, taking into account the weaker fracture zones described in the next section, one can separate most of the observed zones into two groups of parallel fracture planes: one containing unit l, AX, C, K and L which appear in that order from the site and another group containing the Site zone, A, E, F and G. The angle between the zones in the two groups is about 60° in agreement with theoretical predictions for fracturing of granite. The spacing between the zones is also quite regular, particularly in the first group where it is about 70 m.

Zone A

Zone A which is closest to the Crosshole site is easy to correlate though it contains some irregularities: the orientation of A is variable, suggesting that the zone is undulating in some way. The thickness of the zone appears to be at least several meters judging from the reflection measurements. The lower part of the reflection pattern is weakened in measurements from boreholes F4 and F6 suggesting that zone A is less fractured in this direction than near the site. Zone A is also seen in crosshole reflections. It is just outside the volume covered by the tomograms.

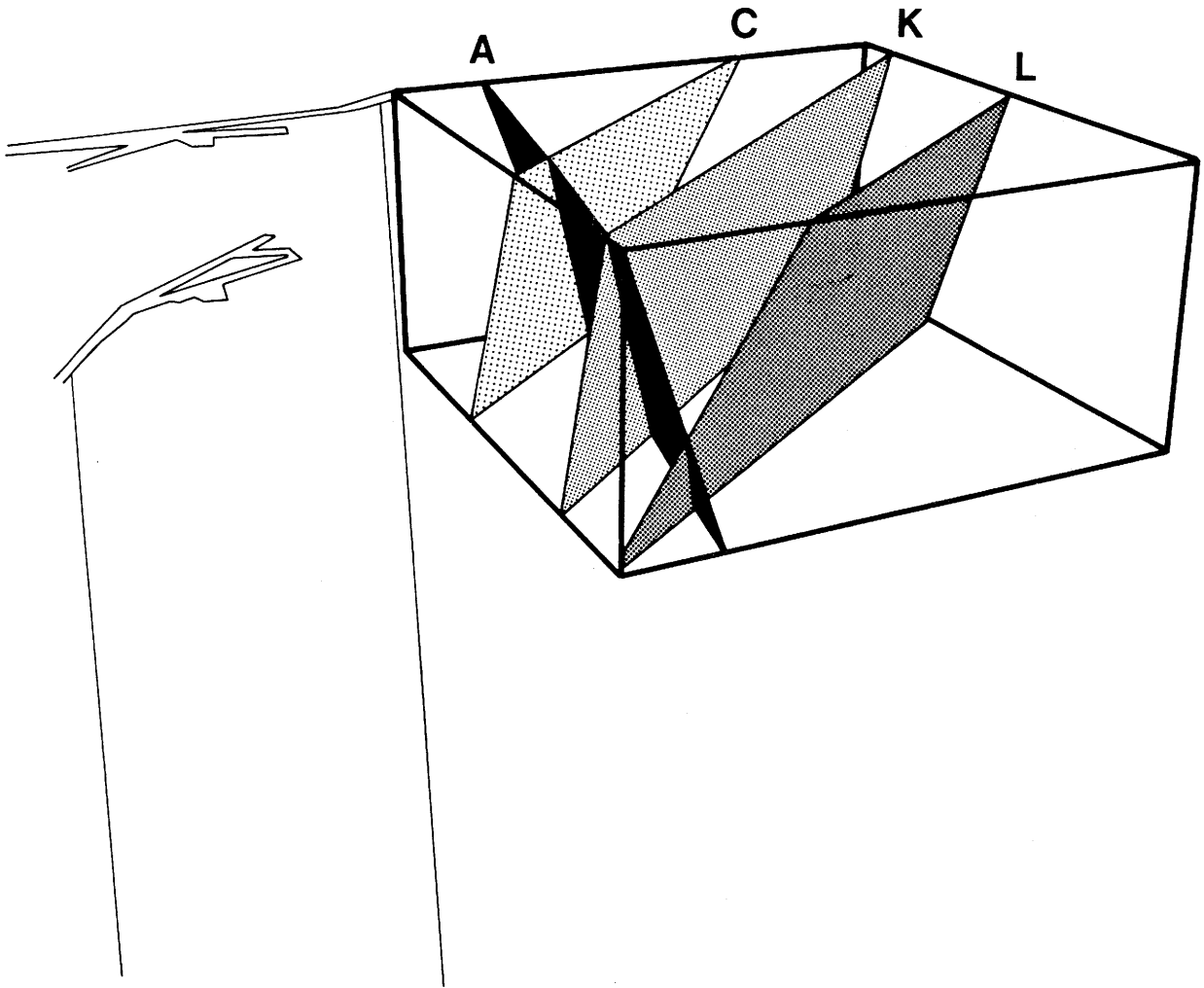


Figure 6.1 The basic model of the Crosshole site showing the four major fracture zones.

Zone C

Zone C is clearly seen from all boreholes as a very strong reflector; it is exceptional because reflections take place from both sides of the fracture plane with similar strength while usually one side tends to dominate. Zone C is seen as one unit in F5 and F6 but in the remaining boreholes it appears to have split into two fracture planes which are close in space but differ by about 10 degrees in direction. The weaker reflector of the two planes was named C2.

The apparent thickness of zone C is nearly 10 m which compares well with the size determined from the resistivity log. The resistivity values have also been used to estimate the radar reflection coefficient and the measured and calculated values agree fairly well (they are on the order of a few percent). Zone C appears very clearly in the radar tomograms. There is an interesting broadening of the zone between the boreholes confirming that fracture zones are rarely the simple planes one often visualizes. This broadening appears in several independent tomograms and it must thus be considered to be real. A broadening of zone C corresponding to the assumed bifurcation can also be noticed near borehole F1 in the tomograms. Zone C is difficult to observe as a crosshole reflection, since due to its central position in the measured volume the reflected pulse is often very close to the directly propagated pulse.

Zone K

Zone K is more difficult to correlate than the previous zone C because of its variable appearance in the different boreholes. It is most prominent in F4 and F6 but even in these measurements it is observed that the reflections are strongest some distance away from the boreholes. The reflections are mostly weak when seen from the other boreholes although the reflecting areas are not too distant from each other. On the other hand zone K is clearly seen in some of the radar tomograms but in this case also the appearance of zone K fluctuates considerably. It appears to consist of several "spots" linked together by weakly fractured areas. Zone K is occasionally observed as a crosshole reflection.

Zone L

Zone L is only observed as a strong reflector far out in some boreholes. It is therefore less well established than the previous zones. The

reflections are very strong and indicate an intensely fractured zone nearly parallel to C and K. Zone L is outside the area covered by the radar tomograms and is not seen as a crosshole reflection.

The drift

The drift passing through the measurement volume is a very good reflector of radar pulses. It also affects the water flow and must thus be included in the basic model of the Crosshole site. The drift is orthogonal to most boreholes so the drift behaves almost like a point reflector in reflection measurements: most of the energy is scattered from the point closest to the boreholes. The drift is clearly seen in the tomograms based on attenuation data. Since the scattered energy is removed from the pulse the tunnel appears as an area of increased attenuation. On the other hand the drift is hardly seen in tomograms using the time delay of the pulse as the early arrival caused by the drift is not registered by the algorithm used for extracting the travel times.

6.3 GEOMETRICAL DESCRIPTION OF ALL ZONES

The fracture zones can both reflect and attenuate the radar waves and their existence is inferred from a combination of data derived from many radar measurements. One must therefore consider carefully how well a particular zone can be identified and its position defined. This question is simplest to answer when the existence of the zone is supported both by tomograms and reflection measurements. Tomograms provide a direct picture of the zone while reflection data must at present be combined with other data to determine the position of the zone. There is however much more reflection data available than fracture zones reliably identified in tomograms and many zones can therefore only be defined as reflectors.

In the following a list is given of all fracture zones identified in the Crosshole site. The existence of the major zones near the site is beyond doubt: these zones are the Site zone and the zones A and C previously described. The following zones, E, F and K, are well established but they are so close to each other in some boreholes that it is quite possible that some reflections have been mixed up. The resulting orientation would not be much affected by such an error since it is determined as a weighted sum of all angles and intersection points. This is the reason why the interpretation becomes particularly complicated if

the zone is missing in some boreholes as seems to be the case with zone B. It is very difficult to separate such cases from those where a fracture zone has been incorrectly identified: zone K shows this erratic behaviour in some boreholes.

It is good strategy to use the strength of the reflected pulse to identify the zones but since the reflection coefficient seems to vary one should also try to see if the pattern persists at large range from the borehole, since a strong fracture zone may well show up in this way. It is interesting to discuss in this context a weak fracture zone called unit 1 found near the site in the core maps. Its orientation agrees with C, K and L but only few and very weak indications of this zone have been found in the radar pictures. It is particularly interesting that unit 1 shows a higher degree of fracturing than for example zone AX which is seen as a weak but clear reflector in the radar maps. On the other hand the resistivity logs show that only zone AX contains large variations in electric properties (Carlsten, Magnusson and Olsson, 1985). Thus as has often been noticed fracturing does not in itself identify a fracture zone.

The tomograms are useful in determining the orientations since some of the zones are clearly visible there, for example zones C and K. One can not expect perfect agreement between tomograms and reflection measurements results since the former measure the electrical properties directly while reflections are caused by the gradient of these properties. The precision of the tomograms is often surprising: the broadening of zone C is for example confirmed in several sections. The tomograms have been combined in a transparent three dimensional model of the investigated volume which can be used to check that zones observed in one tomogram really agree with those found for other borehole combinations.

The correlation between boreholes is difficult to establish at great depth since the distances between the boreholes are then large and the plane model of a zone becomes uncertain. However the strongly reflecting zones G and L seem to be rather well correlated though they can not be seen in all boreholes.

When these zones have been determined there remain only a few strong unidentified reflectors, though the radar maps still contain a large number of weak reflectors that have not been analyzed. The identified zones fall into two groups, which both have a NE strike but dip in opposite directions (see Figure 1.3): the first group consists of the

Site zone, A, E, F and G while the second contains unit 1, AX, C1, C2, K and L, where C2 is assumed to have bifurcated from C. It may be asked whether this fracture system is the only major feature of the investigated rock volume or if the borehole logging and the radar measurements tend to favour the detection of zones which run at about 45° to the boreholes. This is however not likely since there are comparatively more large angles in F6, the borehole which deviates most from the others, and this rather suggests that there actually exist favoured orientations of the fracture zones as predicted both by theory and previous experience.

The radar is not very sensitive to zones orthogonal to the boreholes and the angles are then difficult to measure with any precision. A special effort to look for zones that run parallel to the boreholes resulted in some possibilities. Such reflections are difficult to recognize and the intersection points become so uncertain that the determination of such zones is much less convincing than for those previously mentioned. They have consequently been omitted from this discussion.

The zones discovered during the radar work are listed below with a brief description of their characteristics. Definite values have been selected for each intersection point and intersection angle neglecting the variation between measurements at different frequencies, the angles measured from each side of the pattern, etc. The calculated orientations are also compared with those previously obtained by correlating geophysical and core data (Carlsten, Magnusson and Olsson, 1985).

Site zone

This zone passes directly through the crosshole site where it can be studied in detail. It is 10-20 cm thick and its observed orientation in the site agrees with the orientation obtained from the following radar data. The plot showing how the orientation of the zone is determined from the radar angles is displayed in Figure 6.2.

Borehole	Depth	Radar angle
E1	-10	45
F1	-5	45
F2	-5	43
F3	-5	51
F4	-5	40
F5	-5	61
F6	-4	30
Orientation Radar	Dip 72	Strike 40

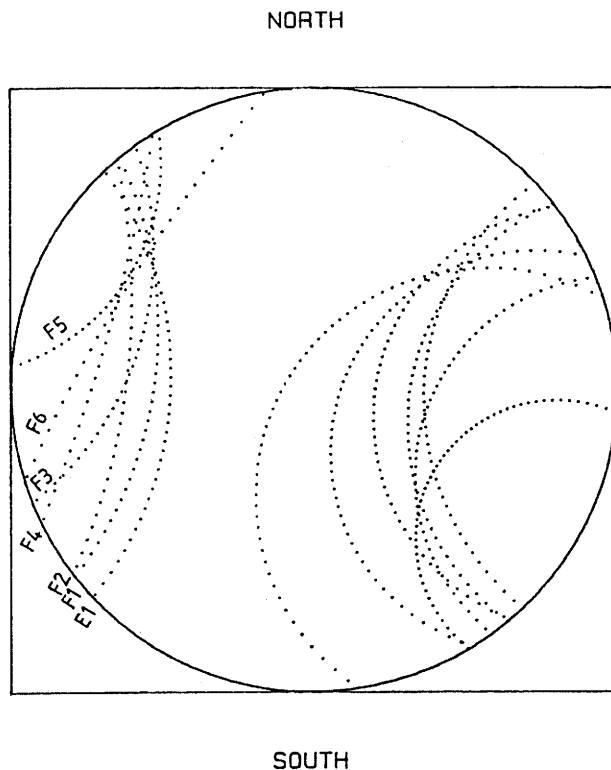


Figure 6.2 Wulff plot of the orientation of the Site zone determined by the radar angles.

Zone A

The orientation of this zone is well determined since it is quite close to the site. The reflections appear to be rather complex and possibly A intersects some other zone. There are two possible reflections in F1 and it is difficult to say which one fits best with the remaining data. A detailed description of how the orientation was determined can be found in Section 4.5. The corresponding plots are repeated for completeness in Figure 6.3. Zone A is also seen in the crosshole reflections as described in Section 5.3.

Borehole	Depth	Radar angle
E1	35	42 (47)
F1	39	48
F2	43	41
F3	39	54
F4	54	40
F5	36	62
F6	71	33
Orientation Radar	Dip 70	Strike 35
Core map	66	5

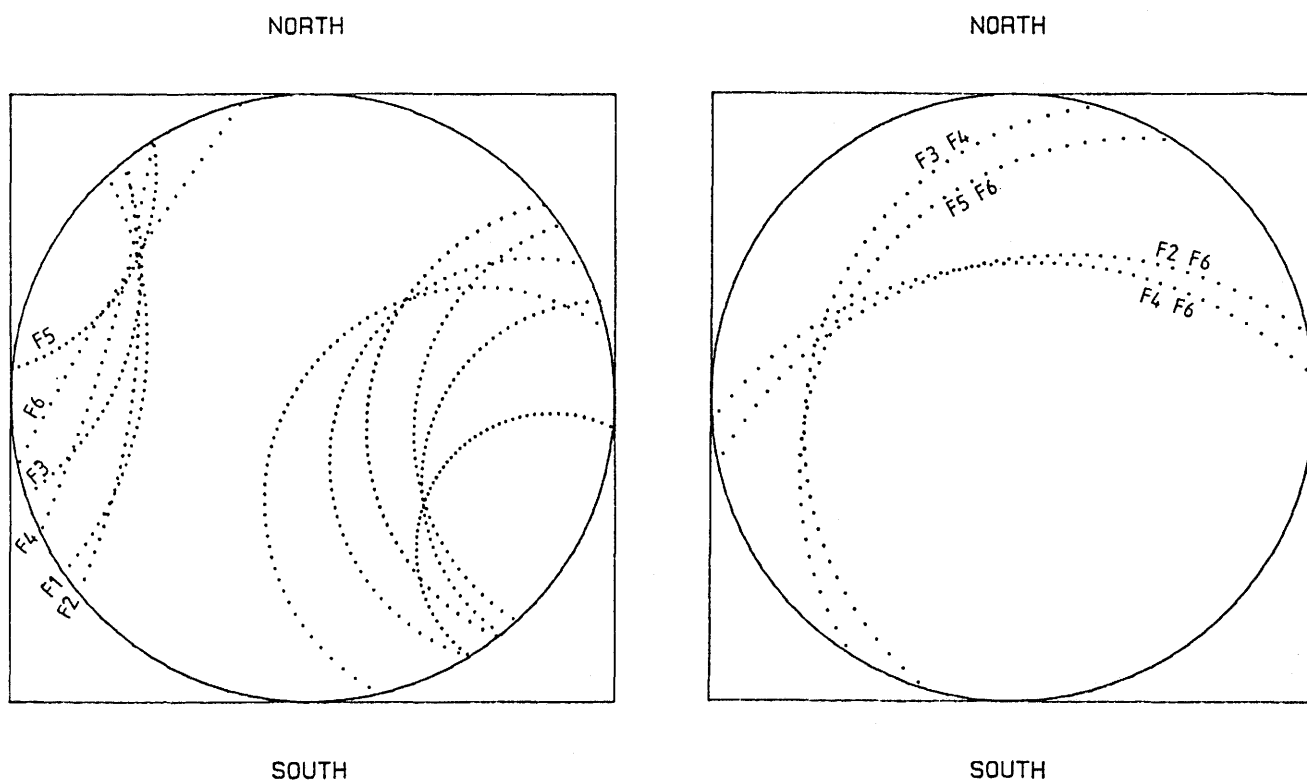


Figure 6.3 Wulff plot of the orientation of zone A determined by the radar angles and by the intersections with the boreholes.

Zone AX

This is a rather weak zone. In some boreholes very little is seen, in particular from F5 which is almost perpendicular to the assumed orientation.

Borehole	Depth	Radar angle
E1	66	52
F1	66	50
F2	65	52
F3	56	57
F4	63	53
F5	missing	
F6	68	45
Orientation	Dip	Strike
Radar	89	231

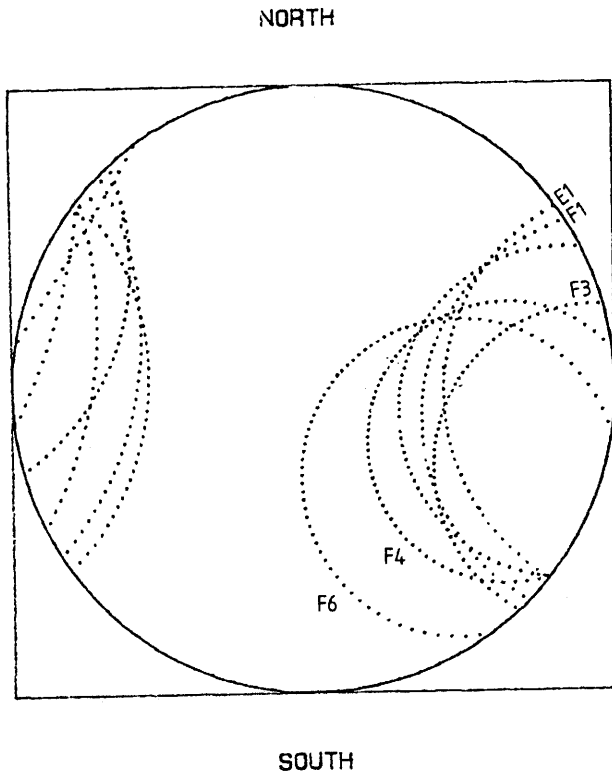


Figure 6.4 Wulff plot of the orientation of zone AX determined by the radar angles.

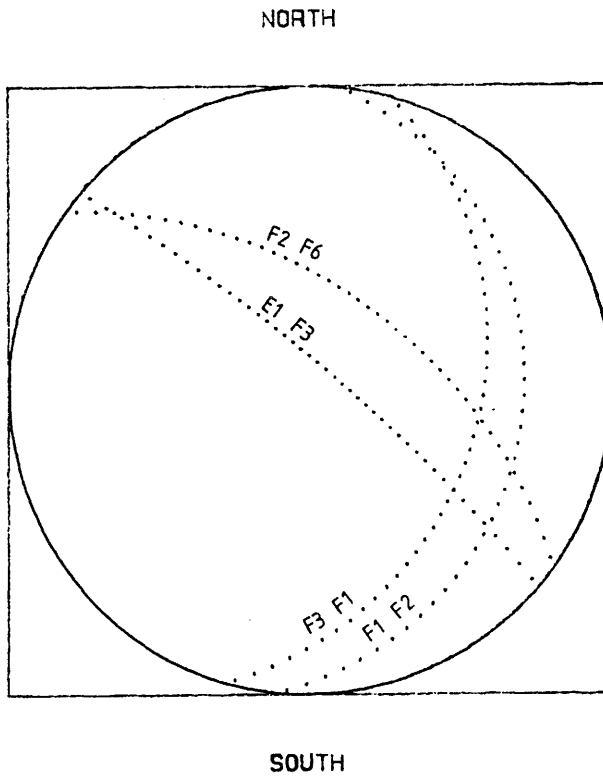


Figure 6.5 Wulff plot of the orientation of zone AX determined by the intersections with the boreholes.

Zone B

This zone is characterised by its high porosity and it differs considerably from the other zones. It is more prominent in the geological record than in the radar picture where only weak reflections can be observed. The zone only extends a short distance: it is observed in the cores only in F1 and F2 while it is also seen in E1 and F3 in the radar measurements. It is possible to obtain a good fit using the radar observations but the choice of data is somewhat arbitrary since there appears to be a group of parallel weak reflections in this section of the boreholes. It is doubtful whether the existence of the zone could have been deduced from the radar data alone considering that the zone is not seen in all boreholes. The plots used to determine the orientation are in Figures 6.6 and 6.7.

Borehole	Depth	Radar angle
E1	98	43
F1	92	49
F2	103	48
F3	85	55
Orientation	Dip	Strike
Radar	75	40

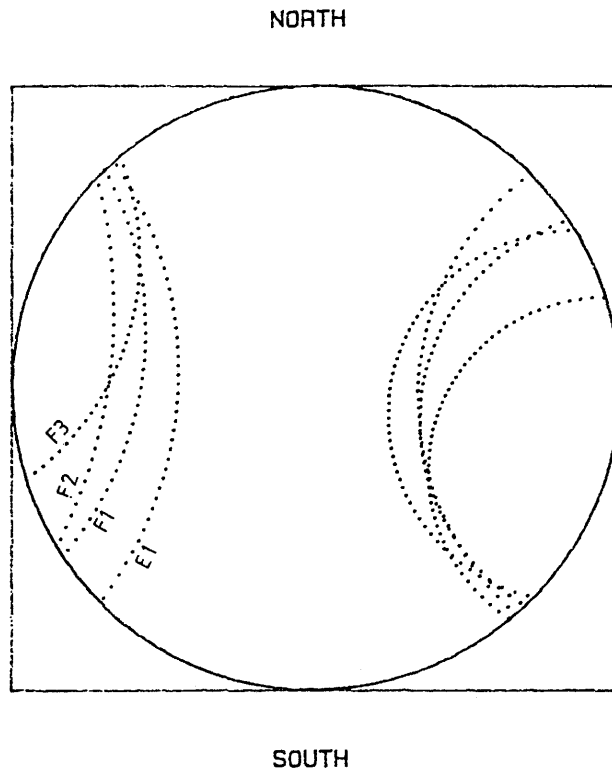


Figure 6.6 Wulff plot of the orientation of zone B determined by the radar angles.

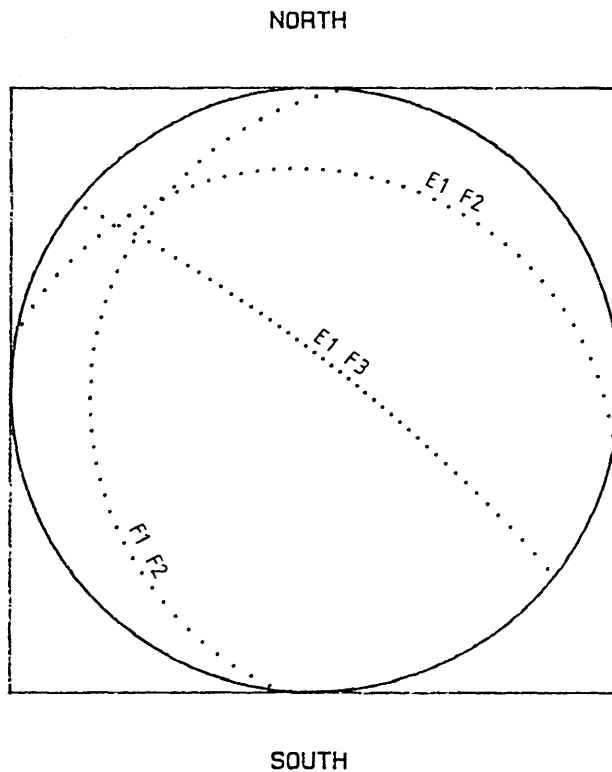


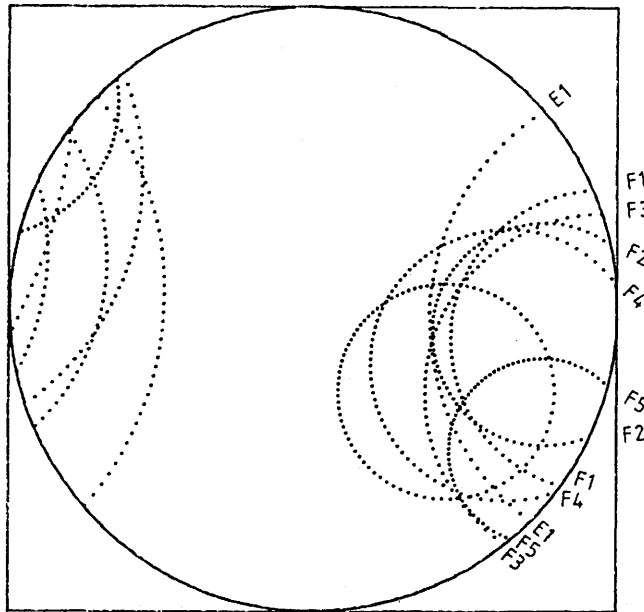
Figure 6.7 Wulff plot of the orientation of zone B determined by the intersections with the boreholes.

Zone C1

This zone is very prominent in all boreholes. Its width is judged to be about 8 m from the radar measurements in good agreement with the geophysical logging results. The zone appears to be split in some way and presently this is thought to be a bifurcation occurring after the zone has passed F5 and F6. The bifurcated zone is called C2 (see below). The curves do not intersect as exactly as was expected considering that the identity of the zone is undoubted. The diagrams displayed in Figures 6.8 and 6.9 give a good determination but some of the angles are in poor agreement with the resulting orientation. Zone C1 is seen in the crosshole reflection measurements but is so close to the direct pulse that the pulses become difficult to separate. The zone appears in the correct position in the tomograms. It is particularly interesting that a broadening of the zone can be observed in several tomograms, e.g. Figures 5.8 and 5.10.

Borehole	Depth	Radar angle
E1	130	47
F1	118	59
F2	119	63
F3	107	54
F4	108	54
F5	93	70
F6	111	58
Orientation	Dip	Strike
Radar	80	223
Core map	75	227

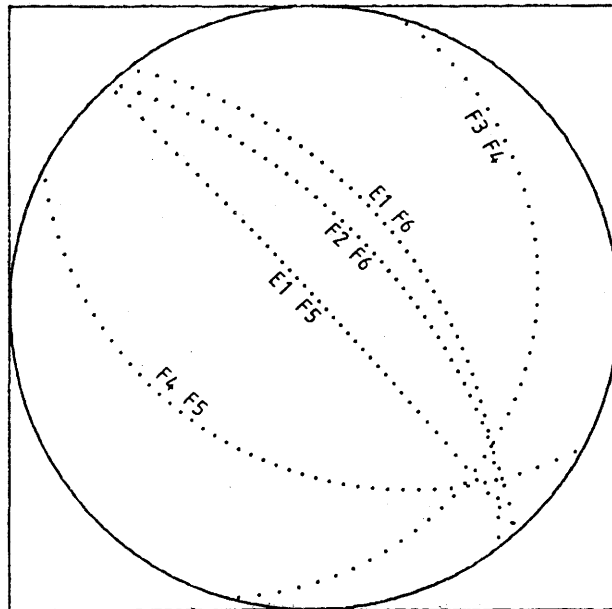
NORTH



SOUTH

Figure 6.8 Wulff plot of the orientation of zone C1 determined by the radar angles.

NORTH



SOUTH

Figure 6.9 Wulff plot of the orientation of zone C1 determined by the intersections with the boreholes.

Zone C2

This zone is clearly visible as a strong companion to zone C in several boreholes. It is presently assumed that zone C2 has bifurcated from zone C1. The intersection of two zones is one possible explanation of the broadening of zone C1 observed in the tomograms 5.8 and 5.10. The curves intersect much better than for zone C1. The angles displayed in Figure 6.10 do not provide much information since there are no reflections seen in F5 and F6. These boreholes tend to be most useful since they differ in direction from the other ones. The plots used to determine the orientation are shown in Figures 6.10 and 6.11.

Borehole	Depth	Radar angle
E1	144	40
F1	124	42
F2	115	45
F3	105	43
F4	93	55
F5	missing	
F6	missing	

Orientation	Dip	Strike
Radar	64	237

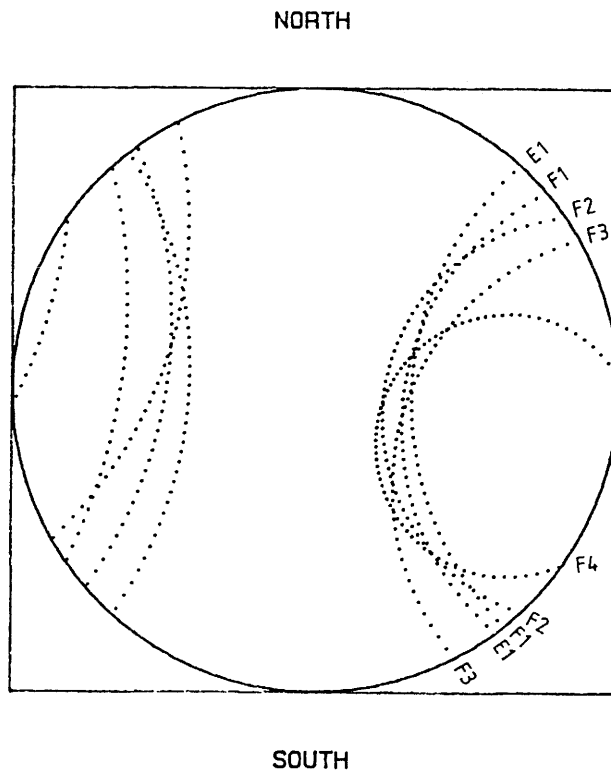


Figure 6.10 Wulff plot of the orientation of zone C2 determined by the radar angles.

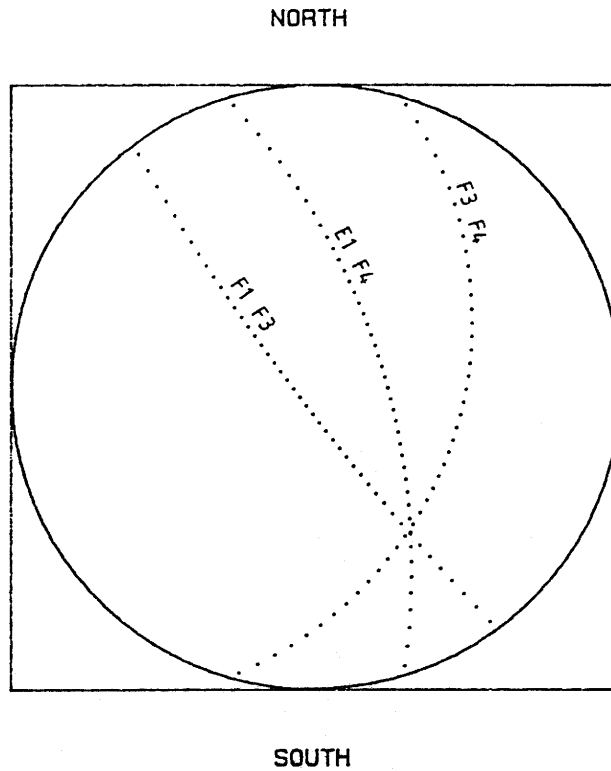


Figure 6.11 Wulff plot of the orientation of zone C2 determined by the intersections with the boreholes.

Zone E

This zone is often clear in the reflections but difficult to see in the tomograms. It is however almost outside the area covered by the tomograms. The position in borehole F5 is uncertain. Zone E is also observed as a crosshole reflection (see section 5.3). The plots used to determine the orientation are displayed in Figures 6.12 and 6.13.

Borehole	Depth	Radar angle
E1	170	47
F1	171	42
F2	207	39
F3	153	42
F4	234	34
F5	150	55
F6	270	27

Orientation	Dip	Strike
Radar	62	42
Core map	67	39

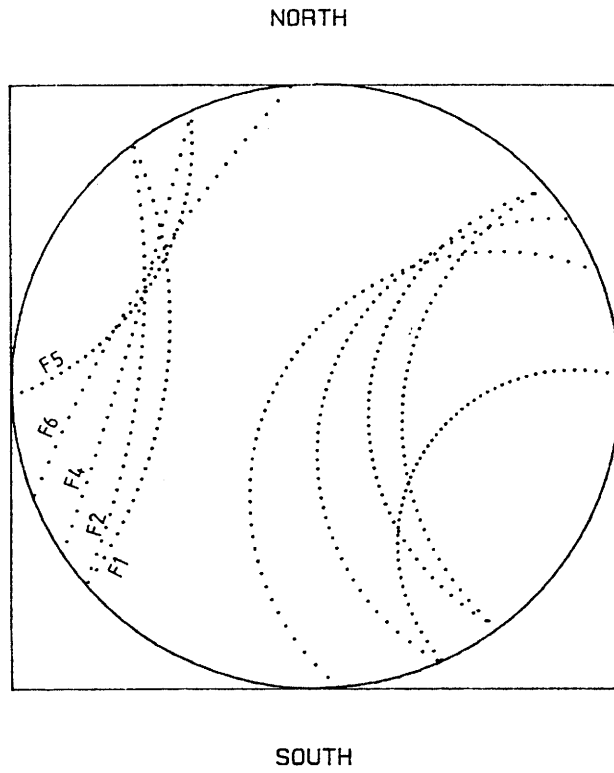


Figure 6.12 Wulff plot of the orientation of zone E determined by the radar angles.

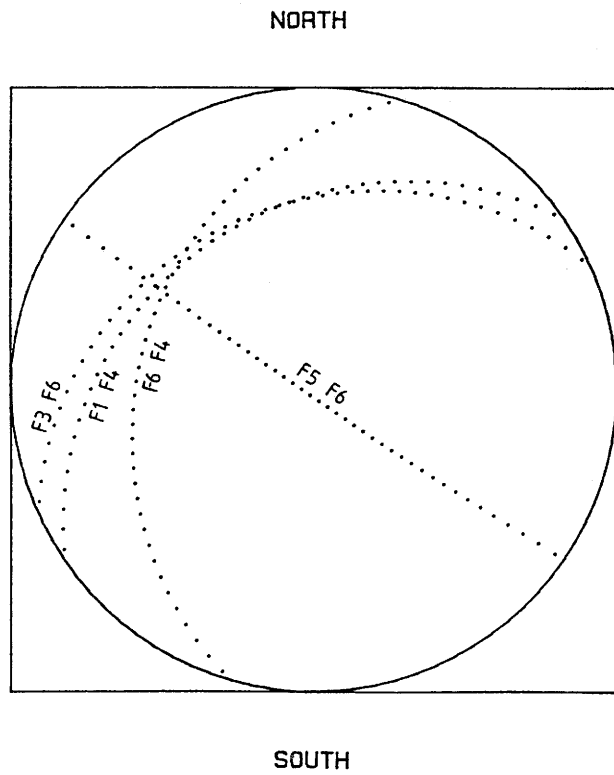


Figure 6.13 Wulff plot of the orientation of zone E determined by the intersections with the boreholes.

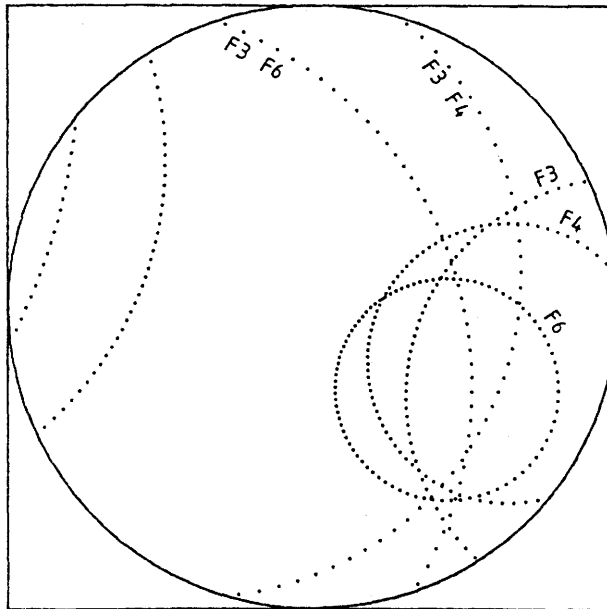
Zone K

The geological investigation revealed a strongly fractured zone around 170 m in F4. This zone lacked an obvious extension to the other boreholes. It is clearly seen in the radar map from F4 and appears to have a strongly varying reflection coefficient. It is also seen in the tomographic model though the orientation is a bit doubtful since the zone gets mixed up with the tunnel (Figure 5.8).

A good intersection is obtained from the strong reflections in F4 and F6 and it is confirmed by data from F3 (Figure 6.14). The zone is not strongly reflecting in all boreholes and the drift tends to obscure the reflections in some cases. Further candidates can however be found in F2 and F5 (Figure 6.15) and also in F1 and E1 (Figure 6.16). In the second case the intersection angles appear to be too large but no other suitable candidates were found. This may be due to a real bending of the zone or simply that the K zone disappears and some other zone has been included in the data.

Borehole	Depth	Radar angle
E1	223	55
F1	192	55
F2	187	45
F3	172	48
F4	169	54
F5	155	60
F6	162	57
Orientation	Dip	Strike
Radar	78	230

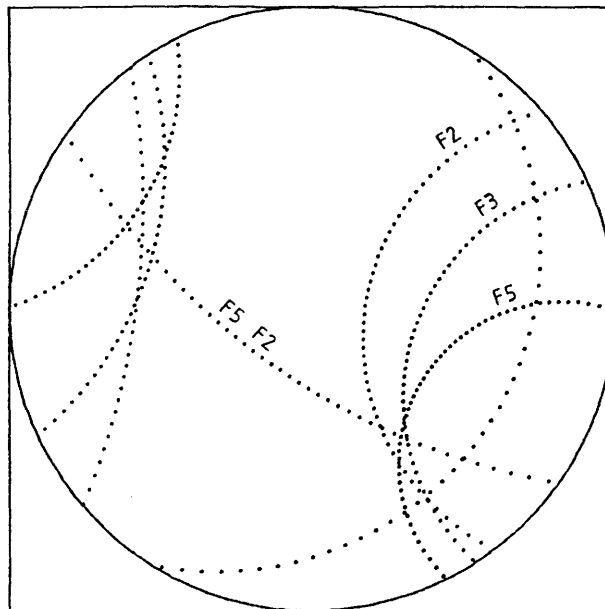
NORTH



SOUTH

Figure 6.14 Wulff plot of the orientation of zone K determined by the radar angles and borehole intersections in F3, F4 and F6.

NORTH



SOUTH

Figure 6.15 Wulff plot of the orientation of zone K determined by the radar angles and borehole intersections in F2 and F5.

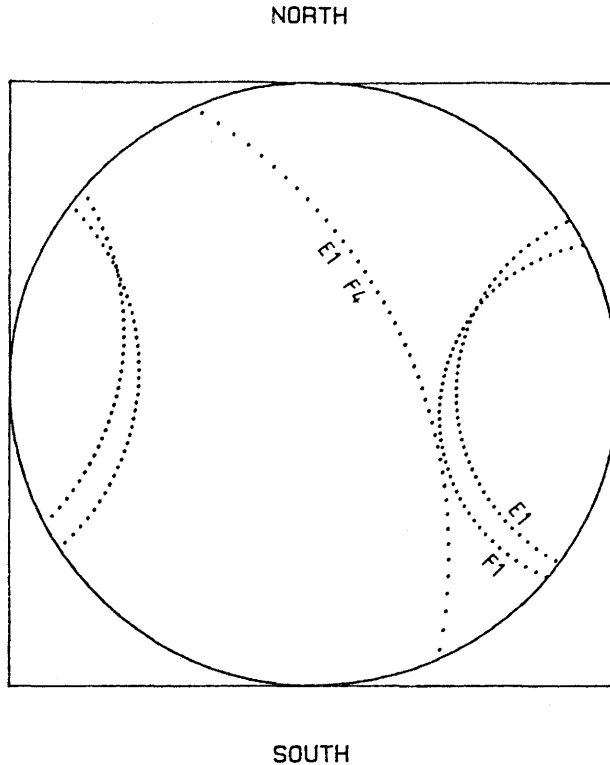


Figure 6.16 Wulff plot of the orientation of zone K determined by the radar angles and borehole intersections in F1 and E1.

Zone F

There is a large number of reflections near the ends of the boreholes indicating a generally fractured part of the rock. Since there are many zones it becomes rather difficult to correlate them. As in the other cases the candidates for zone F do not intersect perfectly but give a reasonable determination of the orientation of the zone as seen in Figures 6.17 and 6.18. This means that there may be confusion with the neighbouring zones, in particular E and K; there is not always sufficient reason to choose either interpretation presently so the curves for F5 are displayed separately in Figure 6.19. The scatter among the possible orientations is also slightly greater in the correlation of zone F than for the previous zones. Unfortunately zone F is just outside the volume covered by the tomograms.

Borehole	Depth	Radar angle
E1	195	43
F1	235	37
F2	229	37
F3	154	51
F4	258	43
F5	173	50
F6	not seen	

Orientation	Dip	Strike
Radar	55	50

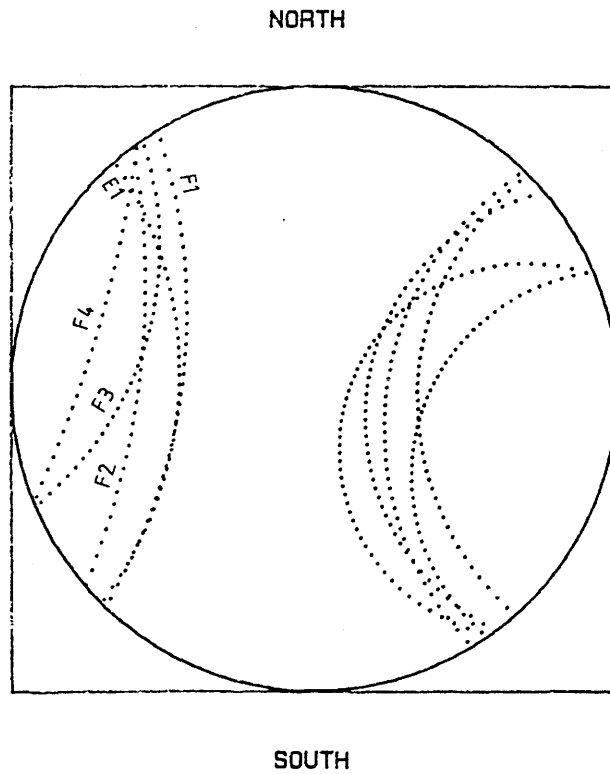


Figure 6.17 Wulff plot of the orientation of zone F determined by the radar angles.

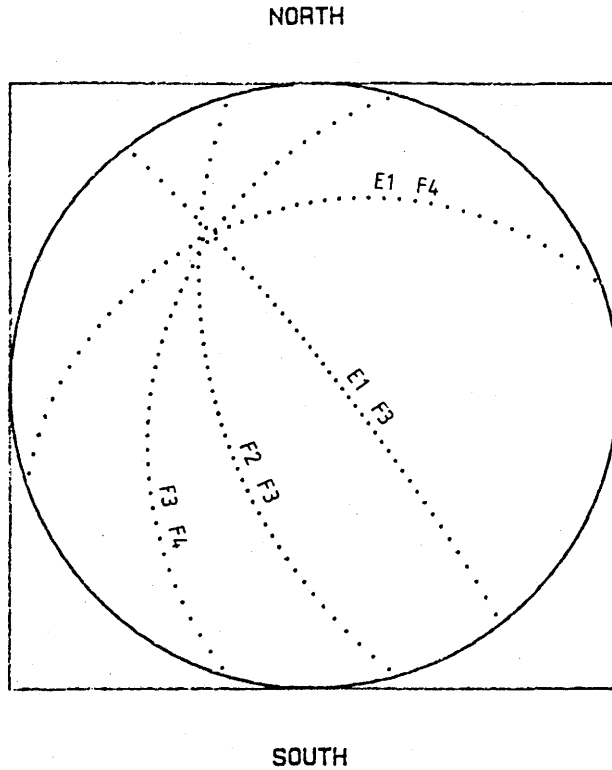


Figure 6.18 Wulff plot of the orientation of zone F determined by the intersections with the boreholes.

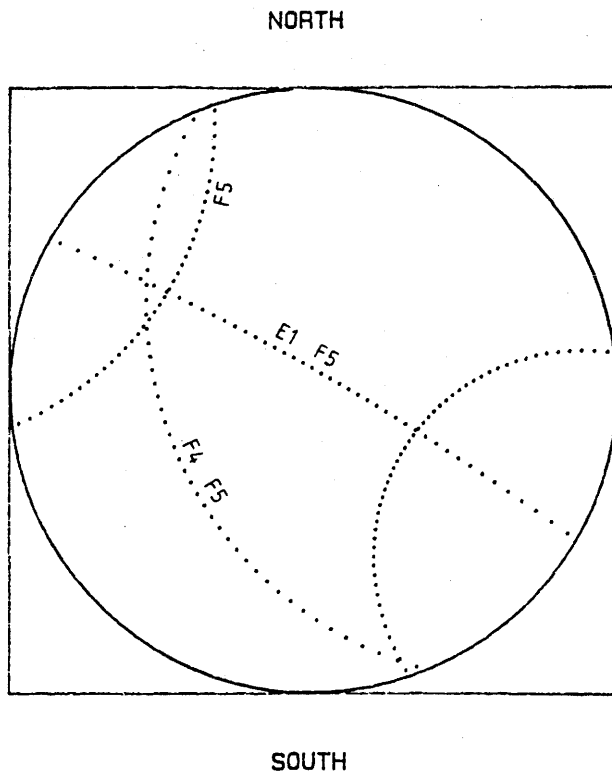


Figure 6.19 Wulff plot of the orientation of zone K determined by the radar angles and borehole intersections of borehole F5.

Zone G

Near the ends of the long boreholes there are some strong reflections which can sometimes be grouped together. Only five boreholes are involved in zone G and some reflections are very far out in the boreholes. In F3 for example the best fit is obtained if we select a reflection which is seen only at large range but appears to be very persistent. These data led to the candidate in F1 which is also hardly seen but fits very well with the intersections. This is a strong reflector which agrees with the character of zone G in the other boreholes. At these large distances one should however not be too impressed by a good intersection since it is often possible to find alternative candidates and the scatter of the possible orientations of known zones is often large as seen in the previous examples. The plots used to determine the orientation are in Figures 6.20 and 6.21.

Borehole	Depth	Radar angle
E1	230	50
F1	235	37
F2	310	30
F3	220	50
F4	too far out to be seen	
F5	280	43
F6	to far out to be seen	
Orientation	Dip	Strike
Radar	50	6

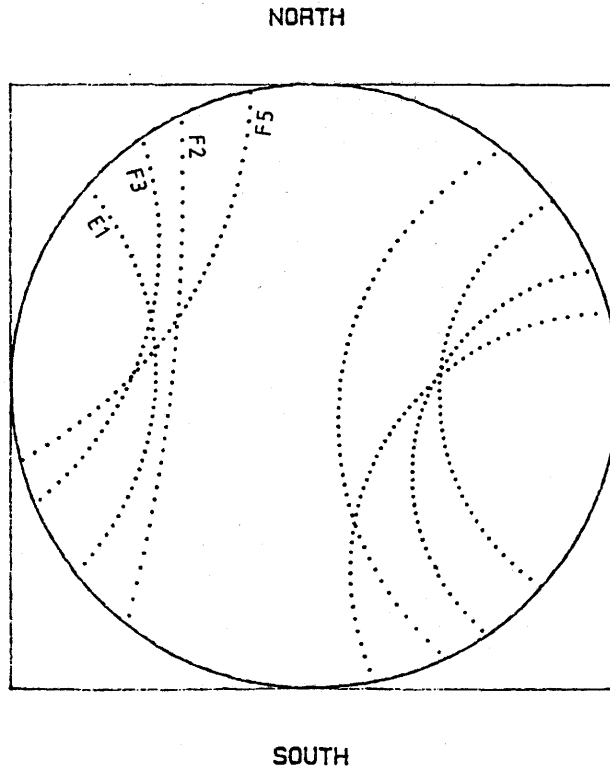


Figure 6.20 Wulff plot of the orientation of zone G determined by the radar angles.

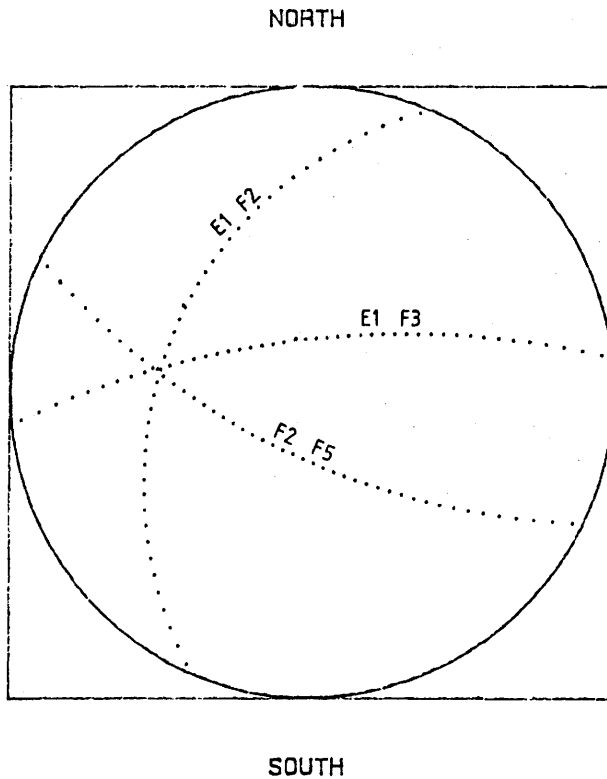


Figure 6.21 Wulff plot of the orientation of zone G determined by the intersections with the boreholes.

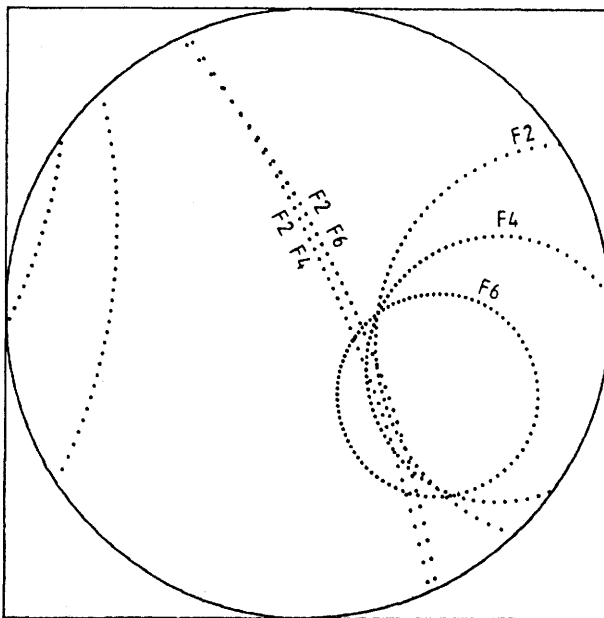
Zone L

This zone is prominent and it is also of great importance since it may explain the main flow of water between the boreholes. Heads are very low near some of the intersection points ascribed to this zone. It appears near the end of the boreholes and consequently the correlation between the boreholes becomes uncertain. It is only seen in the long boreholes and even then only F4 and F6 actually intersect the zone: the other data must be determined by extending the reflections until they intersect the extension of the borehole.

There appears an ambiguity when the candidates from F2, F4 and F6 are combined: two possible intersections occur as seen in Figure 6.22. A fourth candidate was found at the very end of the radar map of borehole E1 but that candidate has the same ambiguity (Figure 6.23). Still when the diagrams are combined the steeply inclined zone appears to be the more likely candidate. The orientation then agrees with zone C. Furthermore with that orientation zone L becomes a candidate for the extremely fractured zone that intersects borehole V1 near the bottom at 475 m depth.

Borehole	Depth	Radar angle
E1	330	37
F1	280	27
		not very good fit; difficult to read
F2	271	46
F3	zone too far out (250 m)	
F4	234	55
F5	far out, possible candidates around	210
F6	205	60
Orientation	Dip	Strike
Radar	67	236

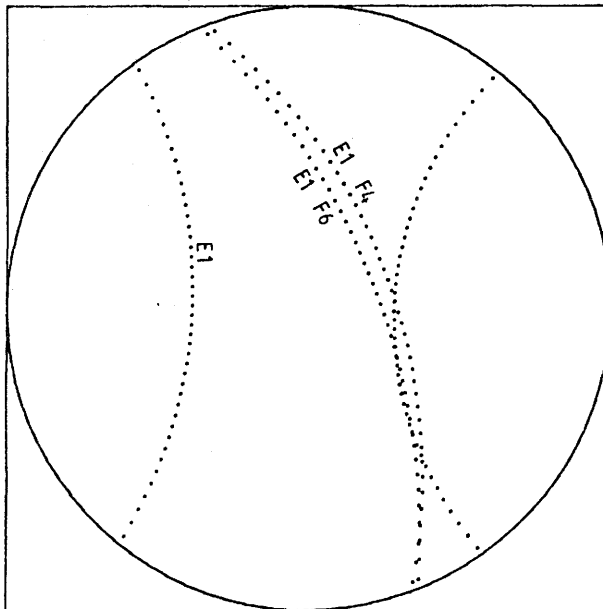
NORTH



SOUTH

Figure 6.22 Wulff plot of the orientation of zone L determined by the radar angles and borehole intersections in F2, F4 and F6.

NORTH



SOUTH

Figure 6.23 Wulff plot of the orientation of zone L determined by the radar angles and borehole intersections of borehole E1.

Borehole	Depth	Radar angle
E1	42	42
F1	39	37
F2	missing	
F3	32	28
F4	200	13
F5	80	23
F6	missing	

Orientation	Dip	Strike
Radar	50	345

DISCUSSION AND CONCLUSIONS

7.1 THE BOREHOLE RADAR SYSTEM

The radar development within the Stripa Project has shown that radar waves can be detected after propagating considerable distances through granitic rock. The radar waves contain information which can successfully be used to characterize the inhomogeneities of a rock mass. The radar method combines a resolution on the order of meters with investigation ranges on the order of hundreds of meters. This makes the radar a unique instrument for rock characterization.

The attenuation of radar waves propagating in rock is significant and increases with frequency. At Stripa radar probing ranges of 300 m have been obtained in crosshole configurations while reflections have been observed at ranges up to 115 m in single hole measurements. These ranges were obtained at a center frequency of 22 MHz where the attenuation of the Stripa granite is approximately 28 dB/100 m. This value of the attenuation implies that the wave loses half its energy for every 10 m of propagation. Thus the signal energy decreases very rapidly but the radar system developed within the Stripa project can still achieve considerable probing ranges. At the frequency 60 MHz the attenuation is about 45 dB/100 m which causes a reduction in radar range to about half the value at 22 MHz.

Since the radar waves decay exponentially a significant increase in radar power output is required to obtain any substantial increase in range. For example a doubling of the output energy will only increase the crosshole range 10 m and the single hole radar range by 5 m. The efforts required to increase the energy output would be substantial while the improvements in the radar results may be comparatively small.

The resolution attainable with the borehole radar is on the order of the wavelength used, about 2 m or 6 m for the frequencies 60 MHz and 22 MHz, respectively. The condition for detection of an anomalous object in the rock can not be defined in detail but some general guidelines can be formulated. As a general rule the object should have at least one length dimension which is on the order of the wavelength. For example thin tubular

structures such as a water filled borehole have been clearly identified at distances more than 30 m from the borehole in which the measurement was made. Experience from the Crosshole site has shown that a fracture zone a few tens of cm thick is sufficient to create a well defined reflection.

Measurements on core samples have shown that the electrical properties of fracture zones are anomalous in the frequency range used for radar work. The fracturing of the rock causes an increase in porosity both because of the presence of the actual fractures and increased microfracturing. The increased water content in the fracture zones leads to a higher dielectric constant and electric conductivity than in the surrounding rock. The variations of these properties which have been observed on core samples also appear during in situ measurements where they result in reduced velocity and increased attenuation of the radar waves. In a granitic rock like the Stripa granite with a negligible content of conducting minerals it appears that the radar response is closely linked to the water content of the rock.

The radar system developed as a part of the Stripa project has been made sufficiently flexible to allow it to be used in several investigation modes. These modes are: single hole reflection, crosshole reflection, and crosshole tomography. All three modes have been used successfully in the characterization of the special test site of the Crosshole Program prepared in the Stripa mine.

7.2 REFLECTION MEASUREMENTS

The single hole measurements provide a possibility to see geological structures outside the borehole. A drawback of the single hole measurements is the axial symmetry of the antennas. The three-dimensional geometry of the real world is then reduced to a two-dimensional representation or map. The information obtained from such a map is the angle of intersection between fracture planes and the borehole and the distance to objects from the borehole. It is also possible to observe variations in the fracture properties as the fracture extend out from the borehole or if there are faults or other discontinuities in the zones.

The two-dimensional representation provided by the single hole measurements is a serious drawback since it becomes impossible to answer directly the main question of interest: what is the exact location and orientation of the fracture zone? The answer can be obtained through measurements in at least two adjacent boreholes. A procedure for

analysis of reflection measurements in adjacent holes has been developed and successfully applied to the radar results from Stripa. The intersection angles for a specific zone are determined in the different boreholes and the possible orientations of the plane are represented in a Wulff projection. In this representation there will be an intersection point representing the orientation of the fracture plane uniquely. The critical step in this interpretation procedure is the identification of the zone in the respective boreholes. The problem is to assure that it is data from one and the same zone that is used in the analysis. If the distance between the holes is small one can be reasonably sure that this is the case but as the distance between the holes increases the assumption becomes less reliable.

The single hole measurements give a distorted image of the structures in the rock. For example, points appear as hyperbolas and the angle at which a plane intersects the borehole is not the true angle. A radar image may however be transformed so that the image becomes geometrically correct. Such a transformation can be made through procedures similar to seismic migration or inversion schemes similar to those used for synthetic aperture radar. In this way it might be possible to extract in the future much information that is now hidden in the data.

The value of the single hole reflection data would increase considerably if the antennas were directional and the orientation of a fracture zone could be determined uniquely from measurements in a single hole. Such a development is feasible and has been included in the Phase 3 of the Stripa Project which was started late 1986.

The crosshole reflection measurements give data similar to those obtained from single hole measurements. The source-receiver geometry is however quite different and consequently the geometrical information contained in the data will be different also. A set of crosshole measurements made between two holes will give a data set which can be used to determine uniquely the orientation of a fracture plane. One requirement for the uniqueness is that the boreholes are not located in the same plane. In such cases there will be a reflection symmetry in the plane spanned by the boreholes and there will appear an ambiguity between two possible orientations of the plane. If the number of crosshole scans is sufficiently large there is usually no problem in identifying the same fracture plane in the different scans. A problem with the crosshole reflection technique is that the distance travelled by a reflected pulse in a

crosshole configuration normally is larger than in a single hole configuration and the magnitude of the reflections is thus much smaller and the zones may be difficult to identify. Image processing would be particularly useful in this case.

The crosshole reflection technique is very promising and the first steps towards the interpretation of such data has been taken within this project. Further development of the interpretation theory is required and more practical experience in interpreting this type of data must be obtained.

7.3 TOMOGRAPHY

The first arrival of the direct wave between transmitter and receiver in crosshole measurements can be used for tomographic analysis of travel times and amplitudes. The experience from Stripa has shown that good results can be obtained through tomographic inversion if the errors in the data set are kept small. The systematic errors are particularly significant since they will cause artifacts in the tomographic image. The methods for data collection used for tomographic inversion within the radar program have given good results for a reasonable effort. The measurements were made with high ray density which provides a redundant data set. The travel time and the amplitudes have been extracted from the recorded traces by an automatic routine. In about 5 to 10 % of the cases this routine generates erroneous values which have to be corrected or discarded. Experience has shown that it is more cost effective to discard the incorrect data rather than to go through a time consuming procedure to correct them. As the crosshole sections have been measured with a high ray density the loss of approximately 10 % of the rays has no severe effect on the resulting tomogram.

The tomographic inversion gives quantitative data on the variation of rock properties in the plane between the boreholes. The radar specifically gives data on the dielectric constant and attenuation which in granitic rock can be related to the water content (porosity). An advantage of tomography compared to reflection methods is that tomography gives data on the properties over a plane and the result thus directly gives information about the location of the anomalies. Another advantage is that tomography provides a quantitative estimate of the rock properties whereas the reflection essentially provides geometric information and qualitative information on the variation of properties. Tomography can only identify fracture

zones with a width of a few meters since it uses the average properties of the zones rather than the gradients measured by reflection methods.

The tomographic results obtained through inversion of radar data from the Crosshole site have generally been of good quality. The tomography has identified the major fracture zones and mapped their extent between the boreholes. The results also reveal that the zones often have a lateral variation in width and electric properties. Moreover, the tomograms give a consistent image of the geological structure of the Crosshole site. The results obtained through inversion of travel times and amplitudes are very similar and data from intersecting crosshole sections give similar results where the planes meet at the intersections.

There are a number of approximations involved in tomographic inversion. Some of them are of a conceptual nature and others mathematical. Further research should go into investigating these approximations to gain more knowledge about the validity of the results to determine when a tomographic analysis should be applied. Currently a tomographic survey and the subsequent data handling and inversion is a relatively time consuming and costly undertaking. Further development of equipment and processing schemes might reduce the costs considerably. Better algorithms for extracting travel times and amplitudes are also an integral part of such a development.

7.4 THE PROPERTIES OF FRACTURE ZONES

The radar results obtained at the Crosshole site at Stripa have provided a detailed three dimensional model of the site. This model is consistent with the geological data originally obtained to characterize the site (Carlsten, Magnusson, and Olsson, 1985). The original model of the site has of course been modified due to the greater capabilities of the radar method compared to the single hole methods but no contradictions have been observed between the radar model and the geological data. The radar responses are caused by fracture zones which are considered to be the main transport paths for groundwater and hence radioactive nuclides. Formulated loosely we may say that the radar maps the geological structure of the rock in three dimensions and it maps the features of interest as potential transport paths for radionuclides, i.e. the fracture zones.

It is not expected that the radar will provide quantitative data on the transport capacity of radionuclides for the fracture zones or even an

estimate of hydraulic conductivity. Such information must be obtained through independent measurements. It should be noticed that a hydraulic measurement hardly provides any geometric information at all and that it is difficult to interpret such measurements without geometric information. The radar can provide geometric information to the hydrogeologists and in that way open new possibilities for the understanding of groundwater flow through a fractured medium.

The radar also increases our understanding of the flow in individual fracture zones. For example, if the flow in a fracture zone is unevenly distributed, as there is presently reason to believe, this can be investigated by radar. The principle of such an experiment is to perform first a reference measurement with the radar and then inject a conductive tracer that will cause a change in the electric properties along the flow paths. Such experiments are currently being planned in some places including Stripa.

7.5 PROSPECTS FOR FUTURE WORK

The development of the borehole radar technique within the Stripa Project has resulted in a new investigation method which can be applied as a standard method in future site investigations. The radar is a unique instrument since it provides the possibility to obtain detailed information about the location of fracture zones and the variation in properties across their extent. The capabilities of the radar method suggests a revision of site investigation programs with respect to the number of holes to be drilled and the investigation methods to be applied in these holes.

The detailed information of the rock structure provided by the radar can also give a better understanding of the geological processes which generate fracture zones. There are also possibilities for investigating the transport of saline tracers through the rock and in this way study aspects of radio nuclide transport, e. g. channeling.

The borehole radar is a new technique where only the first and most basic applications have been developed and applied so far. Further development of equipment and interpretation techniques can greatly improve the precision in detecting and locating different features. An important step for the future is the development of directional antennas. There are also a wide range of new and so far untested applications for the radar.

ACKNOWLEDGEMENTS

The pioneering work on borehole radar in Sweden was performed by Bruno Nilsson, Boliden Mineral AB, and we greatly appreciate that he kindly shared his profound experience with us. The moral support and encouragement from the Stripa Project Management and the Technical Subgroup have been of great value to us. The assistance given by the personell at the Stripa Mine during the field experiments has been appreciated by the project group.

Georg Gabriel has provided invaluable assistance in the processing and filing of the enormous data sets that have been collected. Ulla Bergström and Annika Wettervik drew the figures. Margit Svensk typed the formulas and made the final editing.

REFERENCES

- Agmalm, G., 1985. Parametermätningar på borrhärneprover och jämförelse med borrhålsloggning från Stripa gruva. University of Luleå report 1985:020 E, Luleå, Sweden.
- Annan, A. P., Davis, J. L., 1976. Impulse radar sounding in permafrost. *Radio Science* 11, 383-394.
- Archie, G. E., 1942. The electrical resistivity log as an aid in determining some reservoir characteristics. *AIME Trans.* 146, 54-62.
- Brace, W. F., Orange, A. S., Madden, T. R., 1965. The effect of pressure on the electrical resistivity of water saturated crystalline rocks. *Journal of Geophysical Research*, 70 (22), 5669-5678.
- Brace, W. F., Orange, A. S., 1968. Electrical resistivity changes in saturated rocks during fracture and frictional sliding. *Journal of Geophysical Research*, 73 (4), 1433-1455.
- Bruggeman, D. A. G., 1935. Berechnung Verschiedener Physikalischer Konstanten von Heterogenen Substanzen. *Ann. Phys. Lpz.*, 24, 636-679.
- Carlsten, S., 1985. Hydrogeological and hydrochemical investigations in boreholes - compilation of geological data. Stripa Project IR-85-04, SKB, Stockholm, Sweden.
- Carlsten, S., Magnusson, K-Å, Olsson, O., 1985. Crosshole investigations - Description of the small scale site. Stripa Project, IR-85-05, SKB, Stockholm, Sweden.
- Cook, J. C., 1975. Radar transparencies of mine and tunnel rocks. *Geophysics*, 40, 865-886.
- Hanai, T., 1968. Electrical properties of emulsions. In "Emulsion science". P. Sherman, Ed. New York, Academic Press.
- Ivansson, S., 1984. Crosshole investigations - Tomography and its application to crosshole seismic measurements. Stripa Project, IR-84-08, SKB, Stockholm, Sweden.

Magnusson, K.-Å., Carlsten, S., Olsson, O., 1987. Crosshole investigations - Physical properties of core samples from borehole F1 and F2. Stripa Project, IR-87-10, SKB, Stockholm.

Nelson, P. H., Magnusson, K.-Å., Rachiele, R., 1982. Application of borehole geophysics at an experimental waste storage site. Geophysical Prospecting, 30, 910-934.

Nickel, H., Sender, F., Thierbach, R., Weichart, H., 1983. Exploring the interior of salt domes from boreholes. Geophysical Prospecting 31, 131-148.

Nilsson, B., 1978. Two topics in the electromagnetic radiation field prospecting. University of Luleå, Luleå, Sweden. PhD thesis 1978:03D.

Nilsson, B., 1983. A new borehole radar system. In "Borehole geophysics for mining and geotechnical applications". Geological Survey of Canada Paper 85-27, Ottawa, Canada.

Olsson, O., Sandberg, E., Nilsson, B., 1983. The use of Borehole radar for the detection of fractures in crystalline rock. Stripa Project, IR-83-06, SKB, Stockholm, Sweden.

Olsson, O. and Sandberg, E., 1984. Crosshole investigations - Preliminary design of a new borehole radar system. Stripa Project, IR-84-04, SKB, Stockholm, Sweden.

Sen, P. N., Scala, C., Cohen, M. H., 1981. A self-similar model for sedimentary rocks with application to the dielectric constant of fused glass beads. Geophysics, 46, 781-795.

Sherman, M. M., 1983. The determination of cementation exponents using high frequency dielectric measurements. The Log Analyst, November-December 1983.

Sundquist, H., 1985. Attenuation analysis and digital filtering of measurement data from a borehole radar. Uppsala University report UPTec 85124 E, Uppsala, Sweden.

Thierbach, R., 1974. Electromagnetic reflections in salt deposits. Journal of Geophysics 40, 633-637.

Ulriksen, C. P. F., 1982. Application of impulse radar to civil engineering. Lund University of Technology, Lund, Sweden. PhD thesis.

Unterberger, R. R., 1978. Radar propagation in rock salt. Geophysical prospecting 26, 312-328.

Wait, J. R., 1970. Electromagnetic waves in stratified media, 608 pp. Pergamon, New York.

Wollenberg, H., Flexer, S., Andersson, L., 1980. Petrology and radiogeology of the Stripa pluton. Lawrence Berkely Laboratory report BLB-11654, SAC-36, Berkeley, California, USA.

Wright, D. L., Watts, R. D., 1982. A single-hole, shortpulse radar system. In "Geophysical investigations in connection with geological disposal of radioactive waste", OECD/NEA, Ottawa, Canada.

Wu, T. T., King, R. W. P., 1965. The cylindrical antenna with nonreflecting resistive loading. IEEE transactions on antennas and propagation AP-13, 369-373.

APPENDIX A
RESULTS FROM SINGLE HOLE REFLECTION
MEASUREMENTS AT THE STRIPA MINE

Borehole E1

Figure A.1 Radar reflection map from the borehole E1 at the Cross-hole site in Stripa 84-09-05, measured with a center frequency of 22 MHz. Transmitter receiver spacing 10 m.

Borehole N1

Figure A.2 Radar reflection map from the borehole N1 at the Cross-hole site in Stripa 85-01-10, measured with a center frequency of 22 MHz. Transmitter receiver spacing 10 m.

Borehole V1

Figure A.3 Radar reflection map from the borehole V1 at the Cross-hole site in Stripa 85-01-24, measured with a center frequency of 22 MHz. Transmitter receiver spacing 20 m.

Borehole F1

Figure A.4 Radar reflection map from the borehole F1 at the Cross-hole site in Stripa 85-01-10, measured with a center frequency of 22 MHz. Transmitter receiver spacing 10 m.

Figure A.5 Radar reflection map from the borehole F1 at the Cross-hole site in Stripa 85-09-12, measured with a center frequency of 60 MHz. Transmitter receiver spacing 4 m.

Figure A.6 Radar reflection map from the borehole F1 at the Cross-hole site in Stripa 85-01-09, measured with a center frequency of 22 MHz. Transmitter receiver spacing 4 m.

Figure A.7 Radar reflection map from the borehole F1 at the Cross-hole site in Stripa 85-01-09, measured with a center frequency of 22 MHz. Transmitter receiver spacing 20 m.

Figure A.8 Radar reflection map from the borehole F1 at the Cross-hole site in Stripa 85-01-09, measured with a center frequency of 22 MHz. Transmitter receiver spacing 30 m.

Figure A.9 Radar reflection map from the borehole F1 at the Cross-hole site in Stripa 85-01-08, measured with a center frequency of 22 MHz. Transmitter receiver spacing 40 m.

Figure A.10 Radar reflection map from the borehole F1 at the Cross-hole site in Stripa 83-10-25, measured with a center frequency of 25 MHz using the Boliden equipment. Transmitter receiver spacing 10 m.

Figure A.11 Radar reflection map from the borehole F1 at the Cross-hole site in Stripa 84-06-26, measured with a center frequency of 40 MHz using the Prakla equipment. Transmitter receiver spacing 10 m.

Borehole F2

Figure A.12 Radar reflection map from the borehole F2 at the Cross-hole site in Stripa 85-01-10, measured with a center frequency of 22 MHz. Transmitter receiver spacing 10 m.

Figure A.13 Radar reflection map from the borehole F2 at the Cross-hole site in Stripa 85-11-12, measured with a center frequency of 60 MHz. Transmitter receiver spacing 2 m.

Figure A.14 Radar reflection map from the borehole F2 at the Cross-hole site in Stripa 83-10-25, measured with a center frequency of 25 MHz using the Boliden equipment. Transmitter receiver spacing 10 m.

Borehole F3

Figure A.15 Radar reflection map from the borehole F3 at the Cross-hole site in Stripa 84-11-08, measured with a center frequency of 22 MHz. Transmitter receiver spacing 10 m.

Figure A.16 Radar reflection map from the borehole F3 at the Cross-hole site in Stripa 85-09-26, measured with a center frequency of 45 MHz. Transmitter receiver spacing 8 m.

Figure A.17 Radar reflection map from the borehole F3 at the Cross-hole site in Stripa 85-09-12, measured with a center frequency of 60 MHz. Transmitter receiver spacing 2 m.

Borehole F4

Figure A.18 Radar reflection map from the borehole F4 at the Cross-hole site in Stripa 84-11-07, measured with a center frequency of 22 MHz. Transmitter receiver spacing 10 m.

Figure A.19 Radar reflection map from the borehole F4 at the Cross-hole site in Stripa 85-09-16, measured with a center frequency of 60 MHz. Transmitter receiver spacing 4 m.

Borehole F5

- Figure A.20 Radar reflection map from the borehole F5 at the Cross-hole site in Stripa 84-11-08, measured with a center frequency of 22 MHz. Transmitter receiver spacing 10 m.
- Figure A.21 Radar reflection map from the borehole F5 at the Cross-hole site in Stripa 85-11-12, measured with a center frequency of 60 MHz. Transmitter receiver spacing 2 m.
- Figure A.22 Radar reflection map from the borehole F5 at the Cross-hole site in Stripa 85-09-24, measured with a center frequency of 14 MHz. Pure dipole antennas e.g. antennas without resistive load. Transmitter receiver spacing 24 m.

Borehole F6

- Figure A.23 Radar reflection map from the borehole F6 at the Cross-hole site in Stripa 84-11-07, measured with a center frequency of 22 MHz. Transmitter receiver spacing 10 m.
- Figure A.24 Radar reflection map from the borehole F6 at the Cross-hole site in Stripa 85-11-12, measured with a center frequency of 60 MHz. Transmitter receiver spacing 2 m.

Boreholes E1-N1

- Figure A.25 Radar calibration map from the borehole E1-N1 at the Cross-hole site in Stripa 85-09-09, measured with a center frequency of 22 MHz. Transmitter and receiver moved simultaneously in each borehole.
- Figure A.26 Radar calibration map from the borehole E1-N1 at the Cross-hole site in Stripa 85-09-12, measured with a center frequency of 60 MHz. Transmitter and receiver moved simultaneously in each borehole.

Borehole SBH1

- Figure A.27 Radar reflection map from the borehole SBH1 drilled from the ground surface at the Stripa mine, measured 85-08-06 with a center frequency of 22 MHz. Transmitter receiver spacing 10 m.

Borehole SBH2

- Figure A.28 Radar reflection map from the borehole SBH2 drilled from the ground surface at the Stripa mine, measured 85-08-07 with a center frequency of 22 MHz. Transmitter receiver spacing 10 m.

Borehole SBH3

Figure A.29 Radar reflection map from the borehole SBH3 drilled from the ground surface at the Stripa mine, measured 85-08-08 with a center frequency of 22 MHz. Transmitter receiver spacing 10 m.

Borehole 3DH1

Figure A.30 Radar reflection map from the borehole 3DH1 drilled from the 3D migration drift at the Stripa mine, measured 84-08-31 with a center frequency of 22 MHz. Transmitter receiver spacing 8 m. For definition of zones see Stripa Project Quarterly Report July-September, 1984.

Borehole 3DH2

Figure A.31 Radar reflection map from the borehole 3DH2 drilled from the 3D migration drift at the Stripa mine, measured 84-08-31 with a center frequency of 22 MHz. Transmitter receiver spacing 8 m. For definition of zones see Stripa Project Quarterly Report July-September, 1984.

Borehole 3DH3

Figure A.32 Radar reflection map from the borehole 3DH3 drilled from the 3D migration drift at the Stripa mine, measured 84-08-31 with a center frequency of 22 MHz. Transmitter receiver spacing 8 m. For definition of zones see Stripa Project Quarterly Report July-September, 1984.

Borehole 3DP1

Figure A.33 Radar reflection map from the borehole 3DP1 drilled as a pilot hole for the 3D migration drift at the Stripa mine, measured 84-09-06 with a center frequency of 22 MHz. Transmitter receiver spacing 10 m. For definition of zones see Stripa Project Quarterly Report July-September, 1984.

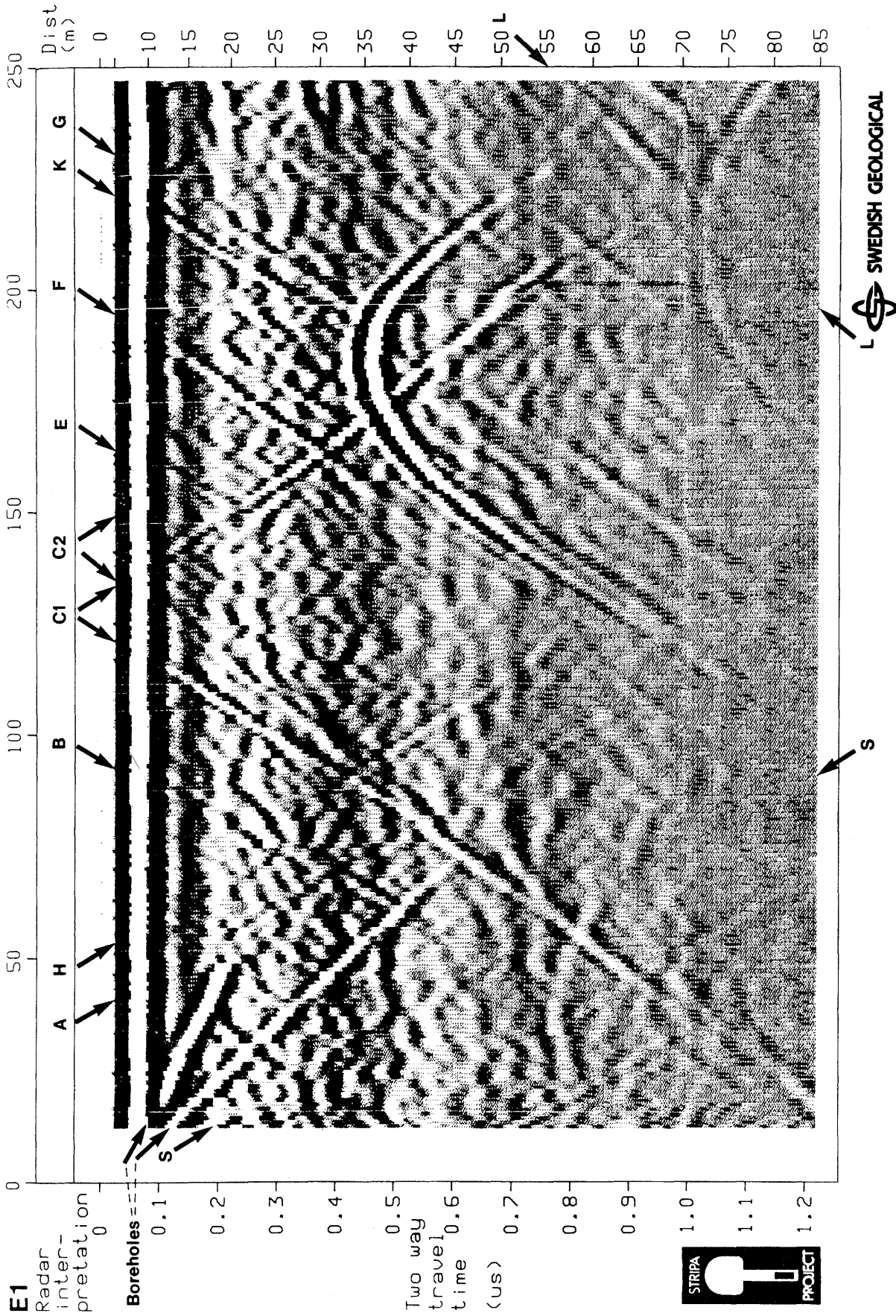


Figure A.1 Radar reflection map from the borehole E1 at the Cross-hole site in Stripa 84-09-05, measured with a center frequency of 22 MHz. Transmitter receiver spacing 10 m.

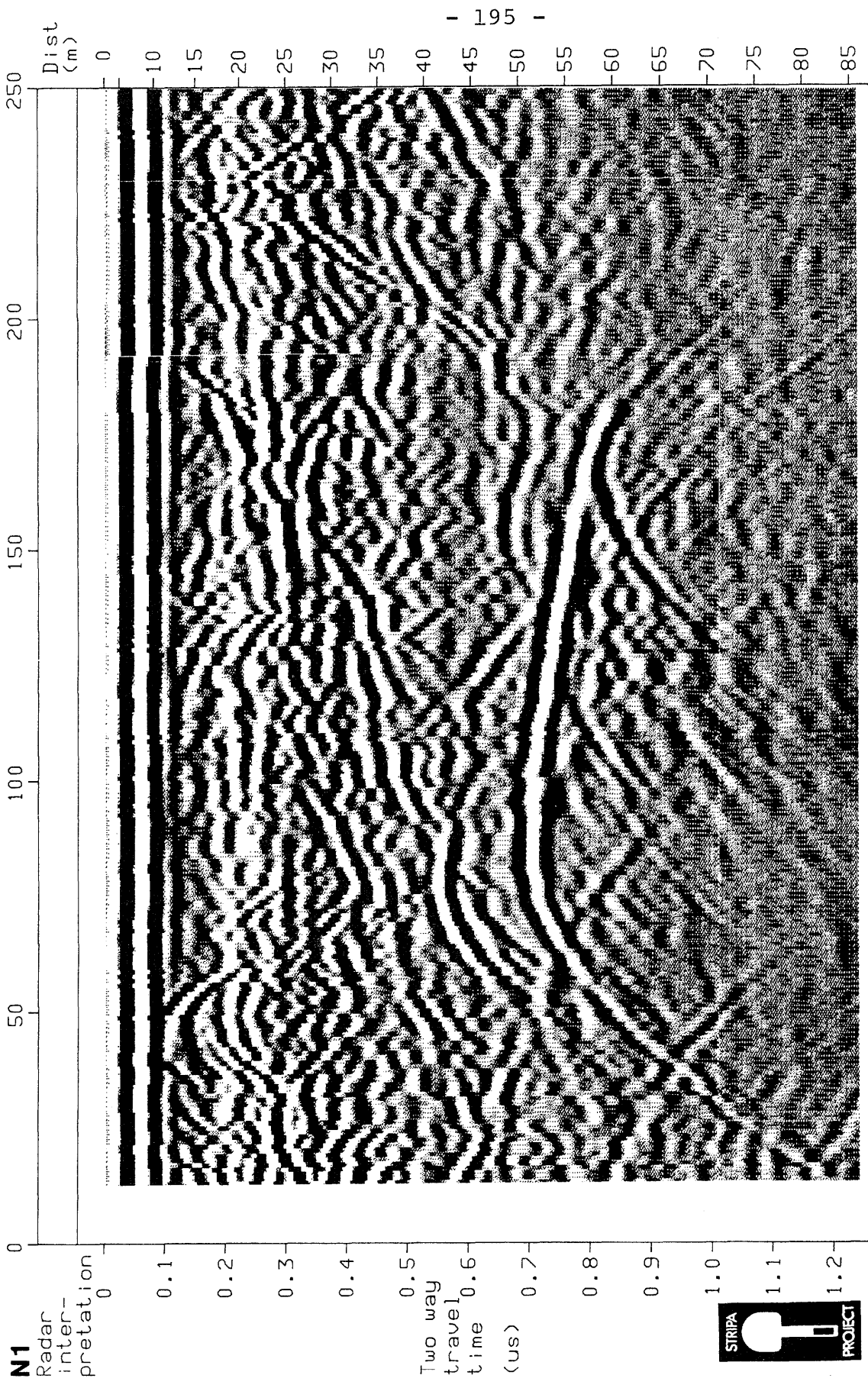


Figure A.2a Radar reflection map from the borehole N1 at the Cross-hole site in Stripa 85-01-10, measured with a center frequency of 22 MHz. Transmitter receiver spacing 10 m.

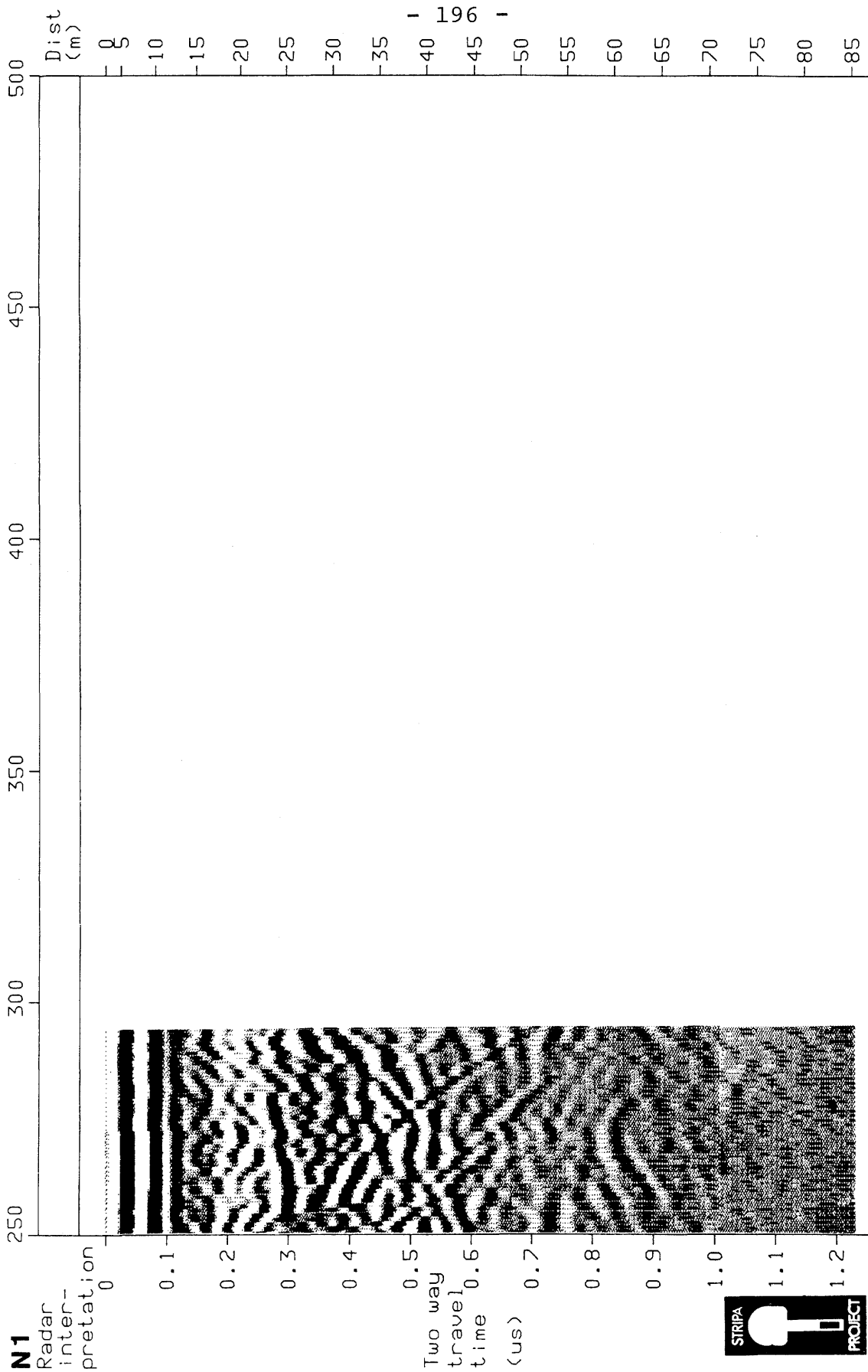


Figure A.2b Radar reflection map from the borehole N1 at the Cross-hole site in Stripa 85-01-10, measured with a center frequency of 22 MHz. Transmitter receiver spacing 10 m.

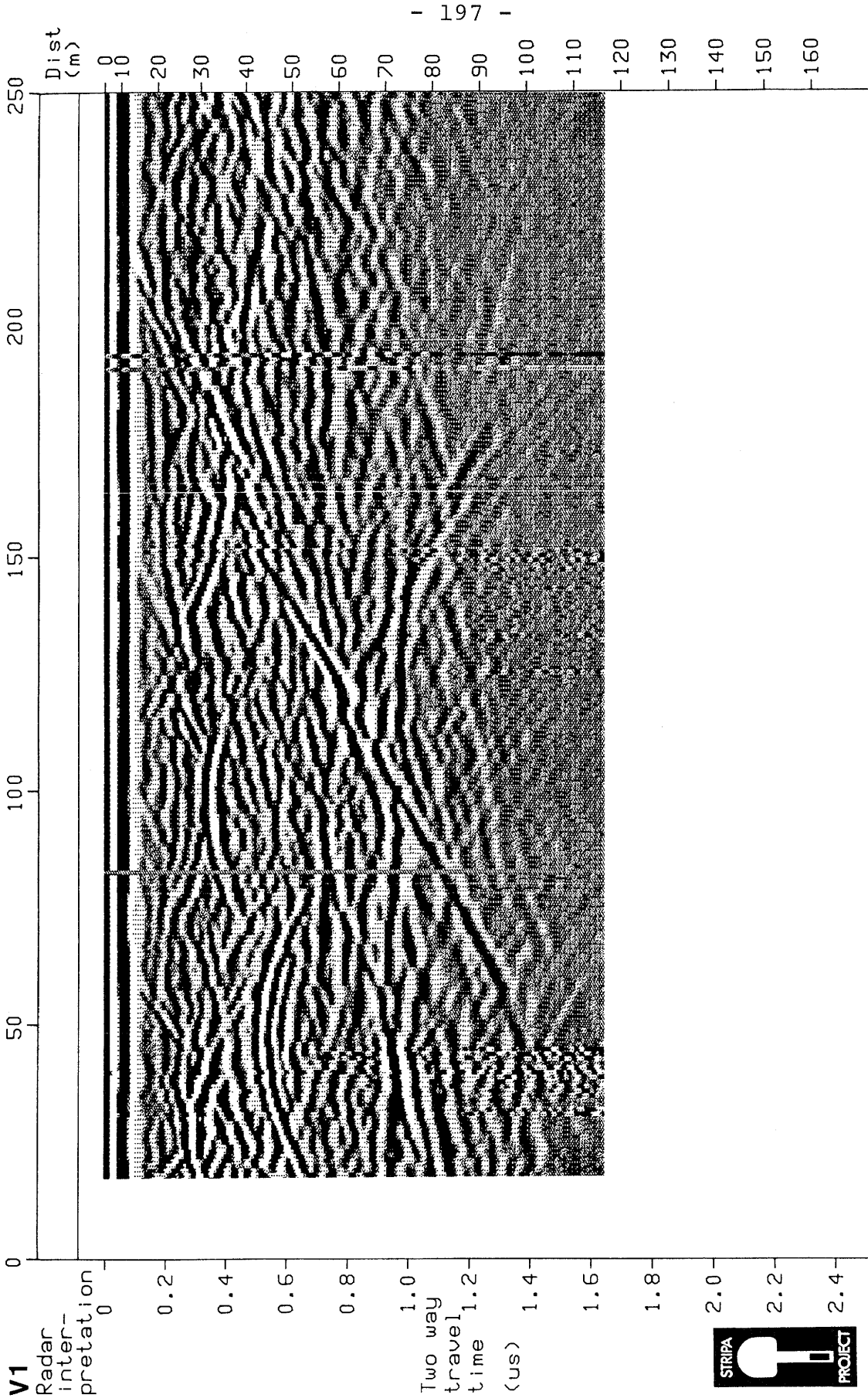


Figure A.3a Radar reflection map from the borehole V1 at the Cross-hole site in Stripa 85-01-24, measured with a center frequency of 22 MHz. Transmitter receiver spacing 20 m.

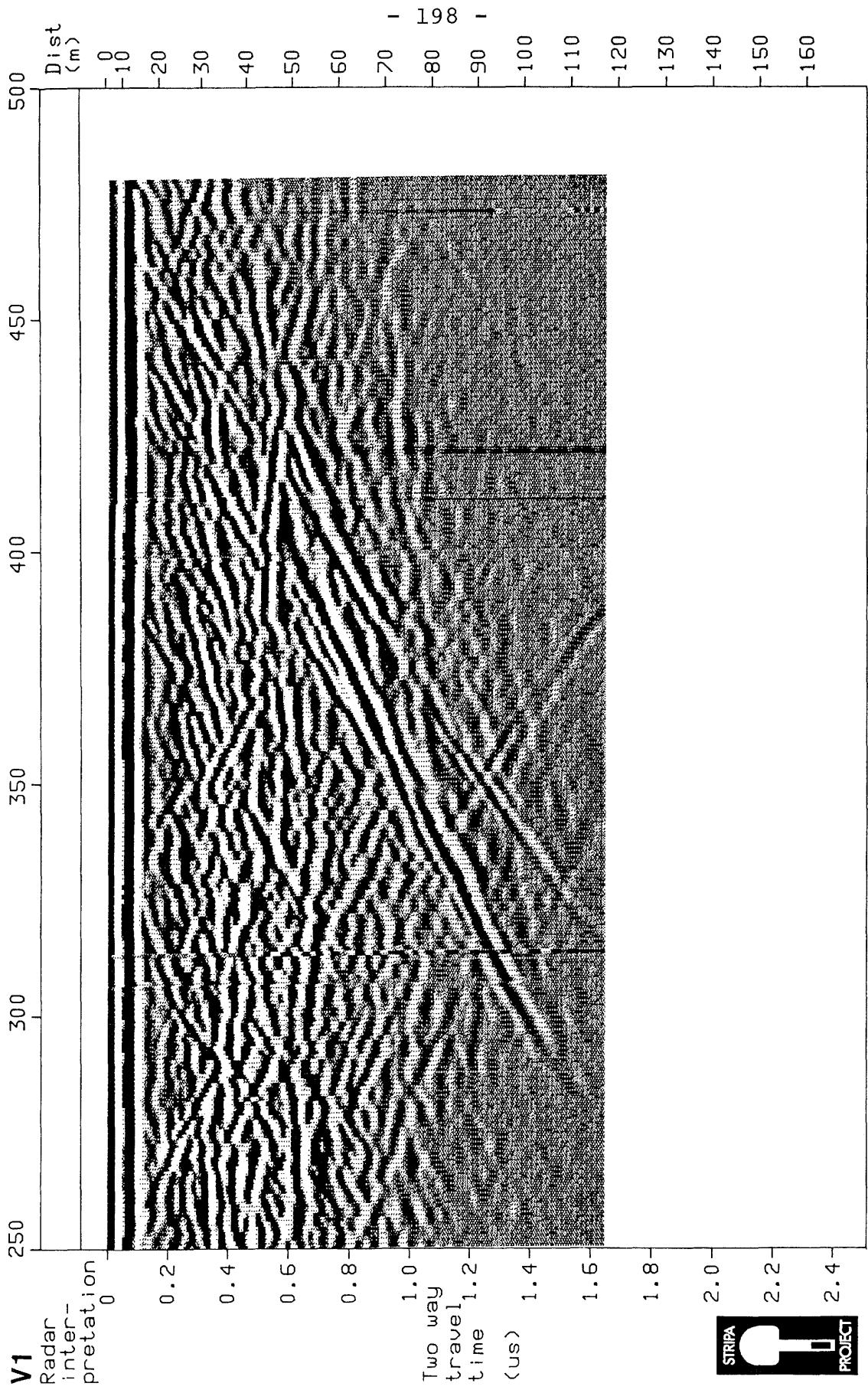


Figure A.3b Radar reflection map from the borehole V1 at the Cross-hole site in Stripa 85-01-24, measured with a center frequency of 22 MHz. Transmitter receiver spacing 20 m.

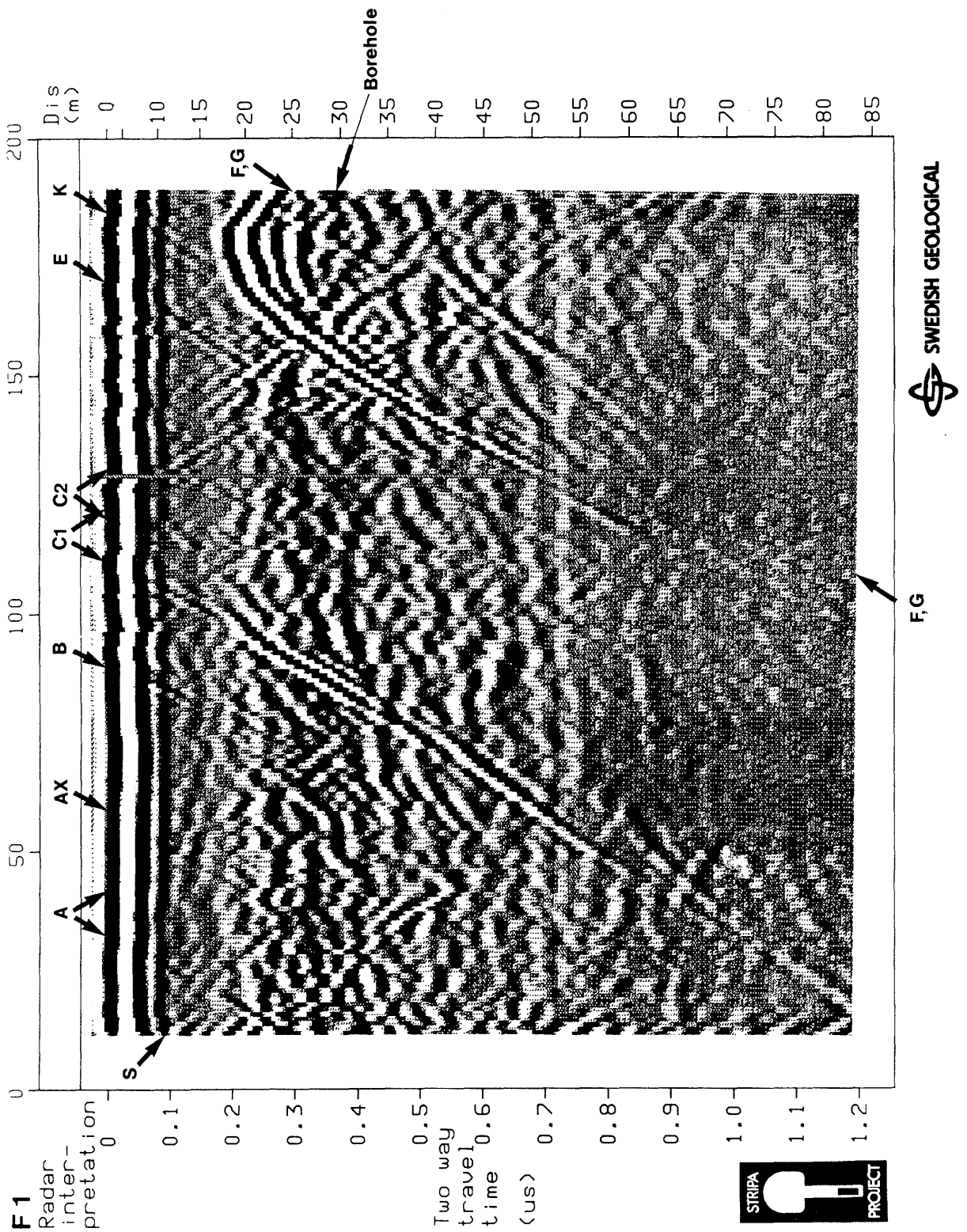


Figure A.4 Radar reflection map from the borehole F1 at the Cross-hole site in Stripa 85-01-10, measured with a center frequency of 22 MHz. Transmitter receiver spacing 10 m.

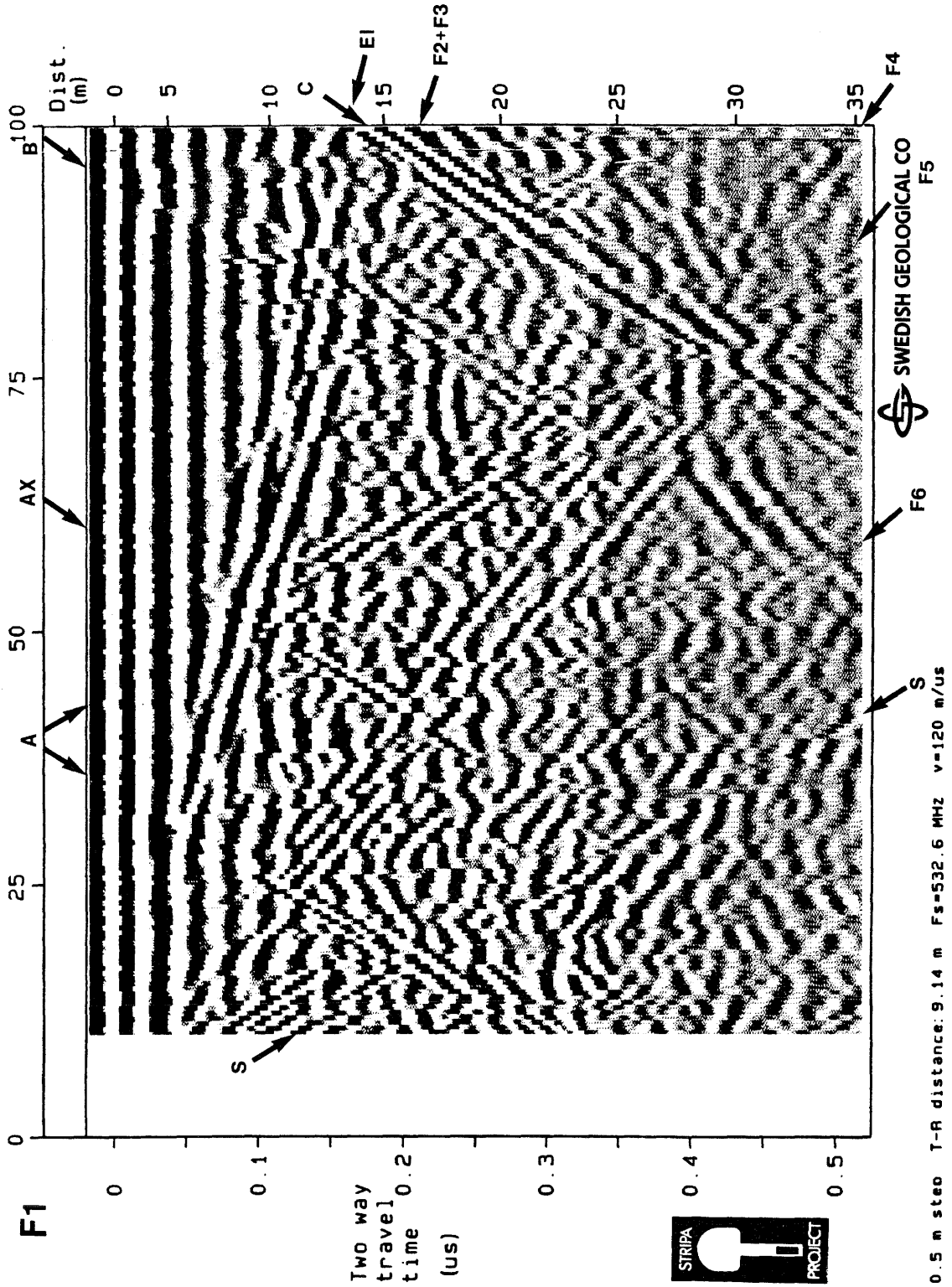


Figure A.5a Radar reflection map from the borehole F1 at the Cross-hole site in Stripa 85-09-12, measured with a center frequency of 60 MHz. Transmitter receiver spacing 4 m.

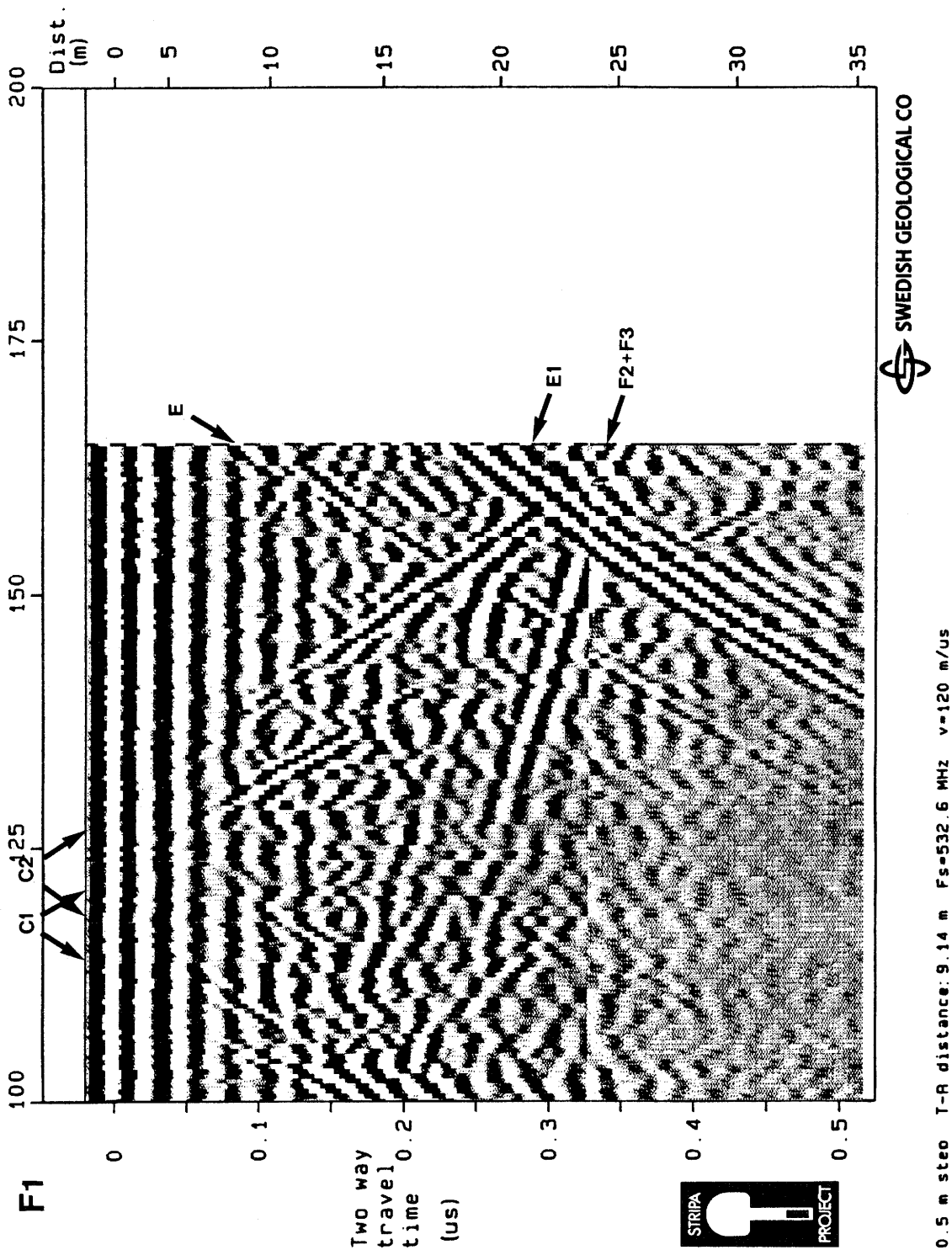


Figure A.5b Radar reflection map from the borehole F1 at the Cross-hole site in Stripa 85-09-12, measured with a center frequency of 60 MHz. Transmitter receiver spacing 4 m.

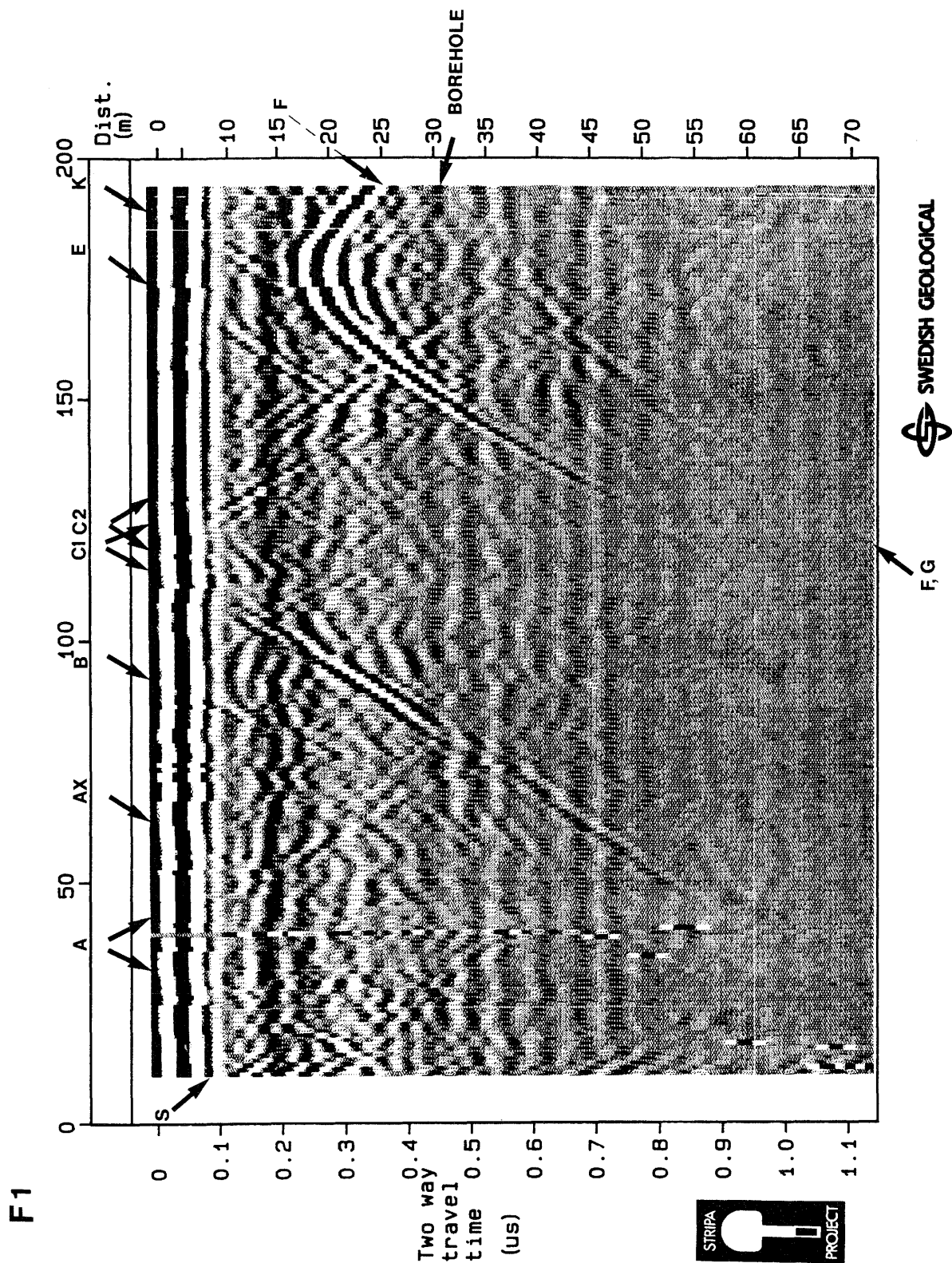


Figure A.6 Radar reflection map from the borehole F1 at the Cross-hole site in Stripa 85-01-09, measured with a center frequency of 22 MHz. Transmitter receiver spacing 4 m.

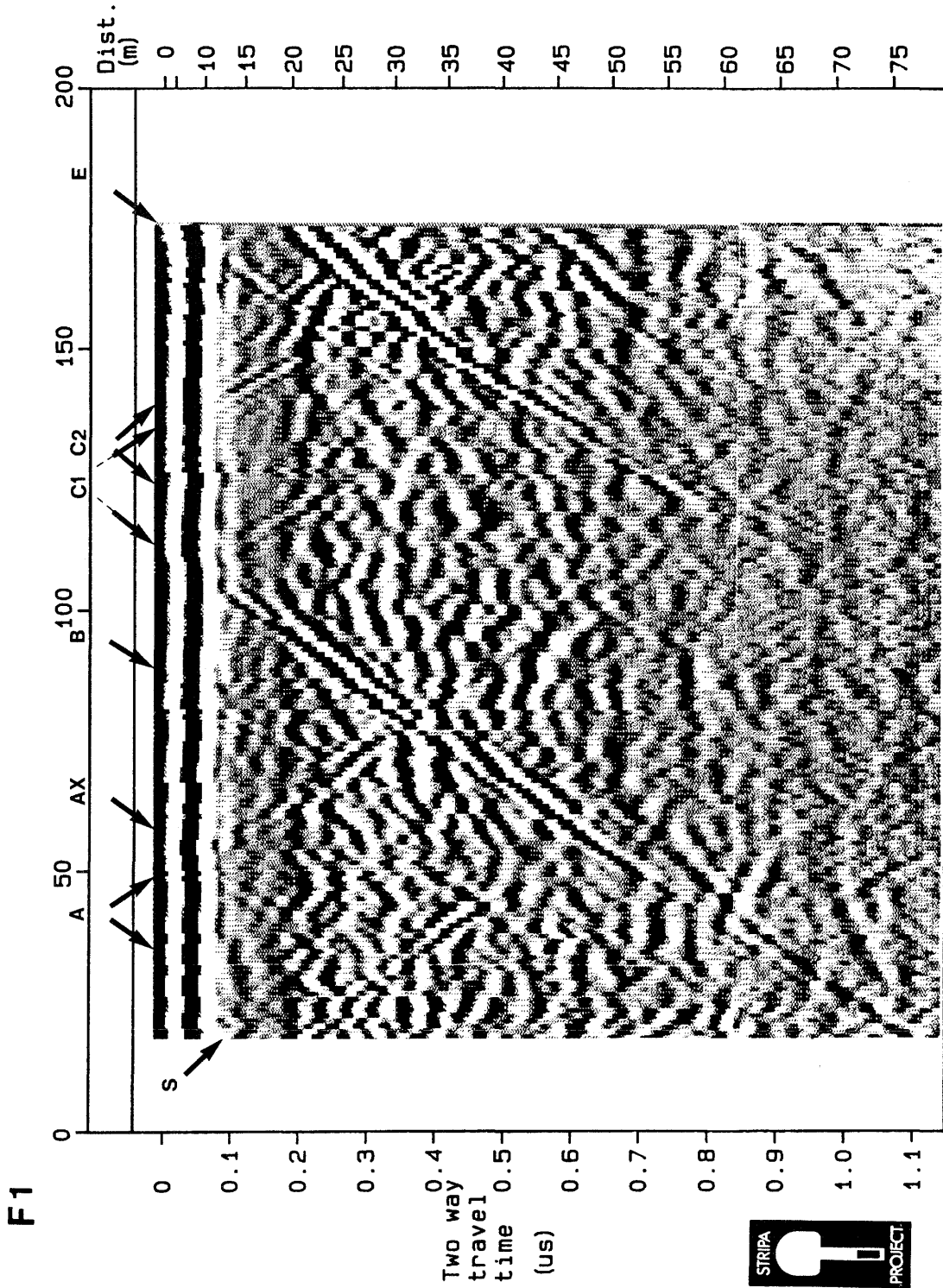


Figure A.7 Radar reflection map from the borehole F1 at the Cross-hole site in Stripa 85-01-09, measured with a center frequency of 22 MHz. Transmitter receiver spacing 20 m.

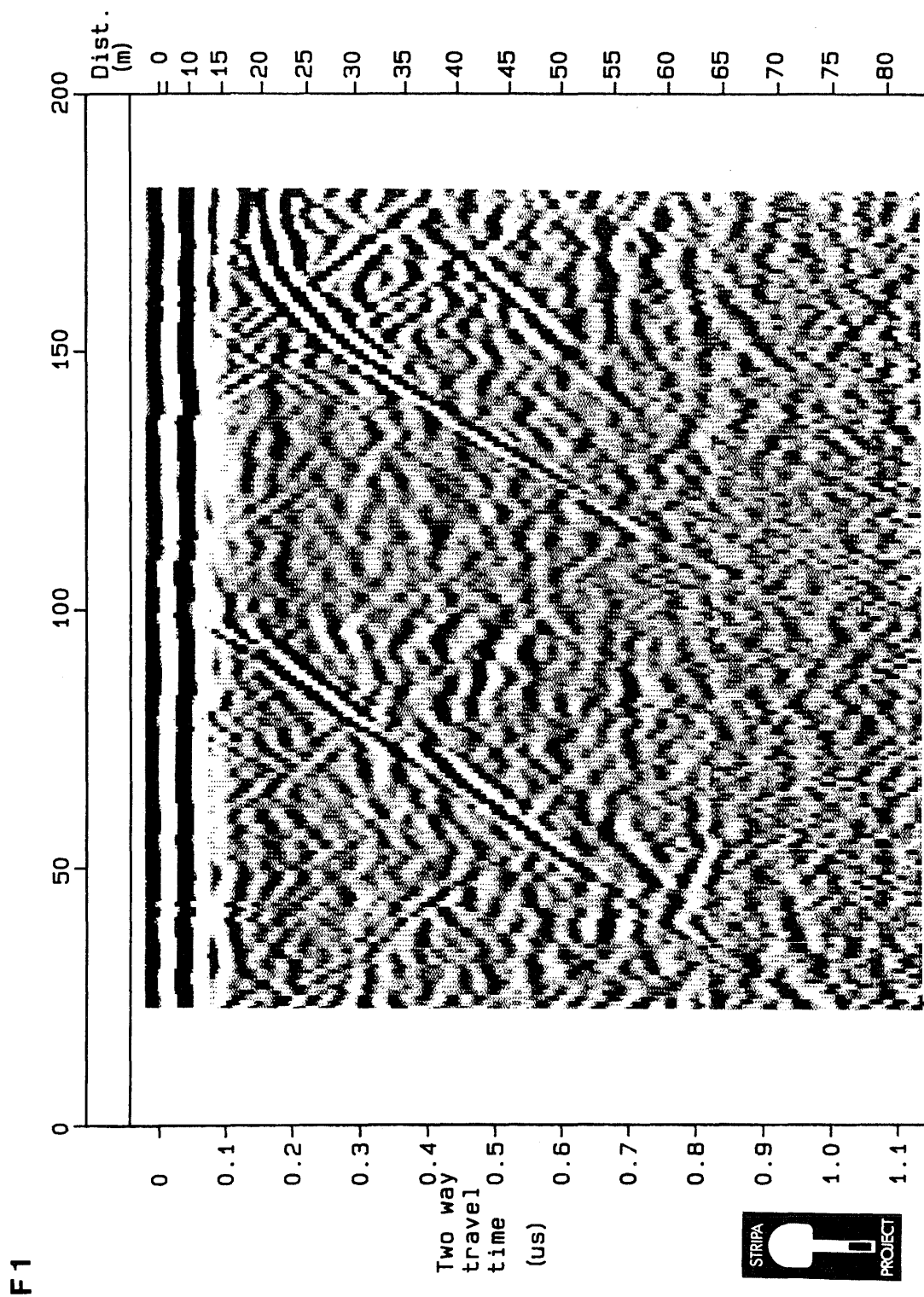


Figure A.8 Radar reflection map from the borehole F1 at the Cross-hole site in Stripa 85-01-09, measured with a center frequency of 22 MHz. Transmitter receiver spacing 30 m.

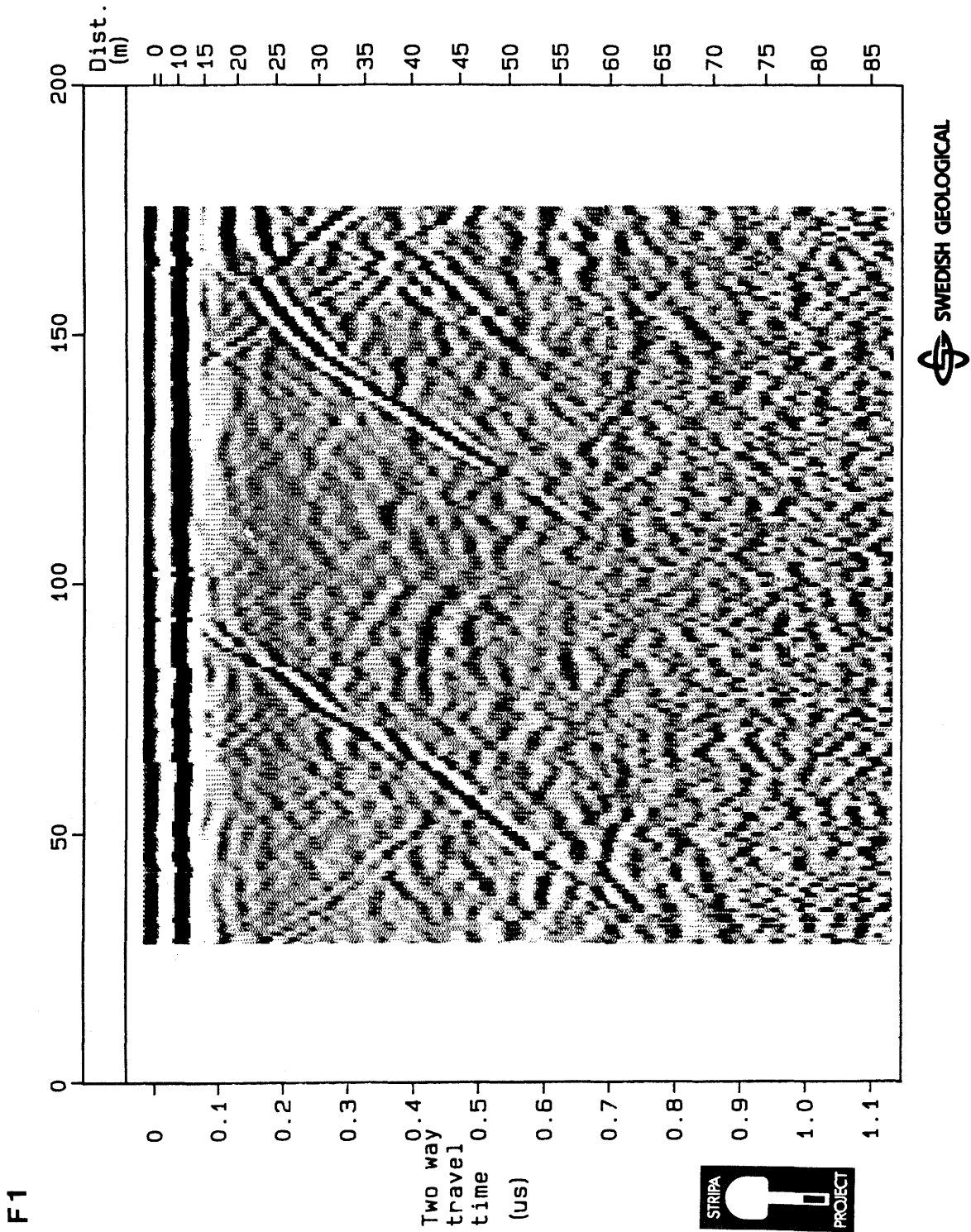


Figure A.9 Radar reflection map from the borehole F1 at the Cross-hole site in Stripa 85-01-08, measured with a center frequency of 22 MHz. Transmitter receiver spacing 40 m.

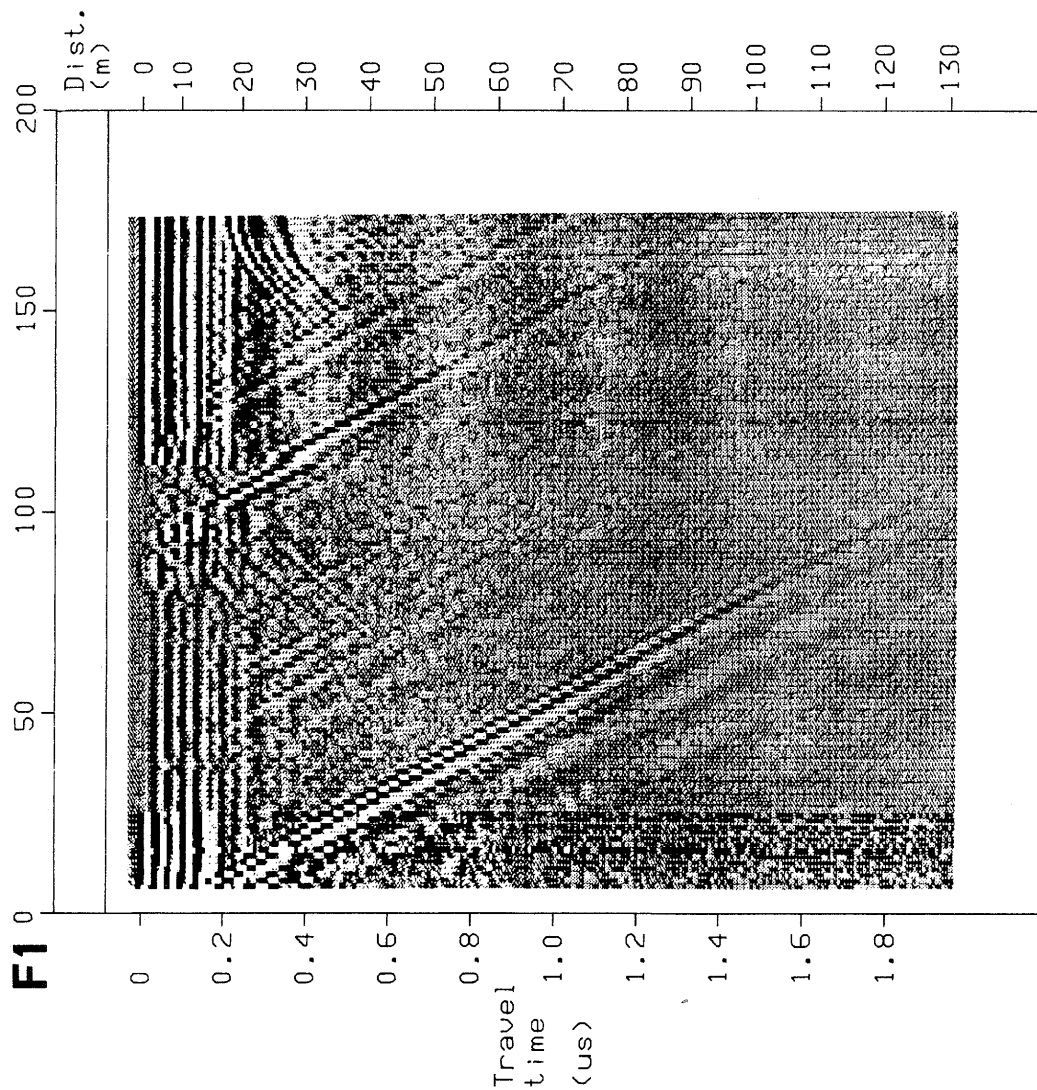


Figure A.11 Radar reflection map from the borehole F1 at the Cross-hole site in Stripa 84-06-26, measured with a center frequency of 40 MHz using the Prakla equipment. Transmitter receiver spacing 10 m.

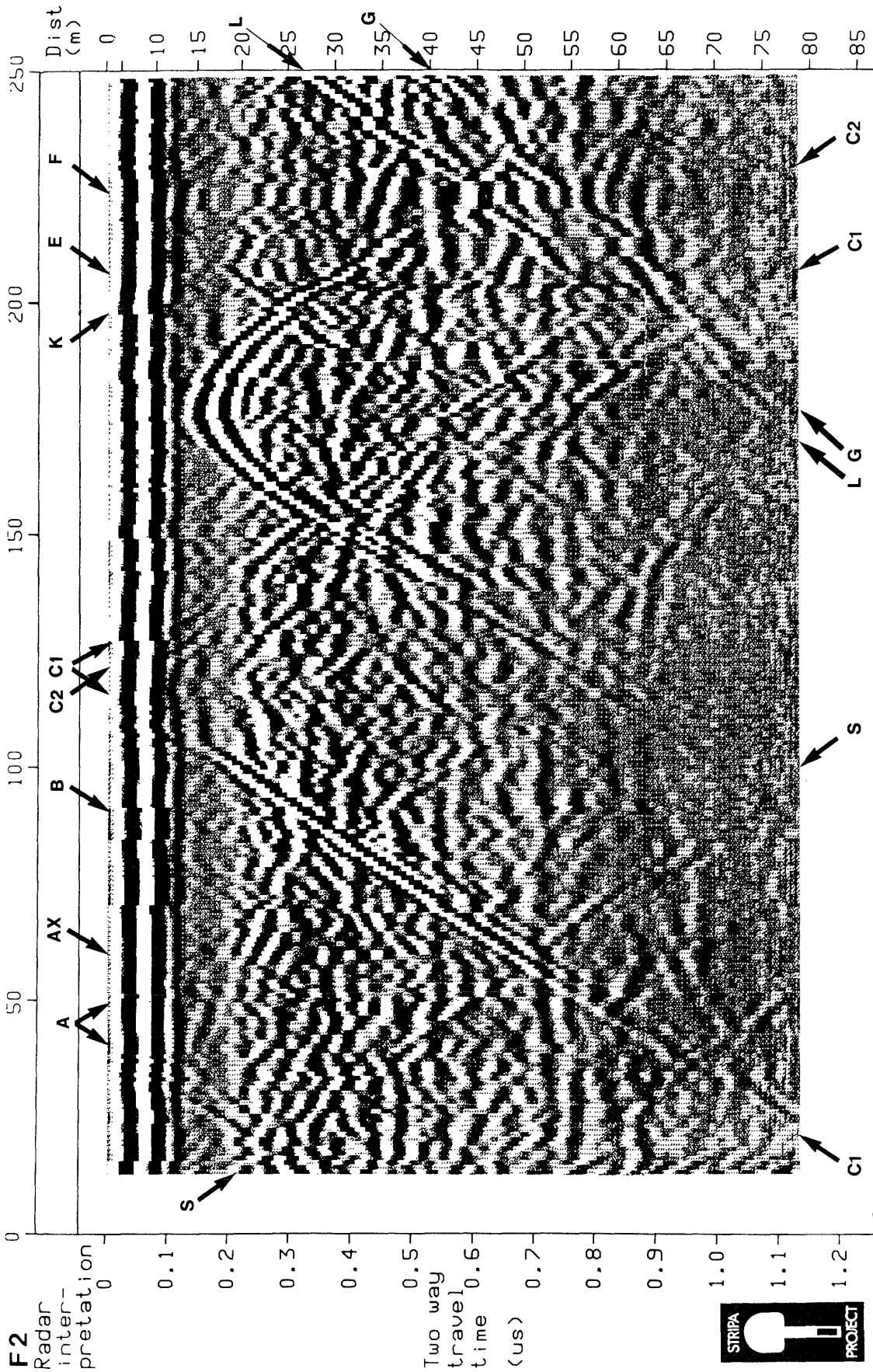


Figure A.12 Radar reflection map from the borehole F2 at the Cross-hole site in Stripa 85-01-10, measured with a center frequency of 22 MHz. Transmitter receiver spacing 10 m.

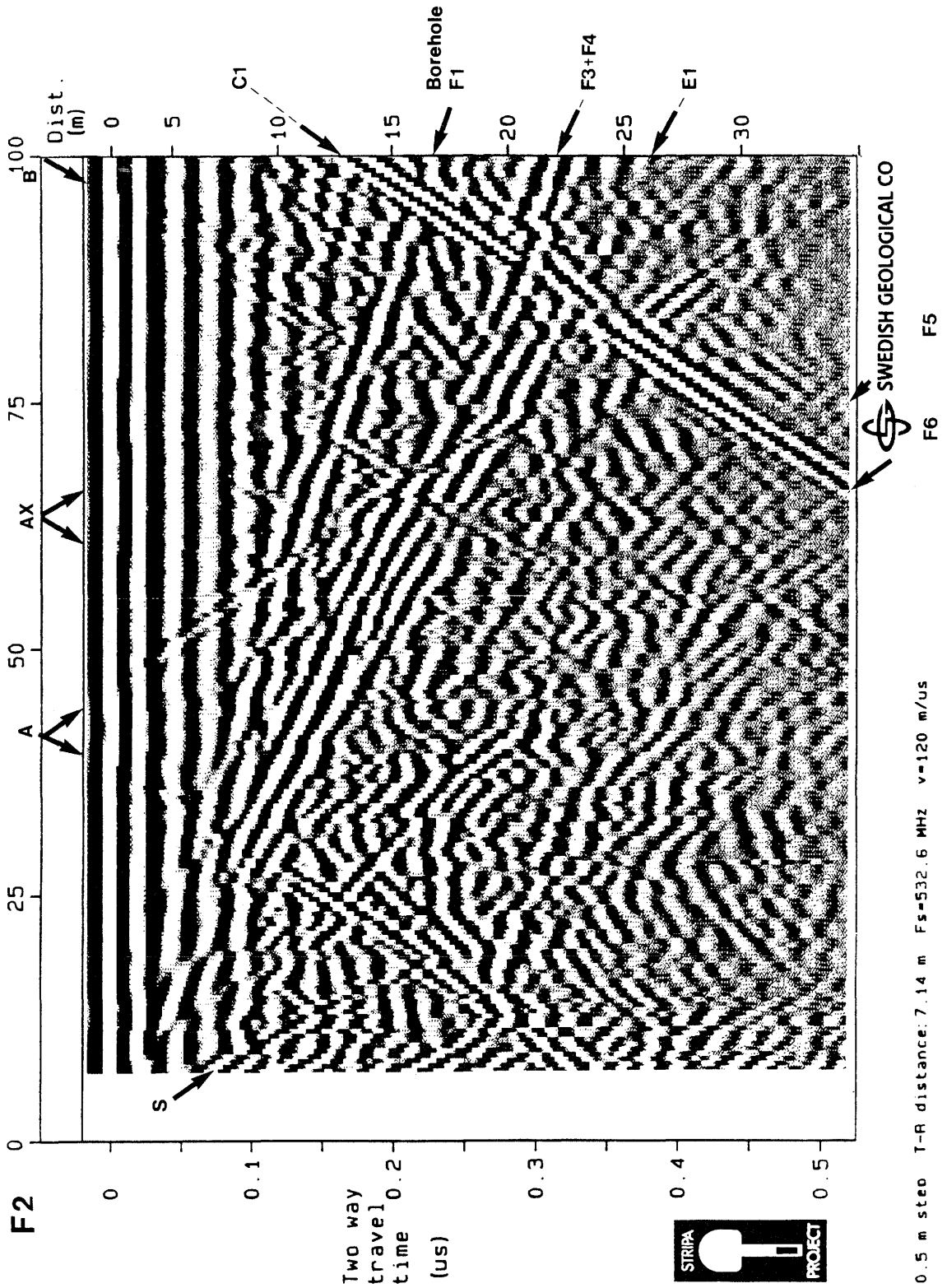
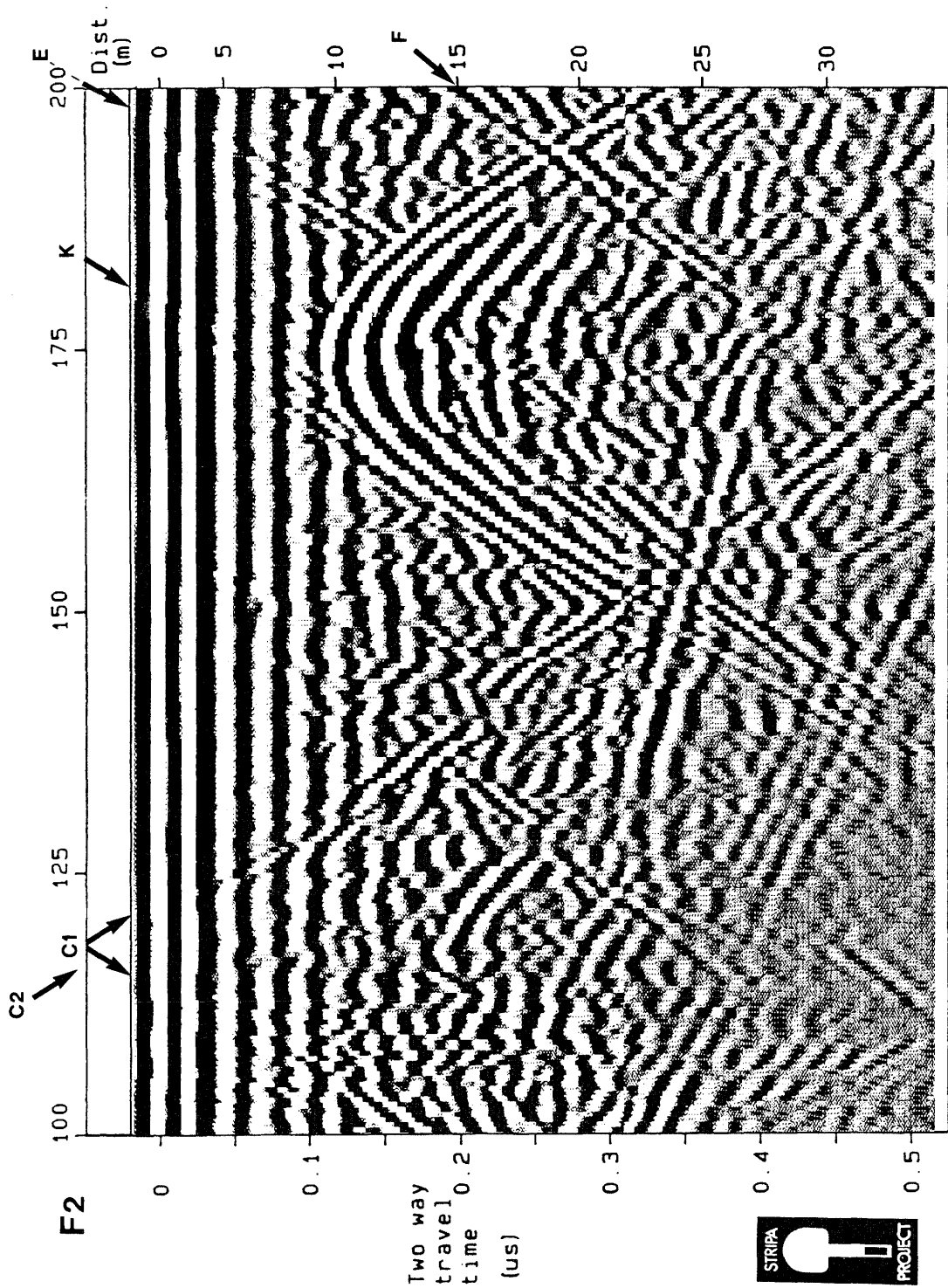


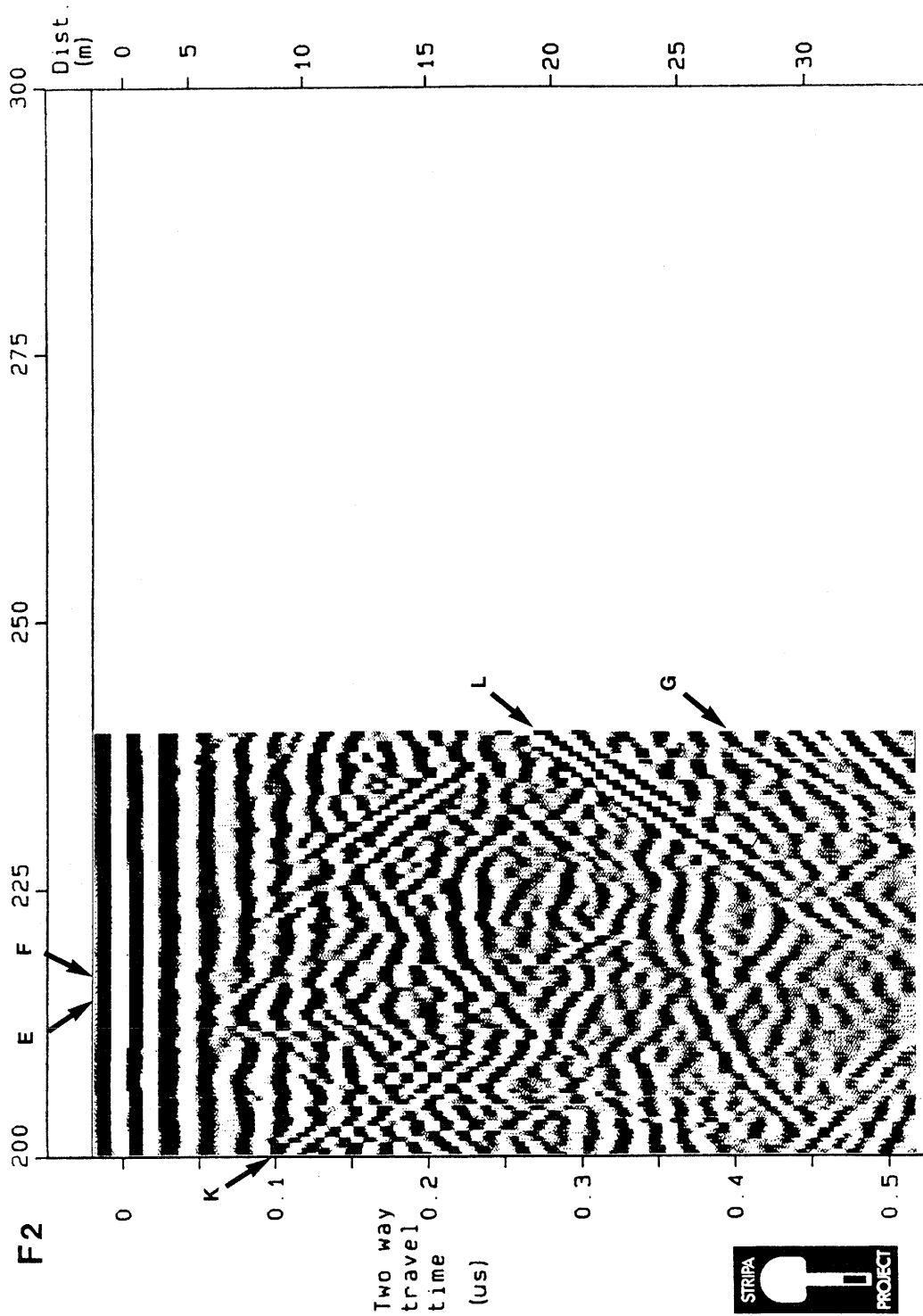
Figure A.13a Radar reflection map from the borehole F2 at the Cross-hole site in Stripa 85-11-12, measured with a center frequency of 60 MHz. Transmitter receiver spacing 2 m.



SWEDISH GEOLOGICAL CO

0.5 m step T-R distance: 7.14 m Fs=532.6 MHz v=120 m/us

Figure A.13b Radar reflection map from the borehole F2 at the Cross-hole site in Stripa 85-11-12, measured with a center frequency of 60 MHz. Transmitter receiver spacing 2 m.



SWEDISH GEOLOGICAL CO

0.5 m step T-R distance: 7.14 m Fs=532.6 MHz v=120 m/us

Figure A.13c Radar reflection map from the borehole F2 at the Cross-hole site in Stripa 85-11-12, measured with a center frequency of 60 MHz. Transmitter receiver spacing 2 m.

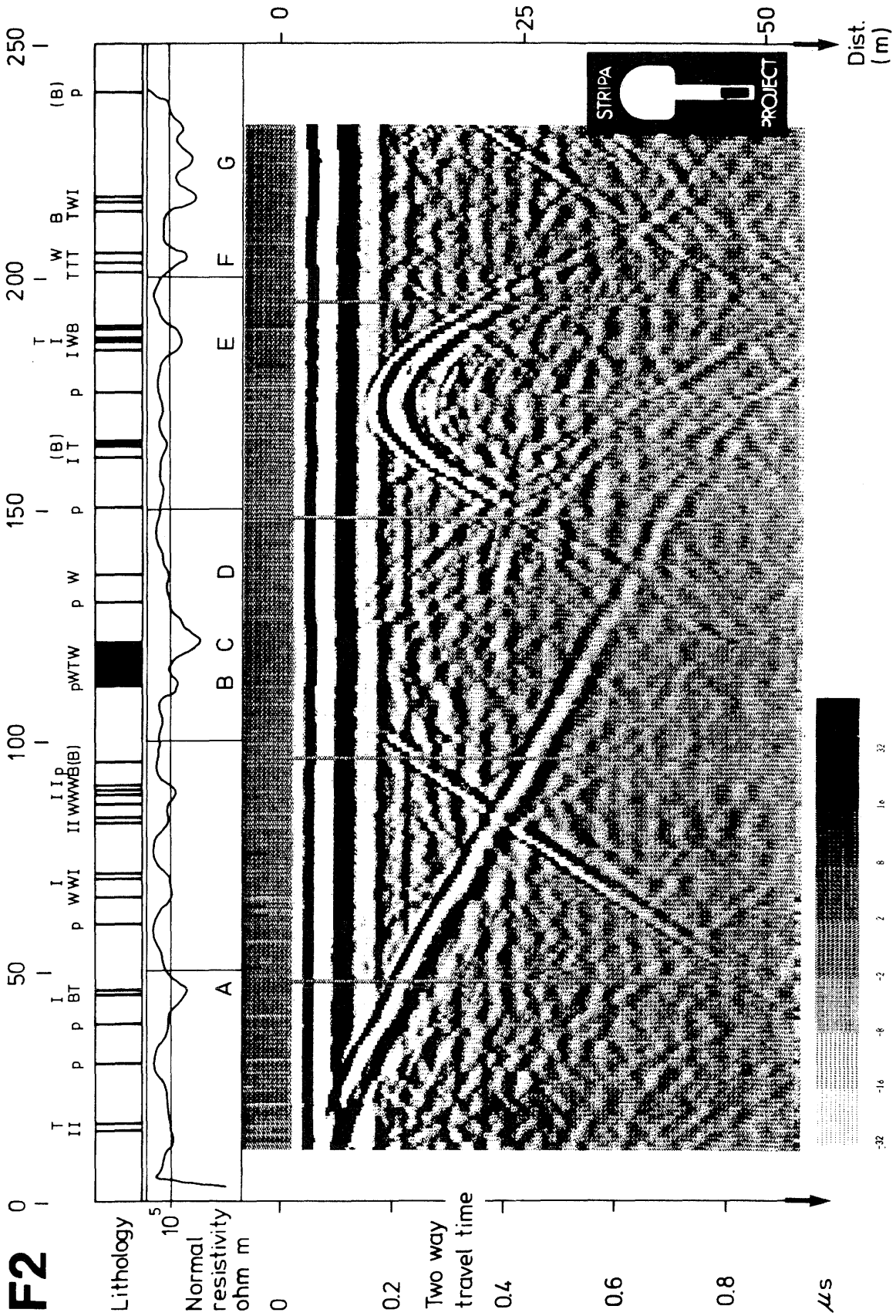


Figure A.14 Radar reflection map from the borehole F2 at the Cross-hole site in Stripa 83-10-25, measured with a center frequency of 25 MHz using the Boliden equipment. Transmitter receiver spacing 10 m.

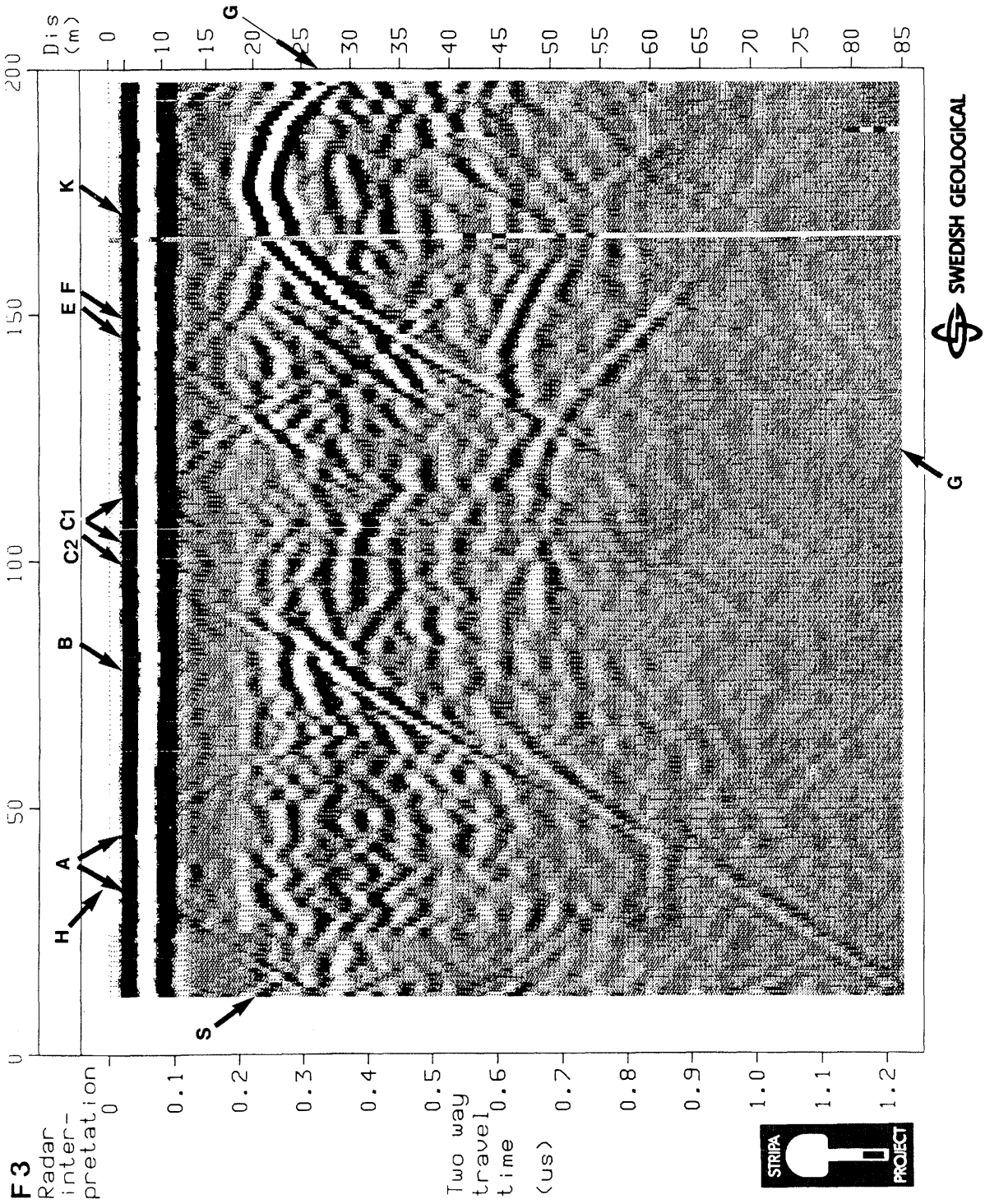


Figure A.15 Radar reflection map from the borehole F3 at the Cross-hole site in Stripa 84-11-08, measured with a center frequency of 22 MHz. Transmitter receiver spacing 10 m.

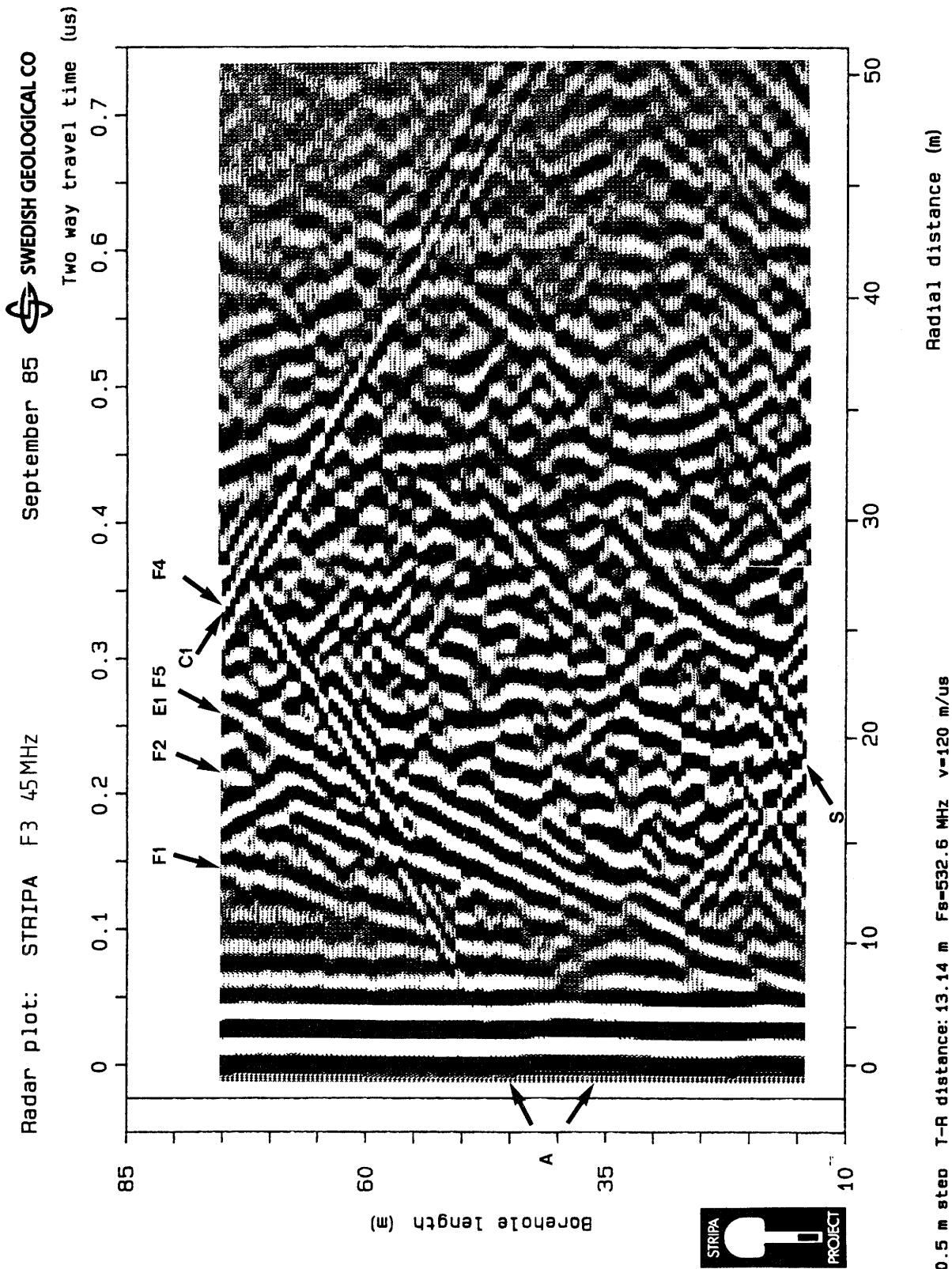


Figure A.16 Radar reflection map from the borehole F3 at the Cross-hole site in Stripa 85-09-26, measured with a center frequency of 45 MHz. Transmitter receiver spacing 8 m.

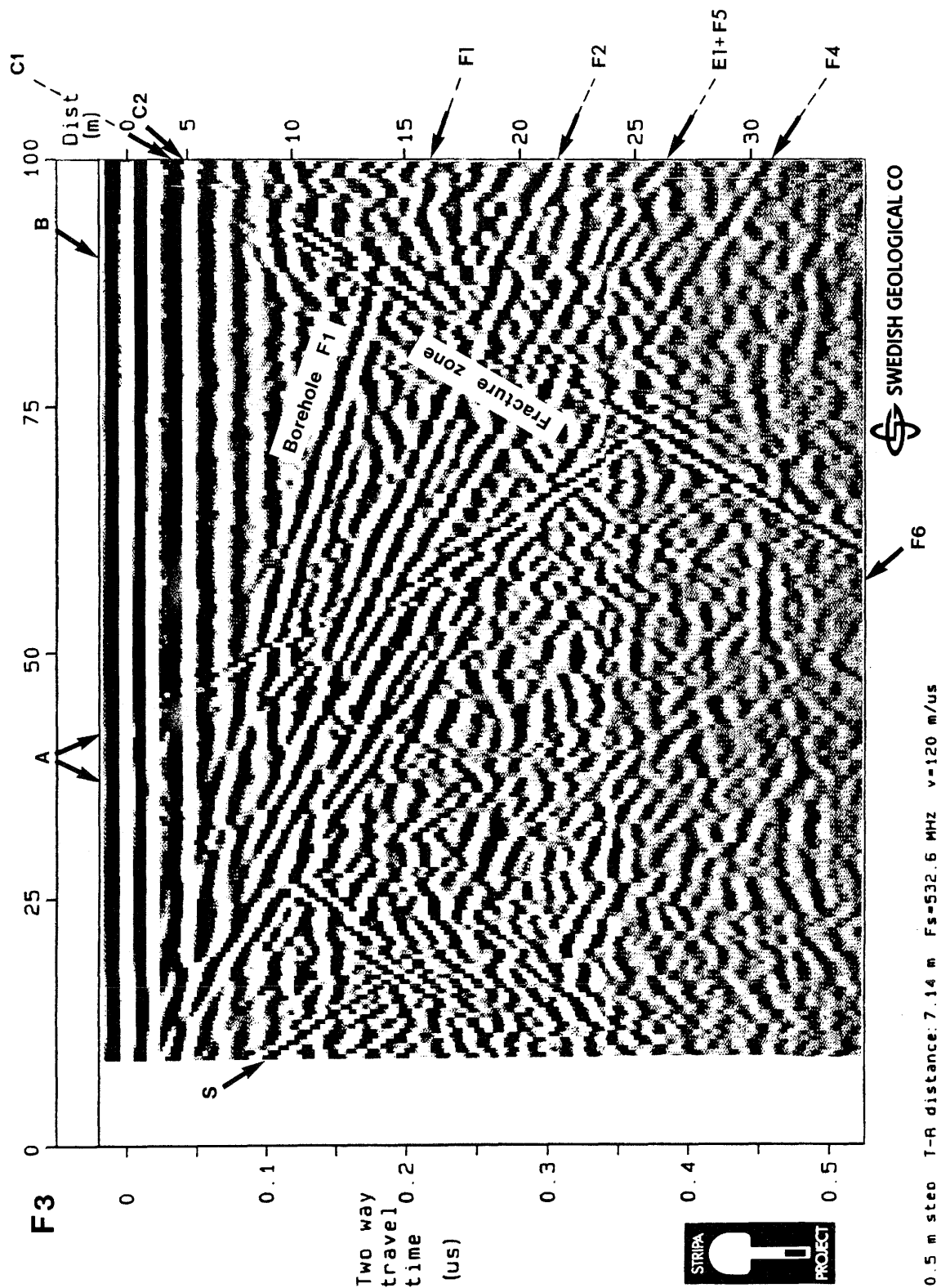


Figure A.17a Radar reflection map from the borehole F3 at the Cross-hole site in Stripa 85-09-12, measured with a center frequency of 60 MHz. Transmitter receiver spacing 2 m.

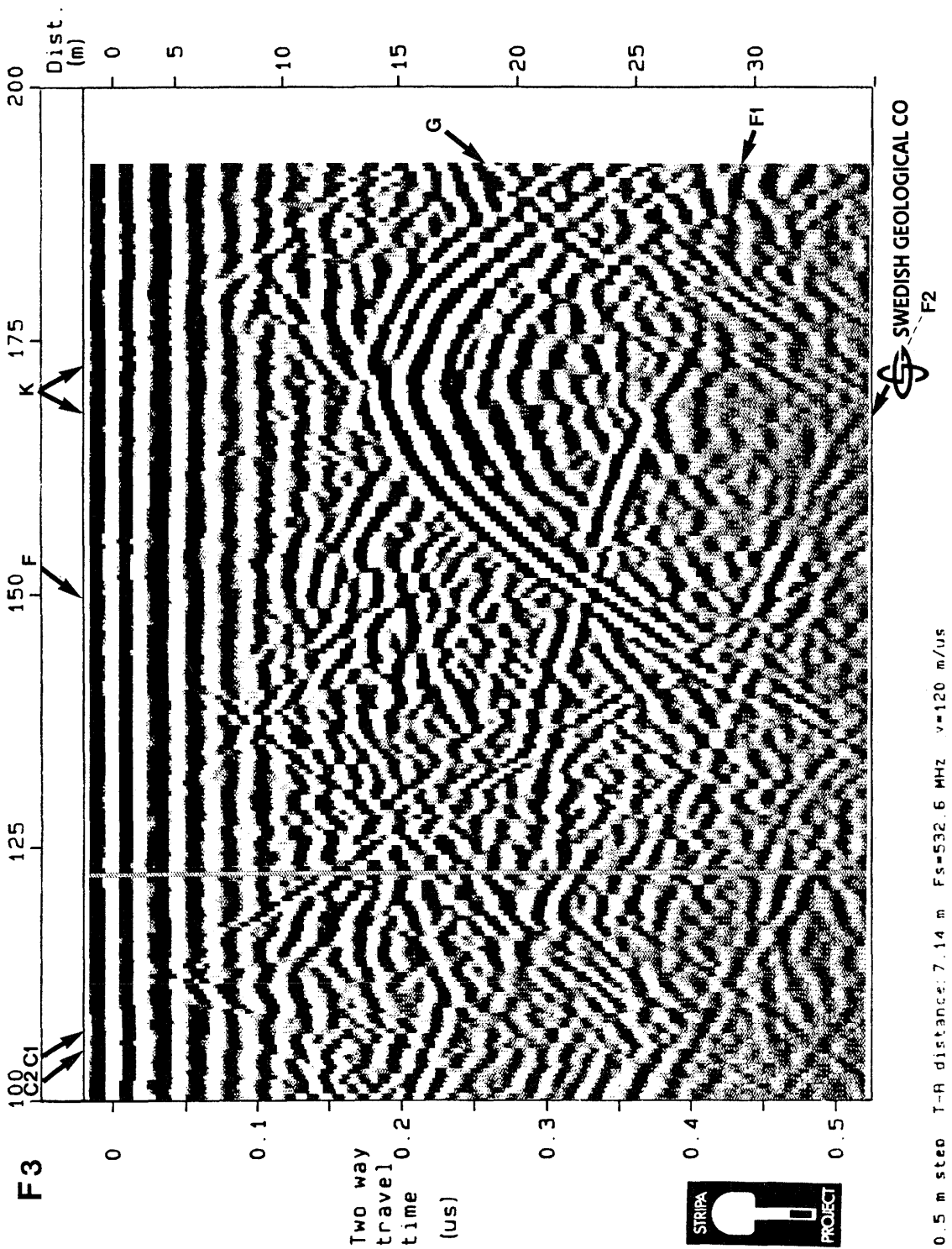
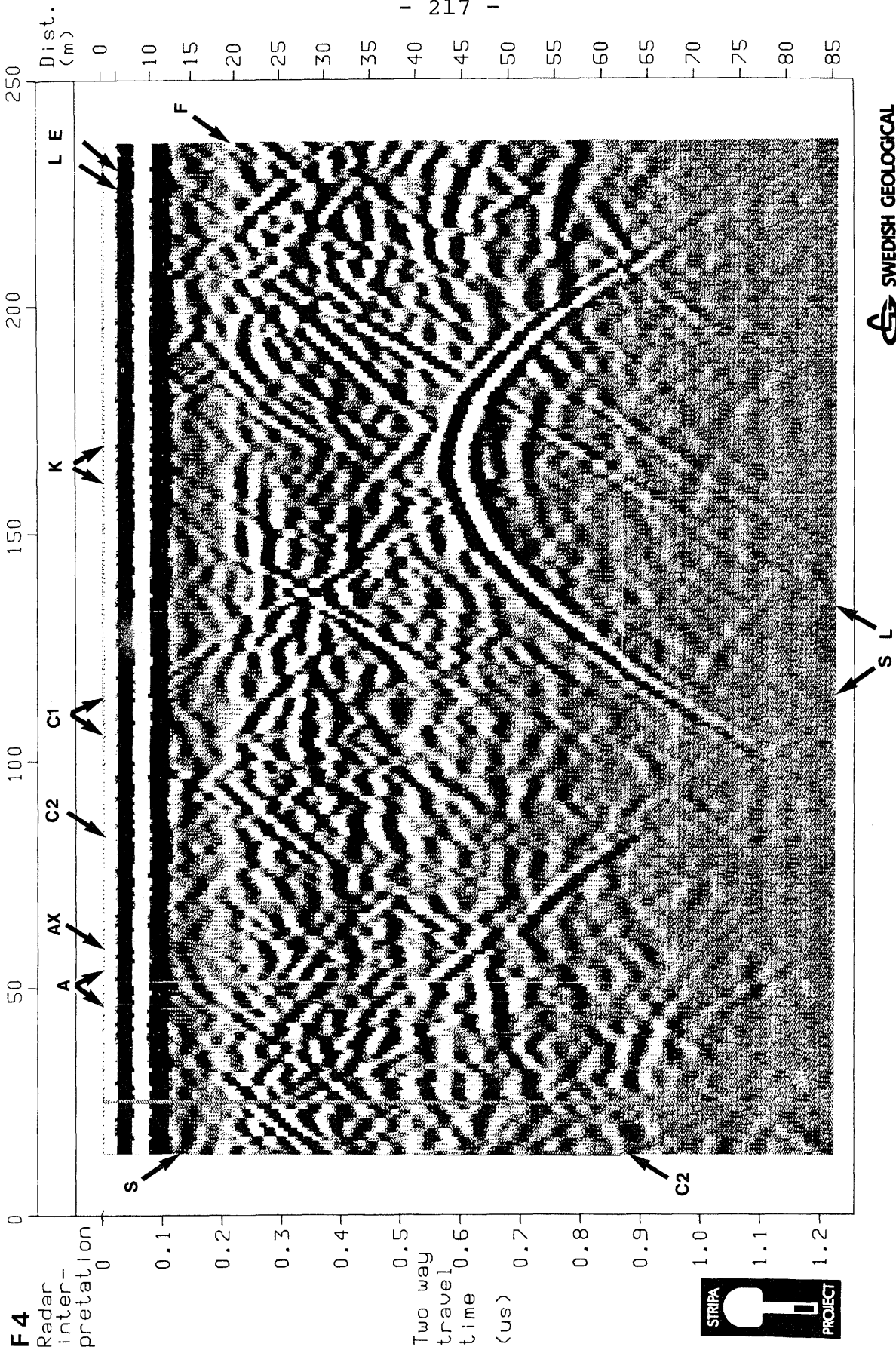


Figure A.17b Radar reflection map from the borehole F3 at the Cross-hole site in Stripa 85-09-12, measured with a center frequency of 60 MHz. Transmitter receiver spacing 2 m.



F4

Radar interpretation

Figure A.18

Radar reflection map from the borehole F4 at the Cross-hole site in Stripa 84-11-07, measured with a center frequency of 22 MHz. Transmitter receiver spacing 10 m.

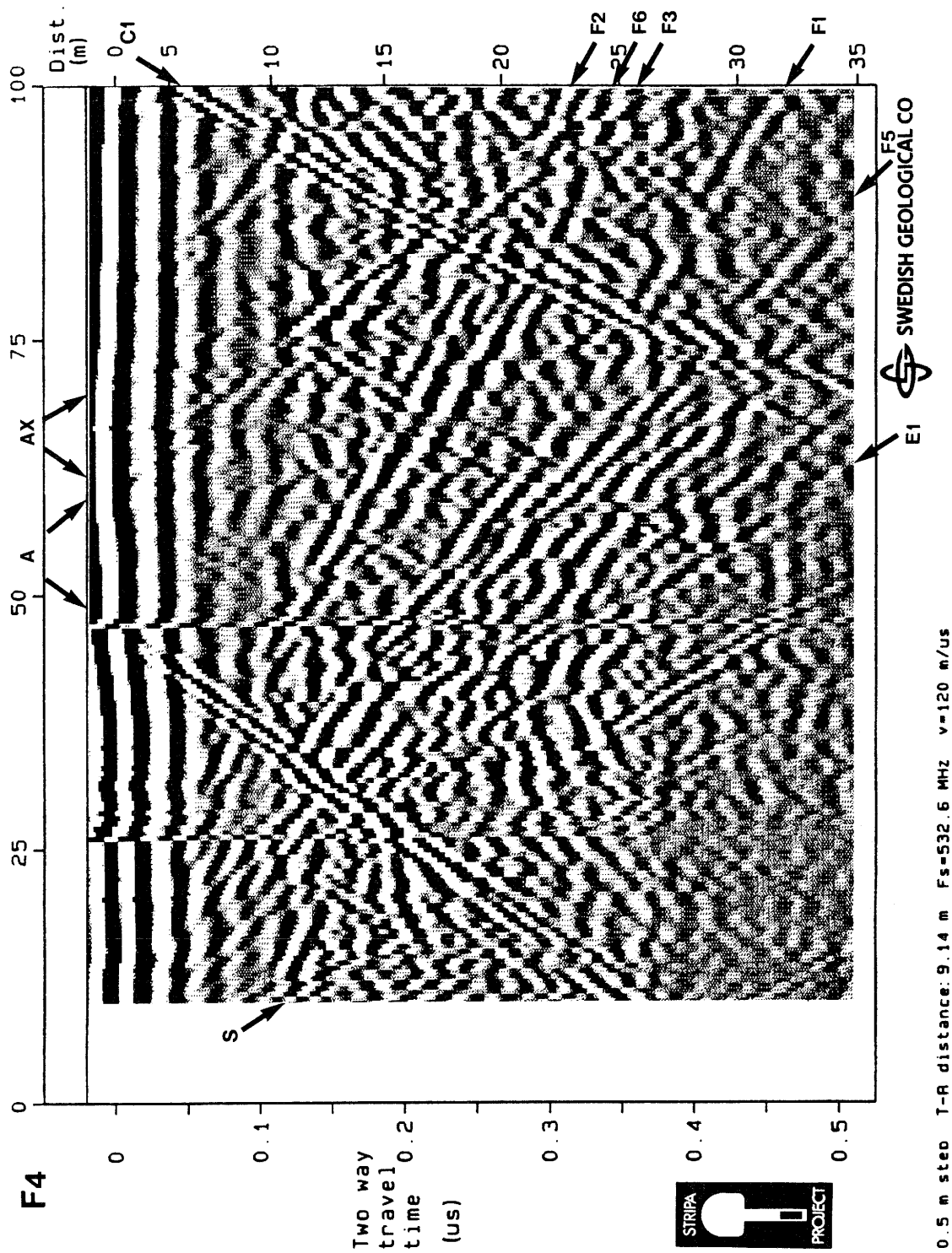


Figure A.19a Radar reflection map from the borehole F4 at the Cross-hole site in Stripa 85-09-16, measured with a center frequency of 60 MHz. Transmitter receiver spacing 4 m.

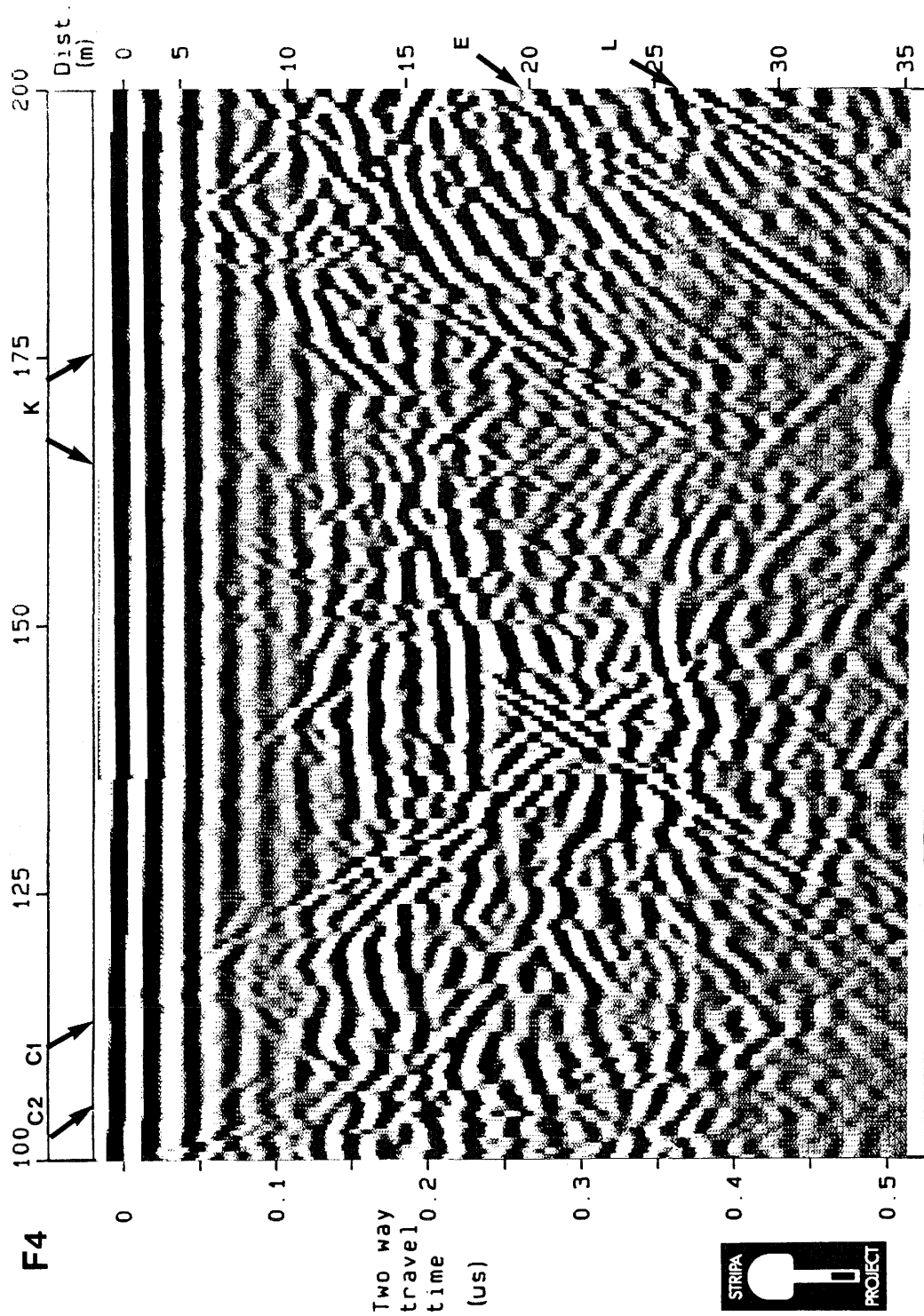


Figure A.19b Radar reflection map from the borehole F4 at the Cross-hole site in Stripa 85-09-16, measured with a center frequency of 60 MHz. Transmitter receiver spacing 4 m.

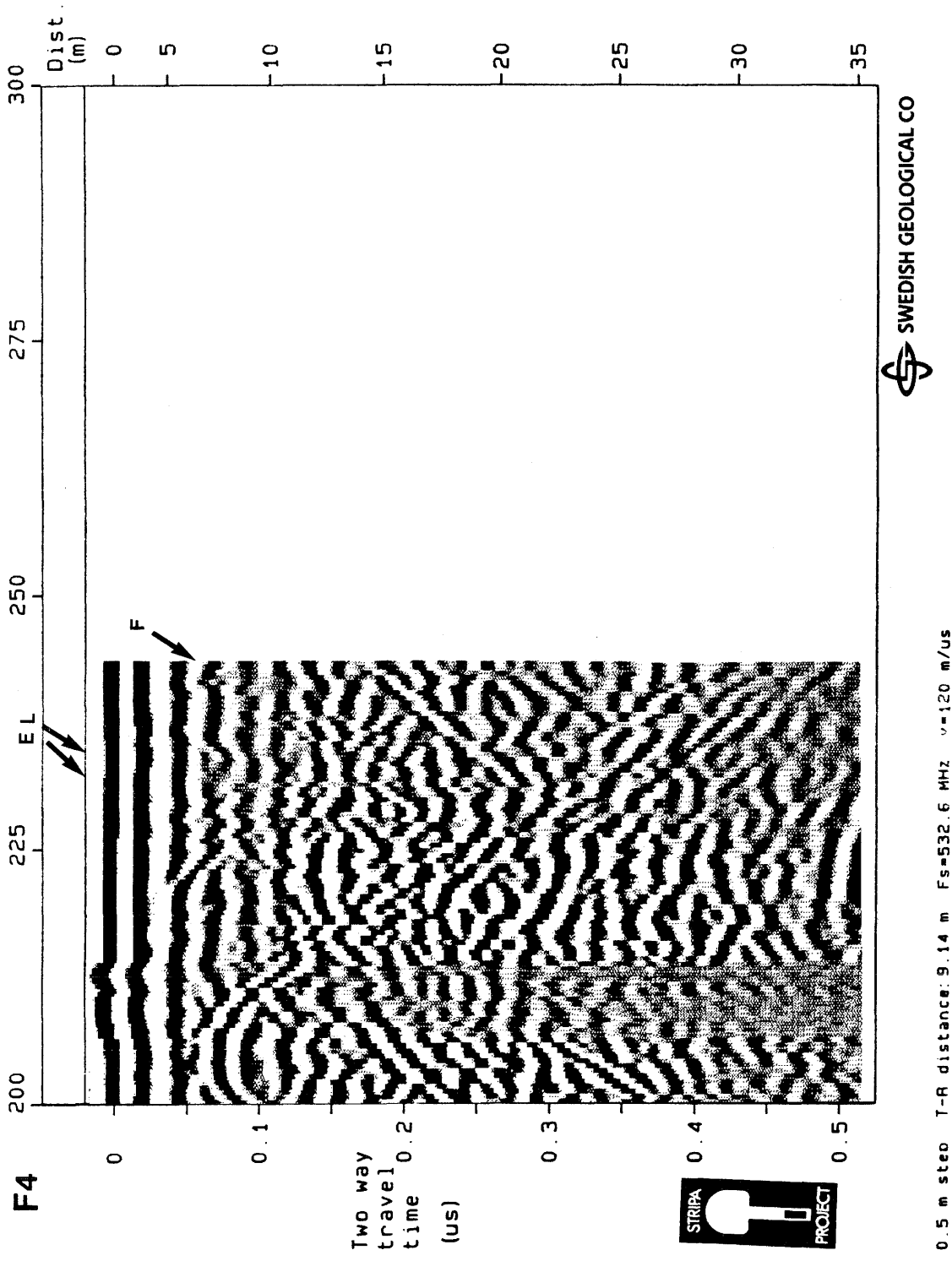


Figure A.19c Radar reflection map from the borehole F4 at the Cross-hole site in Stripa 85-09-16, measured with a center frequency of 60 MHz. Transmitter receiver spacing 4 m.

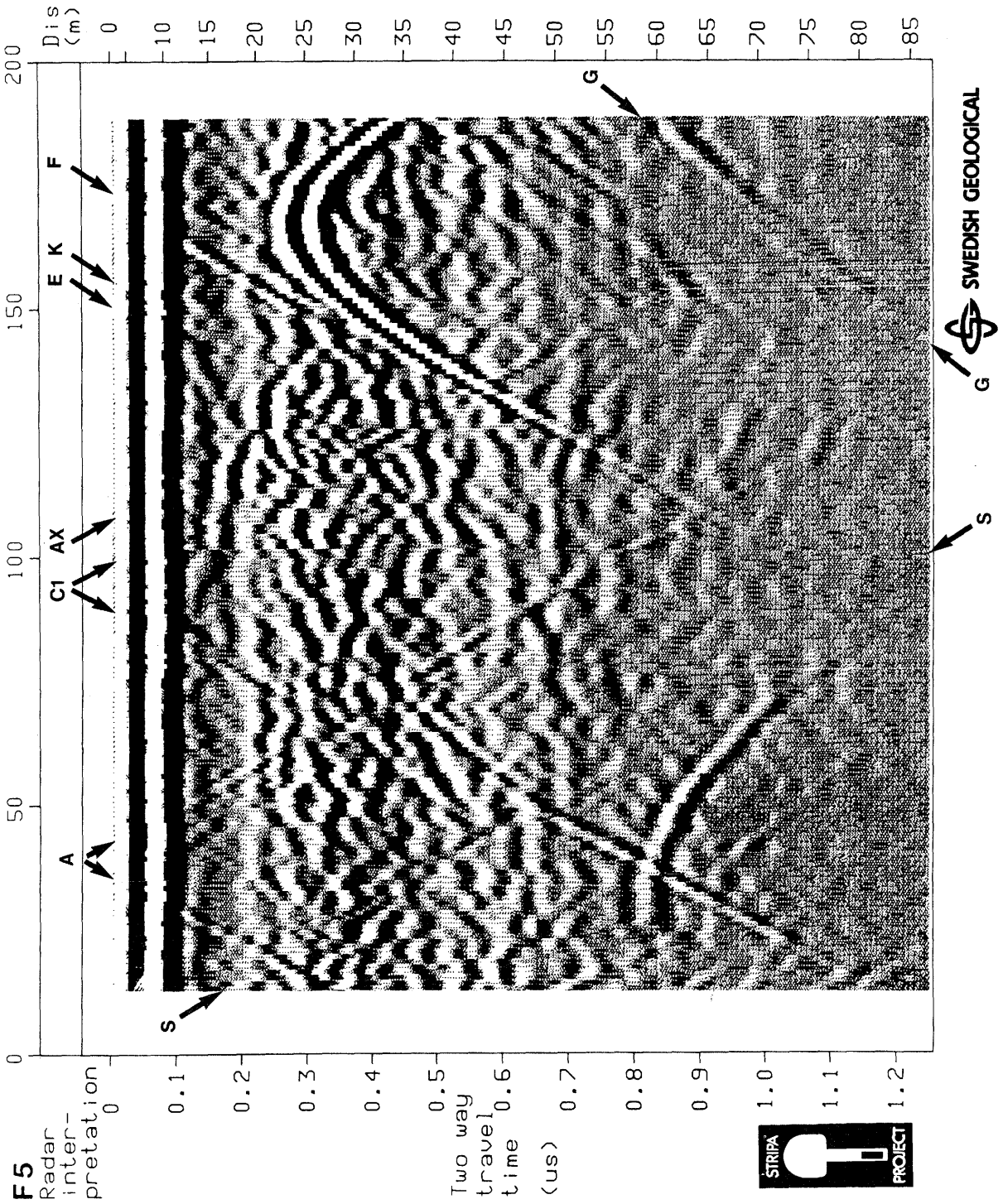


Figure A.20 Radar reflection map from the borehole F5 at the Cross-hole site in Stripa 84-11-08, measured with a center frequency of 22 MHz. Transmitter receiver spacing 10 m.

SWEDISH GEOLOGICAL
G

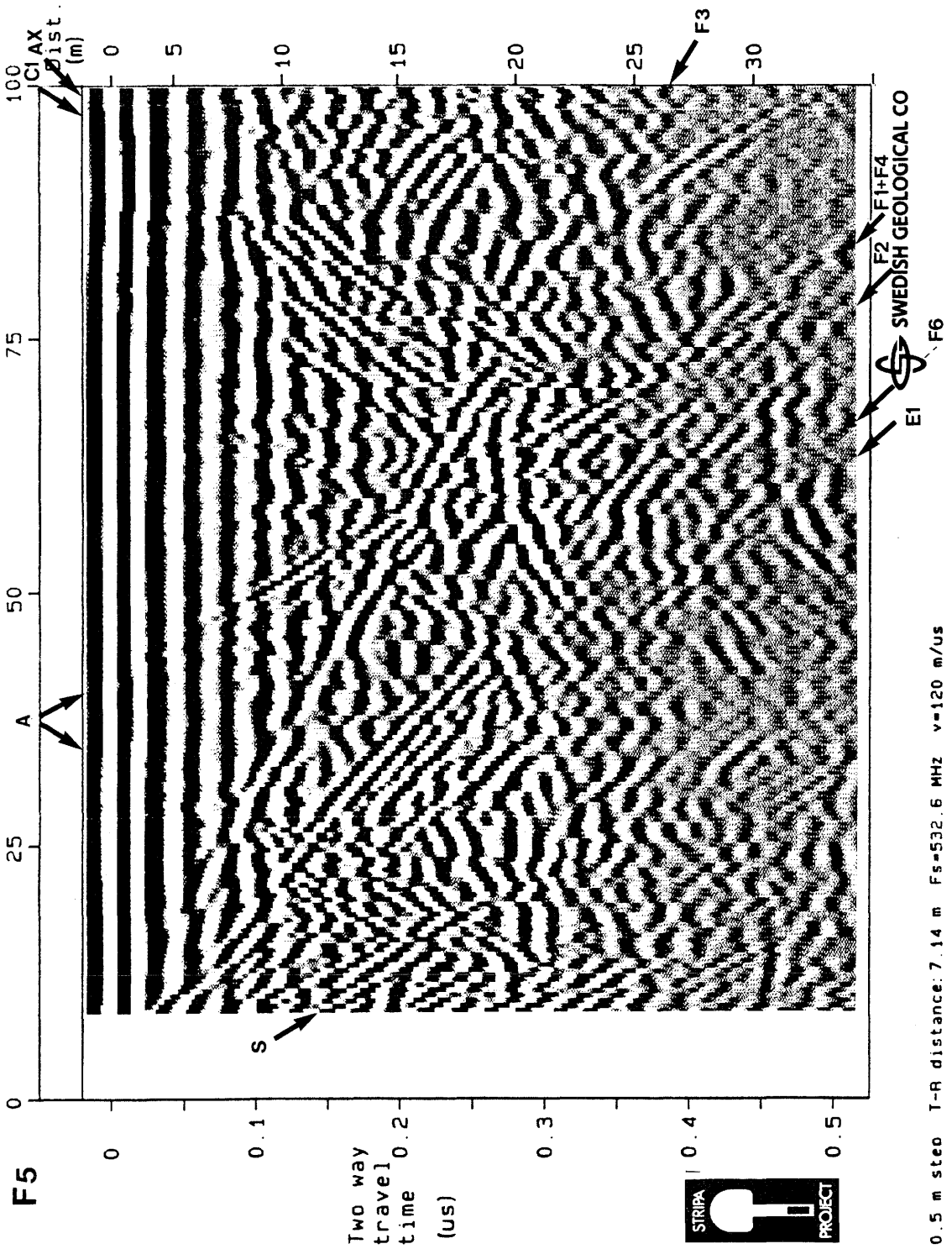
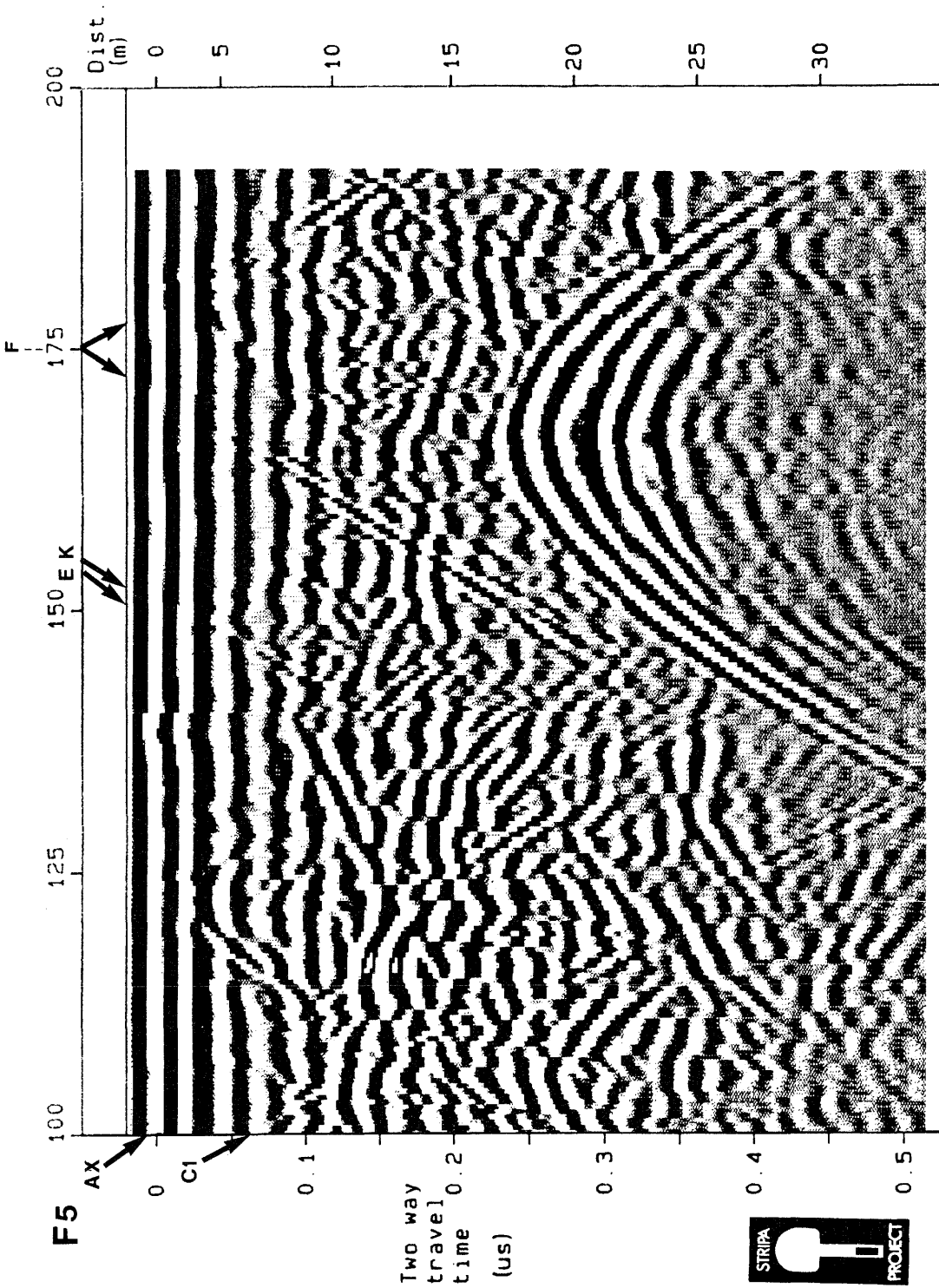


Figure A.21a Radar reflection map from the borehole F5 at the Cross-hole site in Stripa 85-11-12, measured with a center frequency of 60 MHz. Transmitter receiver spacing 2 m.



SWEDISH GEOLOGICAL CO

0.5 m step T-R distance: 7.14 m Fs=532.6 MHz v=120 m/us

Figure A.21b Radar reflection map from the borehole F5 at the Cross-hole site in Stripa 85-11-12, measured with a center frequency of 60 MHz. Transmitter receiver spacing 2 m.

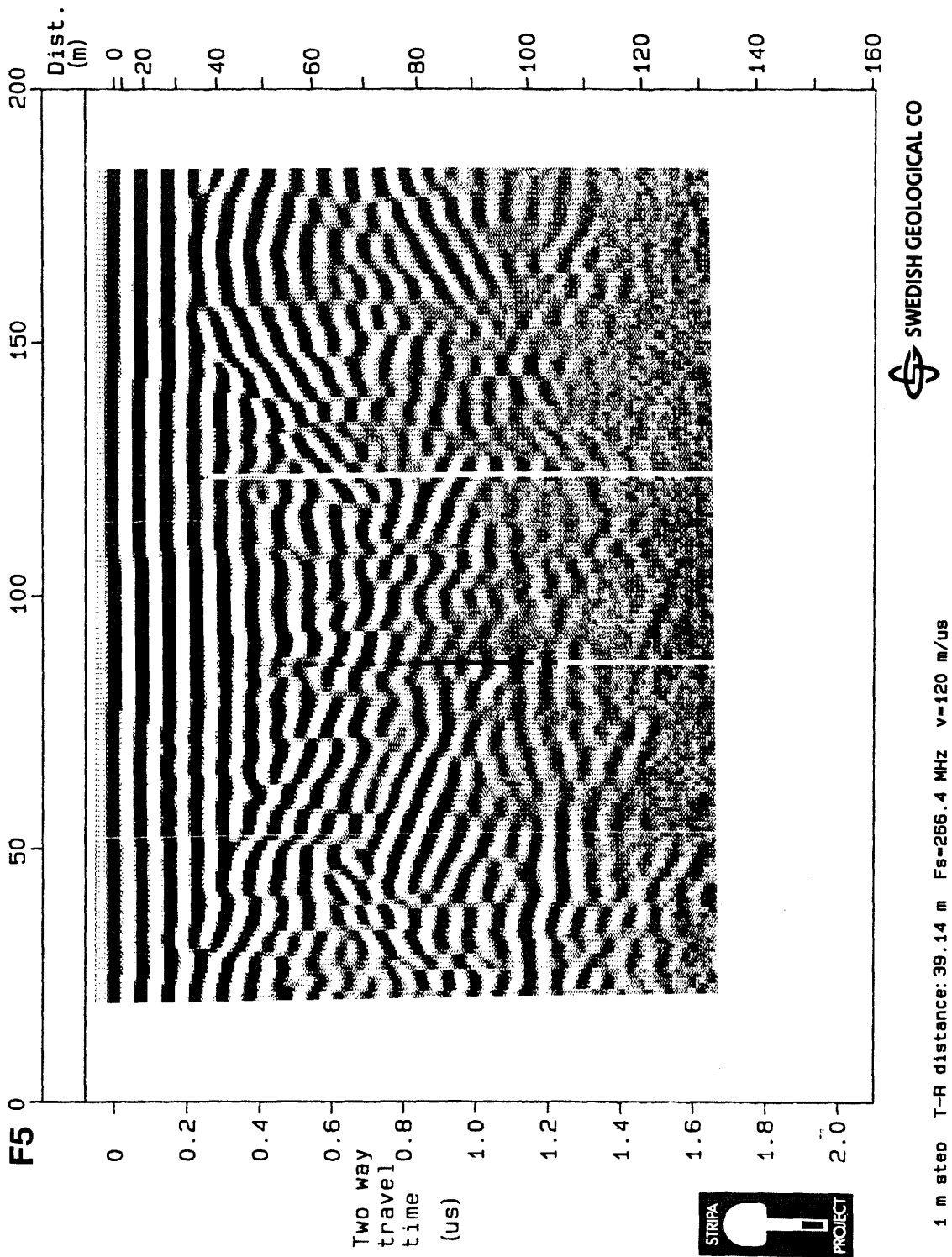


Figure A.22 Radar reflection map from the borehole F5 at the Cross-hole site in Stripa 85-09-24, measured with a center frequency of 14 MHz. Pure dipole antennas e.g. antennas without resistive load. Transmitter receiver spacing 24 m.

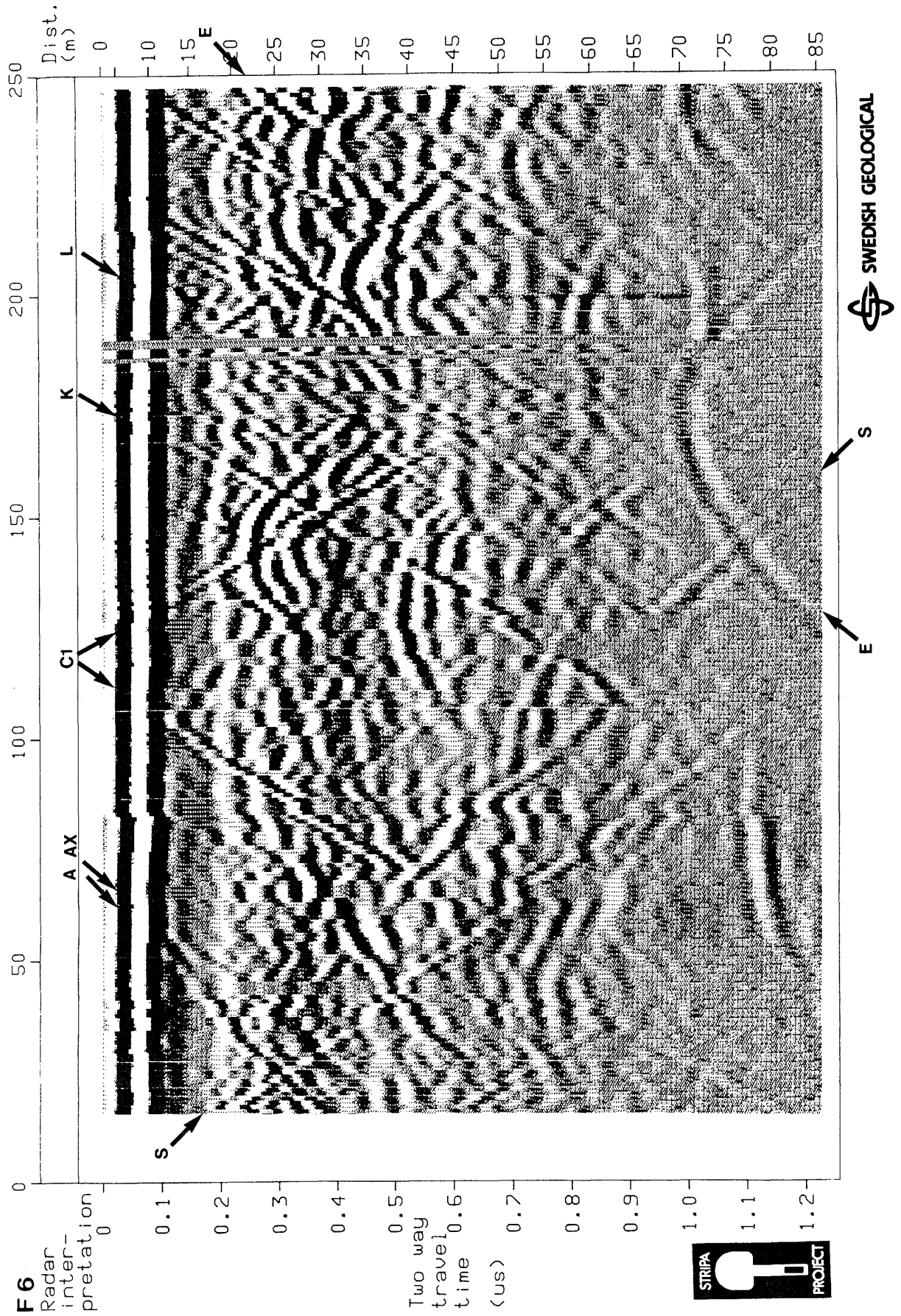


Figure A.23 Radar reflection map from the borehole F6 at the Cross-hole site in Stripa 84-11-07, measured with a center frequency of 22 MHz. Transmitter receiver spacing 10 m.

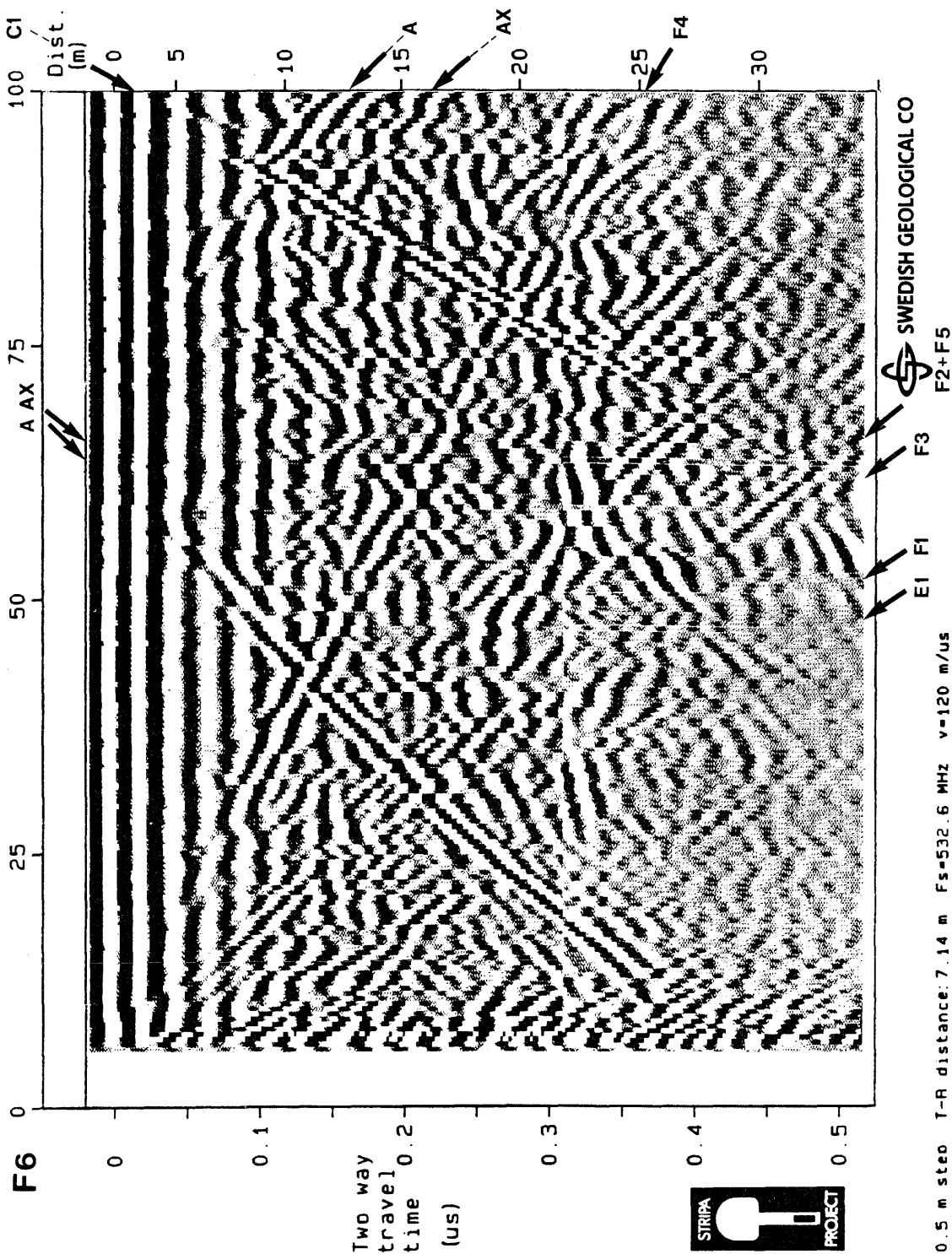


Figure A.24a Radar reflection map from the borehole F6 at the Cross-hole site in Stripa 85-11-12, measured with a center frequency of 60 MHz. Transmitter receiver spacing 2 m.

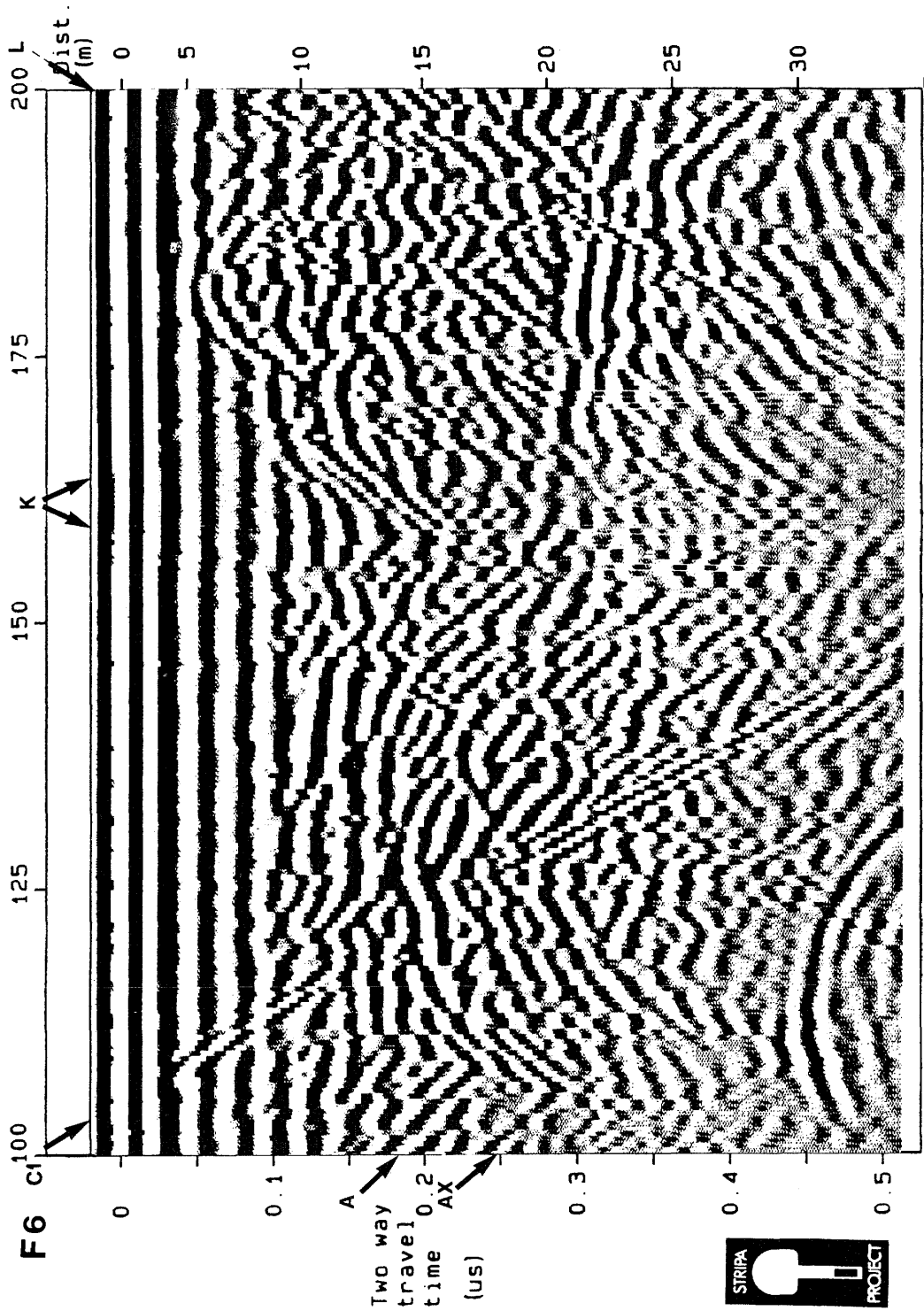


Figure A.24b Radar reflection map from the borehole F6 at the Cross-hole site in Stripa 85-11-12, measured with a center frequency of 60 MHz. Transmitter receiver spacing 2 m.

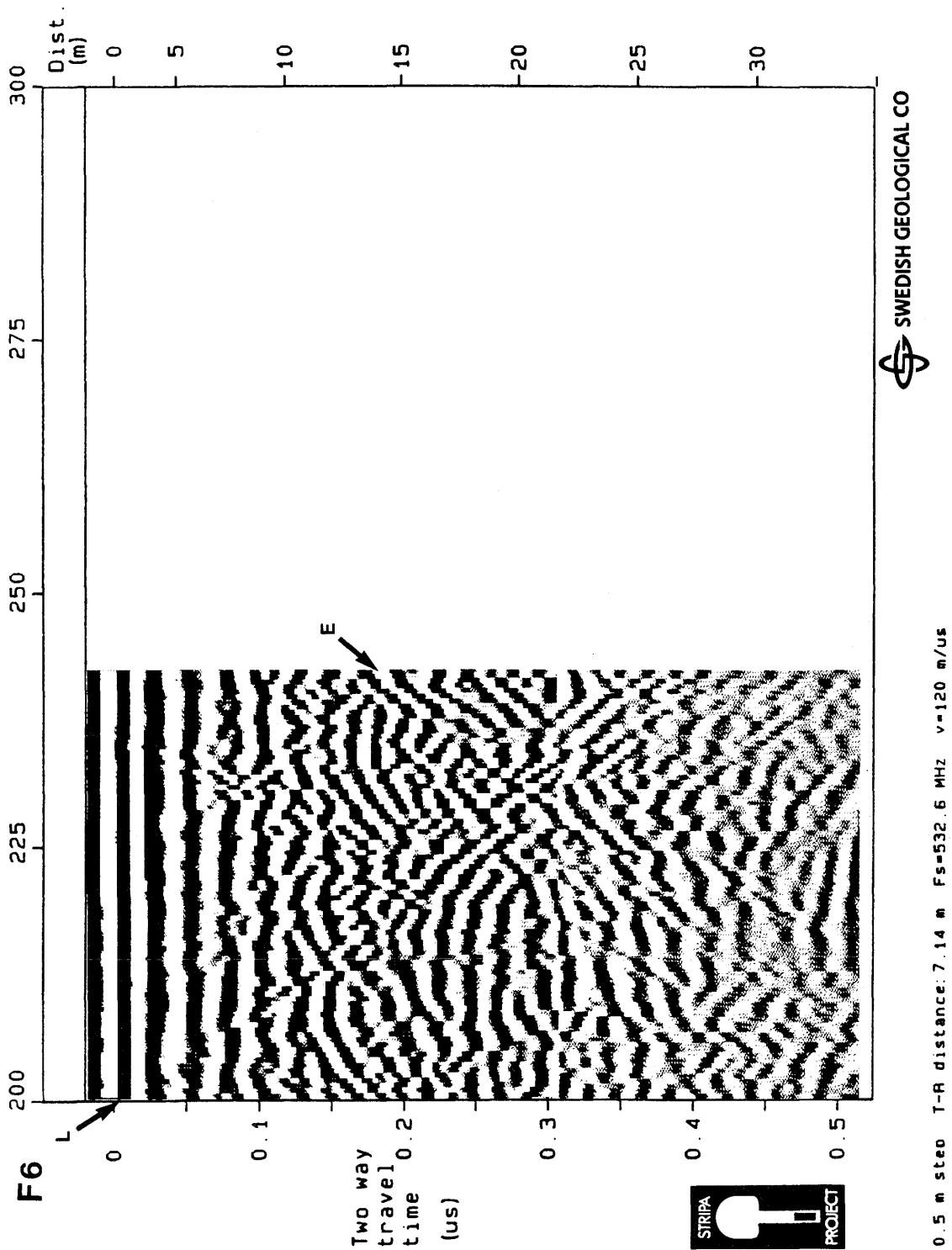


Figure A.24c Radar reflection map from the borehole F6 at the Cross-hole site in Stripa 85-11-12, measured with a center frequency of 60 MHz. Transmitter receiver spacing 2 m.

Radar plot: STRIPA E1-N1

Depth in each borehole
(m)

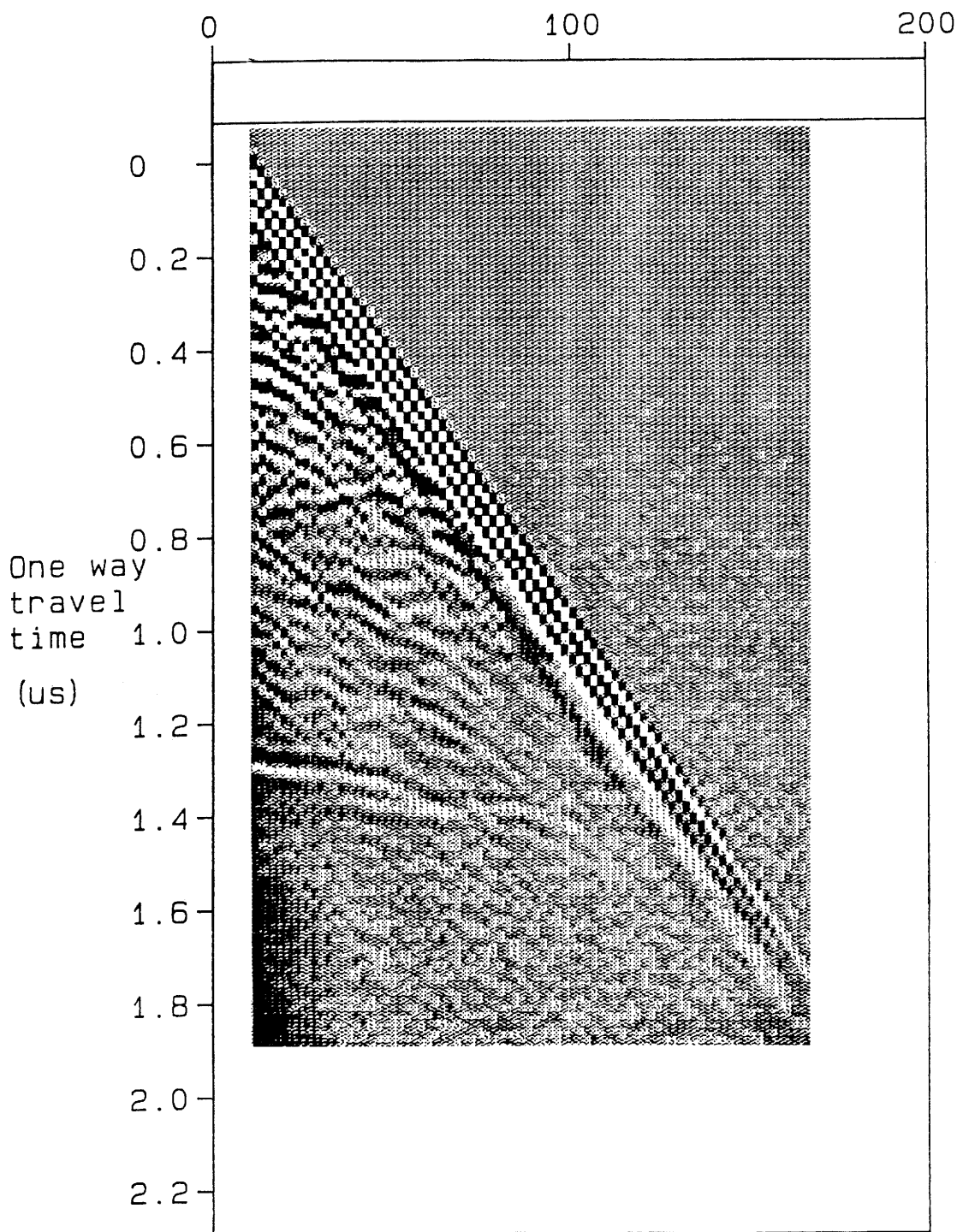


Figure A.25 Radar calibration map from the borehole E1-N1 at the Cross-hole site in Stripa 85-09-09, measured with a center frequency of 22 MHz. Transmitter and receiver moved simultaneously in each borehole.

Radar plot: STRIPA E1-N1

Depth in each borehole (m)

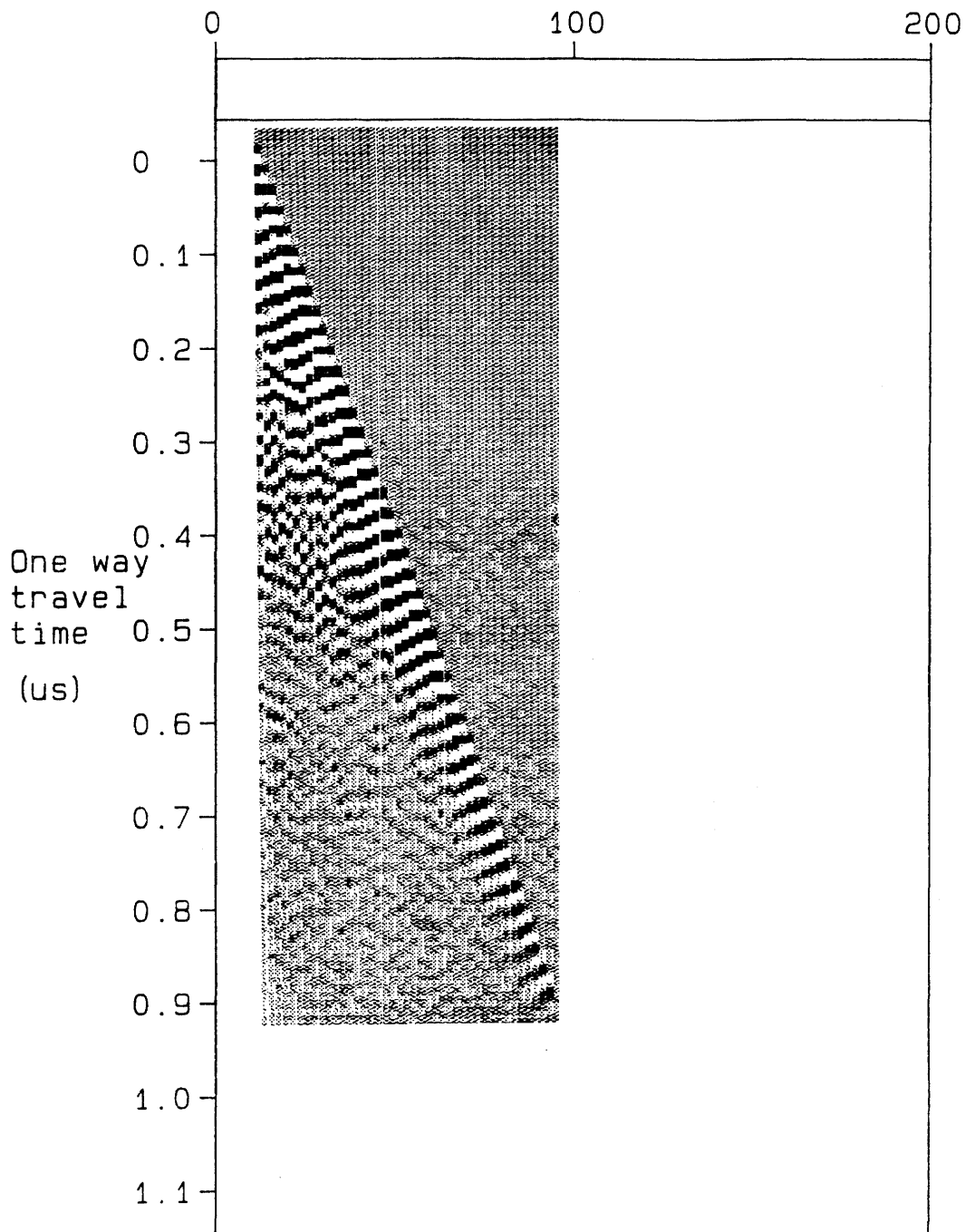


Figure A.26 Radar calibration map from the borehole E1-N1 at the Cross-hole site in Stripa 85-09-12, measured with a center frequency of 60 MHz. Transmitter and receiver moved simultaneously in each borehole.

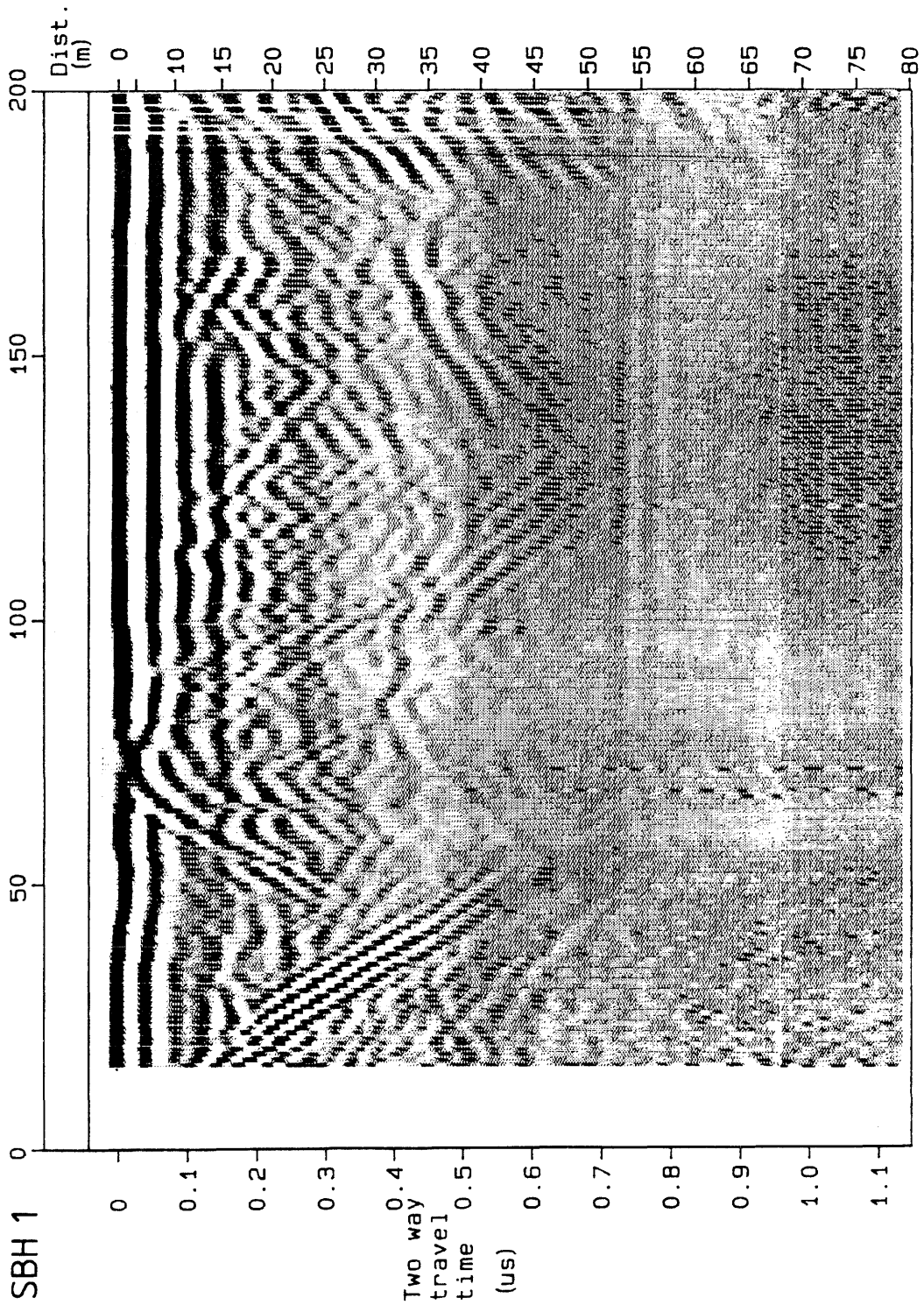


Figure A.27a Radar reflection map from the borehole SBH1 drilled from the ground surface at the Stripa mine, measured 85-08-06 with a center frequency of 22 MHz. Transmitter receiver spacing 10 m.

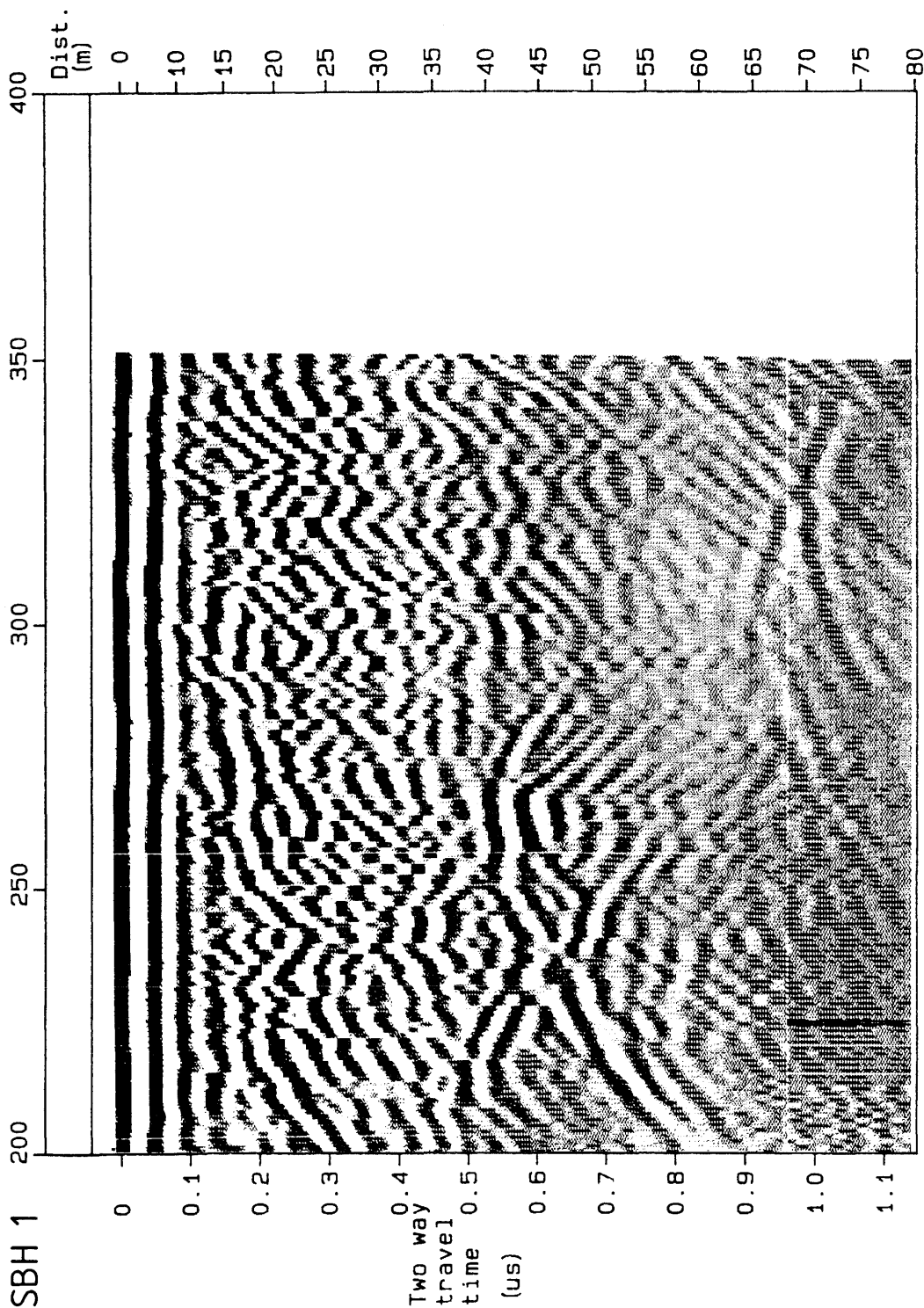


Figure A.27b Radar reflection map from the borehole SBH1 drilled from the ground surface at the Stripa mine, measured 85-08-06 with a center frequency of 22 MHz. Transmitter receiver spacing 10 m.

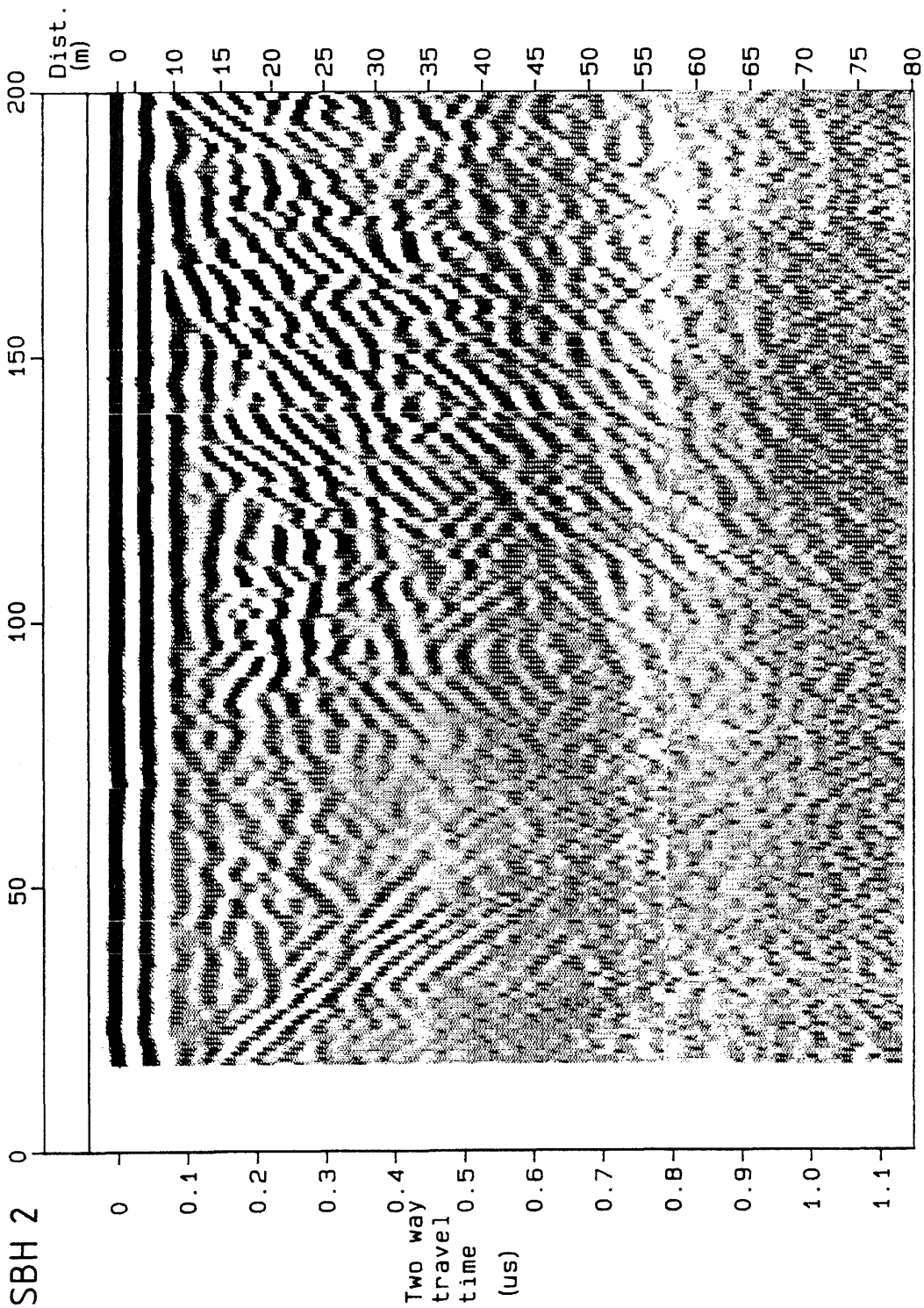


Figure A.28a Radar reflection map from the borehole SBH2 drilled from the ground surface at the Stripa mine, measured 85-08-07 with a center frequency of 22 MHz. Transmitter receiver spacing 10 m.

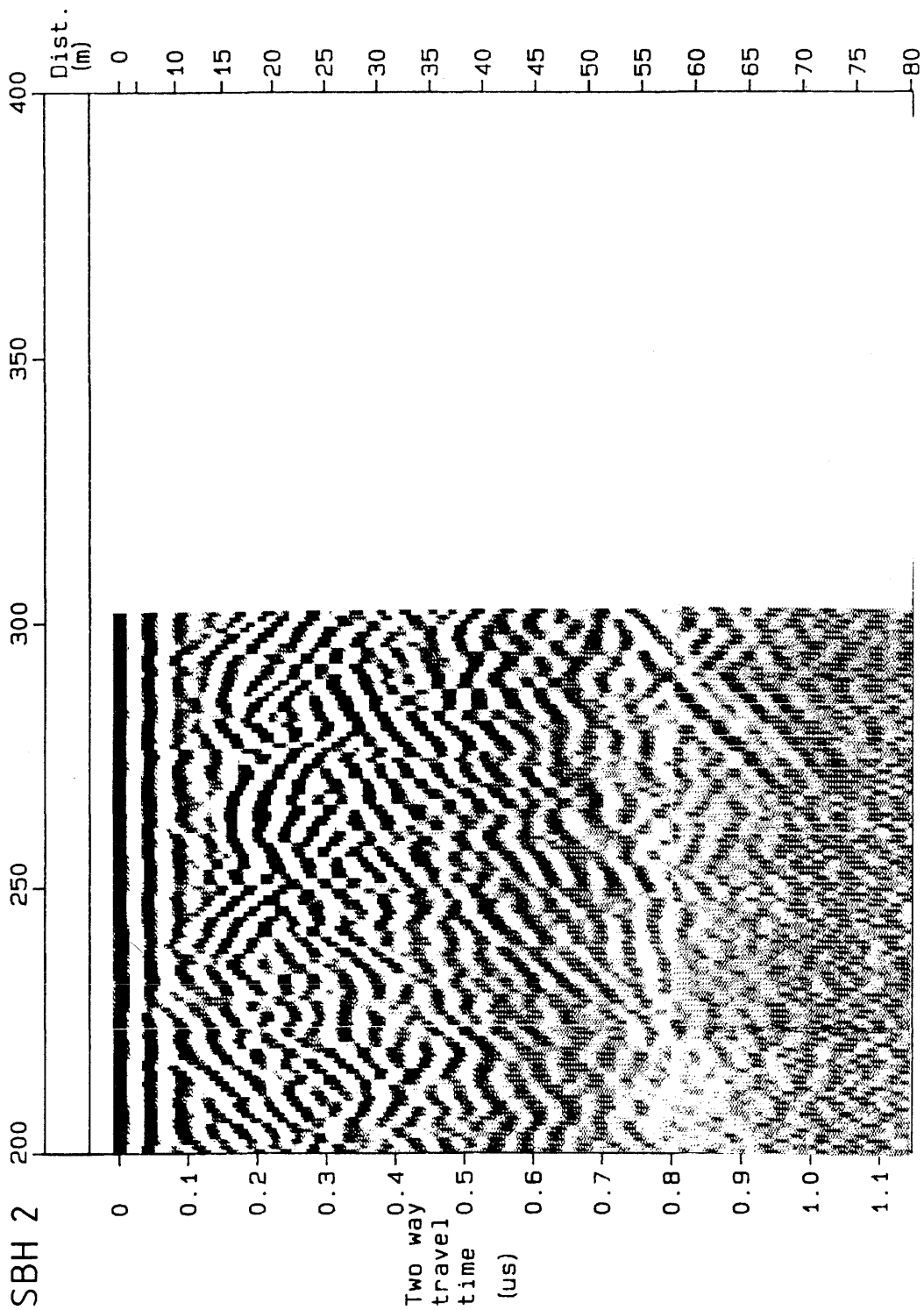


Figure A.28b Radar reflection map from the borehole SBH2 drilled from the ground surface at the Stripa mine, measured 85-08-07 with a center frequency of 22 MHz. Transmitter receiver spacing 10 m.

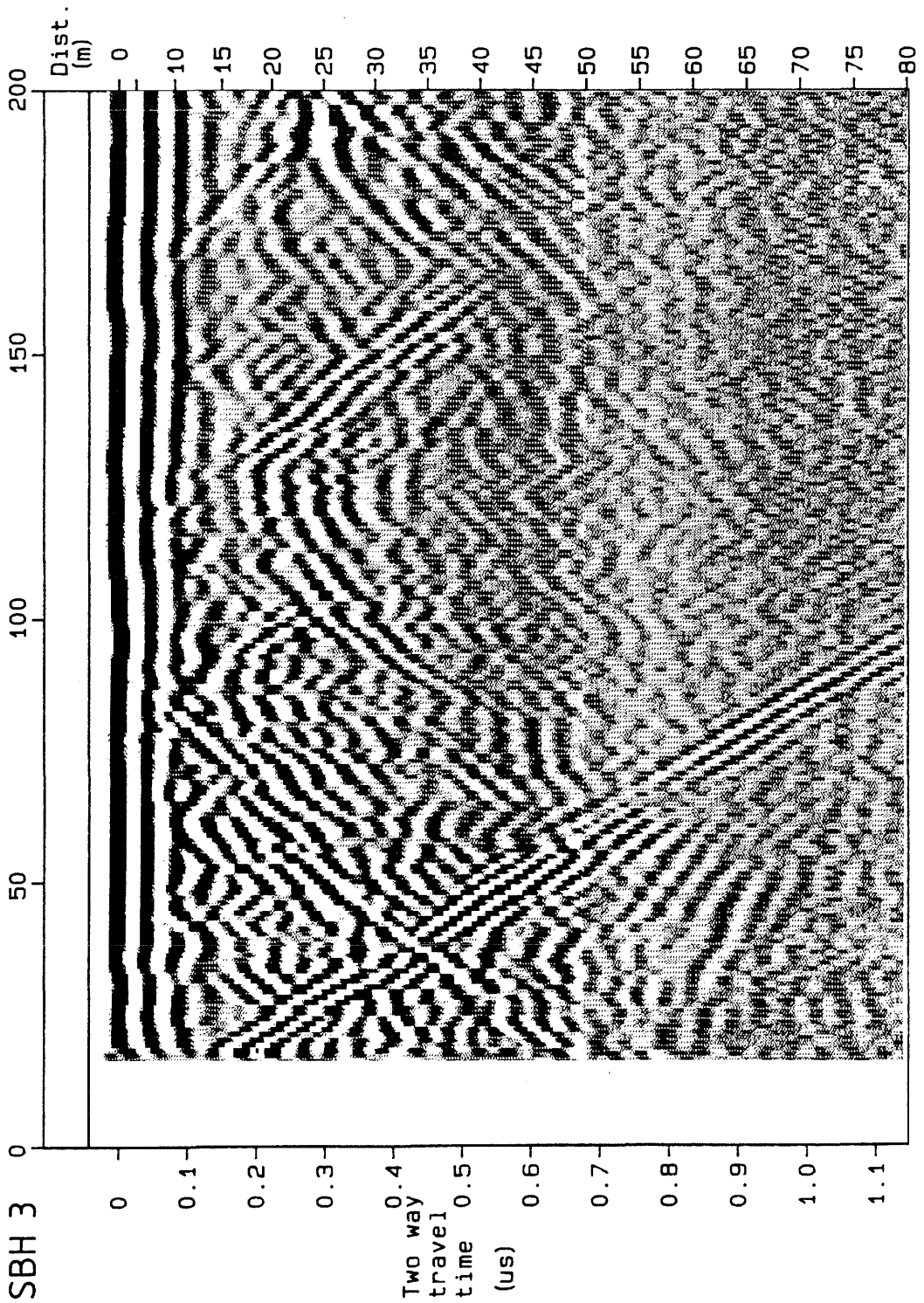


Figure A.29a Radar reflection map from the borehole SBH3 drilled from the ground surface at the Stripa mine, measured 85-08-08 with a center frequency of 22 MHz. Transmitter receiver spacing 10 m.

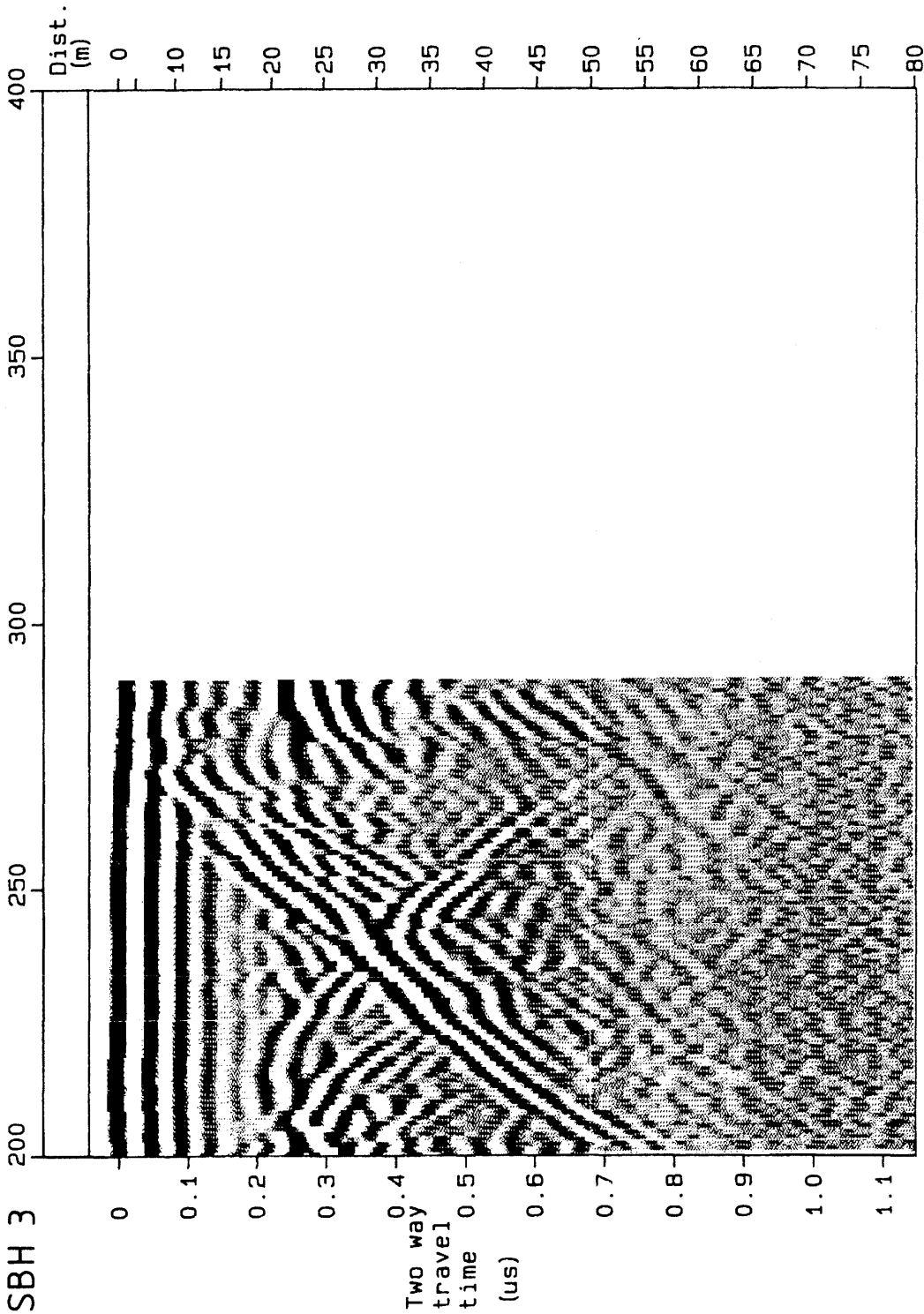


Figure A.29b Radar reflection map from the borehole SBH3 drilled from the ground surface at the Stripa mine, measured 85-08-08 with a center frequency of 22 MHz. Transmitter receiver spacing 10 m.

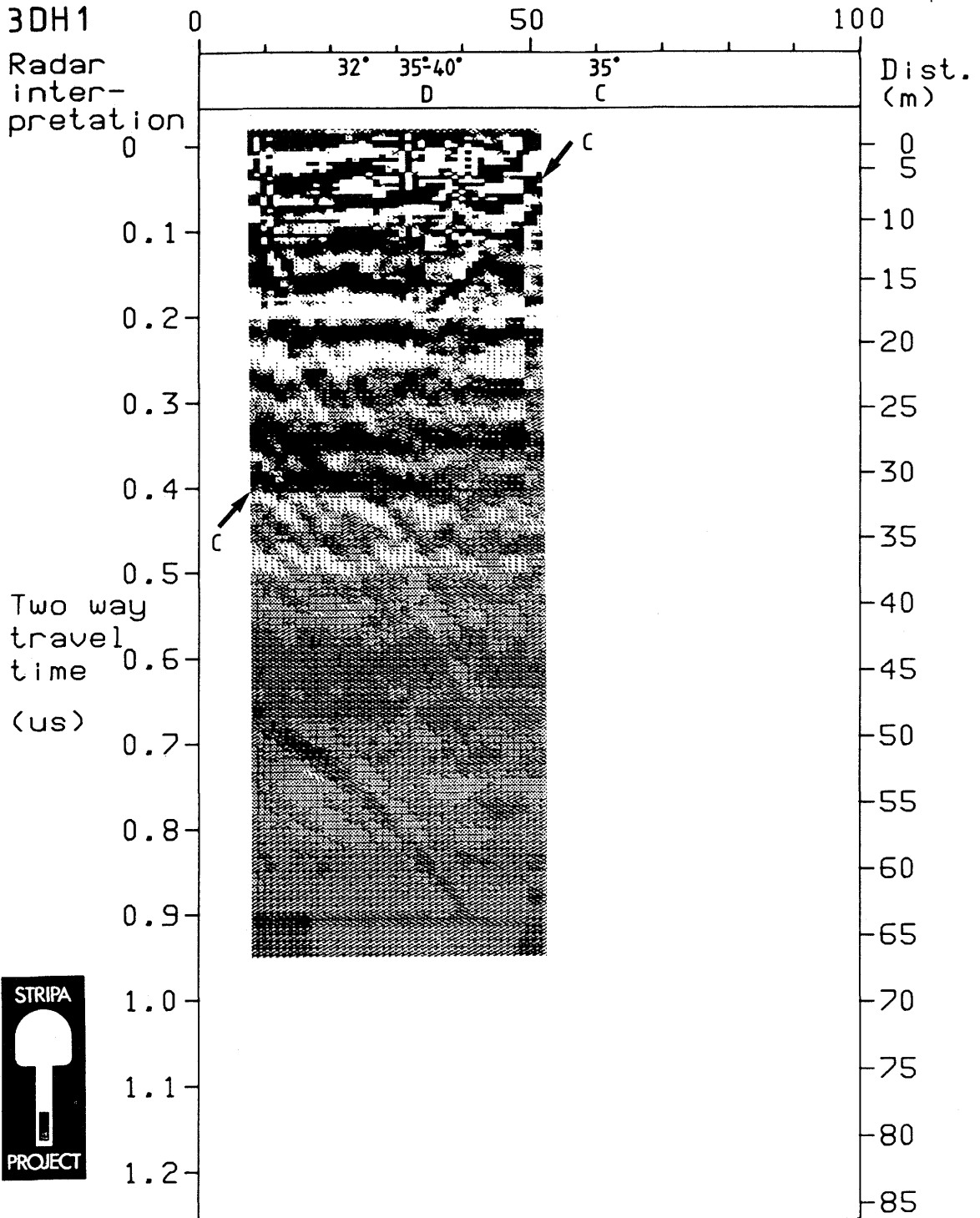


Figure A.30 Radar reflection map from the borehole 3DH1 drilled from the 3D migration drift at the Stripa mine, measured 84-08-31 with a center frequency of 22 MHz. Transmitter receiver spacing 8 m. For definition of zones see Stripa Project Quarterly Report July-September, 1984.

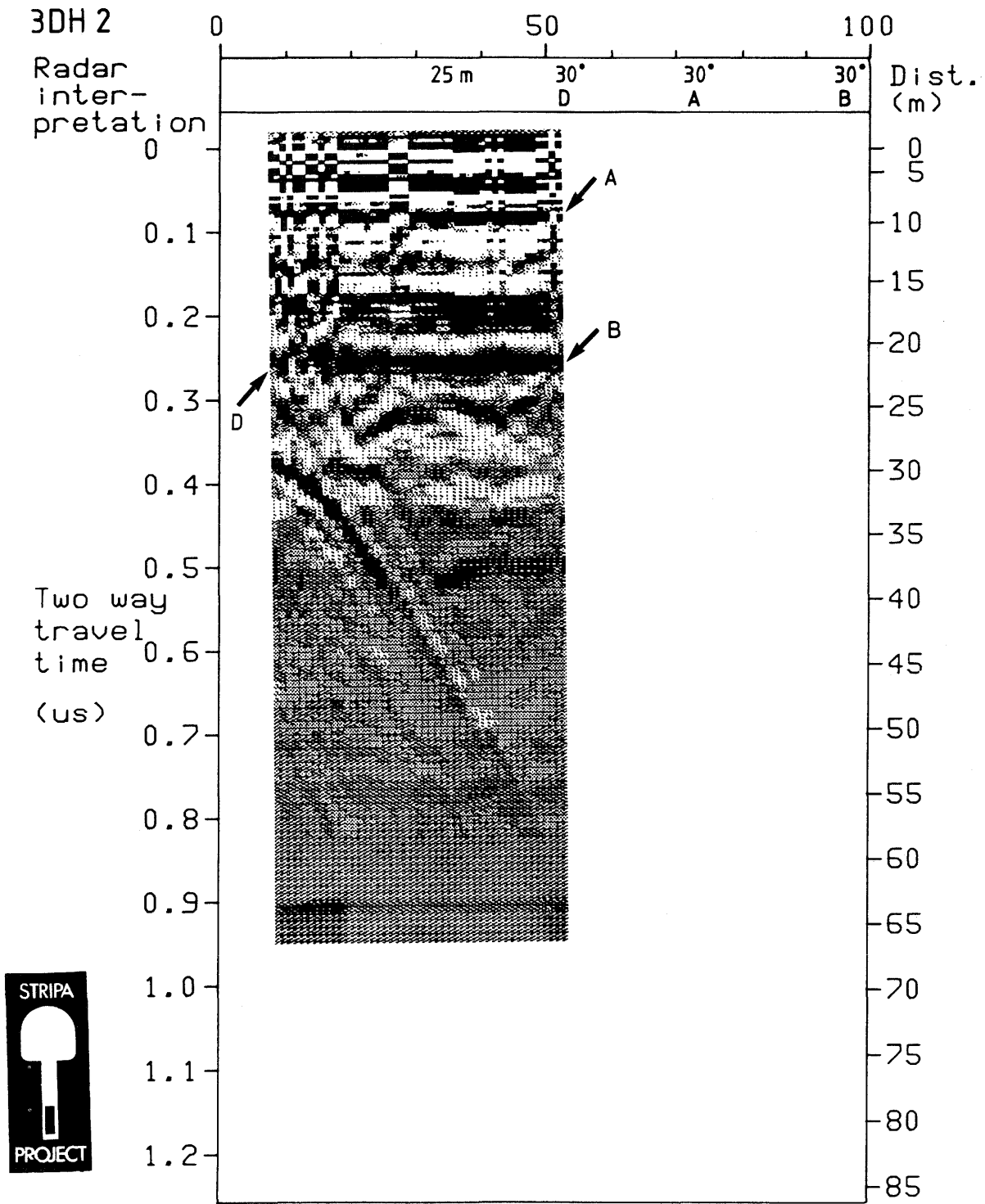


Figure A.31 Radar reflection map from the borehole 3DH2 drilled from the 3D migration drift at the Stripa mine, measured 84-08-31 with a center frequency of 22 MHz. Transmitter receiver spacing 8 m. For definition of zones see Stripa Project Quarterly Report July-September, 1984.

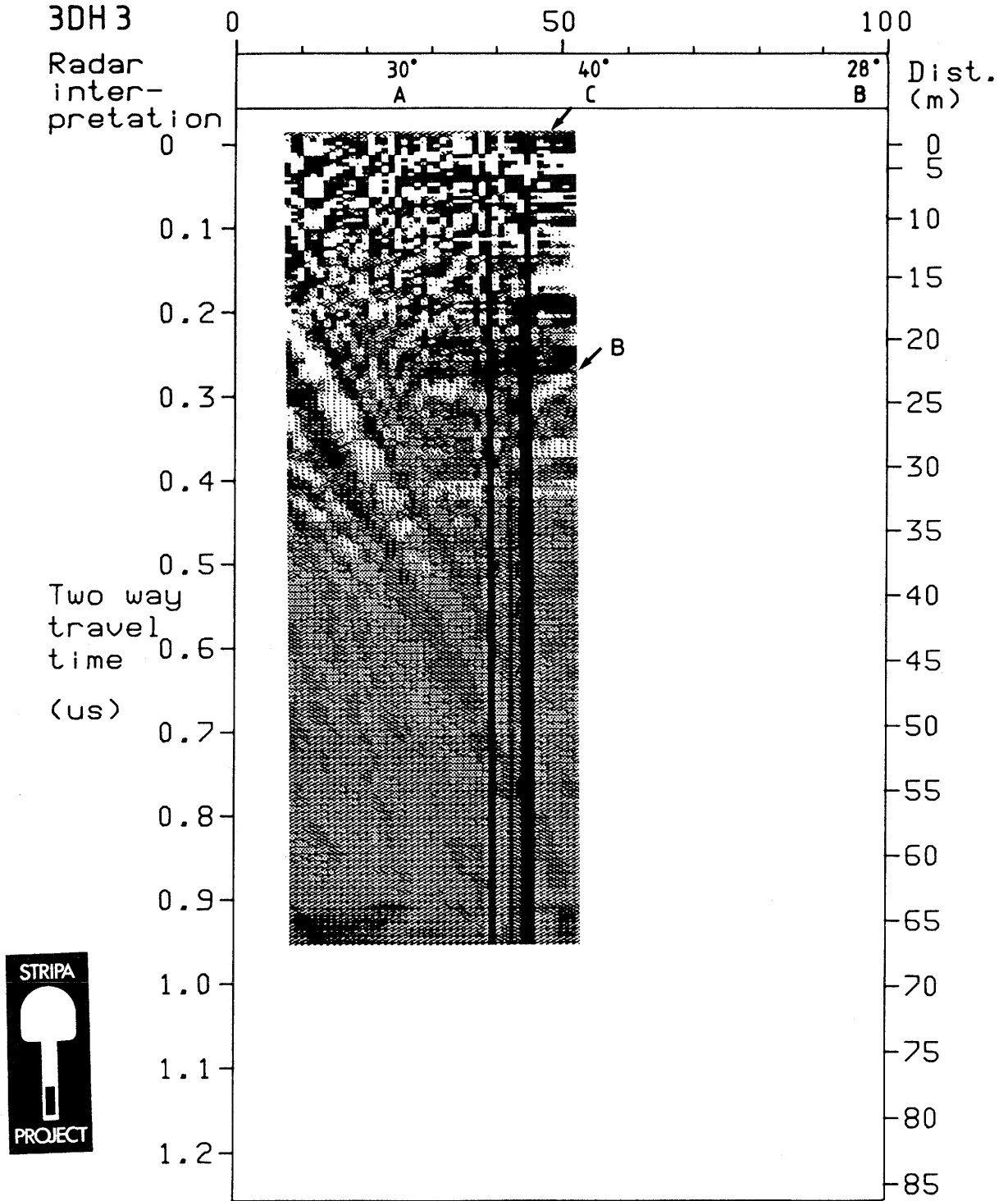


Figure A.32 Radar reflection map from the borehole 3DH3 drilled from the 3D migration drift at the Stripa mine, measured 84-08-31 with a center frequency of 22 MHz. Transmitter receiver spacing 8 m. For definition of zones see Stripa Project Quarterly Report July-September, 1984.

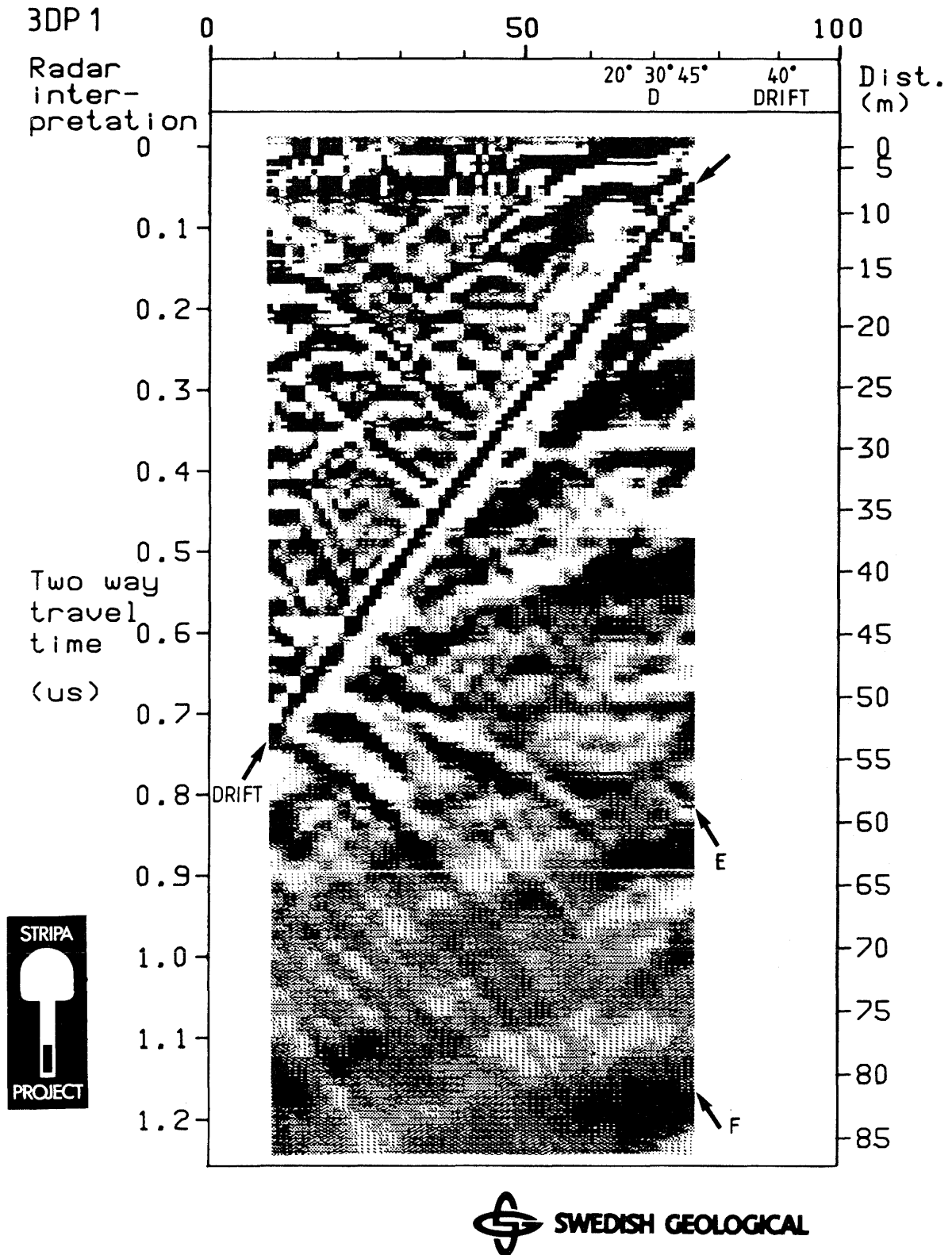


Figure A.33 Radar reflection map from the borehole 3DP1 drilled as a pilot hole for the 3D migration drift at the Stripa mine, measured 84-09-06 with a center frequency of 22 MHz. Transmitter receiver spacing 10 m. For definition of zones see Stripa Project Quarterly Report July-September, 1984.



APPENDIX B

LIST OF REFLECTIONS IDENTIFIED AT THE CROSSHOLE SITE

This list contains all reflections observed in the singlehole measurements performed at the Crosshole Site. The reflections have been analysed independently for measurements performed at the center frequencies 22 and 60 MHz.

The radar angles measured at 60 MHz have been calibrated by direct comparison with the borehole angles which are accurately known. No corrections have been applied the 22 MHz data but the good agreement with 60 MHz measurements indicates that the time calibration was in order. The list indicates for each reflection the borehole depth where the fracture zones intersects the borehole and the angle of intersection judging from the left and right part of the reflection pattern in the radar plots; in many cases only one of these angles can be found.

Only reasonably visible zones have been included in the tables. The strengths of the reflection have been classified according to a simple scale:

- 1 = very strong and persistent reflections corresponding to major fracture zones;
- 2 = a strong and clear reflection often visible at large range from the borehole;
- 3 = a weak but welldefined reflection;
- 4 = barely visible reflection.

Borehole E1

zone	depth		left angle		right angle		strength	
	22	60	22	60	22	60	22	60
Site	-10				45		2	
A	35				47		2	
	42				40		3	
	42				42		3	
AX	66				52		3	
B	98		43		38		3	
	100		52				4	
	105		55				4	
C1	120				35		3	
	130		47		47		1	
	145		38		40		2	
C2	150		35				4	
	170		47				3	
E	170		34				3	
	195		47				2	
F	223		55				1	
K	230		45				2	
G	270		43				3	
	330		37				1	
L								

Borehole F1

zone	depth		left angle		right angle		strength	
	22	60	22	60	22	60	22	60
Site	-5	-5			45	55	2	2
A	39	39	64	59	48	58	2	2
	39				37		3	
		66		50				3
AX								
B	92		52				3	
	100		36				3	
		105		49				3
C1	105		52				3	
	118	118	56	59	61	59	1	1
		124		42		41		2
C2		138		40			4	
		146		56				4
	150		32				4	
E	171	171	57	42			3	4
		176		55				3
								3
K	192		55					
F or G	207		56				3	
	235		37				2	
L	280		27				2	

Borehole F2

zone	depth		left angle		right angle		strength	
	22	60	22	60	22	60	22	60
Site	-5	-5			43	53	2	2
A	42	42	42	48	41	44	2	2
	60				24			4
AX	65	66	52	50		54	4	3
	92	91	52	50			4	3
	98		50				3	
B		103		48				3
	100		65					3
C2	119	115	45	44	47	39	1	1
C1	119	118	49		53	63	1	2
	129	134			47	49	3	3
	157	163	39	38		39	4	2
K	189	185		40	45	45	2	2
E	207	207	39	39		41	3	2
	218		47				4	
F	229	229	43	37			2	2
L	263	271	50	46			1	1
	273		55				2	
	270		14				2	
G	310		30				1	

Borehole F3

zone	depth		left angle		right angle		strength	
	22	60	22	60	22	60	22	60
Site	-5	-6			45	51	3	3
	8				50		4	
	32				28		3	
A	40	39		55	55	59	2	2
		46		38				4
AX	56		57				3	
B	85		55				3	
	89		31				4	
C2		105		41		45		2
C1	109	105	54	56	53	56	1	1
	126	118			28	31	3	3
E	153	154	42	38			2	2
F		154		51				3
K	172	172	48	46		42	2	2
	211		50				3	
G	220	223	50	45			2	2
		227		45				2
	250		50				2	

Borehole F4

zone	depth		left angle		right angle		strength	
	22	60	22	60	22	60	22	60
Site	-5	-4			40	63	2	2
	-2	0			58	50	2	2
A	54	54	36	42	45	35	2	2
	54				32		3	
	70	63			27	24	3	3
AX	64	63	53			53	3	3
C2		93		55				2
	100				30		3	
Cl	109	107	60	56	62	55	1	1
	118	124	47	50		39	3	3
K	170	169	50	53	48	59	2	2
	177	177			34	36	2	3
	177		23					3
		188		55			2	
		190		59			2	
	200		13				2	
		200		59		55		3
	210		22				4	
	210	212	48			45	2	2
E	229	234	34	40			2	2
L	234	234	53	55			1	2
	248		49				3	
F	258		43				2	
		270		38				3
	290		40				2	

Borehole F5

zone	depth		left angle		right angle		strength	
	22	60	22	60	22	60	22	60
Site	-5	-8			58	50	2	2
A	39	36	62	63	62	57	1	1
		41		52				3
	69		32		44		3	
	80				23		3	
C	93	96	67	55	70	70	1	1
		100		36		42		2
	136	127	48	48			4	3
	150		18				4	
E	150	150	55	54		58	3	3
K	155		60				3	
	170	171	16	16			3	2
	170		28				3	
F	173	175	50	48		50	2	2
	211		18				4	
		212		38				3
	215	220	52	48			2	3
	215		12				4	
	243		32				3	
	280		43				1	

Borehole F6

zone	depth		left angle		right angle		strength	
	22	60	22	60	22	60	22	60
		-17				80		3
		-7				90		3
Site	-4				30		1	
	-4				40		1	
	23				27		2	
AX		68		48		42		3
A	72	70	27	32	24	35	2	2
		99		26				3
C	111	103	50	59	56	57	1	1
	130		22				2	
	150		13				2	
	162		33		43		4	
K	168	162	58	57		57	1	2
		187		39		36		3
	205	200	44	46			3	3
L	205		60		60		2	
		213		35		34		2
	218	220	53	50			2	2
	225		10				3	
	240	240	65	63			2	2
	250		29				3	
		266		42				3
E	270		27				3	
	272		53				2	

APPENDIX C
RESULTS OF TOMOGRAPHIC INVERSION OF
CROSSHOLE RADAR DATA

Crosshole section F4-F1, April-85

Figure C.1 Tomographic reconstruction of slowness distribution for the borehole section F4-F1 based on residual travel time data. Cell size 2.5 m. Center frequency 22 MHz.

Figure C.2 Tomographic reconstruction of attenuation distribution for the borehole section F4-F1 based on residual amplitude data. Cell size 2.5 m. Center frequency 22 MHz.

Crosshole section F4-F5, April-85

Figure C.3 Tomographic reconstruction of slowness distribution for the borehole section F4-F5 based on residual travel time data. Cell size 2.5 m. Center frequency 22 MHz.

Figure C.4 Tomographic reconstruction of attenuation distribution for the borehole section F4-F5 based on residual amplitude data. Cell size 2.5 m. Center frequency 22 MHz.

Crosshole section F6-F1, Sept-85

Figure C.5 Tomographic reconstruction of slowness distribution for the borehole section F6-F1 based on residual travel time data. Cell size 2.5 m. Center frequency 22 MHz.

Figure C.6 Tomographic reconstruction of slowness distribution for the borehole section F6-F1 based on residual travel time data. Cell size 5 m. Center frequency 22 MHz. Same input data as for Figure C.5.

Figure C.7 Tomographic reconstruction of attenuation distribution for the borehole section F6-F1 based on residual amplitude data. Cell size 2.5 m. Center frequency 22 MHz.

Crosshole section F2-F5, Sept-85

Figure C.8 Tomographic reconstruction of slowness distribution for the borehole section F2-F5 based on residual travel time data. Cell size 2.5 m. Center frequency 22 MHz.

Figure C.9 Tomographic reconstruction of attenuation distribution for the borehole section F2-F5 based on residual amplitude data. Cell size 2.5 m. Center frequency 22 MHz.

Crosshole section F4-F5, Sept-85, 60 MHz

Figure C.10 Tomographic reconstruction of slowness distribution for the borehole section F4-F5 based on residual travel time data. Cell size 2.5 m. Center frequency 60 MHz.

Figure C.11 Tomographic reconstruction of amplitude distribution for the borehole section F4-F5 based on residual amplitude data. Cell size 2.5 m. Center frequency 60 MHz.

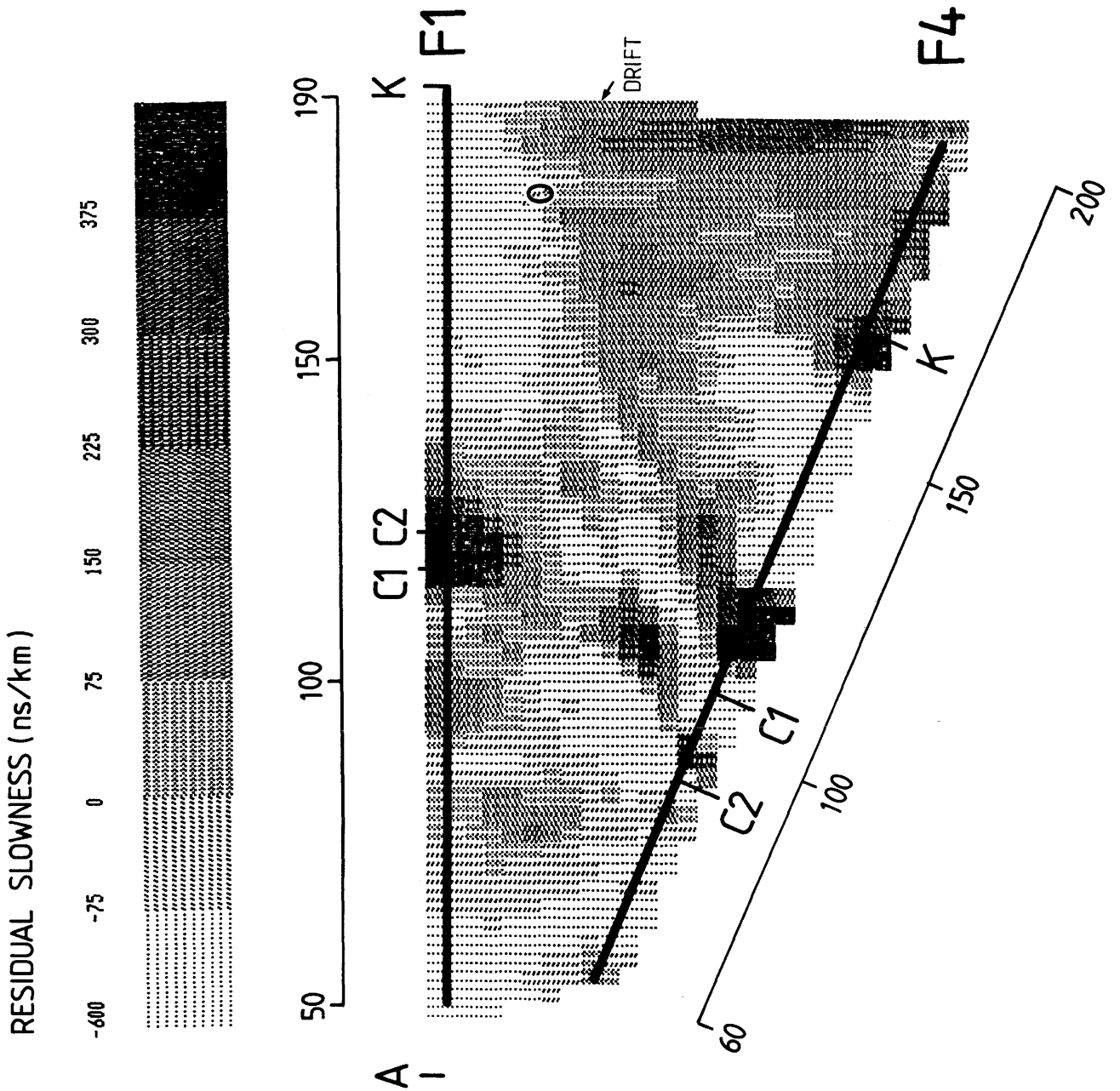


Figure C.1 Tomographic reconstruction of slowness distribution for the borehole section F4-F1 based on residual travel time data. Cell size 2.5 m. Center frequency 22 MHz.

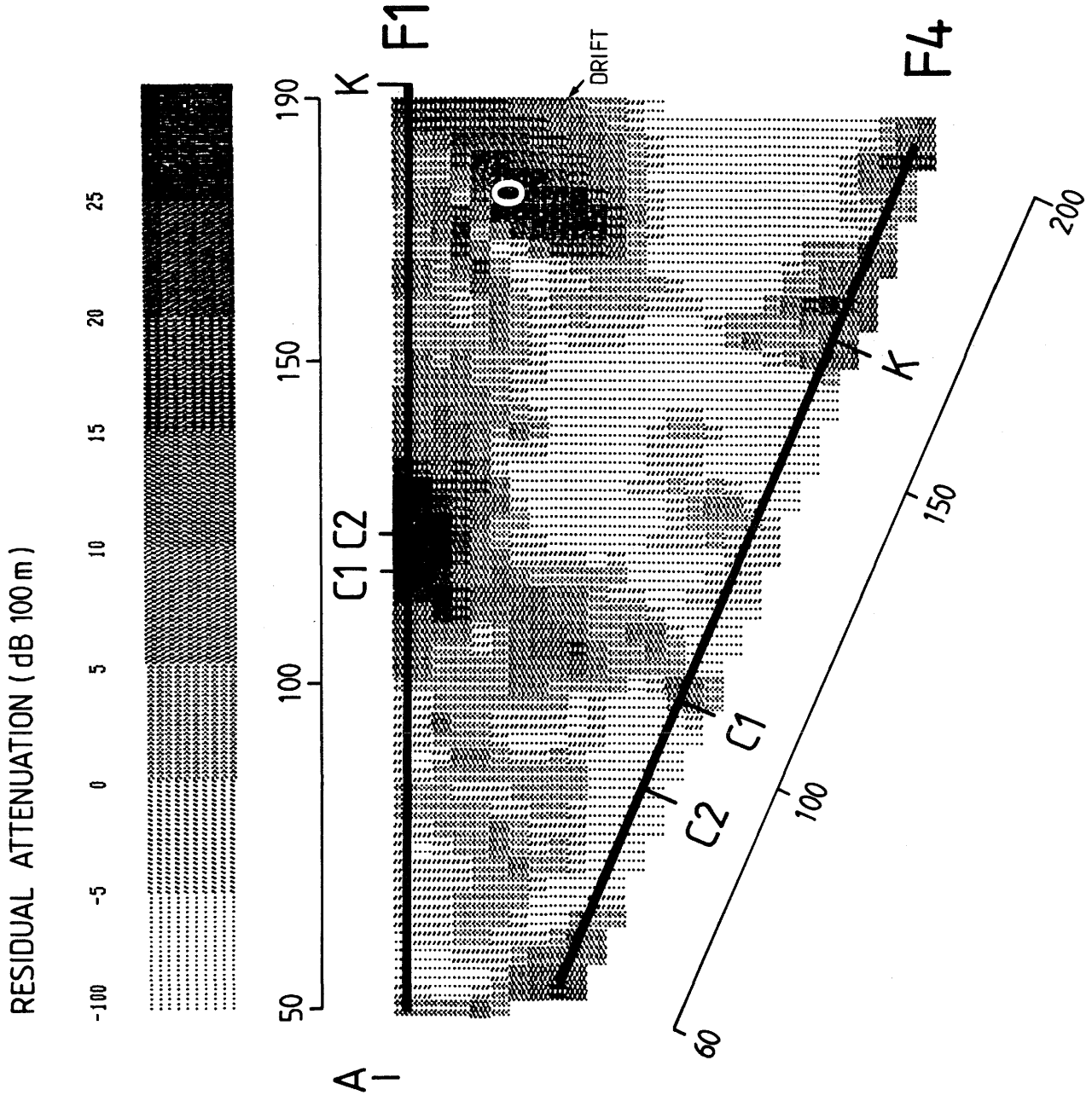


Figure C.2 Tomographic reconstruction of attenuation distribution for the borehole section F4-F1 based on residual amplitude data. Cell size 2.5 m. Center frequency 22 MHz.

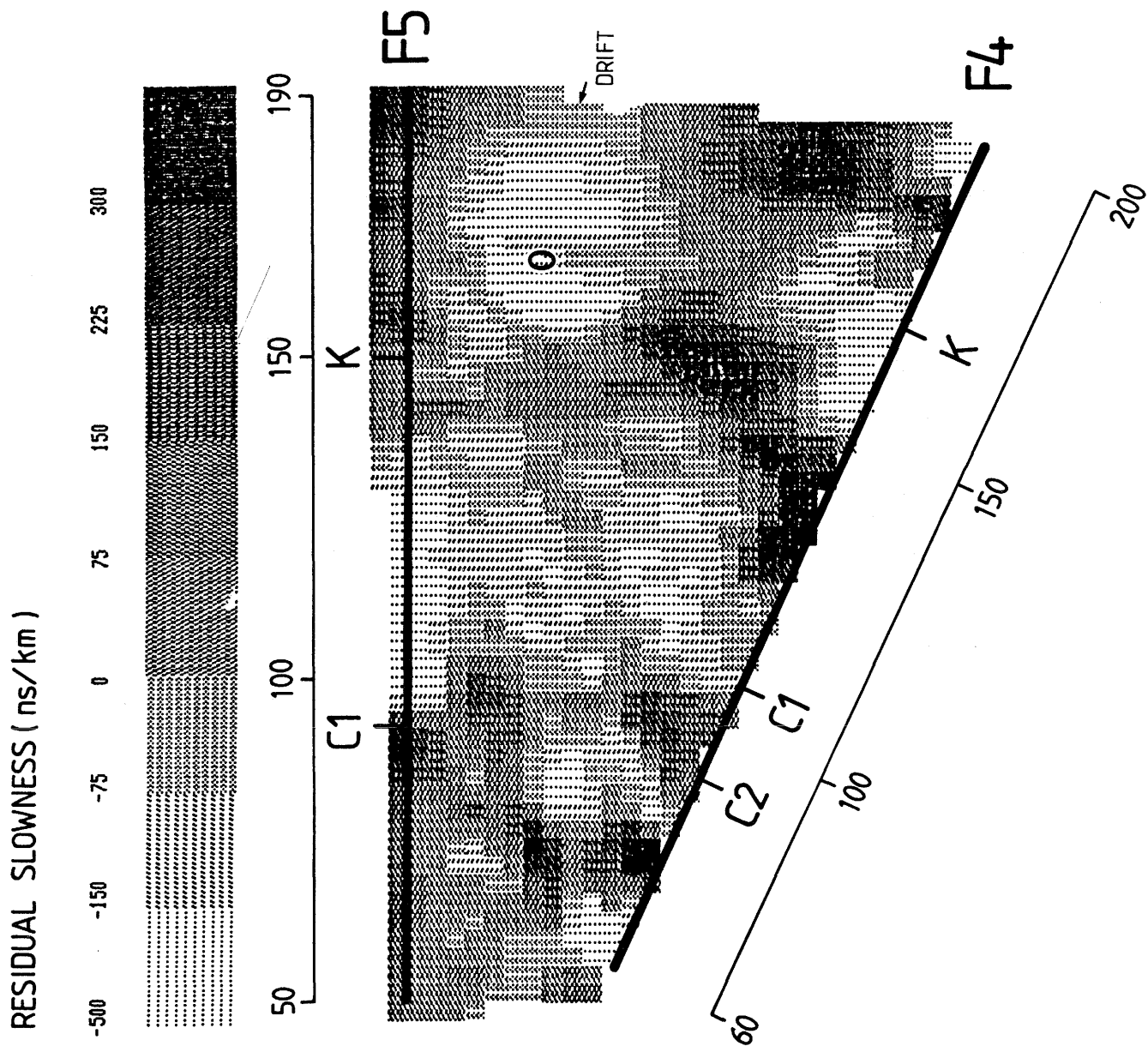


Figure C.3

Tomographic reconstruction of slowness distribution for the borehole section F4-F5 based on residual travel time data. Cell size 2.5 m. Center frequency 22 MHz.

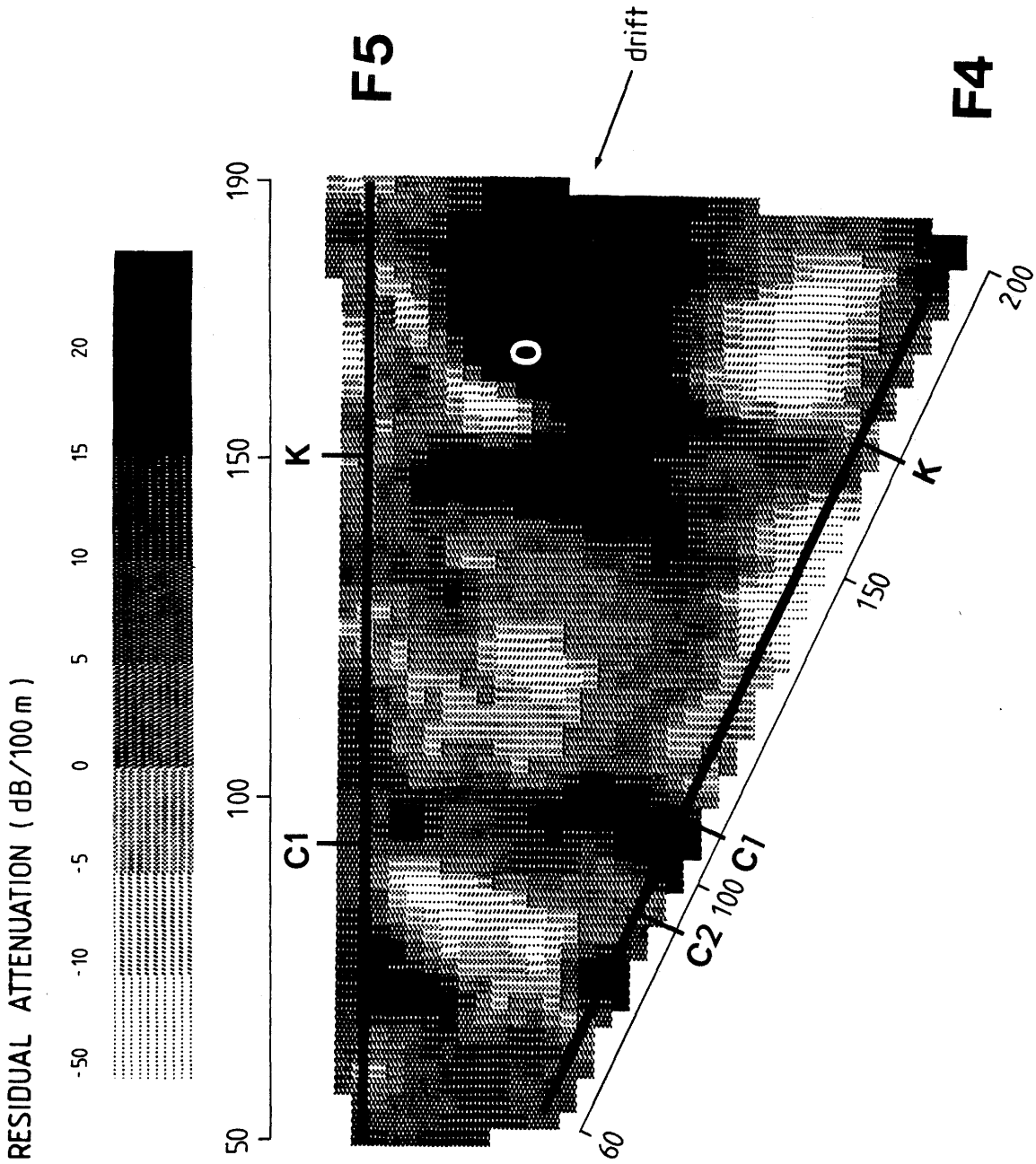


Figure C.4

Tomographic reconstruction of attenuation distribution for the borehole section F4-F5 based on residual amplitude data. Cell size 2.5 m. Center frequency 22 MHz.

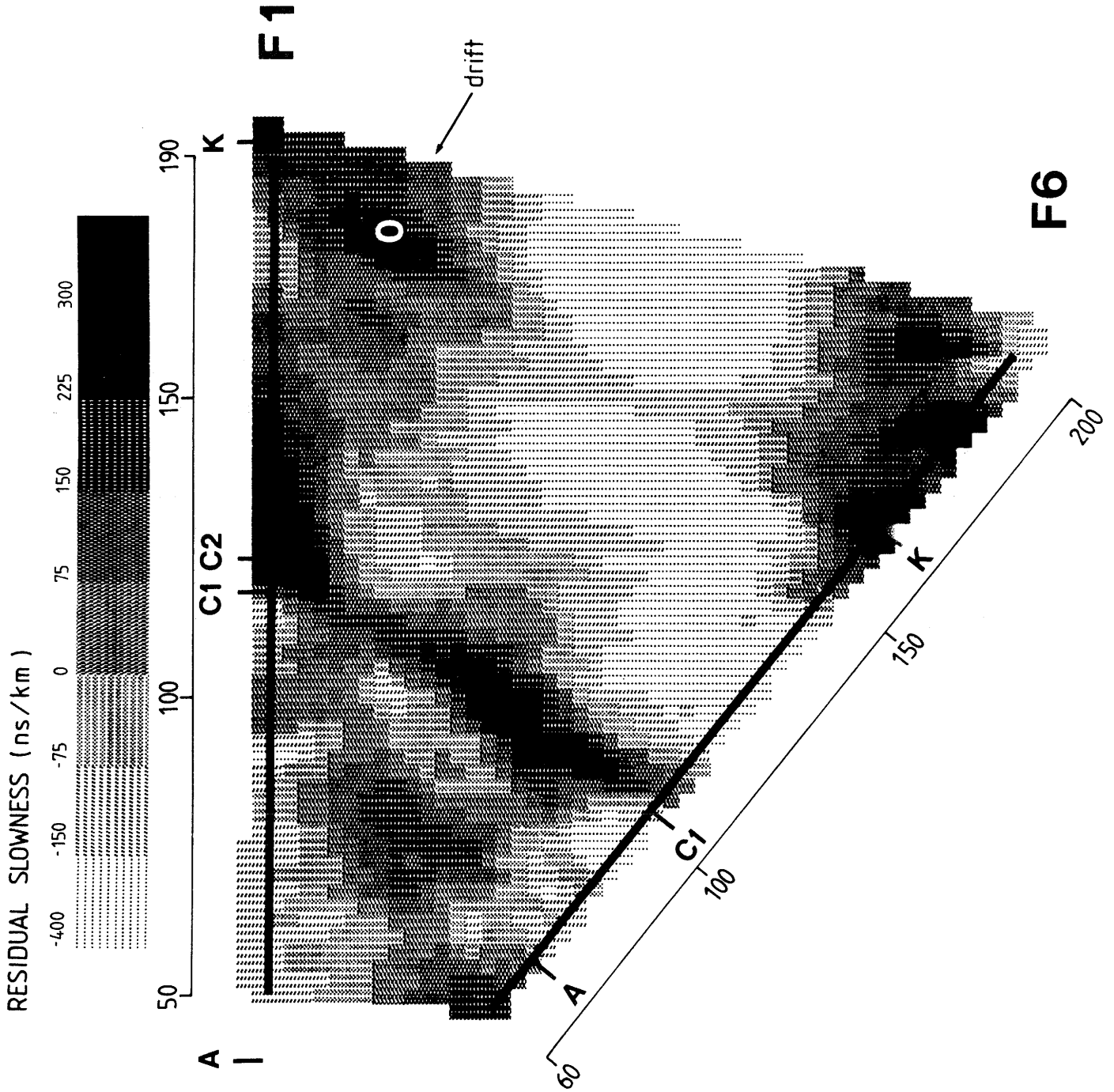


Figure C.5 Tomographic reconstruction of slowness distribution for the borehole section F6-F1 based on residual travel time data. Cell size 2.5 m. Center frequency 22 MHz.

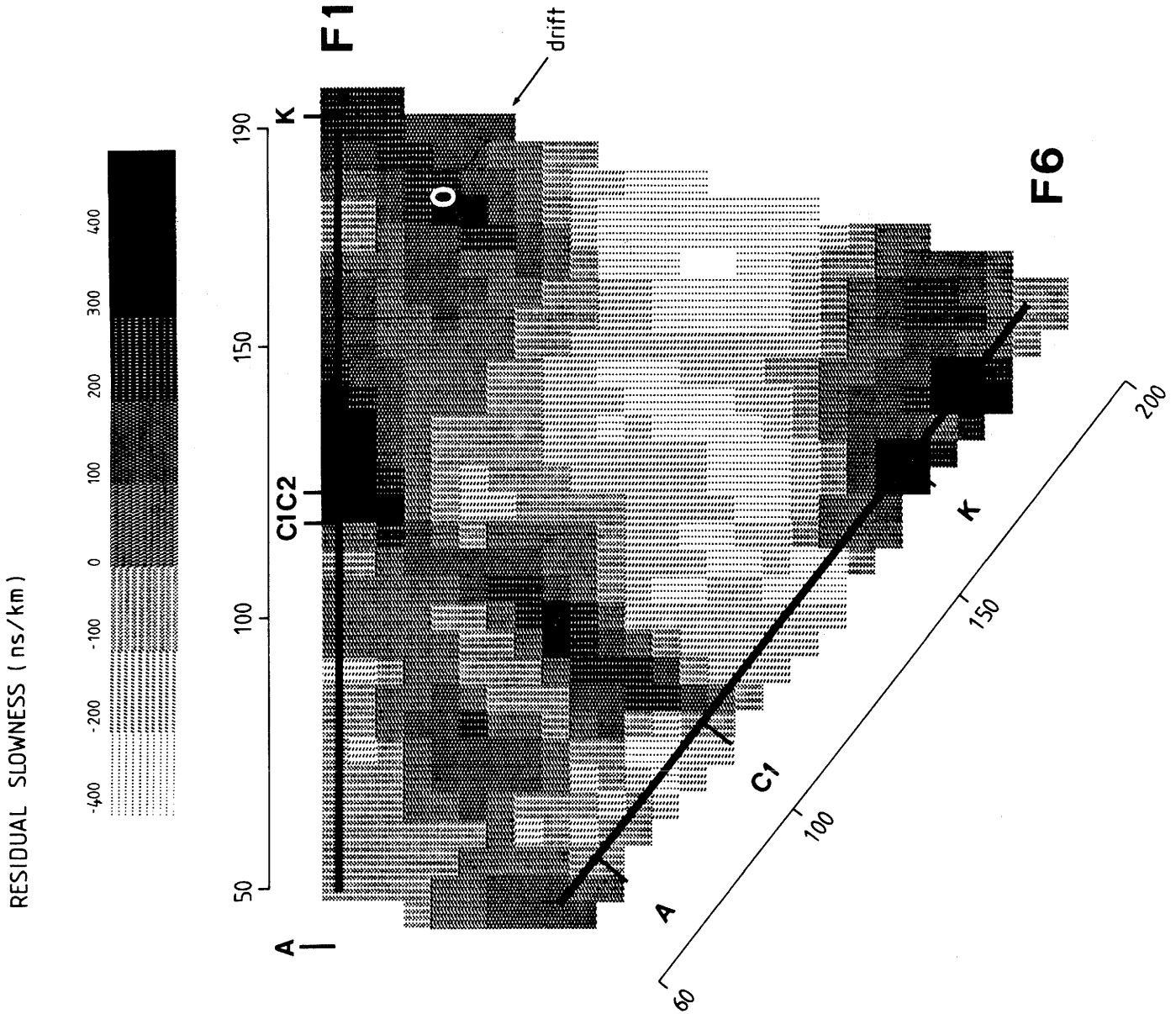


Figure C.6 Tomographic reconstruction of slowness distribution for the borehole section F6-F1 based on residual travel time data. Cell size 5 m. Center frequency 22 MHz. Same input data as for Figure C.5.

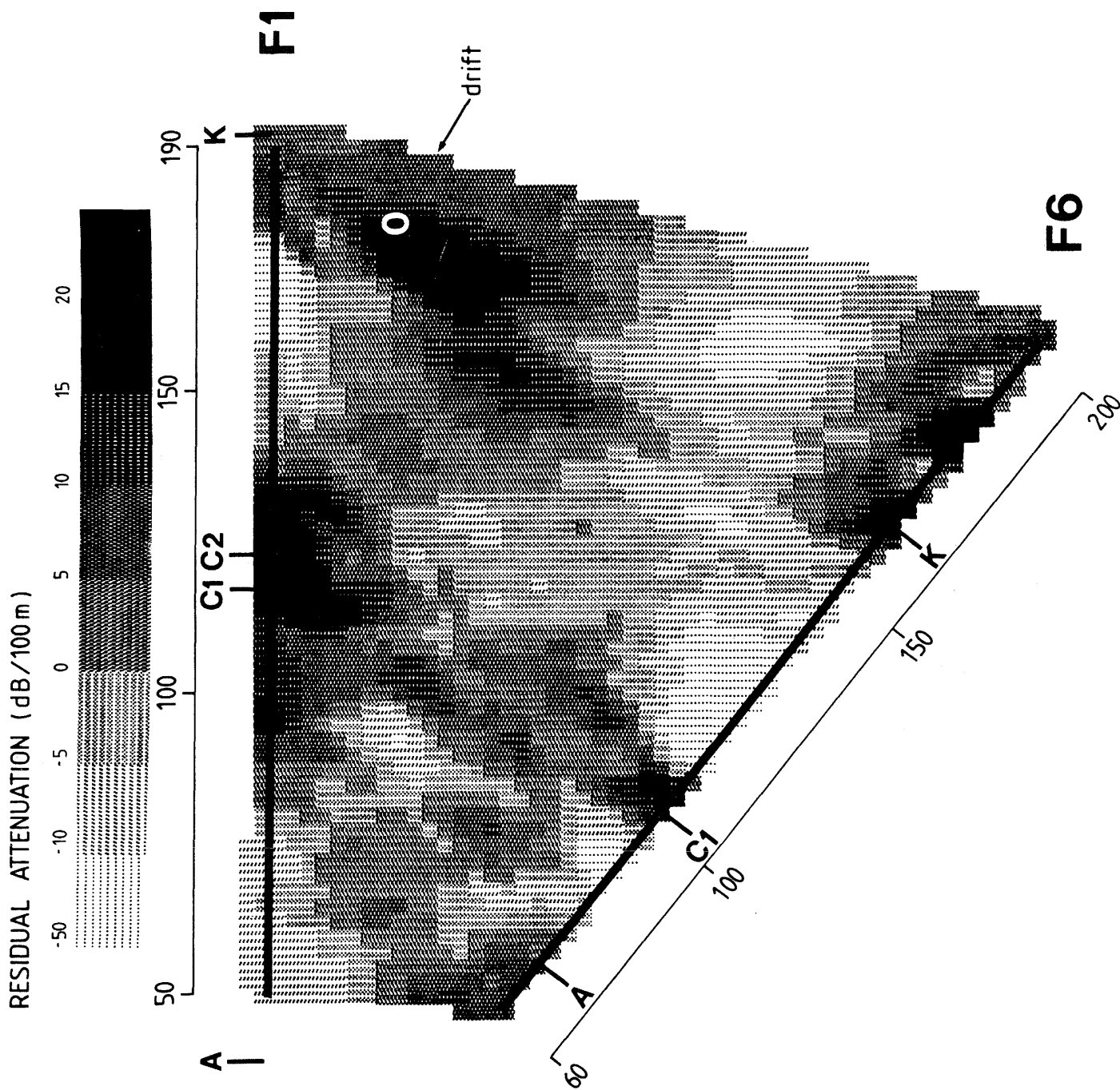


Figure C.7 Tomographic reconstruction of attenuation distribution for the borehole section F6-F1 based on residual amplitude data. Cell size 2.5 m. Center frequency 22 MHz.

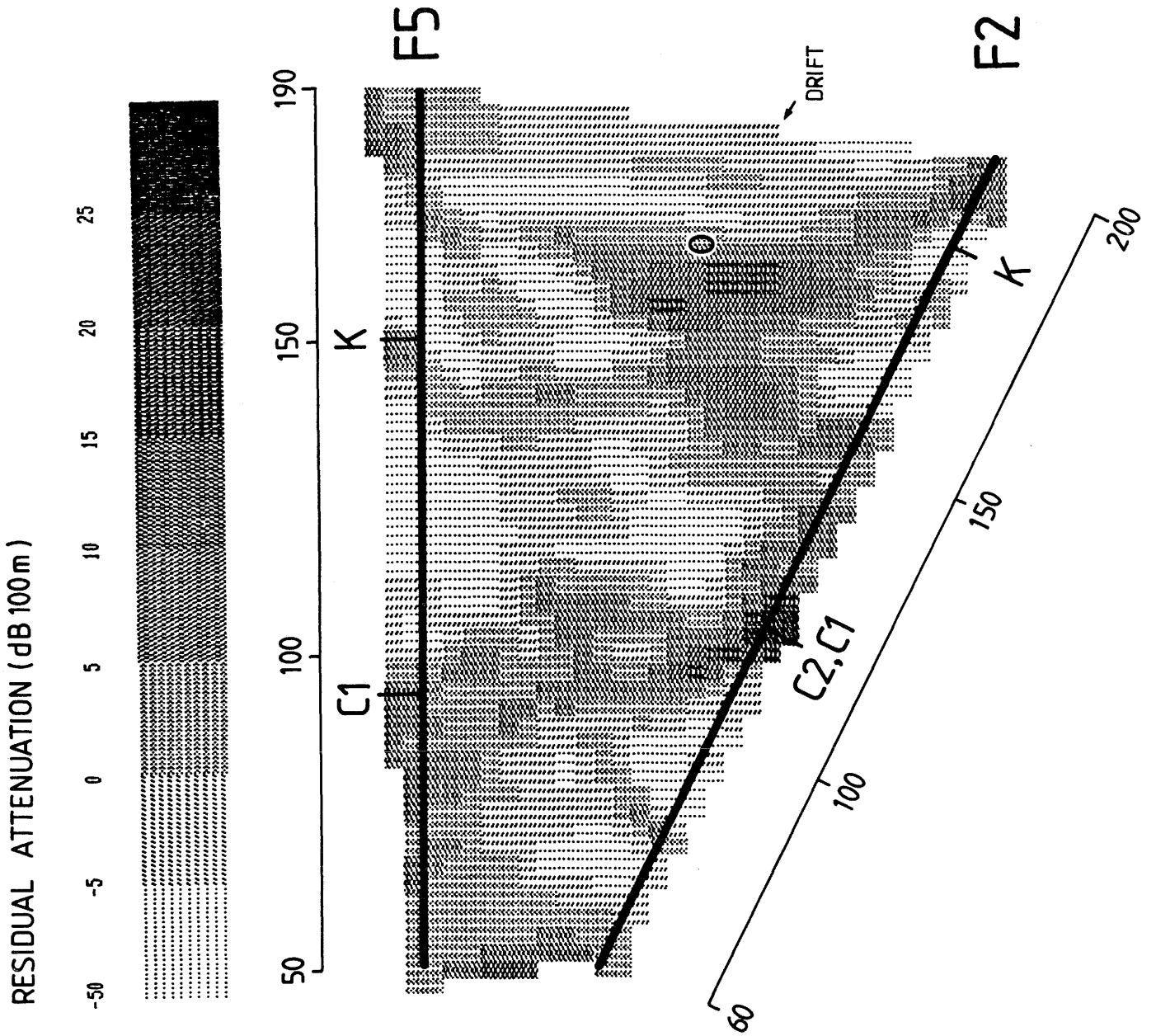


Figure C.9 Tomographic reconstruction of attenuation distribution for the borehole section F2-F5 based on residual amplitude data. Cell size 2.5 m. Center frequency 22 MHz.

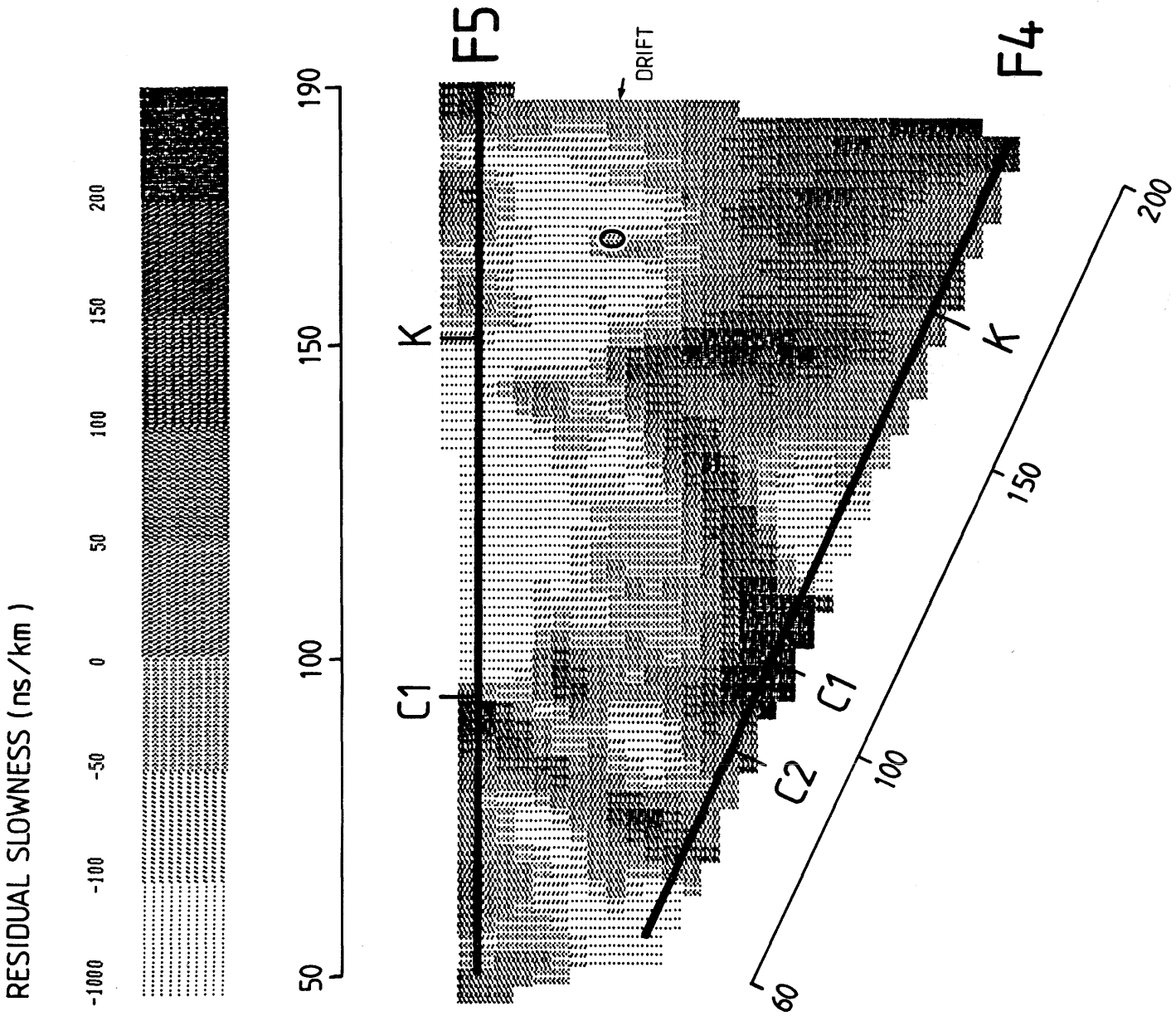


Figure C.10

Tomographic reconstruction of slowness distribution for the borehole section F4-F5 based on residual travel time data. Cell size 2.5 m. Center frequency 60 MHz.

